SCALE-UP OF LATEX REACTORS AND COAGULATORS: A COMBINED CFD-PBE APPROACH

by

Jordan M. Pohn

A thesis submitted to the Department of Chemical Engineering

In conformity with the requirements for

the Degree of Doctor of Philosophy

Queen's University

Kingston, Ontario, Canada

(May, 2012)

Abstract

The successful production of a wide range of polymer latex products relies on the ability to control the rates of particle nucleation, growth and coagulation in order to maintain control over the particle size distribution (PSD). The development of advanced population balance models (PBMs) has simplified this task at the laboratory scale, but commercialization remains challenging as it is difficult to maintain control over the composition (i.e. spatial distributions of reactant concentration) of larger reactors.

The objective of this thesis is to develop and test a combined Computational Fluid Dynamics (CFD) -PBM hybrid modeling framework. This hybrid modeling framework can be used to study the impact of changes in process scale on product quality, as measured by the PSD. The modeling framework developed herein differs from previously-published frameworks in that it uses information computed from species tracking simulations to divide the reactor into a series of interconnected zones, thereby ensuring the reactor is zoned based on a mixing metric. Subsequently, an emulsion polymerization model is solved on this relatively course grid in order to determine the time evolution of the PSD. Examination of shear rate profiles generated using CFD simulation (at varying reactor scales) suggests that, dependent on conditions, mechanically-induced coagulation cannot be neglected at either the laboratory or the commercial scale. However, the coagulation models that are formulated to measure the contributions of both types of coagulation simultaneously are either computationally expensive or inaccurate. For this reason the decision was made to utilize a DLVO-coagulation model in the framework. The second part of the thesis focused on modeling the controlled coagulation of high solids content latexes. POLY3D, a CFD code designed to model the flow of non-Newtonian fluids, was modified to communicate directly with a multi-compartment PBM. The hybrid framework was shown to be well-suited for modeling the controlled coagulation of high solid content latexes in the laminar

regime. It was found that changing the size of the reactor affected the latex PSD obtained at the end of the process. In the third part of the thesis, the framework was adapted to work with Fluent, a commercial CFD code, in order to investigate the scale-up of a styrene emulsion polymerization reaction under isothermal conditions. The simulation results indicated that the ability to maintain good control of the PSD was inversely related to the reactor blend time. While the framework must be adapted further in order to model a wider range of polymerization processes, the value of the framework, in obtaining information that would otherwise be unavailable, was demonstrated.

Co-Authorship

This thesis contains material which has been published in a scientific journal as well as material that is currently being prepared for submission.

Chapter 3: Pohn, J.; Cunningham, M.; McKenna, T. Modeling Orthokinetic Coagulation in a Stirred Tank. Manuscript in preparation for submission.

Chapter 4: Pohn, J.; Heniche, M.; Fradette, L.; Cunningham, M.; McKenna, T. Development of a Computational Framework to Model the Scale-up of High Solid Content Polymer Latex Coagulators. Published in Chemical Engineering & Technology 11 (2010), 1917 – 1930

Chapter 5: Pohn, J.; Cunningham, M.; McKenna, T. Using a Computational Framework to Model the Scale Up of Polymer Latex Reactors. Manuscript in preparation for submission.

Acknowledgements

This thesis represents the culmination of many years of hard work, sprinkled with occasional moments of intellectual creativity. I owe my success to a large number of people. Without their contributions, both large and (seemingly) small, this thesis would not have been written.

I must start off by thanking my supervisors, Timothy McKenna and Michael Cunningham. Both of you were a constant source of intellectual and creative stimulation. I may have tested your patience occasionally, but you always found the time to provide me with honest feedback and encouragement. I hope you find this work a worthy culmination of the effort you invested in me.

I must thank my colleagues and office mates in Kingston for all of their intellectual contributions and the camaraderie they provided. In no particular order: Niels, Jeff, Mary, Nicky, Ula, Eric, Jonas, Dan, Julien, Raul and countless others.

I was fortunate to spend extended periods of time during my thesis in both Lyon and Montreal. I'd like to thank Franck D'Agosto at C2P2 for the time he spent training me in the lab during my stay in Lyon. Although this thesis does not have any NMR spectra (I considered throwing one in gratuitously), the time you spent with me did not go unappreciated. I must express a sincere debt of gratitude to Louis Fradette, Mourad Heniche and all of my colleagues at URPEI. Thank you for taking me in during my nine months in Montreal. The thousands of lines of FORTRAN code that form the foundation of this thesis stand in evidence of your contributions.

To my friends and family, thank you for your loving support and your patience. I'd like to thank my parents, Karen and Stephen. Without your encouragement, I would not have made it to the end of this long journey.

I'd like to dedicate this thesis in memory of my grandfather, Oscar Markovitz. Each time I encountered a roadblock during this journey, stories of your legendary work ethic gave me the strength to surmount all obstacles.

Table of Contents

List of Figures

List of Tables

Nomenclature

a	prefactor parameter
$\mathbf{a}(\mathbf{f}, x, \mathbf{y})$	vector of aggregation terms (part m^{-3} $[x]^{-1}$ s^{-1})
$a(\hat{v}, v_i)$	fraction of chains with $v_{i-1} < \hat{v} < v_i$ to the *i*th class
a_s	minimum area occupied by a surfactant molecule on the particle surface (m^2)
A	Hamaker constant (J)
A_s	area occupied by a surfactant molecule on the particle surface (m^2)
A_{tot}	total particle surface area (m^2 m^{-3})
$b(\hat{v}, v_i)$	fraction of chains with $v_i < \hat{v} < v_{i+1}$ assigned to the *i*th class
b_s	Lagmuir adsorption isotherm parameter (m^3 mol^{-1})
B	birth term (part m^{-3} $[x]^{-1}$ s^{-1})
c	particle concentration (m^{-3})
c_{bulk}	bulk particle concentration (m^{-3})
c_{seed}	seed cell from CFD mesh
C	dimensionless particle concentration
C_i	finite volume cell with centre of r_i
C_{mesh}	total number of mesh cells
$C_{\min}$	minimum number of mesh cells per zone
$C_{\max}$	maximum number of mesh cells per zone
$C_{z,merge}$	number of cells in a zone *z* after a merge attempt
$[CMC]$	critical micelle concentration (mol m^{-3})
$[CMC]_0$	critical micelle concentration in the absence of added ionic species (mol m^{-3})

d_p	particle diameter (m)
D	death term (part m^{-3} $[x]^{-1}$ s^{-1})
D_0	mutual diffusion coefficient between particles (m^2 s^{-1})
$\bar{D}$	particle number average diameter (m)
D_i	particle diameter (m)
D_I	impeller diameter (m)
D_{mp}	diffusivity of monomer in particle phase (m^2 s^{-1})
D_{mw}	diffusivity of monomer in aqueous phase (m^2 s^{-1})
D_{rd}	diffusion coefficient of radical chain end resulting from chemical reaction (m^2 s^{-1})
D_x	x^{th} moment of the particle size distribution
$\mathbf{D}$	diffusion tensor (m^2 s^{-1})
e	charge on a single electron (C)
$\mathbf{e}$	vector of terms to be integrated explicitly (part m^{-3} $[x]^{-1}$ s^{-1})
$[E]$	electrolyte concentration (mol m^{-3})
$\left[EM_i^{\bullet}\right]$	aqueous-phase concentration of exit-derived (desorbed) oligomers of chain length i
$f(\xi,\lambda)$	hydrodynamic interaction potential
$\mathbf{f}_z(r,t)$	vector number density function in zone z (part m^{-3} m^{-1} s^{-1})
$f_{z,m}(r,t)$	number density function for particles containing radicals of type m in zone z (part m^{-3} m^{-1} s^{-1})
f_I	initiator efficiency
F_i	feed rate of species i (kg/s)

F_L	rate of flow exchange in the axial direction ($m^3\ s^{-1}$)
$G(\xi,\lambda)$	hydrodynamic interaction function
h	flux function
$H(\xi,\lambda)$	hydrodynamic interaction function
$He(x)$	Heaviside function
I	intensity of segregation
I	ionic strength ($mol\ m^3$)
$I_{i,j}$	interface between zone *i* and zone *j*
$\left[IM_i^{\bullet}\right]$	aqueous-phase concentration of initiator-derived oligomers of chain length *i*
j_{crit}	critical degree of polymerization for homogenenous nucleation – initiator-derived radicals
j_{Ecrit}	critical degree of polymerization for homogenenous nucleation – exit-derived radicals
k_B	Boltzmann's constant ($J\ K^{-1}$)
k_d	rate coefficient for initiator decomposition in the aqueous phase (s^{-1})
k_{des}	rate coefficient for radical desorption from particles ($m^3\ mol^{-1}\ s^{-1}$)
k_{diff}	rate coefficient for the contribution of reaction diffusion to the overall propagation rate coefficient ($m^3\ mol^{-1}\ s^{-1}$)
$k^i_{e,part}$	entry rate coefficient for *i*-meric radical into a polymer particle ($m^3\ mol^{-1}\ s^{-1}$)
$k^i_{e,mic}$	entry rate coefficient for *i*-meric radical into a surfactant micelle ($m^3\ mol^{-1}\ s^{-1}$)
k_p	particle phase propagation rate coefficient for long chains ($m^3\ mol^{-1}\ s^{-1}$)

k_{p0}	particle phase propagation rate coefficient for monomeric radical (m^3 mol^{-1} s^{-1})
k_{pw}	aqueous phase propagation rate coefficient (m^3 mol^{-1} s^{-1})
k_{pwi}	aqueous phase propagation rate coefficient for *i*-meric radical (m^3 mol^{-1} s^{-1})
k_{pi}	particle phase propagation rate coefficient for *i*-meric radical (m^3 mol^{-1} s^{-1})
k_t	particle phase termination rate coefficient for long chains (m^3 mol^{-1} s^{-1})
k_t^{ij}	particle phase termination rate coefficient between an *i*-meric radical and *j*-meric radical (mol m^{-3} s^{-1})
k_{t0}	termination rate coefficient for monomeric species (m^3 mol^{-1} s^{-1})
k_{tr}	rate coefficient for transfer to monomer (m^3 mol^{-1} s^{-1})
$k_{tw}^{i,j}$	aqueous phase termination rate coefficient between an *i*-meric radical and a *j*-meric radical (mol m^{-3} s^{-1})
$K(x,\mathbf{y})$	rate coefficient of volumetric growth arising from chain propagation (s^{-1})
K_{mic}	partition coefficient of styrene between the micellar and aqueous phases (mol^{-1})
L	end-to-end distance between particles (m)
$\mathbf{m}$	dimensionality vector
$m_{i,j}$	mass of species *i* in phase *j* (kg m^{-3})
M	number of measurement locations
M	number of finite volumes
$[M]_i$	concentration of monomer in phase *I* (mol m^{-3})
$[M]_i^{sat}$	concentration of monomer in phase *i* at saturated conditions (mol m^{-3})
$[mic]$	micelle concentration (mol m^{-3})

Mw_r	molar mass of reactant *r* (kg mol^{-1})
n	nucleation vector
$N(x,t)$	number density function (part m^{-3} $[x]^{-1}$)
n_{agg}	aggregation number of the surfactant
n_i	number of radicals in particle of size *i*
$\bar{n}$	average number of radicals per particle
n_{cutoff}	number of cutoff boundary values
n_{zones}	number of zones
N_A	Avogadro's number (mol^{-1})
N_c	number of carbon chains on a surfactant molecule that reside at the interior of a micelle
N_I	impeller rotational speed (s^{-1})
N_P	total number of particles per unit volume in the system (part m^{-3})
N_r	number of particles containing r radicals (part m^{-3})
$N_{z,i}$	number of particles in cell *i* of zone *z* (part m^{-3})
$N_{z,i}^m$	number of particles of type *m* in cell *i* of zone *z* (part m^{-3})
N_z	number of zones to be created
$N_{z,\min}$	minimum number of zones to be created
$N_{z,\max}$	maximum number of zones to be created
p	pressure (Pa)
p_{ij}	spin ratio
P	power consumed ($J\ s^{-1}$)

Pe	particle Peclet number
q_{yz}	volumetric flow rate from zone y to zone z ($m^3\ s^{-1}$)
$Q(i_z)$	net flow for species i in zone z ($m^3\ s^{-1}$)
$\dot{\mathbf{r}}$	vector of radial growth rates ($m\ s^{-1}$)
r_i	radius of particle i (m)
Δr_i	size of cell i (m)
r_l	lower crossover radius (m)
r_{mic}	radius of micelle (m)
r_{nuc}	radius of nucleated particle (m)
r_s	swollen radius of particle (m)
r_u	upper crossover radius (m)
R	universal gas constant ($J\ mol^{-1}\ K^{-1}$)
R	center-to-center distance between particles (m)
$\mathbf{R}$	kinetic coupling matrix
R_{mic}	rate of micellar nucleation ($mol\ m^{-3}\ s^{-1}$)
$R_{mic,i}$	rate of micellar nucleation due to type-i oligomeric radicals ($mol\ m^{-3}\ s^{-1}$)
R_{hom}	rate of homogeneous nucleation ($mol\ m^{-3}\ s^{-1}$)
$R_{\text{hom},i}$	rate of homogeneous nucleation due to type-i oligomeric radicals ($mol\ m^{-3}\ s^{-1}$)
R_{nuc}	total rate of particle nucleation ($mol\ m^{-3}\ s^{-1}$)
R_{pi}	rate of polymerization in phase i ($mol\ m^{-3}\ s^{-1}$)
R_p	total rate of polymerization ($mol\ m^{-3}\ s^{-1}$)
Re	Reynolds number

s	dimensionless distance between particle surfaces
$\mathbf{s}(\mathbf{f}_z, x, \mathbf{y}_z)_X$	source function vector in zone z for model type X (part m^{-3} $[x]^{-1}$ s^{-1})
$\overline{s}$	average sphere packing coordination number
$[S]$	total surfactant concentration (mol m^{-3})
$\left[S\right]_w$	surfactant concentration in the aqueous phase (mol m^{-3})
t	polymerization time (s)
t_{blend}	reactant blend time (s)
t_{front}	tracer time front (s)
T	temperature (K)
$\left[T_i^{\bullet}\right]$	total radical concentration of length i in the aqueous phase (mol m^{-3})
T_{gi}	glass transition temperature of species i (K)
T_Q	torque (kg m^2 s^{-2})
u'	velocity fluctuation in x direction (m s^{-1})
v	velocity vector (m s^{-1})
$\mathbf{v}_r$	velocity vector in rotating frame (m s^{-1})
v	particle volume (m^3)
$\dot{\mathbf{v}}$	vector of volumetric growth rates (m^3 s^{-1})
v'	velocity fluctuation in y direction (m s^{-1})
$\hat{v}$	unswollen volume of a new particle formed by aggregation (m^3)
v_c	volume of a CFD mesh cell (m^3)
$\mathbf{v}_{conv}$	convective velocity (m s^{-1})
v_i	unswollen volume corresponding to r_i (m^3)

$\mathbf{v}_{\text{int}}$	interaction velocity (m s^{-1})
V_A	attractive potential (V)
V_i	molar volume of species *i* (m^3/mol)
V_{int}	DLVO interaction potential (V)
$\bar{V}_{\text{int}}$	dimensionless DLVO interaction potential
V_f	free volume inside particle system
$V_{f,sat}$	free volume inside particle system when fully-saturated with styrene monomer
V_{fi}	free volume of pure species *i*
$V_{\min}$	minimum volume of a stable particle (m^3)
V_R	reactor volume (m^3)
V_R	DLVO repulsive potential (V)
V_w	volume of aqueous/water phase (m^3)
V_z	total volume of zone *z* (m^3)
w'	velocity fluctutation in *z* direction
W_{ij}	Fuchs' stability ratio
$x_{A,m}$	fraction of component A at measurement location *m*
$\bar{x}_A$	average fraction of component A in a binary mixture
x_i	number fraction of size *i*
X_A	number of additional solubilized monomeric molecules per micelle
$\mathbf{y}_z$	continuous phase vector in zone *z*
z_+	counter-ion valence

z_{feed}	feed zone
z_i	zone *i*
z_{crit}	critical degree of polymerization for entry

Greek Letters

β_{fast}	coagulation rate coefficient between particles *i* and *j* in the absence of particle interaction (m^3 $part^{-1}$ s^{-1})
β_{ij}	coagulation rate coefficient between particles *i* and *j* (m^3 $part^{-1}$ s^{-1})
$\dot{\gamma}$	shear rate (s^{-1})
$\dot{\gamma}_{th}$	characteristic shear thickening time (s)
δ	Stern layer thickness (m)
δ	hydrodynamic interaction boundary layer thickness (m)
$\delta_{i,j}$	Delta Kronecker function
δ_{merge}	homogeneity of merged zones
$\delta\varsigma$	tracer time front homogeneity (s)
ε	rate of turbulent energy dissipation (m^2 s^3)
ε	permittivity of water (s^2 C^2 m^{-1} kg^{-1})
ε_0	vacuum permittivity (s^2 C^2 m^{-1} kg^{-1})
ε_r	relative permittivity of water
$\chi(r)$	hybrid population balance model smoothing function
η	fluid viscosity (kg m^{-1} s^{-1})
η_0	fluid viscosity at zero shear (kg m^{-1} s^{-1})

η_∞	fluid viscosity at infinite shear (kg m^{-1} s^{-1})
η_s	viscosity of aqueous medium (kg m^{-1} s^{-1})
$[\eta]$	intrinsic viscosity
κ	inverse Debye length (m^{-1})
λ	dimensionless particle size ratio
μ_t	turbulent viscosity (kg m^{-1} s^{-1})
ρ	density of continuous phase (kg m^{-3})
ρ_E	rate coefficient of entry of desorption-derived radicals into a latex particle (s^{-1})
ρ_I	rate coefficient of entry of initiator-derived radicals into a latex particle (s^{-1})
ρ_i	density of pure species *i* (kg m^{-3})
ρ_T	rate coefficient of entry of all radicals into a latex particle (s^{-1})
σ	particle surface charge density (C m^{-2})
σ	particle interaction coefficient
σ_r	radius of interaction of reactants (m)
σ_t	turbulent Schmidt number
τ	characteristic shear thinning time (s)
$\bar{\bar{\tau}}$	stress tensor (Pa)
υ	kinematic viscosity (m^2 s^{-1})
Υ	potential correction factor (V)
ξ	dimensionless particle center-to-center distance
ϕ	volume fraction of particles
ϕ_{eff}	effective volume fraction of particles

ϕ_i	volume fraction of species *i* inside a particle
ϕ_m	effective maximum packing fraction
$\phi_{m,hs}$	maximum packing fraction for monodisperse hard spheres
$\phi_{m,i}$	effective maximum packing fraction for monodisperse particles of diameter D_i
ϕ_{ult}	ultimate packing fraction
Φ	time-dependent scalar
Φ_{des}	rate of radical desorption from particles (mol m^{-3} s^{-1})
ψ	particle surface potential (V)
$\mathbf{\Omega}$	angular velocity vector (rad s^{-1})
ζ	zeta potential (V)

Chapter 1

Introduction

Polymer latexes, colloidally-stable dispersions of nanoscale polymer particles dispersed in a continuous medium, are a commercially-important class of materials. Polymer latexes are used in a wide range of applications not limited to interior and exterior surface coatings, paper finishing, adhesives, carpet backing and bulk polymer production.[1] The typical polymer latex recipe is comprised of monomer, water, stabilizer (surfactant), initiator and buffer and most polymer latexes products are produced via emulsion polymerization, although further processing steps (such are particle coagulation) are often required.[2] Early polymer latex formulations and production strategies were often a product of trial and error, perhaps with the aid of an early kinetic model.[3] Today that is no longer the case, as scientists and engineers have a much better grasp on the underlying phenomena that govern the manufacturing process.[4] By carefully manipulating the nucleation, growth and coagulation of polymer particles during all stages of manufacture, the properties of the final latex can be tailored to meet an ever-growing range of applications.

For economic reasons, it is becoming ever more important to increase the solids content in industrial recipes, which requires careful manipulation of the particle size distribution (PSD) at all stages of production.[5, 6] With the assistance of state-of-the-art emulsion polymerization models, i.e. those constructed using a population balance model (PBM) framework,[7, 8] researchers have developed new manufacturing strategies that offer improved control over the particle size distribution.[9] Commercialization of these manufacturing strategies, however, remains a great

challenge because it becomes increasingly difficult to maintain control over reactor composition as the size of the reactor is increased.

Originally, process scale-up strategies were developed using heuristic techniques,[10] and tested via extensive pilot plant experimentation. Today, industry has widely-adopted the use of computational fluid dynamics (CFD) simulation[11] in the scale-up process. CFD simulation, first widely-used in the field of aerodynamics,[12] can predict fluid flow inside stirred tanks, often providing information that is difficult to obtain or unavailable experimentally.[13] CFD simulation is currently used to predict the impact of reactor scale-up on blending time[14] and to identify other mixing problems that may arise[13] (e.g. regions of excessively high shear rates, poor heat transfer). In the production of polymer latexes, the impact of poor mixing on the time evolution of latex PSD can, in theory, be modeled by combining CFD simulation with an appropriate process model. However, the population balance equations that comprise the most advanced polymer latex process models cannot presently be incorporated directly in the CFD code (or vice versa) due to memory restrictions.

These restrictions can be overcome through the clever use of hybrid modeling, where the population balance equations are solved on coarser grid of zonal compartments, which is generated using flow information obtained via CFD simulation. Alexopoulos and Kiparissides[15, 16] and Elgebrandt *et al.*[15, 16] have used CFD simulation to investigate mixing inside emulsion polymerization reactors, identifying regions of high shear where coagulum is more likely to form. These groups subsequently developed hybrid multizonal/CFD models that used the information computed from CFD simulation to study the evolution of latex PSDs under conditions of

inhomogeneous shear. The models were restricted to studying low concentration latexes and the process kinetics were simplified considerably.[16]

The objective of the present work is to develop a combined CFD-PBM modeling framework that incorporates a detailed emulsion polymerization population balance model. The framework is used to investigate the impact of changes in key process length and time scales on the properties of latex products. This was accomplished by developing a set of numerical codes in FORTRAN which were designed to model the nucleation, growth and coagulation of polymer latex particles under different process conditions and interface with different CFD simulation codes. Special attention was paid to the efficiency of the algorithms used within the framework, in order to ensure that the framework could be run on a modern desktop (or laptop) computer, making the approach accessible to a wide audience.

This work represents the first known attempt to develop a hybrid CFD-PBM framework specifically for the purposes of modeling reactor scale-up. With regards to modeling emulsion polymerization, the framework presented in this thesis represents advancement on the previously-published emulsion polymerization hybrid CFD-PBM models found in the literature.[15, 17] First, the model presented in this work is capable of the polymerization and coagulation of polymer latexes over a wider range of conditions (e.g. low and high solids contents). Second, the generation of the network-of-zones (the grid on which the PBM is solved) can be generated automatically using data from transient species blending simulations.

The remainder of the thesis is comprised as follows:

- Chapter 2 is a bibliographic review and overview covering emulsion polymerization, computational fluid dynamics and fluid mixing.
- Chapter 3 deals with the modeling of shear-induced coagulation, as this mechanism is typically neglected in the formulation of emulsion polymerization PBMs.[7] CFD simulation is used to investigate the changes in the distribution of shear forces within in a reactor as the process is scaled-up to assess the importance of shear-induced coagulation at both the laboratory and commercial scales. Even under conditions where shear-induced coagulation is known to be important, modeling particle coagulation in flow conditions where both electrostatic and shear-induced forces interact with each other remains a challenge. To begin addressing this challenge, the modeling predictions of a computationally-efficient coagulation kernel are compared to a recently-developed coagulation model that offers improved predictive capabilities in order to determine if the computationally-efficient kernel could be incorporated into a PBM.
- Chapter 4 discusses, in detail, the construction of a hybrid CFD-population balance model framework. The framework was developed specifically to study non-Newtonian latexes and the POLY3D CFD simulation code was extensively modified in order to function within the framework environment. The hybrid multizonal/CFD framework was used to investigate the effect of vessel scale on the deliberate coagulation of a high solids content latex.
- Chapter 5 builds on the framework developed in the previous chapter. An advanced automatic zoning procedure was developed in order to zone the reactor using the results of species tracking simulations, which is an original approach not employed in

previously-published hybrid modeling frameworks. The hybrid multizonal/CFD framework is used to investigate the impact of reactor scale-up on the production of a polystyrene latex produced via emulsion polymerization.

- Chapter 6 is a summary of the thesis' main conclusions and a list of recommended directions for future study.

Chapter 2

Literature Review

2.1 Polymer Lattices

2.1.1 Early History

The production of synthetic polymer latexes, as a means of developing an alternative to natural rubber, began shortly following the conclusion of World War I with the development of the emulsion polymerization (EP) process technique. Rubber occurs in nature as latex, so the hope was that the mechanical properties of synthetic rubbers would be improved if they were produced under conditions in which the final product resembled the natural product, at least in appearance. In addition to improved product properties, emulsion polymerization was found to sport a number of additional advantages over bulk and solution polymerization, mainly higher rates of productivity and controllability. The outbreak of World War II led to a world-wide natural rubber shortage, which motivated the United States government to form a synthetic rubber program that brought rubber-manufacturing and oil companies together in a cooperative effort. While the main objective of this program was to guarantee a supply of rubber for the war effort, the extensive amount of research carried out by industry and academia during World War II established emulsion polymerization and polymer latex technology as active fields of research following the end of the war. Much of our understanding of the underlying mechanisms of emulsion polymerization is a result of the fundamental research carried out by Harkins,[18] Smith and Ewart.[3] In the years following the end of World War II, researchers extended the range of products and applications that made use of emulsion polymerization technology. Today, a wide range of synthetic latexes, with rubbery and non-rubbery polymers, are produced using emulsion polymerization. Beyond the production of bulk polymer, the range of applications includes[1]
[1]

paints, coatings (including paper finishing), adhesives and carpet backing, with annual production exceeding 20 million tonnes.{{38 de la Cal, J.C. 2005}}

2.1.2 Emulsion Polymerization Fundamentals

A typical industrial emulsion polymerization recipe contains monomer, water, surfactant, initiator and additives, such as buffers and chain transfer agents. Commercial scale emulsion polymerization is typically carried out in large stirred tank vessels operating in semi-continuous mode, although batch and continuous processes are also used. The monomer is dispersed in water along with surfactants (typically anionic or nonionic or a combination of both), forming emulsified monomer droplets (~ 1 – 10 μm in diameter).[19] The surfactant will partition between the surface of the droplets and the aqueous phase. If the surfactant concentration exceeds the critical micelle concentration (CMC), the point at which the surfactant completely covers the monomer droplets and saturates the aqueous phase, micelles will form. The interior of the micelles is hydrophobic and hence the micelles will swell with monomer. Additionally, a small fraction of the total monomer in the system will partition into the aqueous phase, the amount being dependent on monomer solubility. Polymerization is usually initiated using a water soluble initiator, although oil-soluble initiators may be used.{{38 de la Cal, J.C. 2005}} In terms of the decomposition mechanism, thermal initiators (such as potassium persulphate) are the most common type of initiator employed. Redox initiators, such as hydrogen peroxide / ascorbic acid, may be employed when the polymerization is carried out at a lower temperature.[20]

The original EP reaction theory proposed by Harkins sought to divide the EP process into three intervals. While the interval model is applicable to *ab-initio* (non-seeded) batch emulsion polymerization only, the interval theory approach still serves as a helpful starting point for understanding a wider range of EP processes. Interval I is the particle nucleation stage, Interval II

is the particle growth stage, while Interval III is marked by the consumption of remaining monomer in the droplets.

The primary radicals derived from initiator decomposition react with the monomer dissolved in the aqueous phase, adding monomer units. Once a sufficient number of monomer units have been added, the oligomer becomes surface active and is capable of entering the monomer-swollen micelles (if present) to form precursor particles. This is known as micellar or heterogeneous nucleation. The length of the critical length chain length at which the oligomer becomes surface active is dependent on the water solubility of the monomer, increasing with water solubility; for reference, styrene becomes surface active after two chain units have been added. Entry into micelles is statistically favoured over entry into the monomer droplets because total surface area of the droplets ($\sim 10^5$ m^2 / m^3) is relatively small in comparison to the total surface area of the micelles ($\sim 10^8$ m^2/m^3).[19] Surface active oligomers will continue to grow in the aqueous phase, if they are not captured by a micelle or another particle. However, when an aqueous phase oligomer reaches a critical chain length, it will become water insoluble and undergo a coil-to-globule transition, excluding water and becoming a precursor particle.[21] This mechanism is known as homogeneous nucleation. The critical chain length is, like the surface active chain length, directly proportional to the water solubility of the monomer; for styrene, the critical chain length is around five added monomer units. Homogeneous nucleation is dominant when operating below the CMC, as micelles are not present. When operating slightly below the CMC, local micelles may form due to inhomogeneous distribution of the surfactant. Above the CMC, heterogeneous (micellar) nucleation is the dominant mechanism, although homogeneous nucleation still occurs.[22] Micelles that have not been nucleated will dissociate to stabilize the growing particles.

Once the micelles have been depleted, new particles will not form through heterogeneous nucleation, although the micelle population may be renewed when particles coagulate and the total particle surface area is reduced. In systems dominated by homogeneous nucleation, particle formation may continue to occur throughout the course of polymerization, but the precursor particles may quickly coagulate in the absence of free surfactant and will essentially reach a steady-state value.[21] The timescale of monomer diffusion is rapid compared to the rate of polymerization inside the particles. As an example, for styrene EP at 50 ℃, the rate at which monomer molecules are consumed per particle is approximately 1.4×10^4 s^{-1}, while the maximum rate at which monomer molecules can replenished per particle is in the order of 1.0×10^9 s^{-1} (see Gilbert,[4] page 52 for a details). When the maximum rate of monomer replenishment is many orders of magnitude higher than the rate of monomer consumption, the monomer droplets act as monomer stores, keeping the monomer concentration inside particles nearly constant (this is not always the case; see Zubitur *et al.*[23] for a discussion of diffusional limitations).

Once the monomer droplets have been completely depleted the remaining monomer in the particles is exhausted. The onset of the gel effect,[24] a decrease in the bimolecular termination rate due to the viscous environment inside the particles, may lead to an increased rate of polymerization, more-than-offsetting the decrease in monomer concentration inside the particles. Polymerization is ideally carried out as close to 100% conversion as possible, although a limiting conversion may be encountered if the glass transition temperature of the polymer is higher than the reaction temperature. In many end-use applications residual monomer poses a health hazard,

necessitating its removal via stripping, which adds a significant expense to the manufacturing process.

Emulsion polymerization has inherent advantages over solution and bulk polymerization. The use of water as the dispersion medium (as opposed to volatile organic solvents) leads to a reduced environmental impact and low product odor, and effectively functions as a heat sink during polymerization. The viscosity of the product latexes is reduced compared to bulk and solution polymerization processes, allowing for easier handling operation, especially in the case of rubbery and/or film forming materials. The maximum attainable conversion is higher, so emulsion polymerization products contain lower volatile organic compounds (VOCs) compared to products produced using solution or bulk polymerization. Furthermore, under certain conditions, the radicals in emulsion polymerization are compartmentalized and cannot terminate with radicals existing within another particle. This can lead to higher polymerization rates and higher average molecular weights than what would be achievable using bulk or solution polymerization.

2.1.3 Stability of Polymer Latexes

Polymer latexes are thermodynamically unstable. The intermolecular forces of attraction cause molecules in the condensed state to cohere together.[2] Thus, there is a thermodynamic tendency for the polymer particles to coagulate together, eventually resulting in complete phase separation. The aggregation and coalescence of polymer particles reduces the total interfacial area between the particle and the aqueous phases, thereby reducing the total Gibbs free energy of the system. The mechanism by which aggregation and coalescence occurs is the Brownian motion of the

particles, although velocity gradients in the flow field at the microscopic scale (on the order of particle diameter) may enhance the motion of particles relative to one another. While most polymer latexes are thermodynamically unstable, they are kinetically stable; that is, the rate at which the system proceeds towards thermodynamic equilibrium is sufficiently retarded such that it is not uncommon for a polymer latex product to have a shelf life measured in years. The source of this kinetic stability is the presence of a potential energy barrier which discourages particles from approaching one another closely. The barrier arises from a balance between attractive and repulsive forces; as a general rule, the higher the potential energy barrier, the more stable the latex.

The forces of attraction acting between particles in a polymer solution are collectively known van Der Waals forces, which arise from electric dipoles in the atoms. The electric dipoles may be permanent, induced by other molecules or simply a result of fluctuations in the atoms' electron clouds. The magnitude of the van Der Waals forces depends on the composition and shape of the polymer particles and the composition of the medium in which they are dispersed.[2] The forces of repulsion which act between particles can be grouped into four types: (i) electrostatic forces, which depend on the presence of an electric charge at the surface of the particles; (ii) steric forces, which arise from the presence of hydrophilic molecules bound to the surface of the particles; (iii) depletion forces, which arise from the presence of hydrophilic macromolecules dissolved in the aqueous phase; (iv) solvation forces, which arise from the binding of molecules of the dispersion medium to the surface of the particles. Researchers have developed quantitative models for electrostatic and steric stabilization, but the stability conferred through the depletion and solvation forces is difficult to quantify. In particular, depletion stabilization is difficult to

differentiate from steric stabilization due to the tendency of hydrophilic molecules that are dissolved in the aqueous media to adsorb on the surface of the particles.[2]

2.1.4 High Solids Content Latexes

Natural rubber latex, when it flows out from the tree, is only ~30 wt.% polymer, the remainder being mostly water.[2] One of the key developments that led to the commercial exploitation of natural rubber in the earlier 20th century was the discovery of industrially-feasible methods whereby natural rubber latexes could be concentrated to ~60 wt.% polymer without compromising the stability of the latex. For both natural and synthetic polymer latexes, solids concentration is often a key consideration when developing and manufacturing commercially exploitable latexes for two reasons: (i) the production and transport of concentrated latexes is more economical, an especially-important consideration for manufacturers of commodity-grade latexes; (ii) high solid content latexes are uniquely-suited to a wide range of applications (for example, fast-drying paints and coatings). For many synthetic latexes, however, there is a practical loading limit, typically around 55 vol.-%, above which the latex becomes difficult to process due to a sharp increase in latex viscosity and less colloidally-stable as a result of the increasing frequency of particle collisions.[25] This upper loading limit is strongly dependent on the particle size distribution (PSD) and the nature of the stabilizing layer (surfactant). One advantage inherent to synthetic polymer latexes is the ability to control the PSD of the latex product by manipulating the manufacturing process. Recently published results suggest that it is possible to prepare low viscosity, stable latexes with solid loading above 70 vol.-% if the PSD is well-engineered.[26, 27]

Hard (non-deformable) spheres can pack in a variety of ways, ranging from simple cubic (SC; $\phi_m = 0.52$) to face-centered cubic (FCC; $\phi_m = 0.74$), amongst other packing arrangements. At $\phi = \phi_m$ the particles are unable to move past one another, corresponding to infinite viscosity. It has been demonstrated experimentally and computationally that if the hard spheres are introduced into a control volume and gently shaken they will pack randomly; some of the spheres will arrange themselves in a SC scheme and others will take on the FCC packing arrangement; the resulting arrangement is referred to as random close packing (RCP; $\phi_m \approx 0.64$).[28] At high shear limits, however, the energy imparted by the mean flow will cause the particles to align in a denser random packing structure ($\phi_m = 0.71$);[5, 29] these aligned structures are also responsible for the shear thinning.

The stabilization layer surrounding the latex particle is deformable under shear, so latexes are not considered hard spheres; rather they behave as soft (deformable) spheres.[30] Due to this extra layer, the effective volume faction (ϕ_{eff}), is greater than the volume fraction of the solid particles alone (ϕ):

$$\phi_{eff} = \phi\left(1 + \frac{t_s}{r_s}\right)^3 \tag{2.1}$$

where t_s is the thickness of the stabilizing layer. For particles that are stabilized with non-ionic surfactant, t_s is a function of the volume fraction ϕ and the shear rate $\dot{\gamma}$, although at high shear rates t_s is influenced by volume fraction only.[5] When ionic stabilization is present, $t_s = \kappa^{-1}$, the Debye length. The Debye length quantifies the thickness of the counter-ion layer that surrounds the charged particle surface and is typically on the order of 10^{-9} m to 10^{-8} m thick. When

describing the packing limits of soft sphere systems, it is important to note that the packing limits are based on the effective volume fraction (ϕ_{eff}), thus the maximum packing fraction of soft sphere systems is always less than the maximum packing fraction of hard sphere systems. Equation (2.1) states that a stabilizer layer of a given thickness will have a greater impact on the effective packing fraction of a system of small particles compared to a system of large particles, as it takes up a relatively higher volume fraction for small particles than for large ones. For a given fraction of surfactant and ionic strength, all things being equal, the maximum packing fraction of latex particles increases as the particle size increases.

Bimodal and multimodal packing arrangements, with smaller particles filling the interstices that exist in the large particle lattice, offer the potential for increased packing density (a higher maximum packing fraction) compared to monodisperse latexes with narrow PSDs. This is not always the case however. The maximum packing fraction is determined by the thickness of the stabilizer layer and the PSD. Schneider *et al.* demonstrated that a poorly adjusted PSD for a bimodal system (i.e. too many very small particles or "fines") may have a lower maximum packing fraction than a monomodal PSD.[31] The maximum packing fraction is highest when there are just enough small particles to fill all of the interstices of the large particle lattice; research has shown this occurs when volume fraction ratio of large to small particles is around 4 – 5.[32] The size ratio between the large and small particles is just as important as the volume fraction ratio. The small particles must be small enough to fit inside the interstices within the large particle lattice, however if the small particles are too small, multiple occupancy of the interstices may actually push the large particle lattice apart,[28] as illustrated schematically in Figure 1. According to experiments performed by Greenwood *et al.*, the optimal diameter ratio (d_l / d_s) between the

large and small particles is around 6 – 8.[28, 32] For trimodal latexes (three discrete particle populations), experimental studies suggest that latex viscosity is minimized when the latex is composed of 10 - 15 vol.-% small particles, 0 - 10 vol.-% medium particles and 75 - 80 vol.-% large particles, with a diameter ratio of 10 between the large and small particles and a diameter ratio of 1.8 between the large and medium particles. Not all HSC latexes are bimodal or trimodal. It is possible to prepare HSC latexes (~ 70% solids) with monomodal PSDs; Ouzineb showed that very broad monomodal systems can have low viscosities and high solid fractions.[6]

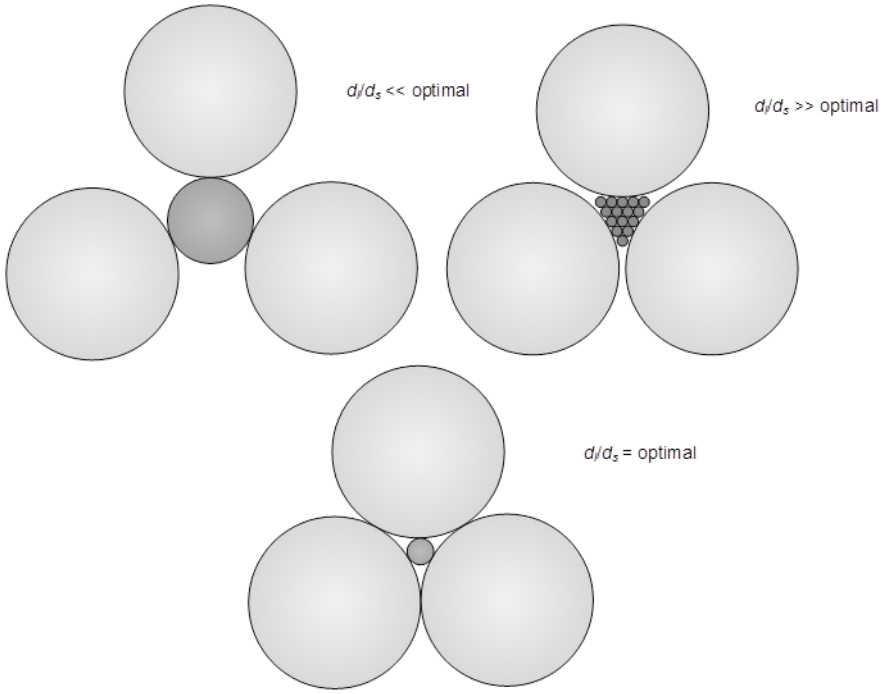

Figure 2.1. Simple schematic illustrating the effect of diameter ratio on a bimodal packing arrangement.

Bimodal and multimodal latexes can be prepared using a number of approaches. Conceptually, the simplest way to produce bimodal and multimodal HSC latexes is to blend seed latexes

together and concentrate them through evaporation under vacuum, an energy-intensive operation. Schneider *et al.*[33] utilized this approach to prepare concentrated pressure sensitive adhesives (78% BA, 19.5% MMA, 2.5% AA) with trimodal PSDs. While conceptually simple, the blending and evaporation approach is unfeasible for commercial production. Concentrated latexes can also be prepared through the growth of multi-modal seed populations in semi-continuous operation. It is extremely difficult to obtain a solid content above 50% with a batch configuration due to uncontrollable homogeneous nucleation (controlling the PSD is key obtaining high solids, as discussed above). In semi-continuous operation the surfactant concentration can be controlled, ensuring the free surfactant concentration remains low enough to maintain control over the formation of new particle. Homogeneous nucleation is essentially unavoidable in the presence of water soluble monomer however the feed rates and types of initiator and surfactant can be adjusted to control whether or not these particles are stabilized. A variation on this approach is to create a large particle seed via *ab initio* emulsion polymerization (semi-continuous operation) then create secondary and tertiary populations through *in situ* nucleation, typically accomplished with a shot of surfactant and monomer. Once all of the particle populations are present, large and small particle alike are grown simultaneously through the continuous addition of monomer (and surfactant) until the desired solid content and PSD are obtained. *Ceteris peribus*, the smaller particles will grow faster, as their higher total surface area leads to preferential radical capture. This approach is popular in industry since it is outwardly the simplest process with the fewest processing and handling steps.[30] Due to the high commercial interest in concentrated multimodal latexes, much of the early research is found in patents rather than the open literature. For an overview of the patents in this field, refer to the review by Guyot *et al.*[30] or Schneider *et al.*[34] Recently there have been some notable studies published in the open literature. Schneider *et al.*

produced a four-part study of HSC latexes in emulsion that included investigations into the synthesis of primary particle seeds[35] and concentrated lattices[34] and the role of oil-soluble initiators in maximizing solids content and latex robustness.[33] Together these papers provide a framework for producing concentrated latexes (> 70 wt.-% polymer) with reasonably low viscosities (between 0.3 and 1.0 Pa-s at a shear rate of 20 s^{-1}). Boutti *et al.*[9, 36, 37] proposed a procedure that can be used to synthesize low viscosity (less than 1.5 Pa-s at a shear rate of 20 s^{-1}) bimodal BA/MMA/MAA latexes with very high solid contents over 70 wt.-% without the use of seed particles, such that the entire process is carried out in a single reactor. Ai *et al.*[27] prepared poly(MMA/BA/AA)/poly(styrene/AA) composite latexes with a solid content of 70 wt.-% and demonstrated that the two-phase structure of the corresponding latex film led to the formation of an integral film at room temperature that sported an improved mechanical strength over the non-composite poly(MMA/BA/AA) latex film.

2.2 Modeling Emulsion Polymerization

2.2.1 Overview of Emulsion Polymerization Kinetics

The polymerization in emulsion systems follows the same basic mechanisms as in bulk polymerization, with the key difference being compartmentalization; that is, radicals existing in one particle cannot terminate with the radicals located in other particles. In bulk and solution polymerization, the rate of polymerization (per unit volume of aqueous phase) is normally defined as the rate of consumption of monomer:

$$R_p = -\frac{d[M]}{dt} = k_p[M][R\cdot] \tag{2.2}$$

where k_p is the propagation rate coefficient, $[M]$ is the concentration of monomer and $[R\cdot]$ is the total radical concentration. In emulsion polymerization (most cases) nearly all polymerization occurs in the particle phase so $[M]$ is replaced with $[M]_p$ and the total radical concentration is $\bar{n}N_p / N_A$, where is the $\bar{n}$ average number of radicals per particle, N_p is the total particle concentration per unit volume of aqueous phase (e.g. m^{-3}) and N_A is Avogadro's number. When modeling emulsion processes that require more than one monomer, the rate expression must be modified. For an example, refer to the modified rate expression based upon the Mayo-Lewis terminal model,[38] which is available in the literature.[1]

Smith and Ewart[3] developed a set of differential equations to track the number of particles containing r free radicals (N_r) based on the adsorption of radicals from the aqueous phase, desorption of free radicals into the aqueous and termination of free radicals within the particles. The population of the latex particles is normalized such that $\sum_{r=0}^{\infty} N_r = 1$ and the average number of radicals per particle is given by $\bar{n} = \sum_{r=1}^{\infty} rN_r$. A population balance takes on the following form:

$$\begin{aligned}\frac{dN_r}{dt} = &\left[N_{r-1} - N_r\right]\rho_T + \left[(r+1)N_{r+1} - rN_r\right]k_{des} \\ &+ \left[(r+2)(r+1)N_{r+2} - r(r-1)N_r\right]k_t\end{aligned} \tag{2.3}$$

Where ρ_T is the average rate of entry of free radicals into the particles, k_{des} is the rate coefficient of desorption of free radicals out of the particles and k_t is the relative rate coefficient

for termination inside the particles. These rate coefficients are dependent on a number of variables including $[I]$ (initiator concentration), N_p, d_p (particle diameter), and $\bar{n}$ itself. At pseudo steady-state ($dN_r / dt = 0$), Smith and Ewart found that there were three limiting cases:

Case 1: $\bar{n} \ll 0.5$ (fast desorption; $\rho_T \ll k_{des}$)

Case 2: $\bar{n} = 0.5$ (no desorption and fast termination; $k_{des} \ll \rho_T \ll k_t$)

Case 3: $\bar{n} \gg 0.5$ (fast absorption relative to termination; $\rho_T \gg k_t$)

Equation (2.3) and the Smith-Ewart limiting cases are valid only under the assumption that radical loss by termination can be expressed using a single rate coefficient, k_t (i.e. the rate coefficient is independent of chain length). It is currently accepted however that the termination coefficient depends on the degrees of polymerization of the two terminating chains.[39] Therefore Equation (2.3) must not only track the number of particles with radicals per particle *r*, but also the number of particles $N^r_{1,2,3,\ldots,n}$ with a degree of polymerization of 1,2,...,*n*. The pseudo-first-order rate coefficient will strongly depend on $N^r_{1,2,3,\ldots,n}$, making Equation (2.3) invalid. However almost every emulsion polymerization system can be categorized as approximately fitting one of two simplifying limits: 'zero-one' and 'pseudo-bulk'.[21]

A 'zero-one' system is one in which the entry of a radical into a particle already containing a growing chain results in 'instantaneous' termination (the timescale of termination is much more rapid than any other event such as propagation or radical desorption); this model does not require a termination coefficient expression. The 'zero-one' limiting version of the Smith-Ewart equations only allows particles to contain zero or one radical at any point in time, reducing

Equation (2.3) to a system of two differential equations. In the case of hydrophobic monomers such as styrene, particles containing one radical are further divided into two types: those containing a single unit radical derived from the transfer-to-monomer reaction (radical desorption is allowed) and those containing one oligomeric or polymeric radical (radicals with chain lengths greater than a single unit are sufficiently hydrophobic that they do not exit the particle), resulting in a system of three differential equations. Two further limit approximations to the 'zero-one' model exist: complete aqueous phase termination whereby all desorbed radicals are terminated in the aqueous phase, and complete re-entry whereby all desorbed radicals re-enter another latex particle. The latter limit (with the additional assumption that the monomeric radicals are far more likely to propagate at least once before exiting a second time) is said to govern most styrene emulsion polymerizations.

The other widely-applicable limit is the 'pseudo-bulk' limit in which the compartmentalization of radicals into particles has no effect on the system kinetics. The 'pseudo-bulk' limit is valid when desorbed free radicals never terminate in the aqueous phase (jumping from particle to particle until eventually propagating) and/or the value of $\bar{n}$ is sufficiently high ($\bar{n} > 0.7$) that intra-particle kinetics are the same as in a bulk system. For monomers with sufficiently high propagation rate coefficients, $\bar{n}$ can be less than 0.5 and the particles will still obey 'pseudo-bulk' kinetics because the rate of termination is diffusion-controlled[40] and the chains propagate to long lengths very quickly upon entering (or re-entering) a particle. Detailed treatment of the 'zero-one' and 'pseudo-bulk' kinetic systems, along with the accompanying time-dependent expressions ($d\bar{n}/dt$) are available in Thickett and Gilbert's published overview of emulsion polymerization kinetics.[21]

2.2.2 Modeling the Particle Size Distribution

The particle size distribution is one of the most important characteristics of a polymer latex with respect to determining its mechanical properties. Careful control over the particle size distribution in the reactor is especially important in the production of HSC latexes, where the dynamics of particle nucleation, growth and coagulation have a large impact on the rate of polymerization and final product properties. The modeling of the rheological properties of the latex depends on knowledge of the PSD. A means of tracking changes to the particle size distribution during the course of polymerization is necessary when modeling emulsion polymerization processes that are sensitive to changes in the PSD. Modeling the evolution of the particle size distribution is accomplished through the addition of a set of population balance equations (PBEs) to the kinetic model. For a review on the use and limitations of PBEs in modeling emulsion polymerization, the reader is referred to the comprehensive review written by Vale and McKenna.[8] The formulation of the PBEs, as they are applied within the framework, is covered in Chapters 4 and 5.

2.2.3 Modeling Particle Coagulation

For modeling purposes, the coagulation between particles is assumed to occur as a result of binary collision events, although the assumption that all particles will coagulate through a binary collision mechanism is valid only when working with dilute systems. However, due to the complexity of formulating and solving the equations for multi-body collisions (never-mind experimental validation of the parameters), binary collision models have been used at all latex concentrations.[7] There are two mechanisms that govern coagulation in emulsion polymerization: perikinetic aggregation and orthokinetic aggregation. Perikinetic aggregation results from the Brownian motion of particles (diffusive forces), while orthokinetic aggregation is facilitated by

the motion of the fluid (convective forces). Many researchers neglect orthokinetic aggregation when modeling emulsion polymerization, as perikinetic aggregation thought to be the dominant mechanism at small particle sizes (~ 50 nm).[41] This simplification is often justified based on experimental results,[42, 43] however theoretical studies of particle coagulation suggest that hydrodynamics can play an important role when ionic strength is low and the double layer is thick.[44] In relatively stable dispersions there is a strong non-linear coupling between convection and diffusion which means that the overall coagulation rate coefficient is not equal to the sum of the two aggregation mechanisms. Until recently, this necessitated the use of empirical expressions (such as the one employed by Lowry *et al.*[45, 46]) when studying systems where both mechanisms were thought to contribute, as the semi-phenomenological models were unable to capture the changing nature of the interaction between the two mechanisms over a full range of shear rates. As will be discussed extensively in Chapter 3, this is no longer strictly the case.[47] In addition to perikinetic and orthokinetic aggregation, experimental evidence provided by Heller *et al.* suggests that surface coagulation may contribute to the overall rate of particle coagulation in mechanically-agitated systems when flow at or near the interface is fully-turbulent.[48-52] The surface coagulation mechanism appears to be related to the partial deweting of particles at the interface, either as a consequence of desorption of the stabilizer or heterogeneity of the particle surface (e.g. a non-spherical shape or parts of the surface are devoid of stabilizer).[2] It has been proposed that particles adsorb at the aqueous phase – air interface where aggregation occurs between pairs of particles (i.e. binary coagulation). The aggregates then desorb from the surface, returning to the disperse phase of the latex. Therefore, surface coagulation is typically modeled under the assumption that adsorption of the particles at the aqueous phase – air interface obeys the Langmuir adsorption isotherm equation and the rate of aggregation at the surface is second-

order. Surface coagulation is not considered in the framework developed in this thesis in order to simplify matters, but this assumption should be removed when modeling systems where significant foaming occurs at the surface of the latex.

Perikinetic aggregation is often modeled using the DLVO approach, in which it is postulated that the coagulation rate coefficient is dependent on the stability of the particles. Particle stability is, in turn, dependent on the total particle potential energy of interaction, V_{int}. As stated prior, the total potential energy of interaction is the net sum of all attractive and repulsive contributions, including van der Waals' attraction and electrostatic, steric, depletion and solvation-based repulsion. The reader may refer to Ottewill[53] for details on calculating each of these contributions and the overall perikinetic aggregation rate coefficient. While the DLVO framework is widely-used in modeling emulsion polymerization coagulation, the theory has limitations. DLVO-based models do not provide accurate predictions of the aggregation rates of colloids when the potential barrier is located at surface distances below 1 – 2 nm and non-DLVO forces dependent on the structure of the solution and particle surface become important. Additionally, DLVO theory assumes dilute dispersions in which the influence of surrounding particles on a pair of interacting particles can be neglected. In concentrated systems (e.g. HSC latexes), the surrounding particles cause an effective reduction in V_{int}, leading to a lower stability ratio. The concentration effect may lead to a higher rate of coagulation that would be predicted by DLVO theory. For a complete overview of the failings of DLVO theory, as applicable to emulsion polymerization, refer to Vale and McKenna's review of PBEs in emulsion polymerization.[8] In the development of DLVO-based models it is assumed that every particle in the system has the same surfactant coverage, while in reality the precursor particles formed from homogeneous nucleation may undergo

coagulation rapidly, such that the surfactant does not have sufficient time to diffuse to the newly-created surface and equilibrate. Despite this, DLVO theory remains the only basis for non-empirical modeling available for particle coagulation and it is possible to fit certain model parameters to obtain coagulation rate coefficients that correctly predict experimental results.

2.2.4 Modeling Latex Viscosity

In the absence of shear thickening, latex viscosity, when plotted as a function of shear rate, can demonstrate two plateaus. At low shear rates, latex viscosity is independent of shear rate and is said to obey Newtonian behaviour. This lower plateau is referred to as the lower Newtonian viscosity. This plateau is readily observed at low to moderate solid concentrations, but does not appear at very high solid contents.[5] At a certain shear rate (characteristic of the latex), the shear stress transmitted through the aqueous medium will begin orienting the particles in the direction of flow. These layered particles offer less resistance to flow, hence a lowering of the viscosity. Once the particles are completely layered, viscosity can no longer decrease with increasing shear rate and this upper plateau is referred to as the upper Newtonian viscosity. If shear rate is increased further, the mean flow may impart enough energy to the particles so that they overcome the forces of repulsion and begin clustering together. This clustering (not to be confused with coagulation) will disrupt the layered flow which results in a large increase in latex viscosity. This clustering phenomenon, known as shear thickening, may also result in coagulation which will exacerbate the increase in viscosity. Shear thickening, if not anticipated, can result in damaged equipment.[54] During the operation of an emulsion polymerization reactor, care must be taken to ensure the maximum shear rate inside the reactor does not approach the thickening limit.

There are a number of equations available for modeling the viscosity of monodisperse dispersions. Dilute suspensions can be modeled using the Einstein equation:[55, 56]

$$\eta = \eta_s \left(1 + [\eta]\phi\right) \tag{2.4}$$

where η_s is the viscosity of the continuous medium and $[\eta]$ is the intrinsic viscosity, a dimensionless measure of the particles' contribution to the suspension viscosity; for hard spheres $[\eta] = 2.5$. Equation (2.4) is valid for dilute suspensions (non-interacting particles) only. More concentrated solutions can be tacked under the assumption that the effect of all particles in a concentrated suspension is the sum of the effects of particles added sequentially. Under this assumption, the Einstein equation can be written in differential form as:

$$d\eta = \eta[\eta]d\phi \tag{2.5}$$

When a particle is added to a relatively concentrated solution it will require more space than its volume due to packing difficulties, such that an increase in volume fraction will result in the particles already present to suffer a 'crowding effect' which amplifies the increase to viscosity. Sudduth[57] proposed that this crowding effect could be captured by replacing $d\phi$ with $d\phi/(1-k\phi)^{\sigma}$ where σ is the particle interaction coefficient (an adjustable parameter) and accounts for the 'crowding factor'. The term $(1-k\phi)^{\sigma}$ can be thought of as the relative amount of unhindered volume that can effect a change in suspension viscosity. The relative amount of unhindered volume is equal to zero when the maximum packing fraction has been reached. Numerically: $(1-k\phi)^{\sigma} = 0$ if $\phi = \phi_m$, therefore $k = 1/\phi_m$. When modeling latexes, recall that ϕ and ϕ_m are the effective volume fraction and effective maximum volume fraction, respectively

and will vary significantly with particle size due to the presence of the stabilizing layer. Equation (2.4) can be rewritten as follows:

$$\frac{d\eta}{\eta} = \frac{[\eta]}{\left(1-\phi/\phi_m\right)^{\sigma}} d\phi \tag{2.6}$$

When $\sigma = 1$ integration of Equation (2.6) yields the Krieger-Dougherty[58] equation:

$$\eta = \eta_s \left(1-\frac{\phi}{\phi_m}\right)^{-[\eta]\phi_m} \tag{2.7}$$

The Krieger-Dougherty equation has been shown to fit the data from a variety of polymer latex systems, provided accurate *a priori* estimates of $[\eta]$ and ϕ_m are available. Equation (2.7) is very sensitive to changes in $[\eta]$ and ϕ_m. Therefore when modeling new formulations it is recommended that new estimations of $[\eta]$ and ϕ_m are obtained.[30] Note that setting σ to 2 and integrating Equation (2.6) will result in the Mooney equation,[59] and fractional values of σ can be used when optimizing the empirical fit of data.

The Carreau-Yasuda model has been shown to best capture the shearing behaviour of concentrated latexes, including the lower and upper Newtonian plateaus and the onset of shear thinning.[5]

$$\eta = \eta_\infty + \frac{\eta_0 - \eta_\infty}{\left[1+\left(\dot{\gamma}\tau\right)^a\right]^{(1-m)/a}} \qquad \left(\text{for } \dot{\gamma} < \dot{\gamma}_{th}\right) \tag{2.8}$$

where a and m are adjustable parameters, η_0 and η_∞ are the zero and infinite shear viscosities, $\dot{\gamma}$ the shear rate acting upon the latex , τ is the characteristic time for the onset of shear thinning and $\dot{\gamma}_{th}$ is the shear rate above which shear thickening occurs. The four parameters vary with the

solid content of the lattice; the concentration-dependence for all four parameters can be modeled with the general form of the Krieger-Dougherty equation:[58]

$$\varepsilon = \varepsilon_s \left(1 - \frac{\phi}{\phi_{m,\varepsilon}}\right)^{-[\eta]_\varepsilon \phi_{m,\varepsilon}} \qquad \varepsilon = \eta_0, \eta_\infty, \tau, \left(1/\dot{\gamma}_{th}\right) \tag{2.9}$$

where ε_s is the value of the parameter at zero solids content.

Modeling the viscosity-loading profiles of multimodal latexes requires an estimation of the maximum packing fraction parameter (ϕ_m). While the optimal PSD can often be determined through extensive experimentation, it is often beneficial to augment experimental efforts with a well-chosen model. Researchers have developed models that are capable of predicting ϕ_m for multi-modal dispersions, provided the related monodisperse maximum packing fraction (ϕ_m^0) is known. Sudduth[57, 60] proposed the following model to determine the maximum packing fraction of a polydisperse system:

$$\phi_m = \phi_{ult} - \left(\phi_{ult} - \phi_m^0\right) e^{\left[\alpha\left(1 - D_5/D_1\right)\right]} \tag{2.10}$$

Where D_5 and D_1 are the 5th and 1st moments of the PSD, α is an adjustable parameter and ϕ_{ult} is the ultimate packing fraction which is calculated as follows:

$$\phi_{ult} = 1 - \left(1 - \phi_m^0\right)^n \tag{2.11}$$

Here, n is the number of discrete particle sizes in the population. For bimodal latex where particles are arranged according to RCP (this would correspond to a latex under low shear) $\phi_m^0 = 0.64$, $n = 2$ and $\phi_{ult} = 0.87$.[28] The x^{th} moment of the PSD is defined as:

$$D_x = \frac{\sum_{k=1}^{n} N_k D_k^x}{\sum_{k=1}^{n} N_k D_k^{x-1}} \tag{2.12}$$

Where N_k is the number of particles with a diameter of D_k. Since the parameter α must be fit to experimental data before Equation (2.10) can be used predicatively, Sudduth's model requires extensive experimental measurement before it can be used as a predictive model.

Recently, Pishvaei *et al.*[5] proposed a model that eliminates the need for additional experimental data beyond the determination ϕ_m^0 and the PSD. This model was adapted from a model proposed by Ouchiyama and Tanaka in a series of papers[61-64] to estimate the porosity of powdered solids represented as a bed of randomly distributed spherical particles with a polydispersed PSD.

$$\phi_m = \frac{\int_{D_s}^{D_l} D^3 x(D) dD}{\int_{D_s}^{D_l} \left[\frac{\pi}{6}\left(D \sim \bar{D}\right)^3 + \frac{1}{\bar{s}}\left(\left(D + \bar{D}\right)^3 - \left(D \sim \bar{D}\right)^3\right)\right] x(D) dD} \tag{2.13}$$

where $\bar{D}$ is the number-average diameter and $x(D)$ is the number-frequency size distribution. D_s and D_l are the small and large diameter limits of the PSD. According to the model, each hypothetical sphere of diameter $D + \bar{D}$ has to share part of its space with other hypothetical spheres. This common space, hatched in Figure 2.2, has an inner diameter equal to $\left(D \sim \bar{D}\right)$ and an outer diameter of $\left(D + \bar{D}\right)$ where

$$\begin{aligned}\left(D \sim \bar{D}\right) &= 0 \qquad \text{for } \mathrm{D} \le \bar{\mathrm{D}} \\ &= \left(D - \bar{D}\right) \quad \text{for } \mathrm{D} \ge \bar{\mathrm{D}}\end{aligned} \tag{2.14}$$

The average number of spheres sharing the common space is calculated with the following formula:

$$\bar{s} = 1 + \frac{4}{13}\left(8\phi_m^o - 1\right)\bar{D}\frac{\int_{D_s}^{D_l}\left[\left(D+\bar{D}\right)^2\left(1-\frac{3}{8}\frac{\bar{D}}{D+\bar{D}}\right)\right]x(D)dD}{\int_{D_s}^{D_l}\left[D^3 - \left(D \sim \bar{D}\right)^3\right]x(D)dD} \tag{2.15}$$

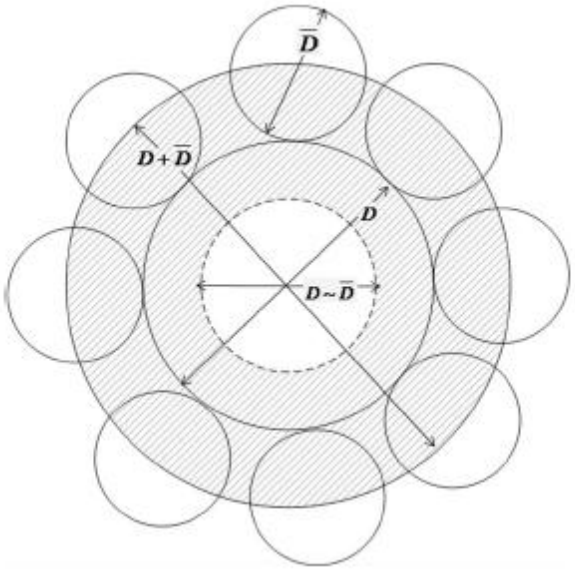

Figure 2.2. A simplified packing model used to determine the coordination number. The hatched area represents common space that is shared with other hypothetical spheres.[63]

Equations (2.13) and (2.15) can be used to estimate the maximum packing fraction of a completely mixed system without experimental parameter fitting. It is important to note that $\bar{n}$ was assumed to be independent of the sizes of the particles during the development of these equations. This holds true only if the stabilization layer surrounding the latex particle is treated as part of the particle. These equations can also be written in discrete form. For a system with discretized particle sizes:

$$\phi_{m,\varepsilon} = \frac{\sum_{i=1}^{m} D_i^3 x_i}{\sum_{i=1}^{m}\left(D_i \sim \bar{D}\right)^3 x_i + \frac{1}{\bar{s}}\sum_{i=1}^{m}\left[\left(D_i + \bar{D}\right)^3 - \left(D_i \sim \bar{D}\right)^3\right] x_i} \tag{2.16}$$

$$\bar{s} = 1 + \frac{4}{13}\bar{D}\frac{\sum_{i=1}^{m}\left(8\phi_{m,i} - 1\right)\left(D_i + \bar{D}\right)^2\left(1 - \frac{3}{8}\frac{\bar{D}}{D_i + \bar{D}}\right)x_i}{\sum_{i=1}^{m}\left[D_i^3 - \left(D_i \sim \bar{D}\right)^3\right]x_i} \tag{2.17}$$

where x_i is the number fraction of the i^{th} component:

$$x_i = \frac{\varphi_i / D_i^3}{\sum_{i=1}^{m}\varphi_i / D_i^3} \tag{2.18}$$

The number average diameter $\bar{D}$ is the weighted sum of the individual particle sizes that compose the discrete mixture:

$$\bar{D} = \sum_{i=1}^{m} D_i x_i \tag{2.19}$$

For a latex composed of two distinct particle populations, $m = 2$. Pishvaei demonstrated that Equations (2.16) - (2.19) can be used to provide reasonable estimates of the loading limits and latex viscosity for a bimodal system based on estimates of these properties from related monodisperse latexes.[65]

2.3 Simulation of Reactor Performance Using Computational Fluid Dynamics

2.3.1 Overview of Computational Fluid Dynamics Simulation

Computational fluid dynamics is concerned with the analysis of and solutions to problems involving fluid and associated phenomena (e.g. heat transfer, species transport) using specialized numerical algorithms. While the numerical techniques that form the backbone of CFD simulation

can trace their roots back almost one hundred years, the techniques were not put into practice until the 1960s, coinciding with the availability of sufficient computing power. The first industry to make extensive use of CFD was the aerospace industry, which integrated CFD techniques into the development and manufacture of aircraft and jet engines. The emergence of more affordable computing power has allowed CFD simulation to fulfill its promise as a complementary addition to experimental analysis, contributing extensively to both our scientific understanding and industrial productivity. Today, CFD is used extensively in the field of chemical engineering to study a wide range of phenomena not limited to: heat transfer, polymeric fluid flow, combustion analysis and separation and mixing.[11]

A typical CFD code consists of three elements: (i) the preprocessor; (ii) the numerical solver; and (iii) the postprocessor. Preprocessing consists of defining the computational domain of interest, division of the domain into a number of non-overlapping subdivisions (the computational grid) and the specification of the problem. Specifying the problem includes the selection of phenomena, definition of the pertinent fluid properties and specification of boundary and initial conditions. Numerical solvers can be divided into classes, depending on the numerical solution techniques they employ: finite difference, finite volume, finite element and spectral techniques (an extension of finite element). Each method has its perceived strengths and weaknesses, although extensive research developments within each method's respective research community have addressed many of these weaknesses. For example, Sukumar developed a finite difference technique capable of solving the Poisson equation on unstructured grids.[66] Once a solution has been computed, a post-processor is used to display the domain geometry and grid, view the solution field, produce graphics and animation and export data. Exported data may undergo

further processing in external software or be used as input in an external process model, allowing for the development of hybrid model frameworks.

2.3.2 Grid Generation

Grid generation strategies can be classified as Cartesian, structured, unstructured, hybrid and gridless.[67] In Cartesian gridding, a network of uniformly-spaced grid lines is placed in a rectangle (2-D) or rectangular box (3-D). Boundary conditions are implemented by cutting grid lines into the interior cells. While Cartesian gridding is the simplest way to discretize a given field, the approach is generally not suited for solving complex computational fluid flow problems. In structured gridding, the grid is a network of curvilinear coordinate lines such that one-to-one mapping can be established between physical and computational space.[67] The structured grid approach is the most accurate way to specify boundary conditions as the curvilinear grid points conform to the shape of the surface/boundary. The main drawback to structured grid generation is that the method is not automated. Should a user wish to generate a structured grid on a complex geometry the user must typically divide the structure into simple sub-regions manually before a set of structured subgrids can be generated. While the process of grid subdivision requires substantial manual input, structured grids are often computationally efficient, requiring fewer cells to compute the solution to a desired level of accuracy. Unstructured meshes composed of either triangles (in 2-D) or tetrahedrons (in 3-D); the grid information is recorded as a set of node coordinates and a connectivity list, where the neighbor set for each node is specified. Unstructured meshes are typically generated using automatic algorithms, with the user merely specifying the desired grid density and (if necessary) the desired increase in mesh density at the boundaries. The drawbacks of unstructured grids are the higher number of elements required

relative to structured grids and the propensity of the automatic generation software to generate poor quality elements (skewed) in regions with high aspect ratios. The skewed cells may potentially introduce errors in the numerical solution. Hybrid grids are a méritage of structured and unstructured meshing, where structured sub-grids are generated in areas that require high aspect ratio cells and the remainder of the domain is filled with an unstructured mesh. This approach is capable of generating high quality meshes with a large degree of automation, but the algorithms are often temperamental and may require the user to be experienced with the pre-processing software before they function properly. Gridless methods allow for the numerical treatment of the conservation equations without requiring the use of a mesh topology. The only structure required is a distribution of cloudless points within the computational domain. Gridless methods are still a nascent field of research, but the approach holds much promise in modeling the unsteady motions of rigid bodies, where mesh quality would tend to degrade during large rigid movements of a body's boundaries.[12]

2.3.3 CFD Solution Methods

CFD software differs from most other modeling software in that most modeling software is designed to produce solutions for any arbitrary set of user-defined equations, while CFD software is tailored to obtain the best solution to very specific set of problems; that of fluid flow. Most commercial CFD packages are well-suited to solving the conservation equations for mass, momentum, heat and energy; should the need arise to simultaneously solve additional processes in parallel (for example, a particle population balance), the code is unlikely to be effective.
The most commonly-encountered discretization techniques in both research and commercial code are the finite element method and the finite volume method. Both methods begin with the integral

form of the conservation equation. The finite element method uses simple piecewise functions (linear or quadratic) to describe variations in the unknown flow variables. The piecewise functions are substituted into the exact conservation equations and the residuals of the resulting approximation are minimized by multiplying them by a set of weighing functions and integrating. The resulting algebraic system of equations is solved to yield the unknown coefficients of the piecewise approximating functions.[68] In the finite volume method, the conservation equations are integrated over all control volumes of the domain, and the resulting integral expressions are discretized to form a system of algebraic equations, which are solved using an iterative method. Both the finite element and finite volume methods are capable of solving fluid flow problems. Originally, the finite volume method was preferred for its relative conceptual simplicity; the finite element method is more abstract in concept, but the element construct was well-suited to unstructured meshes. Over the years, advances in research have addressed both methods' weaknesses. For process engineers, the choice of software is likely to be strongly-influenced by software compatibility and the availability of both technical support and application-specific support in the research community.

2.4 Mixing

2.4.1 Overview of Mixing

Mixing can be defined as the reduction in inhomogeneity to achieve a desired process result. When one refers to inhomogeneity, they are typically referring to concentration, phase or temperature. The failure to achieve good mixing upon process scale-up can lead to myriad problems, most of which will, ultimately, compromise the commercial viability of the product in

question. Mixing is typically said to occur at three scales: (i) macromixing, which is driven by the largest scales of motion in the fluid and takes place at the scale of the vessel; (ii) mesomixing, which is the scale reduction stage where inertial and/or viscous forces play an important role (depending on the flow regime); (iii) micromixing, where molecular diffusivity controls the rate in reduction in segregation. The mechanisms by which mixing occur will be dependent on the flow regime; laminar mixing is mechanistically different from turbulent mixing. Beginning with Danckwerts in the 1950s,[69] researchers have developed numerous definitions to quantify the degree of segregation or inhomogeneity within reactors in order to provide a non-trivial answer to the question: "How well-mixed is the process?" What follows is a brief summary of the differences between turbulent and laminar mixing and an overview of how mixing may be quantified.

2.4.2 Turbulent Mixing

At high Reynolds numbers, flows are observed to become chaotic or turbulent. Turbulent flow is characterized by a random state of motion in which the velocity and pressure change continuously with time over substantial regions of flow.[11] Visualization of turbulence would reveal the presence of rotational flow structures called eddies or vortices. The largest eddies acquire energy through interaction with the mean flow and they, in turn, interact with smaller eddies, transferring energy to them before breaking-up. These smaller eddies transfer their energy to even smaller eddies. This so-called energy cascade continues until the eddies are small enough such that their kinetic energy can be effectively dissipated through viscous action. The energy cascade converts kinetic energy from the mean flow into heat energy at the molecular level. For demonstrative purposes, the eddies are typically divided into three sizes. The largest eddies are integral scale

eddies, which are highly anisotropic in structure and have a length scale on the order of the mean flow. The intermediate eddies, the Taylor microscale eddies, are unaffected by the viscous forces, but can be described by the rate of energy dissipation. The smallest scale eddies are the Kolmogorov eddies, which are the isotropic in structure and represent the smallest scale at which segregation (mixing) occurs through the mechanism of turbulence. Turbulence motion enhances the rate of mixing by breaking up fluid motion, thereby reducing the scale of segregation. In simplified terms, bulk mixing and turbulence mixing are responsible for reducing the length scale at which molecular diffusion must act.[70] Due to the highly-complex physics of turbulence and the potential for interactions between the turbulence field and process kinetics, it is often essential to simplify the modeling of the turbulence field and use scaling arguments to develop relationships between aggregate turbulent quantities (e.g. the rate of dissipation of turbulent energy) and important process dynamics (e.g. the maximum rate of fluid shear in a stirred tank). For further details with regards to turbulence modeling, the reader is referred to Chapter 3 in Versteeg and Malalasekera.[11] For an overview on the role of turbulence in mixing applications, refer to Chapter 3 in the Handbook of Industrial Mixing.[70]

2.4.3 Laminar Mixing

Mixing applications that are carried out at low velocities or involve high viscosity substances will be characterized by a laminar flow environment. While the modeling of the physics of fluid flow is rendered less complex by the absence of turbulence, the quantification of laminar mixing is still a relatively fresh area of research. Laminar mixing is, from a physical perspective, often more challenging than turbulent mixing due to the absence of eddies to promote mixing at the meso-scale. Early researchers, such as Mohr,[71] observed that the blending of polymers visually

consisted of drawing out separated components into progressively thinner striations and developed an expression to compute the rate of reduction in striation thickness as a function of shear rate. However it wasn't until the 1980s that researchers developed a general framework for quantifying the degree and rate of laminar mixing. Aref[72] proposed the extension of dynamic systems theory to study mixing at scales smaller than the scale of bulk fluid flow. Laminar mixing requires the presence of periodic unsteady fluctuations in the velocity field, generating chaotic motion. As fluid elements travel through chaotic flow, they are stretched and folded due to changes in the direction of the flow field acting upon the element. Repetitive exposure to the stretching and folding cycle (reorientation) results in a reduction in striation thickness and an increase in contact area between striations. This mechanism is important in mixing processes because the rate of diffusion of material at the microscopic scale is dependent on the length scale of striation thickness and the total interfacial area available for transport. The ability to measure the spatial distribution of striation thickness using the framework of chaotic flow modeling fills in the gap between macro-mixing and micromixing.[73] It has been found that the metrics that have used successfully to quantify turbulent mixing, such as the coefficient of variance (explained in the next section), are sometimes unable to predict differences in performance of different laminar mixers.[74] There are a number of approaches available for modeling the distribution and evolution of striation thickness in laminar flows, such as computing the stretching field, computing striation thickness distributions directly or predicting them from stretching.[73] In CFD simulation, Lagrangian particle tracking is sometimes employed in place of scalar tracking when modeling the development of striation thickness to avoid numerical diffusion that is inherent to scalar tracking.

2.4.4 Quantifying Mixing

Although the concept of "well-mixed" may seem somewhat-intuitive, there has been extensive effort exerted in the mixing research field to develop a universal approach to quantifying the degree of "mixedness" inside a mixing vessel. Quantitative measurement of mixing time is experimentally determined through the addition of a chemical with a different property to the bulk, followed by measurement of the system to infer the presence and uniformity of the liquid.[75] In the 1950s, Danckwerts[69] proposed that the degree of mixing in a vessel could quantified using sampling data by defining an intensity of segregation:

$$I = \frac{\sum_{m=1}^{M}\left(\bar{x}_A - x_{A,m}\right)^2}{M\left(\bar{x}_A\left(1-\bar{x}_A\right)\right)} = \frac{\overline{\left(\bar{x}_A - x_A\right)^2}}{\left(\bar{x}_A\left(1-\bar{x}_A\right)\right)} \tag{2.20}$$

where x_A is the fraction of component A at a point in space and an instant in time $\bar{x}_A$ is the average fraction of the component A in a binary mixture and M is the number of measurement locations. The point is large enough to contain a meaningful number of molecules, but small enough to have a uniform concentration. If $I = 0$, the mixture is said to be homogeneous down to the molecular scale, while if $I = 1.0$ the system is completely segregated. While the intensity of segregation can be used to quantify the simplest mixing problems, it cannot quantify a number of important mixing processes. In liquid-liquid dispersion, for example, the objective is to achieve a target droplet size, but the intensity of segregation will not vary will time.

Kukukova *et al.*[76] recently proposed that the state of segregation can be characterized using three variables: (i) intensity of segregation, which is the variance in concentration throughout the vessel; (ii) scale of segregation, which is the distribution of length scales; (iii) exposure, which is

the rate of change in segregation. The dominant dimension of mixing is dependent on the mixing problem itself. Turbulent mixing is dominated by a reduction in the intensity of segregation. The reduction in scale of segregation that occurs is related to eddy diffusivity, but it is generally accepted that axial flow impellers operating in the turbulent regime will generate a sufficient level of eddy diffusivity and the mixing process is controlled by macromixing.[77] Process specification for laminar blending, on the other hand, often involves setting a minimum scale of segregation as the main objective.[76] As stated prior, the scale of segregation in laminar mixing is measured using the framework of chaotic mixing analysis.

The intensity of segregation can be computed using a wide range of metrics, including Equation (2.20), all of which are functions of either the variance or standard deviation in tracer concentration. The coefficient of variance is the simplest of these metrics.[76] In an experiment measuring the dispersal of a tracer, the coefficient of variance would be measured by computing the standard deviation in tracer concentration, as measured at a number of sample points, and dividing it by the mean tracer concentration in the reactor. In the analysis of CFD simulation data, the number of sampling points is equal to the number of cells in the computational mesh, and the average concentration is a volume-average concentration computed over the entire domain.

2.4.5 Model Hybridization

CFD remains a powerful tool for the study of hydrodynamics and mixing processes, as it is able to capture the spatial variation of properties (such as viscosity) within complex geometries. For many processes, it is, in principle, possible to incorporate a wide range of phenomena within the CFD equations and to complement them by additional conservation equations. Applied to emulsion polymerization, this would amount to the incorporation of a set of population balance equations into CFD code. In Fluent, a commercial CFD package, additional conservation equations can be incorporated through the User Defined Function interface. In practice however, this approach is impractical for a number of reasons. Often the system resulting from the coupling of mass, momentum and energy equations with a population balance is too large for current computing equipment. Furthermore, the CFD algorithms are often tailored to solve large systems of mildly non-linear equations; they demonstrate a lack of flexibility when they need to be interfaced with external libraries or models or sets of non-linear equations with different time scales.[78]

Multizonal or compartmental representation is a well-established means of describing mixing non-idealities in a system by dividing the unit operation into a network of interconnected zones. An idealized mixing pattern is assumed in each individual zone. Correct use of multizonal/compartmental models may result in a large improvement in predictive accuracy, while the increase in computational cost is only a small multiple of the computational cost of the ideal mixing model. One of the key difficulties encountered when using multizonal models is determining how to distribute the zones and continuously determine the mass and energy fluxes between the zones as system conditions change. In response to this problem, multizonal models

are often hybridized with a CFD model, where the CFD simulation results are used to determine the rate of flow (and directionality) between adjacent zones. In a series of papers,[78-81] Bezzo *et al.* developed a general, formal hybrid multizonal/CFD modeling methodology to standardize the approach across a wide variety of applications. In multizonal modeling, the spatial domain of interest is divided into a number of internal zones, representing spatial regions in the process equipment. Typically in emulsion polymerization the spatial domain is the reactor. The environment interacting with the system may also be divided into a number of environment zones. These environment zones do not correspond to a region in space; rather they are merely gates through which information is passed to the internal zones, linking them to the surrounding environment. Two zones can interact with each other via an interface that connects the port of one zone with the port of the other zone. Each zone must have at least one port (otherwise it is unable to interact with other zones). Each port is connected via exactly one interface to the port of another zone. The flow of material/energy through each interface is assumed to be bidirectional. The transient behavior of a typical internal zone is modeled using a set of differential and algebraic equations (e.g. the kinetic and particle population balances). In practice, the functional form of the model will be the same through all internal zones since all such zones will typically involve the same physical phenomena. The environmental zone models differ from internal zone models in that they contain time-dependent inputs, but do not contain differential equations. The overall multizonal model includes the internal and environmental zone models and connectivity equations, accounting for the interfaces connecting the pairs of ports. The multizonal model can determine the dynamic behavior of the system, provided the fluid flow/mixing parameters within each internal zone and the mass flow rates across each interface can be determined. If one is to assume that the time scale of mixing and fluid flow is much faster than the other phenomena

being modeled (such as particle nucleation and reaction) then the aforementioned quantities can be determined using a steady- state CFD model. The CFD model is kept as compact as possible, comprised of mass and momentum balances along with the physical property relationships for density and viscosity. Determination of the other intensive properties (such as the particle size distribution) is left to the multizonal process model. Density and viscosity are functions of these intensive properties along with spatial position.

The hybrid model is formed by coupling the multizonal model with the CFD model. Bezzo *et al.*[78] note that this coupling is accomplished through two steps. The first task in constructing a hybrid model is to construct a topological map between the two models; that is, each cell in the CFD model must be assigned to a zone in the multizonal model. Once a topological map has been constructed, the computational coupling between the models must be considered. Information that is passed from the CFD model to a zone within the multizonal model must be volumetrically averaged (aggregated) across all the cells belonging to that particular zone. Information needed by the CFD model has to be derived by disaggregation of the corresponding zone fluid properties. Usually this means that the information is passed to the CFD model without any additional treatment; however the accompanying discontinuity in physical properties across CFD cells corresponding to an interzonal interface may lead to problems within the CFD code, in which case a smoothing approximation can be applied. Bezzo *et al.* demonstrated the application of the hybrid multizonal / CFD framework in the modeling of xanthan gum production in a bioreactor, dividing the bioreactor into regions of constant fluid viscosity.[79] In addition to the study of bioreactors, the multizonal / CFD framework has been used to investigate the treatment of water using ozonation.[82]

Alexopoulos *et al.*[83] developed a two compartment model for calculating the PSD in suspension polymerization reactors. CFD was employed to generate the spatial distribution of turbulent energy dissipation rates within the reaction vessel. The turbulent energy dissipation rate was 2 – 3 orders of magnitude higher in the region surrounding the impeller compared to the rest of the vessel. A cut-off energy dissipation rate, was identified and the impeller and circulation compartments were defined as grid cells with energy dissipation rates greater than or less than the cut-off, respectively. The isosurfaces generated using a series of cut-off values indicated that the highest rates energy dissipation were located in a small compartment surrounding the impeller. The shape of the compartment qualitatively resembled a trailing vortex, matching the experimental findings of Schäfer *et al.*,[84] although quantifying the shape of the trailing vortex was not the focus of the simulation work. Alexopoulos *et al.* adapted the two-compartment model to a semi-batch, starved-feed emulsion polymerization reactor.[15] They found that when the rate of flow between the compartments was smaller than the monomer feed rate, representing a poor degree of mixing, the PSD in the monomer-rich compartment differed from the PSD in the monomer-poor compartment. Elgebrandt *et al.*[17] developed a hybrid model to investigate particle size effects in emulsion polymerization. The multizonal model was handled using the process simulation software gPROMS, while the CFD simulation was handled with FLUENT. To reduce computational time, the CFD mesh was generated in 2D and the process model consisted of six zones that were generated manually, based on prior estimations of the shear rate distribution inside a similar reactor.[16] The model was used to investigate the semibatch emulsion polymerization of styrene with a final solid volume fraction of 0.24. The CFD model was implemented with the k-ε turbulence model and the latex was modeled as a Newtonian fluid. The

coagulation submodel was a semi-empirical model originally used in the study of mechanically-induced shear coagulation.[45] The simulation results demonstrated the successful transmission of information between CFD and process models, with the higher shear zones (e.g. the impeller zone) having larger particles and lower particle number concentration. The authors stated their intention to apply the framework to a more complex set of cases, modeled with a 3D CFD mesh and a more complex coagulation kernel, but no follow-up work has appeared in the literature over the past six years.

Due to a number of recent advances in our understanding of important emulsion polymerization kinetic events[47, 85] and the emergence of faster automatic zoning algorithms[86], there is sufficient motivation to revisit the development of a CFD-PBM modeling framework for polymer latex processes. By building upon the ideas proposed in Elgebrandt's work[16], the development of a computationally-efficient modeling framework, capable of running on a modern desktop becomes possible. By automatically generated compartmentalized zones based on the characteristics of the simulated flow field, it is possible to numerically investigating the effect of changing the reactor scale and operating conditions on the quality of latexes produced under a specified set of conditions in either batch or semi-batch operation.

Chapter 3

Modeling Orthokinetic Coagulation in a Stirred Tank

3.1 Introduction

In the production of polymer latex products at the commercial scale, the formation of undesired coagulum, in both the product and on the inside surfaces of the reactor, is a critical issue. The slow build-up of coagulum on the inside surface of the reactor reduces the process throughput via increased reactor downtime while also potentially affecting reaction conditions, leading to off-spec product. These issues are often unanticipated when the products are developed at the laboratory scale because the flow conditions inside a laboratory scale reactors differ from the conditions inside commercial scale reactors.[87] In processes where mechanical destabilization of the latex is desired, changes in the shear rate distribution inside the reactor may affect the rate at which the latex destabilizes.[2] In addition to the rate of mechanical agitation, the rate of particle coagulation is influenced by a range of factors, including the latex particle size distribution (PSD), particle concentration, ionic species concentration, surface stabilizer concentration and temperature.

The emergence of affordable computational power has led to the development of emulsion polymerization modeling frameworks that can be used to numerically investigate process scale-up, thereby potentially reducing process development times and costs.[17, 88] The evolution of latex characteristics during the emulsion polymerization process under a given set of process conditions can be evaluated numerically through the use of a process model, the most detailed of which are based on the population balance modeling technique.[89] Computational fluid dynamics

simulation (CFD) can be used to generate detailed flow fields for a wide range of reactor configurations and operating conditions. Researchers have used CFD simulation to evaluate the mixing performance of different reactor configurations[13] and identify regions within the reactor where the latex will be subjected to high rates of shear.[16] The information abstracted from CFD analysis (such as the shear rate distribution and reactant gradients), when input into a process model, can be used to evaluate the influence of reactor scale and configuration on the evolution of latex properties over the course of a reaction. One of the main issues in the field of emulsion polymerization modeling has been the absence of a semi-phenomenological coagulation model that can predict the rate of coagulation in both the presence and absence of high rates of mechanical agitation.

Fuchs' modified[90] treatment of von Smulochowski's[91] approach to solving the convection-diffusion equation around a reference particle serves as a basis for the quantitative description of aggregation kinetics. In the absence of a velocity gradient the coagulation of the polymer particles is caused by particle collisions arising from the Brownian (diffusive) motion of the particles. The fraction of collisions that result in particle aggregation depends on the nature of the interactions between the particles; typically, the Derjaguin-Landau-Verwey-Overbeek[92] (DLVO) theory is used to model the interaction potential between colliding particle pairs. The imposition of a velocity gradient via mechanical agitation increases the collision frequency between particles, but the effect of the shear field on the overall rate of particle coagulation will be minimal until the rate of convective particle transport is on the same order of magnitude as the diffusive rate of particle transport. Most DLVO-based coagulation models have been formulated and experimentally validated under the assumption that shear-induced coagulation can be effectively ignored and omitted from the model,[41] despite some evidence that mechanically-induced

coagulation may occur at the laboratory scale under certain conditions.[45] The semi-empirical coagulation models that have been validated experimentally require extensive parameter-fitting;[45, 46] therefore, their applicability to a wider range of processes and conditions is limited. Melis *et al.*[44] investigated the case where shear-induced aggregation and DLVO-type interactions are simultaneously present. Their thorough numerical solutions to the convection-diffusion equation provided useful insight, but attempts to develop an analytical expression that matched the numerical data over a full range of shear rates was generally unsuccessful. However, Lattuada and Morbidelli[47] recently developed such an analytical expression. They demonstrated that, through the use of a boundary layer approximation, one can obtain a simplified model which matches the more thorough numerical simulations, even in the moderate shear rate range where the aggregation rate may sharply increase many orders of magnitude. Such an expression could feasibly be incorporated into an emulsion polymerization population balance model, although it is still more resource intensive than DLVO-only coagulation kernels.

The objectives of this chapter are as follows: (i) determine, via CFD simulation, if shear-induced coagulation is expected to become more of an issue as a reactor is scaled-up (maintaining geometric similarity and a constant power-per-unit-volume input); (ii) compare the predictions generated by the Lattuada and Morbidelli[47] coagulation kernel against simpler alternatives. Both Hong[93] and Elgebrandt *et al.*[16] used CFD simulation to investigate the distribution of turbulent shear inside laboratory-scale stirred tanks, but neither group extended their set of simulations to numerically investigate the shear rate distribution in lager vessels. The Lattuada and Morbidelli coagulation model is used to generate aggregation rate data under conditions that are pertinent to the production of polymer latexes in order to determine if particular reaction conditions will

render polymer latexes more susceptible to mechanically-induced coagulation. The feasibility of incorporating the Lattuada and Morbidelli coagulation model within an emulsion polymerization population balance model framework is discussed.

3.2 Overview of Particle Coagulation Modeling

Nearly a century ago, von Smulochowski[94] published a seminal paper which serves as a foundation for modern coagulation models. In this paper, Smulochowski solved the diffusion-convection equation, describing the diffusion of colloidal particles towards a reference particle. The boundary conditions used are as follows: at the reference particle surface, the concentration is set to zero as particles that come in contact with the reference particle are assumed to irreversibly aggregate. At an infinite distance from the reference particle, the particle concentration is set at its bulk value. The motion of particles relative to one another arises from their Brownian motion. Under the assumption that all collisions between particles are of a binary nature, the change in particle concentration (c) with time is:

$$\frac{dc}{dt} = -\beta_{fast} c^2 \tag{3.1}$$

where β_{fast} is the rapid coagulation rate coefficient. Fuchs considered a system in which the interaction potential between particle pairs can be described using a potential energy barrier. The diffusion-convection equation is modified to include a convective term that captures the net effect of the attractive and repulsive forces that may act on a particle as they diffuse towards one-another. In the case of shear aggregation, the velocity gradient in the fluid is captured in a second convective term such that the net convective rate is a sum of the interaction and shear-induced

convective terms. Most modern coagulation models are derived using a variation of the Fuchs-modified version of the Smoluchowski equation:

$$\nabla \cdot \left(\mathbf{D} \cdot \nabla c - \left(\mathbf{v}_{\text{int}} + \mathbf{v}_{conv} \right) c \right) = 0 \tag{3.2}$$

where $\mathbf{D}$ is the diffusion tensor (modeled as Brownian diffusion and often modified with terms to account for hydrodynamic interactions), $\mathbf{v}_{conv}$ is the convective velocity and $\mathbf{v}_{\text{int}}$ is the velocity induced by interparticle interactions. In industrial-scale reactors, $\mathbf{v}_{conv}$ acting at the particle scale is modeled as an extensional flow field arising from isotropic turbulence as the latex particles are smaller than the Kolmogorov scale (the length scale at which the directionality of the turbulent eddies is lost, typically in the order of a few microns). The following expression is used to compute $\mathbf{v}_{conv}$:[44]

$$\begin{aligned} v_{conv,r} &= \frac{\dot{\gamma} r}{2} \left(1 - A(r,\lambda)\right) \left(3\cos(\theta)^2 - 1\right) \\ v_{conv,\theta} &= -\frac{3\dot{\gamma} r}{2} \left(1 - B(r,\lambda)\right) \left(\cos(\theta)\sin(\theta)\right) \end{aligned} \tag{3.3}$$

where r is the radial distance from the center of the reference particle and θ is the colatitude (the difference between the latitude and 90°) and $\dot{\gamma}$ is the local shear rate. $\lambda = r_j / r_i$ is the dimensionless particle size ratio between the interacting particle pairs, where $r_j \geq r_i$. $A(r,\lambda)$ and $B(r,\lambda)$ are hydrodynamic interaction functions that account for hydrodynamic interactions between particle pairs in an axisymmetric linear flow field.[95] Below the Kolmogorov scale, the local shear rate can be expressed as a function of the local rate of energy dissipation (ε):

$$\dot{\gamma} = \left(\sqrt{\frac{2\varepsilon}{15\upsilon}} \right) \tag{3.4}$$

where υ is the kinematic viscosity.

The interaction velocity vector $\mathbf{v}_{\text{int}}$ can be modeled using the DLVO theory framework. It must be noted that the applicability of DLVO theory to modeling emulsion polymerization is somewhat questionable[7] even though it is widely used in the emulsion polymerization modeling field. Behren *et al.*[96] found that while DLVO theory was quantitatively applicable for weakly charged particles (i.e. surface charge less than 3 mC/m^2) and low ionic strengths (< 10 mM), discrepancies emerged between theory and experiments at high ionic strengths. An analysis of the interaction energy profiles suggested that such deviations were closely related to the position of the energy barrier. At high ionic strengths the energy barrier appears at a separation distance less than 1 nm and non-DLVO forces (that are not included in the model) become influential. These non-DLVO forces arise from surface heterogeneities, the discrete nature of charges and the finite size of ions and water molecules. Since higher ionic strengths and higher surface charges are typically encountered in emulsion polymerization, the DLVO interaction model should be used with caution.

Still, the DLVO interaction model is currently the best model available for describing particle coagulation and non-DLVO forces can be accounted for by making adjustments to certain model parameters;[8] for instance, the Hamaker constant. Under the DLVO framework, $\mathbf{v}_{\text{int}}$ may be computed as follows:

$$\mathbf{v}_{\text{int}} = -\frac{\mathbf{D}}{k_B T}\nabla V_{\text{int}} \tag{3.5}$$

where $\mathbf{D}$ is the diffusion tensor, ∇V_{int} is the gradient in the interaction potential, k_B is the Boltzmann constant and T is temperature. The diffusion tensor is expressed as a function of the diffusion coefficient may be modified to account for hydrodynamic interactions that arise between particle pairs as they approach one another (essentially a form of viscous friction). In spherical coordinates:

$$\mathbf{D} = D_0 \begin{bmatrix} G(r,\lambda) & 0 & 0 \\ 0 & H(r,\lambda) & 0 \\ 0 & 0 & H(r,\lambda) \end{bmatrix} \tag{3.6}$$

where $G(r,\lambda)$ and $H(r,\lambda)$ are the radial and angular (polar) hydrodynamic interaction functions, accounting for resistive forces that arise as particles approach one another. The mutual diffusion coefficient, D_0 is calculated as follows:

$$D_0 = \frac{k_B T}{6\pi\eta_s}\left(\frac{1}{r_i} + \frac{1}{r_j}\right) \tag{3.7}$$

where η_s is the viscosity of the dispersion medium.

As two particles approach one another, fluid must be squeezed out from the gap between the particles; this action creates a viscous drag on the particles. The hydrodynamic interaction profiles are typically obtained by numerically solving the equations of motion between pairs of spherical particles in simple flow fields (for example, see the work of Batchelor and Green[95]). The availability of phenomenological expressions that function in both the near and far field is limited. In many cases, polynomial fits are used instead; for example, the polynomial function

developed by Honig *et al.*[97] for two equal-sized spheres in a dilute solution has seen use in some particle stability models:

$$G(\xi, \lambda = 1) = \frac{6\xi^2 - 20\xi + 16}{6\xi^2 - 11\xi} \tag{3.8}$$

The development of an analytical expression for β_{ij} that is entirely phenomenological is unlikely in the near future due to the difficulty in measuring and modeling a number of non-DLVO forces that are known to be important under certain conditions.[98] A simplified coagulation kernel can still provide reasonable a priori predictive capability through the use of adjustable parameters, provided the conditions that are being modeled are based on the experimental conditions used to adjust the model parameters. Within the typical DLVO-based coagulation kernel there are a number of variables whose values are not known exactly. As stated prior, the Hamaker constant is typically treated as a semi-empirical parameter, with possible values ranging between 2.0 to 17 × 10^{-21} J for aqueous polymer latexes.[2] The modeler may make slight adjustments to this parameter to fit experimental data to the model predictions.[99, 100]

Treated within the DLVO framework, the interaction potential $\left(V_{\text{int}}\right)$ is a sum of attractive and repulsive potentials $\left(V_{\text{int}} = V_A + V_R\right)$. The attractive forces are typically lumped together under a single van der Waals expression:

$$V_A = \frac{-A}{6}\left[\frac{2r_i r_j}{R^2 - (r_i + r_j)^2} + \frac{2r_i r_j}{R^2 - (r_i - r_j)^2} + \ln\left(\frac{R^2 - (r_i + r_j)^2}{R^2 - (r_i - r_j)^2}\right)\right] \tag{3.9}$$

where A is the Hamaker constant. The repulsive potential arises from electrostatic forces and a number of non-DLVO contributions (stearic forces, depletion interaction and solvation forces).[2] These contributions are often difficult to isolate so, in modeling applications, the contributions are often lumped together and treated using an electrostatic repulsion model. For example, Fortuny *et al*[100]. were able to model the coagulation of poly(methyl methacrylate) / poly (butyl acrylate) particles that were stabilized with Disponil FES 32 IS, a surfactant that confers both electrostatic and steric stabilization using the strictly-electrostatic repulsion model. The most widely used expression for computing the electrostatic repulsion is the Hogg-Healy-Fürstenau (HHF) expression.[101] The HHF expression is valid for low surface potentials $\left(\psi < 25\ mV\right)$ only, a condition that is often violated when modeling the stability of polymer latexes. The expression recently developed by Liu and Hsu, based on a boundary integral-based approach, is valid at higher surface potentials and may be used in place of the HHF expression.[102] For constant surface potential, the Liu-Hsu (LH) expression has the following form:

$$V_R = \left(\frac{k_B T}{e}\right)^2 \left(\frac{\varepsilon \pi r_i r_j}{R}\right)\left(\left(\Upsilon_i^2 + \Upsilon_j^2\right)\ln\left(1-\mathrm{e}^{-2\kappa L}\right) + 4\Upsilon_i^2\Upsilon_j^2 \tanh^{-1}\left(e^{-\kappa L}\right)\right) \qquad (3.10)$$

where ε is the permittivity of the dispersion medium, R is the center-to-center distance between the particles, L is the surface-to-surface distance between the particles and Υ_i is a correction factor (for particle *i*) accounting for the overestimation of repulsive potential that arises from the approach used to derive Equation (3.10):

$$\Upsilon_i = 4e^{\kappa L/2} \tanh^{-1}\left(e^{-\kappa L/2} \tanh\left(\frac{z_+ e\psi_i}{4k_B T}\right)\right) \qquad (3.11)$$

where z_+ is the counter-ion valence, ψ_i is the surface potential on particle *i* and e is the electron charge constant. The LH expression under constant surface charge is identical to Equation (3.10), but the correction factor is computed using an iterative procedure (see the original paper for details[102]).

The boundary conditions of the convection-diffusion equation, Equation (3.2) are as follows: $c = 0$ at $r = r_i + r_j$ and $c = c_{bulk}$ at $r = \infty$. The PDE is conveniently solved in spherical coordinates (refer to the papers of Melis[44] or Lattuada[47] for more details regarding the numerical techniques employed). Once the particle concentration field has been obtained, the coagulation rate coefficient is computed by computing the inward particle flux through an arbitrary spherical envelope drawn around the reference particle:

$$\beta_{ij} = \int_S \left(\mathbf{D}\nabla c - \mathbf{v}_{conv} - \mathbf{v}_{\text{int}} \right) \cdot \mathbf{n} dS \tag{3.12}$$

According to divergence theorem, flux will be conserved regardless of the radial location of the envelope surface.

Cast in spherical coordinates and rewritten in dimensionless form, Equation (3.12) reads as follows:[47]

$$\begin{aligned} &\frac{1}{\xi^2}\frac{\partial}{\partial \xi}\left(\xi^2 \left(G(\xi,\lambda)\frac{\partial C}{\partial \xi} - C\left(Pe \cdot f_1(\xi,\lambda)\left(3\cos(\theta)^2 - 1\right) - G(\xi,\lambda)\frac{d\bar{V}_{\text{int}}}{d\xi} \right) \right) \right) \\ &+ \frac{1}{\xi \sin(\theta)}\frac{\partial}{\partial \theta}\left(\sin(\theta)\left(\frac{H(\xi,\lambda)}{\xi} \right)\frac{\partial C}{\partial \theta} - C\left(Pe \cdot f_1(\xi,\lambda)\cos(\theta)\sin(\theta) \right) \right) = 0 \end{aligned} \tag{3.13}$$

where $\xi = \frac{2r}{r_i + r_j}$ is the dimensionless distance, $C = c / c_{bulk}$ is the normalized particle concentration and $\bar{V}_{\text{int}} = V_{\text{int}} / k_B T$ is the normalized interaction potential. For extensional flow, the velocity profiles functions, $f_1(\xi, \lambda)$ and $f_2(\xi, \lambda)$ are defined as follows:

$$f_1(\xi, \lambda) = \frac{\xi}{2}\left(1 - A(\xi, \lambda)\right)$$
$$f_2(\xi, \lambda) = \frac{-3\xi}{2}\left(1 - B(\xi, \lambda)\right) \tag{3.14}$$

The dimensionless number that quantifies the relative magnitude of convection to diffusion is the Peclet number (Pe), which is defined as:

$$Pe = \frac{3\pi\eta\dot{\gamma} r_i r_j (r_i + r_j)}{2k_B T} \tag{3.15}$$

Lattuada and Morbidelli found that, in order to reach convergence, approximately 290 discretization points were required to discretize the domain along the colatitude while more than 9200 discretization points were required along the radial direction.[47] Computing hundreds of β_{ij} values at multiple time steps, as required to solve a complete population balance model, would therefore require a very large amount of computing power. Currently, the computational resources required to numerically solve Equation (3.13) are too high to consider direct implementation within a population balance framework.

Melis *et al.* used the numerical solution to Equation (3.13) to conduct a theoretical investigation into the changes that arise in magnitude of β_{ij} as the ratio of fluid convection to particle diffusion changes (i.e. varying Pe).[44] An attempt was made to develop an analytical expression to fit the

simulation data. Under unstable conditions (i.e. low electrostatic forces), the rigorous model results could be fit with the following semi-empirical expression, whereby the perikinetic and orthokinetic contributions were assumed to be additive in nature:

$$\beta = \beta_{diff} + \beta_{conv} = \frac{8\pi D r_i}{W} + p_1 \dot{\gamma}^{0.86} \tag{3.16}$$

where p_1 is an adjustable parameter. At low shear rates, $\beta = \beta_{diff}$ (i.e. the lower limit is independent of shear rate), while at high shear rates, β varies nonlinearly with shear rate (or Peclet number). Melis found that Equation (3.16) provided a poor fit for more stable systems, where the β vs. $\dot{\gamma}$ plots exhibit a sigmoidal shape, with the transition between the two limits occurs over a much narrower range of $\dot{\gamma}$.

Very recently, Lattuada and Morbidelli derived an analytical expression that reproduces the results of the numerical simulation, even in the intermediate Pe region where β transitions from diffusion-controlled to fully convective. The analytical expression was obtained by replacing the two velocity profile functions in Equation (3.13) with a simplified velocity profile $f(\xi,\lambda)$ where the angular dependence is neglected:

$$f(\xi,\lambda) = \frac{-\xi\left(1 - A(\xi,\lambda)\right)}{3\sqrt{3}G(\xi,\lambda)} \tag{3.17}$$

The simplified expression reads as follows:

$$\frac{1}{\xi^2}\frac{d}{d\xi}\left(\xi^2\left(G(\xi,\lambda)\frac{dC}{d\xi} + \left(G(\xi,\lambda)\frac{d\bar{V}_{\text{int}}}{d\xi} - Pe\cdot f(\xi,\lambda)\right)C\right)\right) = 0 \tag{3.18}$$

The Lattuada and Morbidelli model requires the use of a boundary layer approximation, as the expression used to compute the radial velocity will diverge as ξ approaches ∞. Outside of the boundary layer, the interaction potential is neglected and a simple velocity profile function is imposed, yielding the following expression:

$$\frac{1}{\xi^2}\frac{d}{d\xi}\left(\xi^2\left(G(\xi,\lambda)\frac{dC}{d\xi}-\left(Pe\cdot f_s(\xi,\lambda)\right)C\right)\right)=0 \tag{3.19}$$

where $f_s(\xi)=\alpha/\xi$ and α is an adjustable parameter used to capture the size dependence on the rate of aggregation (arising from hydrodynamic interactions) at high Pe values. The expression used to compute the boundary layer thickness is:

$$\delta = p_\delta\sqrt{\frac{2}{Pe\kappa\left(r_i+r_j\right)}} \tag{3.20}$$

Where p_δ is an adjustable pre-factor that is used to fit the simplified expression's predictions to the numerical data generated from the rigorous solution. Using the Fuchs derivation approach,[2] Equation (3.18) is integrated from $\xi=2$ to $\xi=2+\delta$ and Equation (3.19) is integrated from $\xi=2+\delta$ to $\xi=\infty$, obtaining an expression for β_{ij}. Expressed in terms of a stability ratio, W:

$$W=\frac{\beta_{ij}}{\beta_{ij}^{fast}}=\frac{1}{2\int_2^\infty \frac{e^{He(2+\delta-\xi)\left(\int_{2+\delta}^{\xi}\left(-Pe\cdot f(\xi)+\frac{dV_{int}}{d\xi}\right)d\xi-Pe\frac{\alpha}{2+\delta}\right)-Pe\cdot He(\xi-2-\delta)\frac{\alpha}{\xi}}}{G(\xi,\lambda)\xi^2}d\xi} \tag{3.21}$$

where $He(x)$ is the Heaviside function and β_{ij} is the diffusion-limited rate of aggregation:

$$\beta_{ij}^{fast}=\frac{2k_BT\left(r_{s,i}+r_{s,j}\right)}{3\eta}\left(\frac{1}{r_{s,i}}+\frac{1}{r_{s,j}}\right) \tag{3.22}$$

The presence of two adjustable parameters in Equation (3.21) may limit its applicability, but it captures the sigmoidal shape of the stability curve that is predicted by the rigorous expression. In the presence of particle interaction (e.g. for latex particles that are stabilized by adsorbed surfactant), but no fluid convection ($Pe = 0$), Equation (3.23) simplifies to the following expression:

$$\beta_{ij} = \frac{\beta_{ij}^{fast}}{2\int_2^{\infty} \frac{e^{\bar{V}_{\text{int}}(\xi,\lambda)}}{G(\xi,\lambda)\xi^2} d\xi} \tag{3.23}$$

The denominator of Equation (3.23) is the Fuchs stability ratio (W). Equation (3.23) has found widespread use in emulsion polymerization modeling field[8, 99, 103, 104] where it is typically assumed that fluid convection on the microscopic scale can be neglected. If the complex velocity function is replaced by a symmetrical velocity gradient $\left(v_{conv,r} = \dot{\gamma} r\right)$, the following expression can be obtained (refer to section 4.6.1.3 of Blackley[2] for the derivation):

$$\frac{\beta_{ij}}{\beta_{ij}^{fast}} = \frac{1}{2\int_2^{\infty} \frac{\exp\left(\frac{V_{\text{int}}}{k_B T} - \frac{4Pe\left(r_{s.1} + r_{s,2}\right)}{3\pi\xi}\right)}{G\left(\xi,\lambda\right)\xi^2} d\xi} \tag{3.24}$$

3.3 Outline of CFD Simulation Method

The reactor investigated in this work was a round-bottom vessel agitated by a centered four-bladed 45° pitched blade turbine with two round baffles. The reactor geometry considered in this work is shown in Figure 3.1, along with the key vessel and impeller dimensions. While the

baffles are prone to fouling, they are necessary when operating in the turbulent regime to eliminate vortex formation.[87]

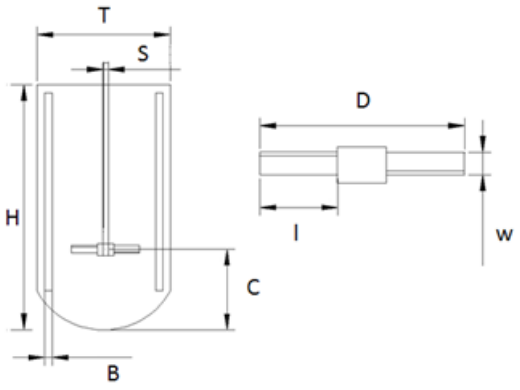

Part	Symbol	Relative Dimension
tank diameter	T	T
tank height	H	1.4 T
blade diameter	D	T/3
shaft diameter	S	T/30
baffle diameter	B	D/12
blade width	W	D/5
blade length	l	(7/15) D
blade clearance	C	H/3

Figure 3.1. Schematic of the reactor geometry used in this work and the key design dimensions.

In order to investigate the impact of reactor scale-up, CFD simulations were run across three (geometrically similar) reactor scales: 1 L, 100 L and 10 m^3, corresponding to tank diameters (T) of 9.69×10^{-2} m, 4.50×10^{-1} m and 2.09 m, respectively. The impeller rotational speed was set to 100 RPM at the 1-L scale, a value chosen to provide sufficient emulsification at the laboratory scale.[41] Based on the objective of maintaining a constant volumetric power input, the impeller rotational speed is lowered when the vessel is scaled-up, based on the following relationships:[87]

$$\frac{P}{V} \propto N_I^3 D_I^2 \tag{3.25}$$

$$N_{I,2} = N_{I,1}\left(\frac{D_{I,1}}{D_{I,2}}\right)^{\frac{2}{3}} \tag{3.26}$$

Application of Equation (3.26) results in the impeller rotational speed being lowered to (approximately) 35.9 RPM and 12.2 RPM as the reactor is scaled-up to 100 L and 10 m^3, respectively. Equation (3.25) holds true for turbulent conditions only, where inertial forces dominate.

The base case reactor fluid modeled is a 44 vol.-% solids content polymer latex, with an average particle diameter of 150 nm and a particle polydispersity index of 0.10 (narrowly distributed). An additional set of simulations were run in which the solids content of the latex was increased to ~ 60 vol.-% in order to examine the effect of solids content on the shear rate distribution inside the reactor. Latex viscosity was modeled using the Carreau-Yasuda model, which has been shown to correctly capture the shearing behavior of concentrated latexes;[5]

$$\eta(\dot{\gamma}) = \eta_\infty + \frac{\eta_0 - \eta_\infty}{\left[1+(\dot{\gamma}\tau)^a\right]^{(1-m)/a}} \qquad (\text{for } \dot{\gamma} < \dot{\gamma}_{th}) \tag{3.27}$$

where η_0 is the zero-shear viscosity, η_∞ is the infinite-shear viscosity, τ is the characteristic time for the onset of shear-thinning and γ_{th} is the shear rate beyond which the latex will begin to shear thicken. Pishvaei found that setting the values of the adjustable parameters, a and m, to 1.0 and 0.65, respectively, provided the best fit to their experimental data. The four model parameters are dependent on the latex solid content (ϕ) and the (PSD-dependent) effective maximum packing fraction (ϕ_m) according to general form of the Krieger-Dougherty equation.[58]

$$\zeta = \zeta_s \left(1 - \frac{\phi}{\phi_{m,\zeta}}\right)^{-[\eta]_\zeta \phi_{m,\zeta}} \qquad \zeta = \eta_0, \eta_\infty, \tau, (1/\dot{\gamma}_{th}) \tag{3.28}$$

where The intrinsic viscosity $[\eta]$ and hard sphere maximum packing fraction parameters $\phi_{\max,\zeta}$ needed to utilize Equation (3.28) are listed in Table 3.1. The stabilization layer surrounding the latex particle is deformable under shear, such that the latexes behave as deformable spheres.[30] Therefore, the effective volume fraction of the dispersed phase that is greater than the volume faction of the polymer particles alone. The thickness of the stabilizing layer is estimated by the Debye length $\left(\kappa^{-1}\right)$ such that the effective maximum packing fraction of a particle with radius r_i can be computed as:

$$\phi_{m,i} = \phi_{m,hs}\left(1+\frac{1}{\kappa r_i}\right)^3 \tag{3.29}$$

Table 3.1. Parameters used to model the solid concentration-dependence of the Carreau-Yasuda model parameters for a polystyrene latex.[5]

η_0		η_∞		τ		$\tau_{th}=1/\dot{\gamma}_{th}$	
$\phi_{m,0}$	$[\eta]_0$	$\phi_{m,\infty}$	$[\eta]_\infty$	$\phi_{m,\tau}$	$[\eta]_\tau$	$\phi_{m,th}$	$[\eta]_{th}$
0.64	4.2	0.71	2.5	0.64	7.0	0.71	7.0

The computational mesh was designed and generated in Gambit 2.4 (Ansys) using hexahedral cells to reduce the size of the mesh required to obtain a grid-independent flow field.[13] The number of cells required to achieve grid-independence was approximately 4.41×10^5. A two-dimensional slice of the computational grid is shown in Figure 3.2.

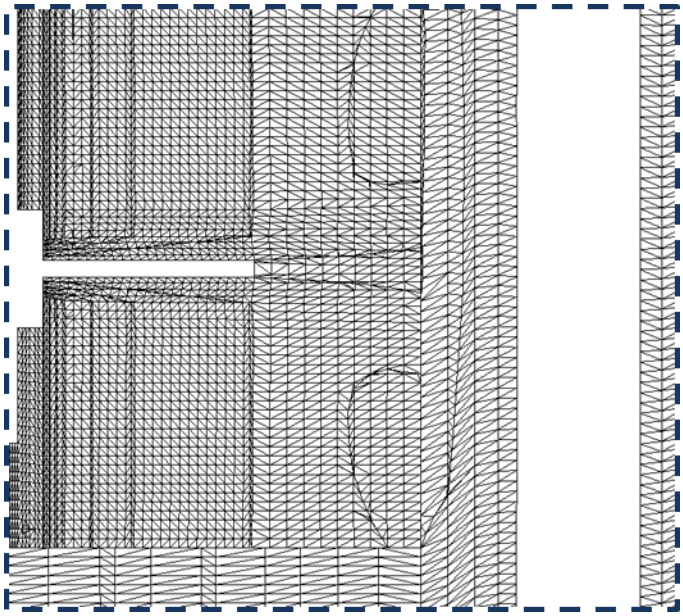

Figure 3.2. Two-dimensional slice of the computational mesh showing the hexahedral elements and the grid refinement near the impeller where velocity gradients are expected to be highest.

In turbulent conditions, the flow field is expected to be unsteady due to impeller-baffle interactions. While a transient solution method would be necessary if an accurate measurement of the impeller power draw was desired, a steady-state solution is acceptable given the objectives of this work. The CFD simulation was implemented in Fluent 6.3 using the steady-state Multiple Reference Frame (MRF) method to address the rotation of the impeller (for details, refer to the Fluent User's Manual[105]). The following boundary conditions were used: (i) constant angular velocity along the impeller surface; (ii) no slip condition at the baffles and along the vessel wall; (iii) no normal velocity at the fluid surface, which is assumed to be flat.

Turbulence was modeled using a Reynolds-Averaged Navier Stokes (RANS) approach, whereby the turbulent fluctuations are time-averaged. Closure to the RANS equations was provided via the

standard $k-\varepsilon$ model, which has been shown to provide acceptable agreement with experimental results, particularly with regards to the overall flow field.[74, 106] Deglon and Meyer[107] found that the MRF method coupled with the $k-\varepsilon$ turbulence model could accurately model the fine scale turbulent structures (including the trailing vortices) in a stirred tank, however, a high grid resolution (~ 2×10^6 cells) was required. The turbulence models included in the Fluent commercial CFD simulation package were developed for modeling Newtonian fluids; that is, fluids with shear-rate independent viscosity. The RANS approach to turbulence modeling requires the decomposition of instantaneous variables (e.g. velocity, pressure) into mean and fluctuating components. The additional fluctuating terms (known as Reynolds stresses) that show up in the conservation equations require the derivation of additional conservation equations to provide closure. In the k-ε model, closure is provided through the specification of two additional conservation equations: one for kinetic energy (k) and one for turbulent energy dissipation (ε).[11] For non-Newtonian fluids, the conservation equations include extra stress terms, sometimes referred to as polymeric stresses, due to fluctuations in apparent viscosity. The classic $k-\varepsilon$ model does not take these extra source terms into account, so the predictive capabilities of Newtonian turbulence models, as applied to non-Newtonian fluids, is questionable. Since the closure of RANS equations for non-Newtonian fluids is still a topic of current research,[108] it is unlikely that commercial CFD software will include specialized turbulence models for non-Newtonian fluids in the near future. While there has been some progress in modeling the turbulent flow of non-Newtonian fluids using Direct Numerical Simulation (DNS),[109] the computational requirements of DNS are still highly restrictive. Therefore, the modeling of fluid rheology under fully turbulent flow for non-Newtonian fluids inside stirred vessels requires the use of an approximate method. The most-commonly applied approach is the Metzner-Otto

method, whereby a constant apparent viscosity is employed in lieu of a non-Newtonian viscosity model; the apparent viscosity is computed using a representative shear rate via Equation (3.4). The Metzner-Otto method has been shown to provide acceptable predictions when used to model turbulent mixing of non-Newtonian fluids inside reactors, [17, 74, 106] although strictly speaking, it was developed for reactors in the laminar regime.[110] Recently, Wu and Chen modeled the flow inside an anaerobic digester using a power-law viscosity model in conjunction with the standard $k-\varepsilon$ turbulence model and found that the model's predictive capabilities were acceptable.[111]

Based on the findings of Wu and Chen, the decision was made to proceed with the use of the Carreau-Yasuda model to compute fluid viscosity, with a secondary set of simulations being run for comparison by replacing the non-Newtonian rheological model with an apparent viscosity (computed using the Metzner-Otto approach):

$$\eta_{aa}\left(\dot{\gamma}\right)=\eta_{\infty}+\frac{\eta_0-\eta_{\infty}}{\left[1+\left(KN\tau\right)^{a}\right]^{(1-m)/a}} \tag{3.30}$$

where K is an adjustable proportionality constant..

Although it is often misapplied to a wider range of flow conditions, the Metzner-Otto method was designed (and validated) strictly as a means of computing power consumption for mixing tanks operating in the laminar regime, where the Power number is inversely proportional to the Reynolds number. For fully-turbulent flow, the high rate of energy dissipation in the impeller region generates additional shear (refer to Equation (3.4)) such that the contributions of turbulence to shear may be at least one order of magnitude greater than the contribution from the mean velocity field gradient.[110] In such a scenario, the Metzner-Otto method will under-

approximate the shear field within the impeller region. To account for shear generated through the dissipation of the smallest eddies, Nouri and Hockey[112] recommended setting the proportionality constant, K, to 54, which is outside the range of 10 – 12 recommended for the computation of power consumption in the laminar regime.[87] While this adjustment may yield a better fit for computing the power consumption, the Metzner-Otto method is still inappropriate for modeling liquid blending because the shear rate outside of the impeller region will be orders of magnitude lower. The increase in the proportionality constant meant to extend the Metzner-Otto method's applicability to operation in the transition and turbulent regimes will exacerbate the overestimation of shear within the region far away from the impeller, thus underestimating blend time. Thus from the perspective of blend performance, the predictions generated using the Metzner-Otto approximation for dynamic viscosity can be thought of as an optimistic scenario (i.e. an underestimation of the blend time).

3.4 Results and Discussion

3.4.1 CFD Simulation Results

At 44 vol.-% solids, the computed rheological parameters of the latex were as follows:

$$\eta_0 = 2.05\times10^{-2}\ \text{kg/m/s} \qquad \eta_\infty = 5.67\times10^{-3}\ \text{kg/m/s}$$
$$1/\gamma_{th} = 1.96\times10^{-2}\ \text{s}$$

Using η_0 and η_∞, a Reynolds number operating range can be estimated as

$$\text{Re}_{\min} = \frac{\rho N D^2}{\eta_0} \qquad \text{Re}_{\max} = \frac{\rho N D^2}{\eta_\infty} \tag{3.31}$$

The computed Reynolds number (Re) ranges are:

$$\begin{aligned} &\text{1L:} && 7.63\times10^{2} - 2.76\times10^{3} \\ &\text{100 L:} && 5.89\times10^{3} - 2.13\times10^{4} \\ &\text{10 m}^3\text{:} && 4.31\times10^{4} - 1.56\times10^{5} \end{aligned}$$

Using the rule-of-thumb guideline that a reactor is operating in the transitional regime when $10^2 < \mathrm{Re} < 10^4$ and fully-turbulent regime when $\mathrm{Re} \geq 10^4$, the 10 m^3 reactor is the only reactor scale which is operating under fully-turbulent conditions, while the laboratory and pilot scale reactors are operating in the transitional regime. The computed power numbers $\left(N_P\right)$ were as follows:

$$\begin{aligned} &\text{1L:} && N_P = 6.87\times10^{-1} \\ &\text{100 L:} && N_P = 5.01\times10^{-1} \\ &\text{10 m}^3\text{:} && N_P = 4.56\times10^{-1} \end{aligned}$$

For pitched blade turbines,[87] $N_P \sim 3\times10^{-1}$, which is reasonably close to the value computed at the 10 m^3-scale. It can be seen from the computed N_P values (above) that they are decreasing with Re, which further suggests that the lab and pilot scale reactors are not operating in the fully turbulent regime, as N_P is independent of Re in the fully-turbulent regime. This conclusion is reinforced when the flow profiles along a vertical cross section cut through the center of the vessel (Figure 3.3) are examined. It can be seen that the flow pattern predicted at the 1-L scale differs to a large degree from the predicted flow patterns seen at the 100 – L and 10-m^3 scales.

The change in flow profile with vessel scale does not provide much insight towards the study of mechanically induced particle coagulation, beyond establishing the expectation that the shear rate distribution will change with the reactor scale. Using Equation (3.4), the local shear rate

distribution can be computed from the local turbulent energy dissipation rate distribution. The change in the local shear distribution with reactor scale is shown in Figure 3.4.

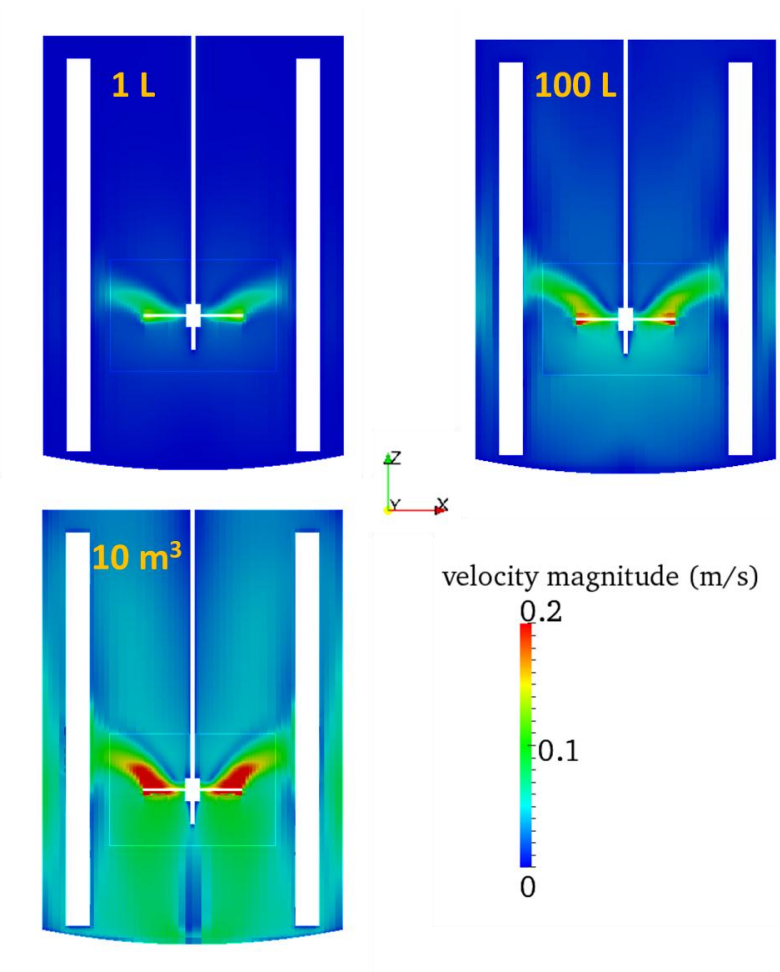

Figure 3.3. Vertical cross-sectional slices showing the change in the velocity magnitude profile as the tank geometry is scaled from 1 L to 10 m^3, maintaining a constant volumetric holding power input (P/V ratio). N_I is set to 100 RPM at the 1-L scale, 35.9 RPM at the 100-L scale and 12.9 RPM at the 10-m^3 scale.

The predicted simulation results are interesting. It can be seen that the shape of the localized shear rate profile changes with vessel scale, as would be expected from the change in the flow

profile. The volume-averaged turbulent shear rate decreases as the vessel is scaled up from 1 L to 10 m^3. Computed over the entire domain, the volume-averaged (turbulence-induced) shear rate decreases from 7.9 s^{-1} at the 1-L scale to 5.4 s^{-1} at 10-m^3 scale. The maximum shear rate in the flow (due to turbulence) is 1250 s^{-1} at the 1-L scale and 134.9 s^{-1} at the 10 m^3-scale. In addition to the extensional flow generated from the smallest turbulent eddies, the shear at the impeller tips should be briefly considered as well. Unfortunately the mesh resolution at the impeller tips is not fine enough to determine the shear rate precisely, but heuristic guidelines propose the following scaling relationship:

$$\dot{\gamma}_{\max} \propto \pi ND (= \text{tip speed})$$

From the 1–L to the 10-m^3 scale, the maximum shear arising from the fluid velocity gradient is expected to increase by a factor of ~ 2.8, although Melis notes that the inertial forces from the main flow field can be neglected for particles that are smaller than a few microns (i.e. at the microscopic particle scale, the shear arising from the Kolmogorov scale turbulence is more important).[44] Furthermore, it should be noted that this expression does not account for the high rate of shear generated from turbulence in the trailing vortices near the impeller tips, which is likely to be higher. [84]

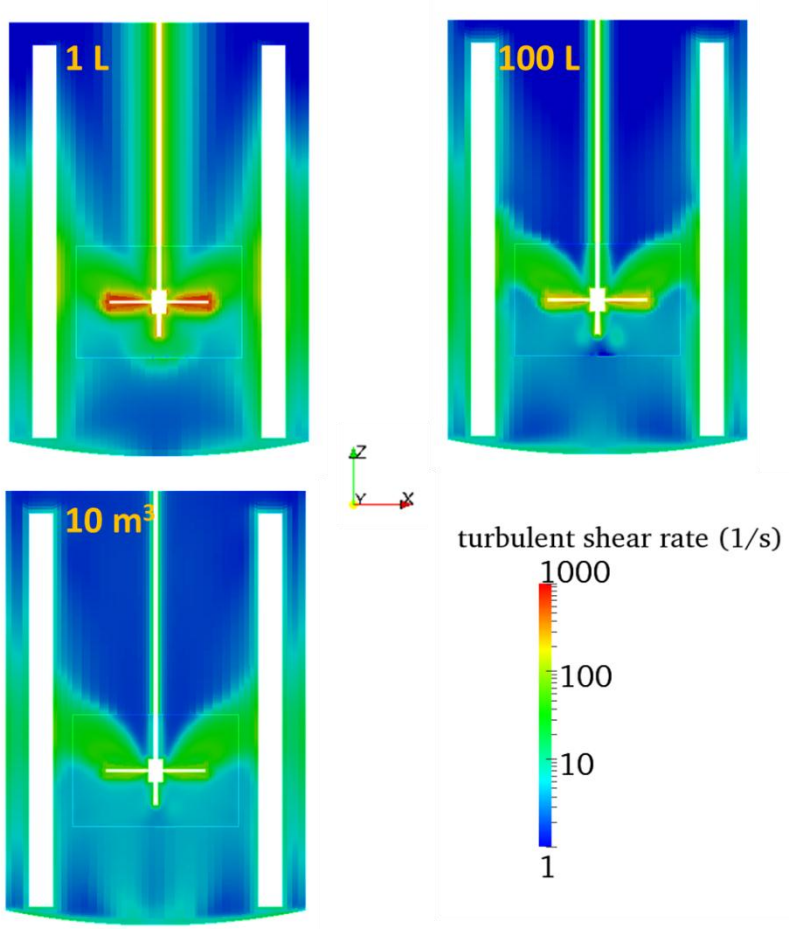

Figure 3.4. Vertical cross-sectional slices showing the evolution in the localized shear rate profile, computed with Equation (3.4), as the tank geometry is scaled from 1 L to 10 m^3, maintaining a constant volumetric holding power input (P/V ratio). N_I is set to 100 RPM at the 1-L scale, 35.9 RPM at the 100-L scale and 12.9 RPM at the 10-m^3 scale.

The manner in which the shear rate distribution evolves with reactor scale (Figure 3.4) suggests that any increase in the rate of particle coagulation arising from turbulence is likely to be observed in both lab- and commercial- scale vessels. Similarly, if experiments performed at the laboratory scale indicate that the rate of particle coagulation is independent of the impeller rotational speed (as was observed by Kemmere *et al.* during the emulsion polymerization of styrene and vinyl acetate[41]), the system may remain uninfluenced by mechanical coagulation at

the pilot plant and commercial scales. Using Equation (3.15) and setting $r_i = r_j$, the impact of vessel scale-up on the local Pe can be visualized (Figure 3.5).

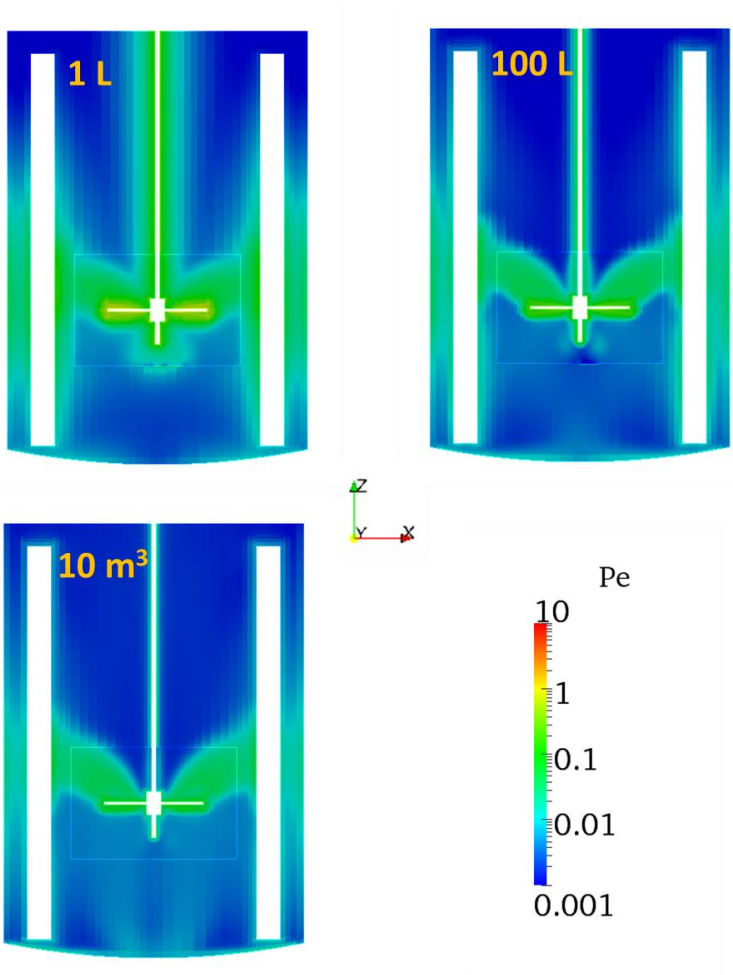

Figure 3.5. Vertical cross-sectional slices showing the change in the Peclet number profile as the reactor is scaled from 1 L to 10 m^3, maintaining a constant volumetric holding power input (P/V ratio). N_I is set to 100 RPM at the 1-L scale, 35.9 RPM at the 100-L scale and 12.9 RPM at the 10-m^3 scale.

The Pe distribution is similar to the $\dot{\gamma}$ distribution as $Pe \propto \varepsilon^{1/2}$. Within the impeller region, the maximum local Pe is 1.2 at the 1-L scale, 0.33 at the 100-L scale and 0.13 at the 10-m^3 scale. Melis[44] noted that the Peclet number does not identify the situation where convection starts to

play a role, but modified Peclet number $\left(\overline{Pe}\right)$ does and can be computed for equal radii particles with the following expression:

$$\overline{Pe} = Pe\frac{\left(1+\kappa r_s\right)}{\left(\kappa r_s\right)^2} \tag{3.32}$$

Since the modified Peclet number depends on the inverse Debye length, more detailed reaction conditions must be specified before $\overline{Pe}$ can be computed. For example, at 44 vol..-% solids content, a sodium dodecyl sulphate concentration of 5.3×10^{-3} wt.-% and a sodium chloride salt concentration of 2.65×10^{-2} wt.-%, $\kappa^{-1} = 1.05\times10^{-9}\,\text{m}$. For $r = 7.5\times10^{-8}\ \text{m}$, $r\kappa = 75$ and $\overline{Pe} = Pe/74$. Under these conditions, $\overline{Pe}$ takes on the following maximum values:

$$1\text{ L reactor}: \ \overline{Pe} = 1.7\times10^{-2} \qquad 10\ \text{m}^3\ \text{reactor}: \ \overline{Pe} = 2.0\times10^{-3}$$

If the surfactant and salt concentrations are drastically reduced, κ^{-1} would increase. $\kappa^{-1} = 3\times10^{8}\ \text{m}$ is a realistic upper limit, which corresponds to corresponding to $r\kappa = 2.5$ and $\overline{Pe} = Pe/1.79$. Under these conditions, the maximum value of $\overline{Pe}$ in the reactors is:

$$1\text{ L reactor}: \ \overline{Pe} = 7.2\times10^{-1} \qquad 10\ \text{m}^3\ \text{reactor}: \ \overline{Pe} = 8.4\times10^{-2}$$

In the 1-L reactor, $\overline{Pe}$ is above the threshold of $\overline{Pe} = 0.1$, which according to Melis[44], indicates that the reactor fluid dynamics are likely to play a role in the aggregation rate.

A direct relationship between $\overline{Pe}$ and r can be obtained by setting $r_1 = r_2 = r$ in Equation (3.15) and substituting the resulting expression into Equation (3.32):

$$\overline{Pe} = \frac{3\pi\eta_s\dot{\gamma}r}{k_bT}\frac{\left(1+\kappa r\right)}{\left(\kappa\right)^2} \tag{3.33}$$

This indicates that Pe increases in proportion to $\left(r + r^2\right)$ and in inverse proportion to κ^2. According to Equation (3.33), if the aggregation of 150 nm particles is influenced by the shear field in the impeller region, then the aggregation rate of particles larger than 150 nm in diameter would be affected in a larger region of the reactor. Equation (3.33) also indicates that latexes may become more sensitive to shear under conditions where the double layer is diffuse (i.e. an environment of low ionic strength). Therefore, shear-induced coagulation may or may not enhance the rate of particle coagulation at both the laboratory scale and the industrial scales, depending on the reactor conditions and the latex particle size distribution. Therefore it is not surprising to find conflicting conclusions regarding the importance of shear-induced coagulation throughout the literature.[41, 45] Interestingly, the latex may become more sensitive to mechanical agitation under conditions where the latex is stabilized against Brownian coagulation. In reactors where the latex is purposefully destabilized through the addition of an electrolyte (thereby raising the ionic strength) the flow field is unlikely to enhance the rate of particle aggregation.

Due to the difficulty faced in modeling non-Newtonian fluids in the turbulent regime, it is useful to investigate the effect of the viscosity modeling approach on the qualitative CFD predictions. An additional set of simulations were run, where the Carreau-Yasuda model was used in place of the Metzner-Otto approximation to model the apparent viscosity of a 44 vol.-% latex. At 44 vol.-%, the difference between the viscosity limits is on the order of 3.5, thus is not surprising to observe that the qualitative characteristics of the flow fields does not change appreciably between the two approaches to modeling fluid viscosity. The velocity magnitude profiles are show in Figure 3.6, while the particle Pe distribution profiles are shown in Figure 3.7. At 44 vol.-% solids content, the choice of fluid viscosity model does not appear to have an appreciable effect

on the CFD simulation predictions. The difference between the zero-shear and infinite-shear viscosity is approximately a factor of four, but the values of the volume-averaged viscosity computed with both methods differ by less than 15% :

$$\text{Carreau-Yasuda:} \quad \bar{\eta} = 2.02\times10^{-2} \text{ kg/m/s}$$

$$\text{Metzner-Otto} \quad \eta_a = 1.78\times10^{-2} \text{ kg/m/s}$$

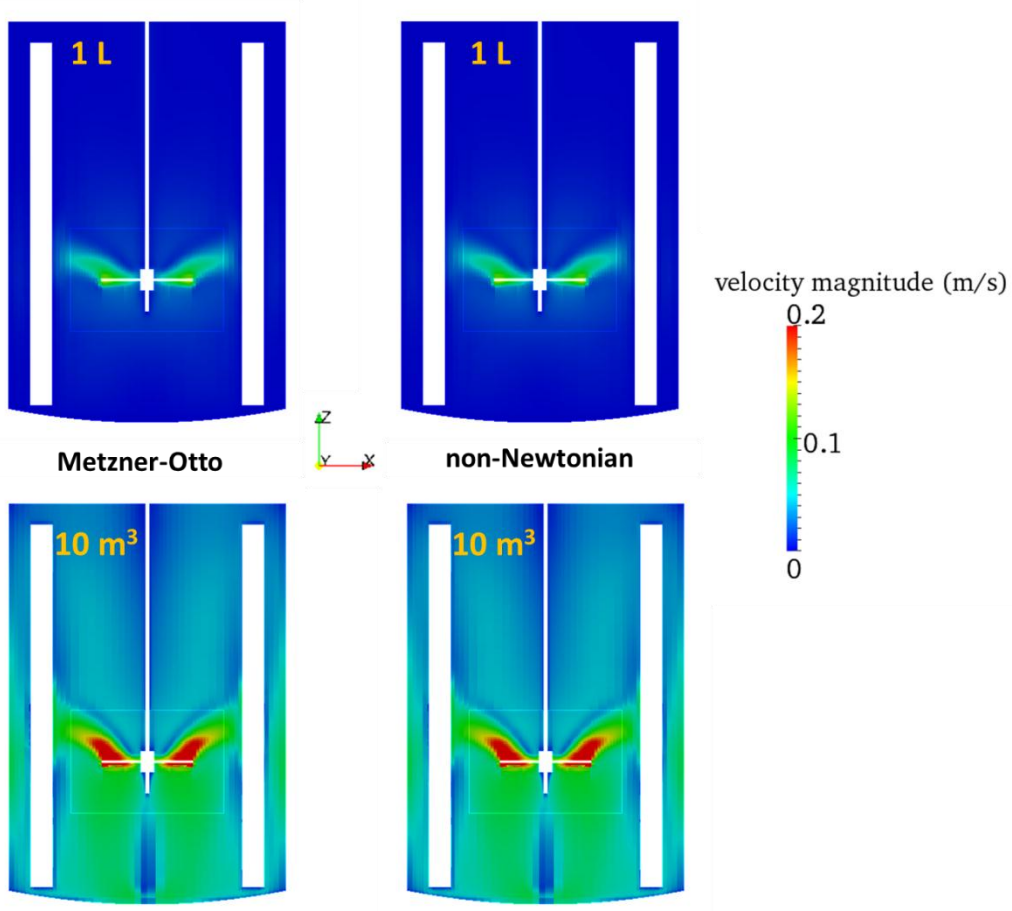

Figure 3.6. Vertical cross-sectional slices showing the variation in the flow profile at both the 1-L (top) and 10-m^3 (bottom) reactor scales when the dynamic viscosity model is set as constant (left) or modeled with the Careau-Yasuda model (right). N_I is set to 100 RPM at the 1-L scale and 12.9 RPM at the 10-m^3 scale.

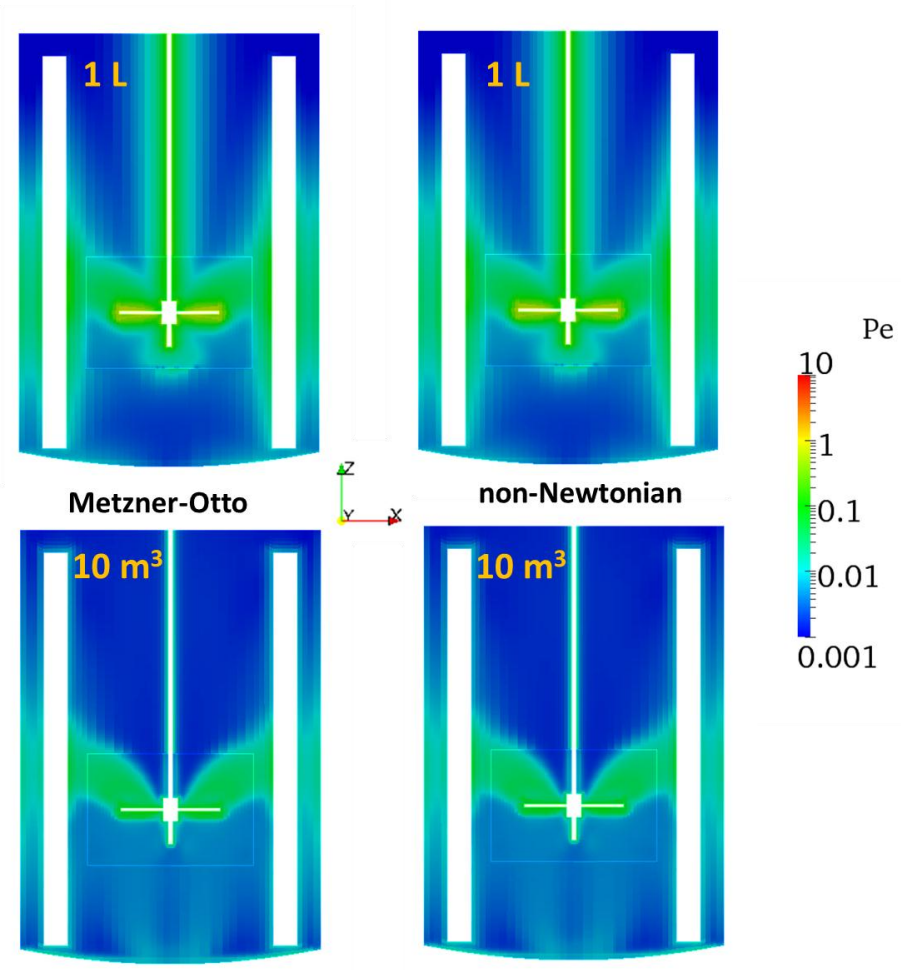

Figure 3.7. Vertical cross-sectional slices showing the variation in the particle Peclet number profile at both the 1-L (top) and 10-m^3 (bottom) reactor scales when the dynamic viscosity model is set as constant (left) or modeled with the Carreau-Yasuda model (right). N_I is set to 100 RPM at the 1-L scale and 12.9 RPM at the 10-m^3 scale.

At 59-vol.%, however, the latex is highly non-Newtonian, with the following plateaus:

$$\eta_0 = 1.87 \times 10^0 \text{ kg/m/s} \qquad \eta_\infty = 2.93 \times 10^{-2} \text{ kg/m/s}$$

Examining the flow fields (Figure 3.8), it is apparent that the approach used to model fluid viscosity will impact model predictions. It turns out that both the Metzner-Otto method and the

Carreau-Yasuda model are ill-equipped to model highly-pseudoplastic flow in the turbulent regime. Examining the volume-averaged properties of the fluid (Table 3.2), it can be seen that the Metzner-Otto model predicts higher average values for velocity magnitude and the particle Peclet number. If the impeller region is considered separately from the rest of the vessel, the discrepancy in the model-predicted average property values is reduced because the average apparent viscosity in the impeller region is approaches η_∞, regardless of the model used for the apparent viscosity. Outside of the impeller region, it is likely that the Metzner-Otto method under-predicts the fluid's dynamic viscosity, while the Carreau-Yasuda model is likely to over-predict fluid viscosity as the contribution of turbulence is not included in the computation of the shear rate used to compute the viscosity (see below for further discussion). At very high solids contents (> 59 vol.-%), however, this may not hold true due to latex becoming visco-elastic,[113] although at such high solids contents, fluid viscosity will be very high and the reactor will likely be operating in the laminar regime.

Table 3.2. Effect of viscosity model used in CFD simulation on average flow field properties for a 10 m^3 reactor filled with a high solid content latex (59 vol.-%). N_I was set to 35.9 RPM.

Property	**Metzner-Otto** (η_a)	**Carreau-Yasuda** $(\eta[\dot{\gamma}])$
$\overline{V}_{mag}$ (m/s)	Overall: 3.31×10^{-2} Impeller Region: 8.54×10^{-2}	Overall: 2.21×10^{-2} Impeller Region: 7.94×10^{-2}
$\overline{Pe}$	Overall: 2.22×10^{-3} Impeller Region: 6.82×10^{-3}	Overall: 1.46×10^{-3} Impeller Region: 6.11×10^{-3}
$\overline{\eta}$ (kg/m/s)	Overall: 1.12×10^{-1}	Overall: 7.67×10^{-1} Impeller Region: 2.73×10^{-1}

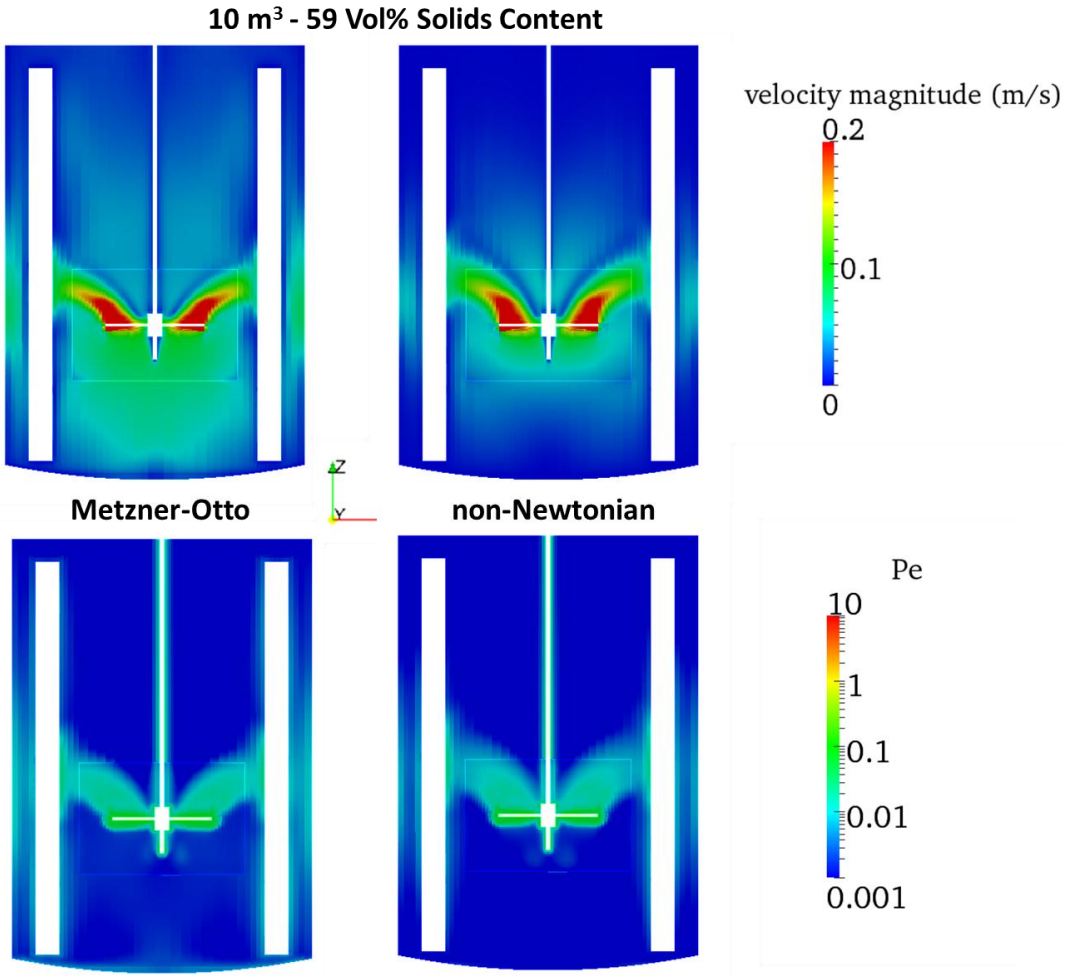

Figure 3.8. Vertical cross-sectional slices showing, for a higher solids content (59 vol.-%), the differences in the velocity profile (top) and the particle Peclet number profile when the dynamic viscosity model is changed from a constant approximation (left) to the Carreau-Yasuda (right). N_I is set to 12.9 RPM.

Direct implementation of a non-Newtonian viscosity law within the CFD code presents its own set of issues that call into question the quality of the predictions. Within the impeller region, the amount of shear acting upon the fluid is likely to be underestimated as the shear rate used to compute the fluid viscosity does not include any additional shear that may arise from the turbulent eddies. On the other hand, the Newtonian RANS models are expected to overestimate

the amount of turbulence present for a given set of flow conditions. As mentioned prior, the Newtonian turbulence closure models do not account for local fluctuations in the fluid viscosity. These fluctuations, if modeled as polymeric stress terms, would act opposite the Reynolds stresses; that is, if the Reynolds stresses transfer energy from the mean flow to increase the fluctuating components, the polymer stresses would reduce this effect.[108] Since the Carreau-Yasuda model implemented neglects the shear field arising from the dissipation of turbulence entirely, fluid viscosity is likely to be over-estimated. To further complicate matters, as the particle concentration in a latex approaches the maximum packing fraction, the latex will begin to display viscoelastic behavior[113]. The high viscosity coupled with viscoelasticity may lead to cavern formation, whereby mixing is confined to a small region around the impeller and the fluid outside this region will remain stagnant. Taking all of these factors into consideration, it would be unwise to rely upon CFD simulation, in its current state of development (commercial or otherwise), to model the mixing of high solid content polymer latexes at the commercial scale, where turbulence may be present yet confined to a small cavernous region surrounding the impeller.

3.4.2 Comparison of simple shear model vs. rigorous solution to the convection-diffusion equations

Lattuada and Morbidelli recently presented an expression for computing coagulation rate coefficients (Equation (3.21)) that reproduces the results obtained from the rigorous numerical solution to the Fuchs-Smoluchowski convection-diffusion equation in two dimensions. A coagulation model that can be used at both low and high Pe would be particularly useful for modeling industrial emulsion polymerization reactions from start to finish, where fluid rheology

and ionic conditions may vary by orders of magnitude over the course of the reaction. The results of Figure 3 of Lattuada and Morbidelli are reproduced below in Figure 3.9 (the lines with symbols).

Examining the curves produced using the Lattuada and Morbidelli model in Figure 3.9, one is drawn to the counterintuitive relationship between the ionic strength of the dispersion medium and the critical Pe at which the orthokinetic coagulation begins to contribute to (and eventually dominate) the overall rate of coagulation. As ionic strength is increased, both Equation (3.21) and the rigorous numerical simulation indicate that, while the system will become more susceptible to Brownian coagulation at the low shear limit, the critical Pe at which the system becomes susceptible to the effect of the shear field will increase. This falls in line with the trend predicted by Equation (3.33). Lattuada and Morbidelli reasoned that the magnitude of the electrostatic force $\left(F_{\text{int}}\right)$ is inversely proportional to the thickness of the double layer $\left(F_{\text{int}} \sim \nabla V_{\text{int}} \sim \kappa \mathrm{e}^{-\kappa L}\right)$; therefore, a thicker double layer (and hence smaller κ) results in the magnitude of the electrostatic force being smaller. From Equation (3.5) it can be seen that the velocity contribution due to interaction potential $\left(\mathbf{v}_{\text{int}}\right)$ is proportional to the electrostatic force, thus it too will decrease in magnitude if κ is decreased and its contribution to the overall convective flux will be smaller. As a result, a weaker convective contribution $\left(\mathbf{v}_{conv}\right)$ is needed to transition from the DLVO-controlled regime to the convective or shear-controlled regime. When the double layer thickness is decreased, the low Pe aggregation rate will increase due to a reduction in the electrostatic energy barrier, but the electrostatic forces will increase, leading to the regime transition occurring at a higher Pe.[47] The curves generated under the same conditions using the

simple shear coagulation model (Equation (3.24)) do not show this trend, despite having a very similar form to Equation (3.21); in fact, Equation (3.24) predicts that the Pe at which transition occurs is independent of ionic strength.

Examining Equation (3.21) in more detail, there are a number of components that set it apart from the simpler expression, Equation (3.24). The most significant difference between the two models is the inclusion of the boundary layer approximation in Equation (3.24). When the dimensionless distance of particle separation is less than the dimensionless thickness of the boundary layer, the total potential between the particles is computed by integrating the following expression:

$$\int_{2+\delta}^{\xi}\left(-Pe\cdot f\left(\xi\right)+\frac{dV_{\text{int}}}{dt}\right)d\xi-Pe\frac{\alpha}{2+\delta} \tag{3.34}$$

Slight rearrangement of this expression, coupled with substitution of the appropriate hydrodynamic function for extensional flow (Equation (3.17)) results in the following expression:[47]

$$Pe\left[\int_{2+\delta}^{\xi}\frac{\xi\left(1-A\left(\xi,\lambda\right)\right)}{3\sqrt{3}G\left(\xi,\lambda\right)}d\xi-\frac{\alpha}{2+\delta}\right]+\left(V_{\text{int}}\left(\varepsilon\right)-V_{\text{int}}\left(\delta\right)\right) \tag{3.35}$$

As the thickness of the double layer increases, δ will likewise increase. As $\delta\to\infty$, the first term of Equation (3.35) (and indeed, the entire expression) will approach $-\infty$. Recall that the first term arises from the use of a diverging velocity field. The further the boundary layer is extended outwards, the greater the influence of the convective potential and the lower the Pe at which the convective contribution becomes important. Numerically, it is the changes in the convective potential, rather than the interactive potential that result in the slightly counterintuitive trend seen in Figure 3.9. The velocity field function in Equation (3.24) is similar in to the velocity

field function used in the Lattuada kernel outside the boundary layer, a profile that does not diverge as $\mathcal{E} \to \infty$.

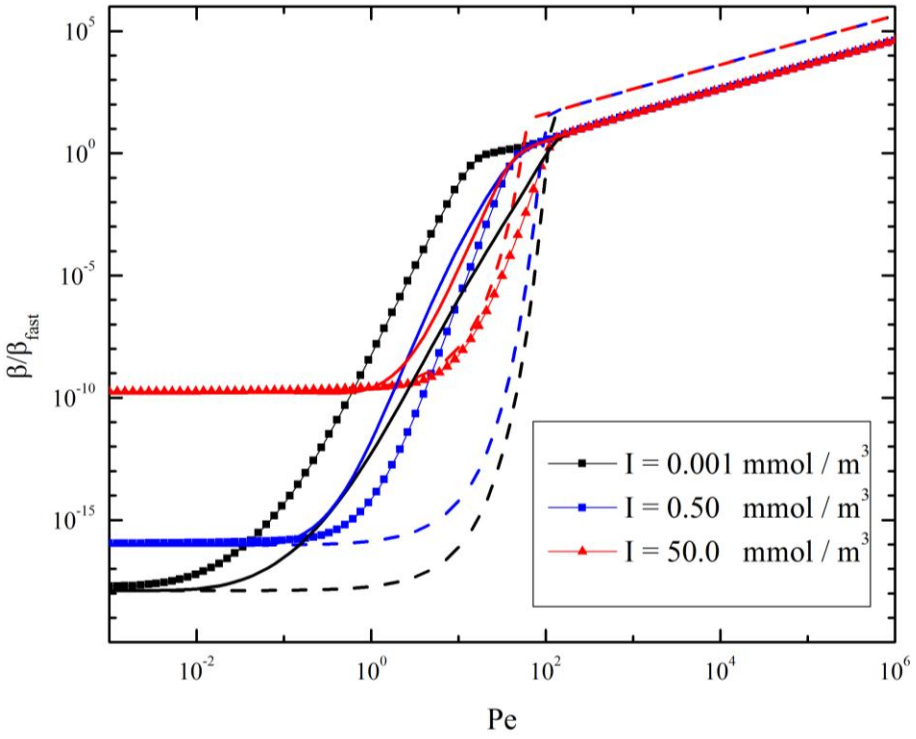

Figure 3.9. Normalized rate of aggregation between equal sized colloidal particles in the presence of an extensional flow field as a function of Pe. T = 298K, $r_1 = r_2 = 25$ nm, $\varepsilon = 6.91 \times 10^{-10}$ $s^2C^2m^{-1}kg^{-1}$, $\psi = 50$ mV, for varying ionic strength; conditions are identical to those used to generate Fig. 3a in Lattuada *et al.*[47]). The lines with symbols were generated using Equation (3.21), accounting for hydrodynamic interactions in the velocity field; the solid lines (no symbols) were generated using Equation (3.21), assuming a = 1.0; the dashed lines (no symbols) were generated using Equation (3.24) which does not account for hydrodynamic interaction effects in the computation of the velocity field.

It is apparent that the boundary layer term is critical to the Lattuada model's predictive capabilities. In the model's current state of development, computation of $\mathcal{S}$ requires the estimation of prefactor a. Determining a requires the use of a fairly involved procedure based on an empirical correlation; this procedure utilizes numerical integration and numerical

differentiation (refer to the supporting information of Lattuada and Morbidelli for details[47]). The computation time required to estimate α is not insignificant, given that it is a function of particle size and κ. To evaluate the necessity of estimating α, a third set of coagulation curves were generated. It can be seen that when $a = 1$ (thus multiple α values must be computed), the model predictions are incorrect in the transition region, but the relationship between ionic strength and the threshold Pe, beyond which the system begins transitioning to convective-dominant is qualitatively preserved.

In Figure 3.10, the Lattuada and simple shear models are compared across a larger range of particle sizes and Pe on the magnitude of the stability ratio. The rightmost graphs are plotted using a linear Pe scale in a manner similar to Figure 1 in Elgebrandt *et al.*[16] It can be seen that in the Brownian region (low Pe) that the stability ratio is inversely proportional to Pe, a trend that is not readily apparent from the double logarithmic 2-D plots. Further investigation will be necessary to determine whether the use of Equation (3.21) in the absence of a subroutine to estimate α would provide better predictive results compared to Equation (3.24). In any case, caution must be taken when employing a comparably simple coagulation kernels such as Equation (3.24) within a computational framework, as the contribution of mechanically-induced coagulation to the overall rate of coagulation is not likely to be estimated correctly.

Under the (reasonable) assumption that the rigorous solution to the convection-diffusion equation provides the most accurate prediction of coagulation conditions, examination of the local Peclet number conditions (Figure 3.7) suggests that the use of Equation (3.21) may produce erroneous predictions in the impeller region if the local ionic strength is high. In the absence of added

electrolyte, however, the rate of particle coagulation in a polymer latex that is sufficiently stabilized is predicted to be very low for the range of shear rates encountered in a stirred tank reactor (see Figure 3.10). At low Pe, it appears that logarithm of the stability ratio increases with particle diameter in a linear fashion. Comparing the predictions generated using Equation (3.21), the Lattuada kernel, with the predictions generated using Equation (3.24), it can be seen that the predictions differ in two aspects. First, as a whole, Equation (3.21) predicts a less-stable system at most conditions. The discrepancy arises from the use a boundary layer approximation and the slight difference in the two convective terms:

$$Pe\frac{\alpha}{\xi} \qquad \text{vs.} \qquad \frac{4Pe\left(r_{s.1}+r_{s,2}\right)}{3\pi\xi}$$

where $\alpha=\alpha_0 c_1\left(r_i / r_{i,ref}\right)^{-n_1}$ and α_0, c_1, n_1 are parameters that were fit adjusted to fit the simulation data, while $r_{i,ref}$ is a baseline radius, which was chosen as 50 nm in Lattuada and Morbidelli.[47] While both convective terms have similar form, the experimentally-fit expression takes hydrodynamic interactions into account, whereas the expression developed using a simplified flow field does not. It was found that if one of the convective expressions was swapped for its counterpart, both models predicted nearly identical lower limit stability ratios.

Due to the dependence of Pe on the radii of the colliding pair, it is beneficial to re-plot the data of Figure 3.10 as a function of local shear rate. This is done in Figure 3.11 and two observations can be made. Firstly, at low and moderate shear rates, if particle radius is held constant, the rate of coagulation appears to be, qualitatively, independent of the shear rate. Secondly, the models predict that, under stable conditions, mechanical agitation may only affect the rate of particle coagulation if there are regions in the tank where the shear rate approaches 10^3 s^{-1}, while the

maximum observed shear rate in the CFD simulations was on the order of 10^2 s^{-1}. Additional CFD simulations using higher resolution grids are required in order to resolve the fine structure of the trailing vortices and whether the maximum rate of shear surpasses 10^3 s^{-1}.

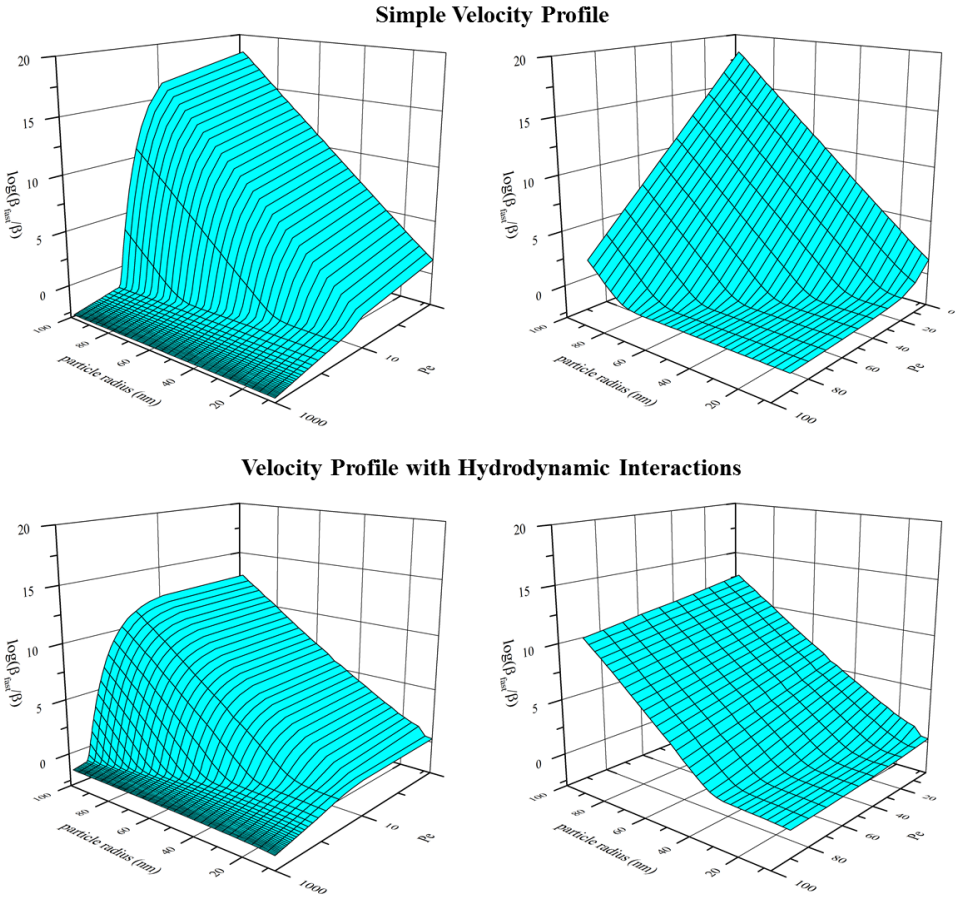

Figure 3.10. Dependency of the stability ratio on the local particle Peclet number for binary collisions between equal-sized colloidal particles, as computed using Equations (3.21) and (3.24). $\varepsilon = 6.91 \times 10^{-10}$ $s^2C^2m^{-1}kg^{-1}$, T = 298 K, $\kappa = 3.21\times10^8$ m^{-1} and $\psi = 3.35\times10^{-2}$ V.

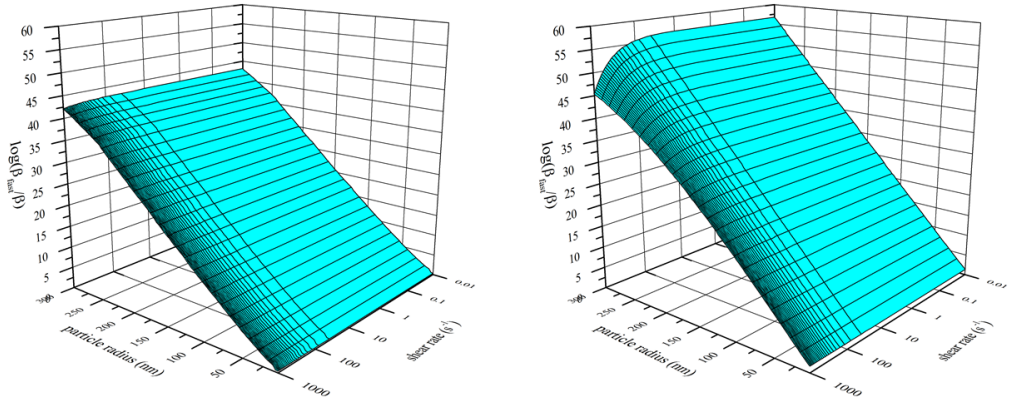

Figure 3.11. Dependency of the stability ratio on the local shear rate for binary collisions between equal-sized colloidal particles, as computed using Equations (3.21) and (3.24). $\varepsilon = 6.91 \times 10^{-10}$ $s^2C^2m^{-1}kg^{-1}$, T = 298 K, $\kappa = 3.21\times10^{8}$ m^{-1} and $\psi = 3.35\times10^{-2}$ V.

Controlled coagulation, where the polymer latex is purposefully coagulated using mechanical and/or chemical means, is employed in the production of polymeric materials for powders, coatings and cosmetics.[114] The addition of electrolyte is predicted to change coagulation behavior, as can be seen in Figure 3.12. The Lattuada model predicts that the smallest particles will coagulate rapidly $\beta \approx \beta_{fast}$, while the rate of shear in the impeller region may be high enough to enhance the rate of coagulation of larger particles. As might be expected, the coagulation kernel based on a simple velocity profile predicts, on a while, a much higher rate of particle coagulation and a greater sensitivity to mechanical agitation. Recall from Figure 3.9 that both the Lattuada model and the thorough numerical simulation data suggest that the compression of the electrostatic double layer will reduce the latex's sensitivity to mechanical agitation; this is the same effect that gives rise to the discrepancy between the model predictions in Figure 3.12. While a coagulation kernel based on the Lattuada model would be challenging to implement

effectively in a population balance model due to the additional computational requirements of the parameter fitting routines (not to mention the second integral term), improper implementation of the coagulation kernel with the simple velocity field approximation may be lead to population balance modeling predictions that are incorrect. In reactors where the maximum rate of shear is on the order of 10, the use of a DLVO-only coagulation kernel may produce more realistic results than the DLVO-based kernel that includes a simple convective component. This is due to the tendency of the simple convective model to under-predict the Pe at which the rate of coagulation will start to become influenced by the fluid dynamics inside the reactor. Replacement of Pe in Equation (3.24) with the normalized Peclet number $\left(\overline{Pe}\right)$ may help, although the aggregation rate at moderate $\overline{Pe}$ values may not be estimated properly (refer back to Figure 3.9).

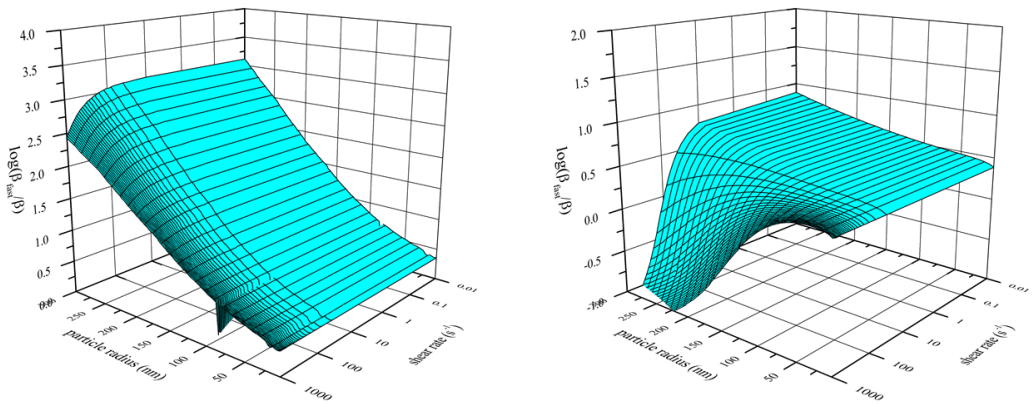

Velocity Profile with Hydrodynamic Interactions

Simple Velocity Profile

Figure 3.12. Dependency of the stability ratio on the local shear rate for binary collisions between equal-sized colloidal particles under unstable conditions, as computed using Equations (3.21) and (3.24). Simulation conditions are based on those used to generate Figure 3.10, except $\kappa = 1.52\times10^{8}$ m^{-1} and $\psi = 2.04\times10^{-2}$ V.

3.5 Conclusions

Recent advances in the modeling of particle coagulation may potentially improve the performance of existing population balance models, providing them with the functionality to correctly estimate the rate of particle coagulation over a wide range of flow conditions. CFD simulations suggested that the maximum shear rate and range of shear rates that the latex particles are exposed to will change as the reactor is scaled-up and the flow regime changes from transitional to fully-turbulent. Unexpectedly, the CFD simulations suggested that the maximum rate of shear arising from the turbulent eddies will decrease rather than increase with reactor scale. Further CFD simulation on higher resolution grids is likely necessary, in order to ensure the behavior of the trailing vortices is being modeled accurately. Regardless, the shear field may influence the rate of aggregation at all reactor scales, especially when the average latex particle diameter is large and the double layer is diffuse due to a low disperse phase ionic strength. The simple shear model, which was derived assuming a uniform velocity gradient at the microscopic scale, does not match the predictions of the more thorough coagulation model that includes adjustable parameters to account for additional hydrodynamic effects. The simple shear kernel is likely to severely over-predict the contribution of the shear field in unstable conditions, such as when a polymer latex is coagulated through the addition of an electrolyte. Therefore the use of a DLVO-only coagulation kernel is preferable to the simple shear kernel when modeling the scale-up of a controlled coagulation processes.

Chapter 4

Development of a Computational Framework to Model the Scale Up of High Solid Content Polymer Latex Coagulators

4.1 Introduction

Synthetic polymer latex products, which are colloidally stable dispersions of nano-scale polymer particles in a continuous medium, are an important class of synthetic materials. Polymer latex products are used in a wide range of applications, including the production of bulk polymer, paints, coatings, adhesives and carpet backing, with annual production exceeding 20 million tonnes.[1] Most industrial polymer latex formulations contain between 40 to 55 vol.-% solids, the remainder being dissolved species and water. There is ongoing commercial interest in developing high solid content latexes that contain as much as 75 vol.-% solids; this push toward higher solid contents is motivated by potential cost savings in production and transportation, along with improvements in the quality of the end-use product.[30] However formulation of these dispersions typically requires a well-defined particle size distribution (PSD) in order to maintain both colloidal stability and an acceptable product viscosity.[25] A number of recently-published results have shown that it is possible to produce low viscosity latexes with solid loadings above 70 vol.-% if the PSD is well-engineered;[26, 27] typically, the target PSD will be broad and bimodal, with the small particles designed to fit in the interstices created by the large particle lattice.

Commercial interest in driving up the solid content of existing recipes provides sufficient motivation to adapt many of the novel production techniques outlined in the academic literature

to larger scale production. Careful attention must be paid to any changes in process-critical time and length scales that may arise from changes in process scale. A survey of the academic literature reveals that high solid content polymer latexes are typically produced by growing a primary population of seed particles while simultaneously creating a secondary population of smaller particles via homogeneous nucleation.[30] Control over the PSD is achieved by adjusting the feed rates and ratios of monomer, initiator and surfactant species. Particular attention needs to be paid to the dispersion of ionic species as local variations in the ionic strength can have a major impact on particle coagulation, and therefore the PSD and viscosity. At the laboratory scale the impeller rotational speed can be increased to ensure that feed dispersion is instantaneous relative to the rate of polymerization; such adjustments are physically and/or economically unfeasible at the commercial scale. Concentrated polymer latexes will exhibit non-Newtonian flow characteristics; in the laminar flow regime, this leads to segregation outside the impeller zone and characteristic mixing times on the order of minutes.[14] It is therefore of interest to understand the relationship between the coagulation, reaction and mixing rates as the process is scaled-up.

There are a number of general texts available that provide general guidelines for process scale-up, including Tatterson,[115] Oldshue[10] and Kresta.[116] The most popular scale-up approach is to assume that geometric similarity can be maintained and that the mixing objectives can be met by maintaining a constant power input per unit volume (a constant P/V ratio). In polymerization processes, heat removal is often the limiting factor for reactor performance, necessitating an increase in the tank height to tank diameter ratio. Neglecting the issue of heat transfer, the classical heuristics are only a starting point and they provide no information regarding flow

patterns, mixing mechanisms and the degree of homogeneity inside the reaction vessel. Advanced experimental methods such as Laser Doppler Velocimetry (LDV) and Particle Image Velocimetry (PIV)[117] can provide further insight, however these methods are unsuitable for studying flow in industrial-scale vessels, where the vessels are made of non-transparent materials and the process liquids are opaque.[74]

The availability of affordable high-performance computing hardware and experimentally-validated process simulation software has led to the demand for process-specific models to assist in the scale-up process. Due to myriad assumptions that are made during model development to ensure reasonable calculation time(s), computational modeling does not eliminate the need for pilot plant experimentation. Good predictive tools can, however reduce development lead times and costs. In the production and processing of polymer latexes, the computational framework must be designed with the goal of predicting changes in product quality that arise from changes in production scale; in high solid content latexes, product quality is dependent on maintaining a well-defined PSD. Over the past decade, significant progress has been made in the development of mathematical models for predicting the evolution of PSD under different operating conditions. The complex PSDs required to produce high solid content (HSC) latexes necessitate the use of population balances for PSD prediction.[8]

Over the past two decades, computational fluid dynamics (CFD) has become a powerful tool in the process industry, as CFD simulations are capable of imparting detailed insight regarding the flow patterns, mixing mechanisms and degree of homogeneity within a reactor vessel. CFD simulation has provided unique insight into a number of polymerization processes including bulk polymerization[118] and suspension polymerization.[119] It is theoretically possible to incorporate the

population balances directly into the CFD code by defining additional conservation equations.[78] In practice, directly integrating the population balances into the CFD simulation is impractical as the resulting system of equations would be far too large to solve and process with current computing equipment.

Given limited computational resources, the simplest way to couple the CFD simulation and population balance models is to use them in a sequential manner. The hydrodynamics obtained from CFD are used to identify a number of interacting spatial regions or zones, with each zone being approximated as well-mixed; additionally the CFD is used to determine the rate of flow exchanged between adjacent zones. The population balance models are then solved on this coarser grid of interconnected zones. In many cases, it is expected that the hydrodynamics will evolve significantly during the process, as the PSD changes (rheology is highly dependent on PSD); this necessitates two-way coupling between CFD simulation and population balance models. In a series of papers, Bezzo *et al*.[78, 80, 81, 120] developed a generalized hybrid multizonal/CFD modeling methodology to standardize the approach across a wide variety of applications such as crystallization and bioreactor modeling.

The two compartment model framework developed by Alexopoulos *et al.* for liquid-liquid dispersion in suspension polymerization[83] and later emulsion polymerization[15] represents one of the first attempts to utilize the information provided by CFD to improve the predictive capabilities of a polymerization process model, although the models are only coupled sequentially. Elgebrandt *et al.*[17] were the first group to adapt the general hybrid multizonal/CFD framework to emulsion polymerization. Although they suggested that their framework could be adapted to study the production of concentrated latexes, they limited the scope of their study to

operation in the turbulent regime and lower solid content latexes (a solid volume fraction of ~ 25%) where latex rheology is Newtonian. The combined model relied on a 2D CFD mesh and an essentially-qualitative coagulation kernel, leaving plenty of room for improvement. There has been little follow-up since this work was published.

This chapter focuses on evaluating the feasibility of a hybrid multizonal/CFD model framework to capture the dynamics of the final production stages of high solid content latexes, specifically operation under conditions where fluid rheology is non-Newtonian and the reactor is operating in the laminar or lower transition flow regimes. The hybrid model is employed to investigate the impact of process scale-up on mixing performance in the controlled coagulation of concentrated polymer latexes in the absence of chemical reaction in this initial step. Controlled coagulation is employed in the production of polymeric materials for powders, coatings and cosmetics, but is discussed very sparingly in the literature.[114] The process model for controlled coagulation is essentially a limited version of the process model for emulsion polymerization, ideal for preliminary assessment of the framework's capabilities in this set of applications.

4.2 Overview of Framework Components

4.2.1 Mixing System

The mixing system consisted of a centered four-bladed 45° pitched blade turbine and two round baffles. In order to investigate the impact of reactor scale-up, CFD simulations were run across three (geometrically similar) reactor scales: 1 L, 10 L and 10 L, corresponding to tank diameters (T) of 9.69×10^{-2} m, 2.09×10^{-1} m and 4.50×10^{-1}, respectively. As in Chapter 3, the liquid

level (H) was 1.4 times the tank diameter (T) and the impeller diameter was set to $(T/3)$. The remaining tank dimensions can be found on Figure 3.1 (Section 3.3) in Chapter 3. Although baffles are not necessary for laminar mixing of viscous liquids, they are likely to be present in a polymer latex reactor as they serve to eliminate vortex formation[87] at early stages in the polymerization when latex viscosity is low and flow is turbulent.

4.2.2 The Population Balance

Due to the fact that this paper is meant only as an overview and demonstration of the hybrid multizonal/CFD framework, the current investigation is restricted to modeling controlled coagulation. This eliminates the particle nucleation and particle growth via polymerization terms from the population balance equation (PBE), but is still reflective of common polymerization processes such as those outlined in Fortuny[100] and Konstansek.[114] The multizonal model is comprised of a series of interconnected, well-mixed zones, thus eliminating the need to define an external coordinate domain. The particle population is described using with the number density function, $f(v,t)$, such that $f(v,t)dv$ is the number of particles (per unit volume) with a volume between v and $v+dv$. The total number concentration of particles in the system can be calculated by integrating the number density function over the entire size range of particles found in the latex

$$N_P = \int_{v_{\min}}^{\infty} f(v,t)dV \tag{4.1}$$

In the case where coagulation is the only mechanism of particle creation and destruction, the total mass of particles in the system will remain constant. Under the assumption that all coagulation

events are binary in nature, the population balance for a homogeneous zone, *z*, that exchanges flow with neighboring zones will take on the following form:

$$\frac{df_z(v,t)}{dt} = \int_0^v \beta_z(v', v-v')\, f_z(v',t)\, f_z(v-v',t)dv - f_z(v,t)\int_0^\infty \beta_z(v,v'')\, f_z(v'',t)dv + \sum_{y, y\neq z} \left[f_y(v,t) - f_z(v,t) \right] q_{z,y} \tag{4.2}$$

where $q_{z,y} = 0$ when zones *z* and *y* are not connected. Interpreting the coagulation terms is straightforward: a particle of size v is created when two particles with a total volume of v undergo aggregation. A particle of size v is consumed when it undergoes aggregation with any other particle in the system. The coagulation rate coefficient, $\beta_z(v', v-v')$, represents the collisions between particles of size v' and $v-v'$; further detail is provided in the coagulation kernel section. The assumption that all aggregation events are binary is made because of the impracticality associated with modeling multi-body collisions and validating the results.[8] In order to solve Equation (4.2), initial conditions, in the form of an initial particle size distribution, must be specified.

The continuous PBE is discretized using the fixed pivot technique, an internally-consistent framework first proposed by Kumar and Ramkrishna.[121] The particle size domain is partitioned into a series of contiguous and discrete size intervals and the particle populations are concentrated at a series of pivot values. The number density of particles whose values fall between v and $v+dv$ is then defined as follows:

$$N_i(t) = \int_{v_i}^{v_{i+1}} f(v,t)dv \tag{4.3}$$

All particles are lumped together at single pivot size of $\overline{v}_i$, which represents all of the particles with a size between v_i and v_{i+1}. Generally, the pivot points are bin averages, such that $\overline{v}_i = (v_i + v_{i+1})/2$. Following the fixed pivot framework, the discretized PBE for the concentration of particles of size *i* in zone z, $N_{i,z}$, can be written as follows:

$$\begin{aligned}\frac{dN_{i,z}(t)}{dt} = & \sum_{\substack{j,k \\ (\overline{v}_{i-1}<(\overline{v}_j+\overline{v}_k)\le\overline{v}_i)}}^{i-1-j} (1-\frac{1}{2}\delta_{j,k}) b(\hat{v},\overline{v}_i)\beta_{jk,z}N_{j,z}(t)N_{k,z}(t) \\ & + \sum_{\substack{j,k \\ (\overline{v}_i<(\overline{v}_j+\overline{v}_k)\le\overline{v}_{i+1})}}^{i-1-j} (1-\frac{1}{2}\delta_{j,k}) a(\hat{v},\overline{v}_i)\beta_{jk,z}N_{j,z}(t)N_{k,z}(t) \\ & - N_{i,z}(t)\sum_{j=1}^{M}\beta_{ij,z}N_{j,z}(t) + \sum_{y,y\neq z}\left[N_{i,z}(v,t) - N_{i,z}(v,t)\right]q_{z,y}\end{aligned} \tag{4.4}$$

where

$$a(\hat{v},\overline{v}_i) = \frac{\overline{v}_{i+1}-\hat{v}}{\overline{v}_{i+1}-\overline{v}_i} \tag{4.5}$$

$$b(\hat{v},\overline{v}_i) = \frac{\hat{v}-\overline{v}_{i-1}}{\overline{v}_i-\overline{v}_{i-1}} \tag{4.6}$$

When particles of volumes $\overline{v}_j$ and $\overline{v}_k$ aggregate together, their combined volume, $\hat{v} = \overline{v}_i + \overline{v}_j$ will fall between the average particle volumes characterizing the two contiguous classes N_i and N_{i+1}, such that $\overline{v}_i \le \hat{v} \le \overline{v}_{i+1}$. The fraction of the newly-created particles assigned to class N_i is $a(\hat{v},\overline{v}_i)$, while the fraction assigned to class N_{i+1} is $b(\hat{v},\overline{v}_i)$. Further details regarding the development of Equations (4.5) and (4.6) can be found in Section 5.3.1.5 of Chapter 5 and in the well-written conceptualization provided by Butté *et al.*[122] A uniform particle concentration is specified to satisfy the requirement of an initial condition.

4.2.3 Coagulation Kernel

The coagulation kernel used in this work is essentially the same electrostatic stabilization model presented in Coen *et al.*,[99] although there were a number of modifications made. As mentioned in Chapter 3, orthokinetic coagulation can be neglected for two reasons. First, Kolmogorov scale turbulent eddies are thought to be the main source of shear acting on the particles at the microscopic scale,[44] but the simulations in this chapter are run in laminar regime. Second, under the destabilizing conditions simulated in this chapter (i.e. high ionic strength), the threshold shear rate beyond which orthokinetic coagulation becomes important is very high.

The coagulation rate coefficient between two particles of size *i* and *j*, β_{ij} is computed from the Fuchs-modified[90] Müller-Smoluchowski[94] equation:

$$\beta_{ij} = \frac{2k_B T}{3\eta_s W_{ij}}\left(2 + \frac{r_i}{r_j} + \frac{r_j}{r_i}\right) \tag{4.7}$$

Fuchs' stability ratio (W_{ij}), which is the inverse of the collision efficiency, accounts for the presence of colloidal interactions between the particles. Neglecting hydrodynamic interaction effects, the normalized stability ratio is computed with the following expression:[123]

$$W_{ij} = \frac{\int_0^\infty \frac{\exp\left(\frac{V_{\text{int}}(s)}{k_B T}\right)}{s^2} ds}{\int_0^\infty \frac{\exp\left(\frac{V_A(s)}{k_B T}\right)}{s^2} ds} \tag{4.8}$$

where *s* is defined by the following expression:

$$s = \frac{L}{r_i + r_j} \tag{4.9}$$

The distance between the two particles' surfaces (L), is a function of the particles' radii and the center-to-center distance between the particles (R)

$$L = R - (r_i + r_j) \tag{4.10}$$

Use of the normalized stability ratio ensures that the computed rate of coagulation cannot exceed the rate of coagulation computed in the absence of colloidal interactions, which is desirable when comparing simulation predictions to experimental results. The overall potential energy of interaction is assumed to be a sum of attractive (V_A) and repulsive (V_R) components (for more details on calculating the interaction potential, refer to Ottewill).[53]

$$V_{\text{int}} = V_A + V_R \tag{4.11}$$

Neglecting retardation and screening effects, the van der Walls attractive potential energy is computed using the Hamaker-De Boer equation for unlike spheres:[8]

$$V_A = \frac{-A}{6}\left[\frac{2r_i r_j}{R^2 - (r_i + r_j)^2} + \frac{2r_i r_j}{R^2 - (r_i - r_j)^2} + \ln\left(\frac{R^2 - (r_i + r_j)^2}{R^2 - (r_i - r_j)^2}\right)\right] \tag{4.12}$$

The repulsive potential is calculated using the Hogg-Healy-Fürstenau expression[101]

$$V_R = \frac{\varepsilon r_i r_j (\zeta_i^2 + \zeta_j^2)}{4(r_i + r_j)}\left[\frac{2(\zeta_i \zeta_j)}{\zeta_i^2 + \zeta_j^2}\ln\left(\frac{1 + e^{-\kappa L}}{1 - e^{-\kappa L}}\right) + \ln(1 - e^{-2\kappa L})\right] \tag{4.13}$$

In concentrated systems, the surrounding particles can cause an effective reduction in V_{int}, leading to a lower stability ratio. The expression used to compute the inverse Debye length is modified to account for concentration effects[124]

$$\kappa = \sqrt{\left(\frac{4\pi e^2}{\varepsilon k_B T}\right)\left(\frac{2N_A I + \frac{A_{tot}\sigma}{e}}{1-\phi}\right)} \tag{4.14}$$

The expression $A_{tot}\sigma / e$ accounts for the counterions carried by neighboring particles, while the denominator of $1-\phi$ accounts for the reduced solution volume available to ions. The ionic strength of the solution (*I*) is defined as

$$I = [S] + [E] \tag{4.15}$$

while the permittivity of water (ε) is defined in CGS units by multiplying the relative permittivity (ε_r) by the permittivity of free space (ε_0):

$$\varepsilon = 4\pi\varepsilon_0\varepsilon_r \tag{4.16}$$

For a discrete population of particles, the total surface area of the latex particles is computed as follows:

$$A_{tot} = \sum_{i=1}^{m} 4\pi n(r_i) r_i^2 \tag{4.17}$$

In the absence of initiator, the surface charge on each particle is dictated by the adsorption of surfactant onto the particle surface

$$\sigma = \frac{z_+ e}{A_s} \tag{4.18}$$

where the counter-ion valence (z_+) is equal to one for an initiator such as potassium persulphate. The area occupied by a surfactant molecule (A_s) is dependent on the partitioning of added surfactant between the aqueous phase and the surface of the latex particles which follows the Langmuir adsorption isotherm:[99]

$$A_s = a_s\left(1+\frac{1}{[S]_w b_s}\right) \tag{4.19}$$

The concentration of surfactant in the aqueous phase $\left([S]_w\right)$ is dependent on the concentration of surfactant added in the continuous phase $\left([S]\right)$ and the total amount of surfactant adsorbed onto the particles' surfaces

$$[S]_w = [S] - \frac{A_{tot}}{N_A A_s} \tag{4.20}$$

Combining Equations (4.19) and (4.20) and solving for the positive root yields the relationship used to compute $\left([S]_w\right)$.

$$[S]_w = \left([S] - \frac{A_{tot}}{a_s N_A} - \frac{1}{b_s}\right) + \frac{\sqrt{\left(\frac{A_{tot}}{a_s N_A} + \frac{1}{b_s} - [S]\right)^2 + \frac{4[S]}{b_s}}}{2} \tag{4.21}$$

Finally, the surface potential and zeta potential are calculated following the approach used by Coen *et al.*[99] The surface potential is calculated from the surface charge density using one of the two following relationships (valid for $\psi < 25$ mV) :

$$\psi = \frac{4\pi r_s \sigma}{\varepsilon(1+\kappa r_s)} \qquad \text{for} \quad \kappa r < 1 \tag{4.22}$$

$$\psi = \frac{2k_B T}{e}\sinh^{-1}\frac{2\pi e\sigma}{\varepsilon\kappa k_B T} \qquad \text{for} \quad \kappa r > 1 \tag{4.23}$$

If $\kappa r < 1$, the curvature of the particle surface must be taken into account, as shown in Equation (4.22); however, if $\kappa r > 1$, the surface can be approximated as a flat plate and Equation (4.23) is used instead. The zeta potential is computed with the following expressions:

$$\zeta = \frac{2k_B T}{z_+ e} \ln\left(\frac{\exp(\lambda_4)+1}{\exp(\lambda_4)-1}\right) \tag{4.24}$$

$$\lambda_4 = \kappa\delta + \ln\left(\frac{\exp(\lambda_5)+1}{\exp(\lambda_5)-1}\right) \tag{4.25}$$

$$\lambda_5 = \frac{z_+ e\psi}{2k_B T} \tag{4.26}$$

It must be noted that Equations (4.22) and (4.23) are derived assuming a Boltzmann distribution of electrostatic potential at the particle surface; this is not the case since the ions do not move freely at the surface.

4.2.4 CFD Model

Due to the presence of baffles within the tank, the flow field within the tank may be unsteady in nature, requiring a non-steady-state simulation when operating in turbulent conditions. This is not necessarily the case in the laminar and lower transition regime, so a preliminary set of CFD simulations were run to evaluate the degree of unsteadiness in the flow field. The non-stationary flow field, generated using the fictitious domain method to handle impeller rotation, was compared to the stationary flow field generated using a rotational boundary condition on the impeller surface. It was found that the shape of the non-stationary flow field remained qualitatively constant regardless of impeller position and the variation in the computed power consumption during a period of rotation was less 10%. Given that the framework architecture requires that the flow field be re-computed each time the properties of the liquid change significantly, a decision was made to switch to a steady-state CFD model in order to reduce total computation times from the scale of days to hours

The flow field was predicted by solving the momentum and continuity equations with a standard 3D Galerkin finite element method. Fluid density and temperature are assumed to be constant. In the absence of polymerization, the assumption of isothermal operation is reasonable.

$$\rho\left(\frac{\partial \boldsymbol{v}}{\partial t}+\boldsymbol{v}\cdot\nabla\boldsymbol{v}\right)=-\nabla p+\nabla\cdot\left(2\eta\left(|\dot{\gamma}|\right)\dot{\gamma}\right) \tag{4.27}$$

$$\nabla\cdot\boldsymbol{v}=0 \tag{4.28}$$

The boundary conditions were as follows:

- Constant angular velocity along the impeller surface (N_I = const)
- No slip condition at the baffles and along the vessel wall ($\boldsymbol{v}$ = 0)
- No normal velocity at the fluid surface which is assumed to be flat (v_z = 0)

The 3D unstructured CFD mesh was generated with GAMBIT (Ansys), commercial CFD pre-processing software. The mesh was refined near the impeller region and at the baffle walls in order to provide sufficient resolution in regions with large velocity gradients (this was verified by refining the mesh until the computed power consumption converged). The details of the mesh are shown in Figure 4.1, using a vertical slice to cut through the center of the vessel. MINI finite elements were used to approximate the velocity and pressure fields, as this element type has been shown to be accurate and very computationally efficient relative to other element types.[125] The resulting computational mesh consisted of approximately 240,000 elements and 285,000 nodes, resulting in a system of 150,000 equations. The non-linearity imposed by the non-Newtonian rheological model was handled using an augmented Lagrangian approach in which the rheological non-linearity is removed from the momentum equation and handled separately with an auxiliary equation, yielding a Lagrange multiplier. A fully-coupled approach was used in

which the momentum equations and Lagrange multiplier were solved simultaneously by penalization. The Bi-CGSTAB method was used to handle the resulting large asymmetric matrices. For additional details regarding the numerical methods employed, refer to Coesnon *et al.*[125]

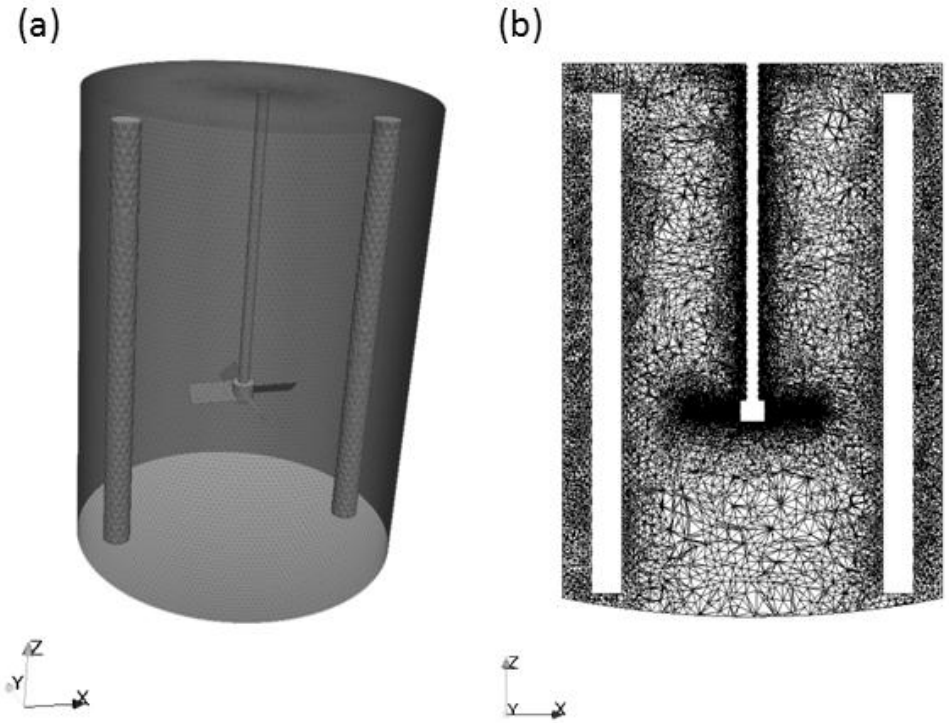

Figure 4.1. Computational domain: (a) three-dimensional structure of the vessel including main features, (b) vertical slice through the z-axis showing details of unstructured mesh.

4.2.5 Latex Rheology

Above approximately 40 vol.-% solids, polymer latexes exhibit non-Newtonian behavior. In the absence of shear thickening, latex viscosity, when plotted as a function of shear rate, can demonstrate two plateaus. At low shear rates, latex viscosity is independent of shear rate and is

said to obey Newtonian behavior. This lower plateau is referred to as the lower Newtonian viscosity. At a certain shear rate (characteristic of the latex), the shear stress transmitted through the aqueous medium will begin orienting the particles in the direction of flow. These layered particles offer less resistance to flow, hence a lowering of the viscosity. Once the particles are completely layered, viscosity can no longer decrease with increasing shear rate and this upper plateau is referred to as the upper Newtonian viscosity. If shear rate is increased further, the mean flow may impart enough energy to the particles so that they overcome the forces of repulsion and begin clustering together. This clustering (not to be confused with coagulation) will disrupt the layered flow which results in a large increase in latex viscosity. This clustering phenomenon, known as shear thickening, may also result in coagulation which will exacerbate the increase in viscosity. The phenomenon of shear thickening is not accounted for in this study, but care should be taken to ensure that the maximum shear rate in the vessel does not approach the thickening limit which is deleterious to the health of mixing equipment.[54] The non-Newtonian rheology was modeled with the Carreau-Yasuda model, which has been shown to correctly capture the shearing behavior of concentrated latexes.[5] The equations employed are the same as those employed in Chapter 3. For further details, refer to Equations (3.27) to (3.29) and Table 3.1 in Section 3.3.

The maximum packing fraction of a polymer latex made up of *m* discrete particle sizes can be calculated using a model proposed by Pishvaei *et al.*[65] The advantage of this model is that it eliminates the need for experimental data beyond the determination of the effective maximum packing fractions $\left(\phi_{m,i}\right)$ and the PSD. For a system with *m* discretized particles sizes:

$$\phi_{m,\xi}(t) = \frac{\sum_{i=1}^{M} D_i^3 x_i(t)}{\sum_{i=1}^{M}\left(D_i \sim \bar{D}\right)^3 x_i(t) + \frac{1}{\bar{s}(t)}\sum_{i=1}^{M}\left[\left(D_i + \bar{D}\right)^3 - \left(D_i \sim \bar{D}\right)^3\right] x_i(t)} \tag{4.29}$$

$$\bar{s}(t) = 1 + \frac{4}{13}\bar{D}\frac{\sum_{i=1}^{M}\left(8\phi_{m,i} - 1\right)\left(D_i + \bar{D}\right)^2\left(1 - \frac{3}{8}\frac{\bar{D}}{D_i + \bar{D}}\right) x_i(t)}{\sum_{i=1}^{M}\left[D_i^3 - \left(D_i \sim \bar{D}\right)^3\right] x_i(t)} \tag{4.30}$$

where

$$\left(D_i \sim \bar{D}\right) = \begin{cases} 0 & \textbf{for} \quad D_i \le \bar{D} \\ D_i - \bar{D} & \textbf{for} \quad D_i > \bar{D} \end{cases} \tag{4.31}$$

and $x_i(t)$ is the number fraction of the i^{th} component

$$x_i(t) = \frac{\phi_i / D_i^3}{\sum_{i=1}^{m} \phi_i / D_i^3} \tag{4.32}$$

The number average diameter $\bar{D}$ is the weighted sum of the individual particle sizes that compose the discrete mixture:

$$\bar{D} = \sum_{i=1}^{m} D_i x_i(t) \tag{4.33}$$

The effective maximum packing fraction of a particle with radius r_i is computed by

$$\phi_{m,i} = \phi_{m,hs}\left(1 + \frac{1}{\kappa r_i}\right)^3 \tag{4.34}$$

where $\phi_{hs,m} = 0.64$ in the absence of applied shear [28] and $\phi_{hs,m} = 0.71$ at high shear limits.[5, 29]

From Equation (4.34) it can be seen that the effective maximum packing fraction scales with

particle size, approaching the hard sphere value at the limit. For further details, refer to Section 2.2.4 in Chapter 2.

Pishvaei demonstrated that Equations (4.29) through (4.33) provide reasonable estimates of the loading limits for bimodal systems based on estimates of these properties from related monodisperse latexes.[65] In this work, the model is extended to work with multimodal PSDs in which the distributions are broader. The continuous PSDs encountered in experimental work can be approximated in the discretized form if the population balance mesh is sufficiently refined (m ~ 100).

4.3 Framework Overview

The computational framework comprised three components: the multizonal population balance model, the CFD model and the interface that handles the transmission of data between the models. The computational fluid simulations were performed on fine mesh, while the population balance model was solved on a much coarser grid. The manner in which the three components work together is schematically depicted in Figure 4.2.

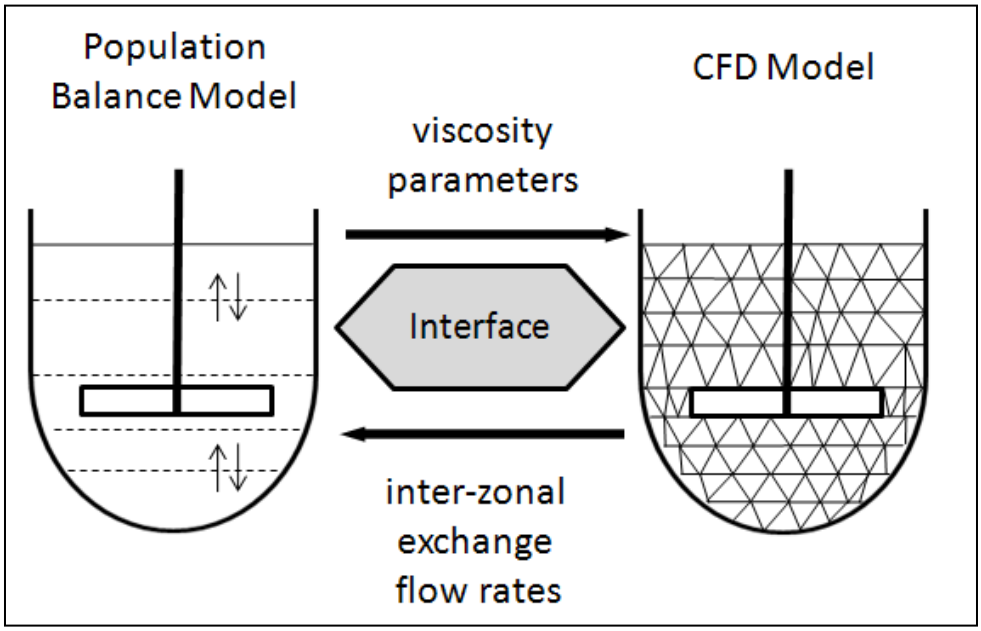

Figure 4.2. Schematic diagram of the framework, outlining the direction(s) of communication between the different framework components.

It has been assumed for the purpose of this work that the main cause of non-homogeneity in the tank is poor flow in the vertical direction. For this reason, a simple network-of-zones is generated by dividing the vessel into sections along its vertical axis, such that the net flow rate between any two zones is zero. The rate of material exchange between zones is quantified by calculating a rate of flow exchange at each zone interface. The number of zones was an adjustable parameter, but the size of the zones was automatically determined using a preliminary flow field generated by the CFD model (see Figure 4.3). The rate of flow exchanged in the axial direction is computed as a function of axial location by projecting the normal components of the velocity data onto a series of planes (a minimum of fifty planes was used). This axial flow distribution and its maximum value are used to compute the spacing of cutoff boundary values. Since the vessel is divided into

an equal number of zones above and below the well-mixed impeller region, the number of cutoff boundary values required can be computed as follows:

$$n_{cutoff} = \frac{n_{zones}}{2} - 1 \tag{4.35}$$

The zone boundaries were set using the normalized distribution of axial flow. At all reactor scales simulated, it was found that the absolute maximum rate of axial flow exchange, $\left(\log_{10}\left[F_L / F_{L,\max}\right] = 0.0\right)$, is located slightly above the impeller, but there is a second local maximum at $\left(\log_{10}\left[F_L / F_{L,\max}\right] = -0.15\right)$ located slightly below the center of the impeller, which is marked by a local maximum $\left(\log_{10}\left[F_L / F_{L,\max}\right] = -0.75\right)$. It was found that the numerical solution was unstable (i.e. the solution did not converge as the number of zones was increased) if the center zone did not enclose both maxima. Enclosure was ensured by locating the center zone boundaries where $\left(\log_{10}\left[F_L / F_{L,\max}\right] = -0.75\right)$ drops just below this local minimum, as illustrated in Figure 4.3 . Note that the normalized value of the local minimum was found to be independent of the reactor scale. The outermost zones corresponded to regions where mixing was poor and the normalized rate of axial flow exchange was low. From preliminary simulation data it was determined that the solution did not change as long as the outer boundaries were located at $\left(\log_{10}\left[F_L / F_{L,\max}\right] = -2.0\right)$. Since the location of the outer and inner zone boundaries are specified, a minimum of five zones was specified. If more than five zones are desired, additional cutoff values are generated at equally spaced intervals between the two extrema (-0.75 and -2.0). For example, for seven zones, the three cutoff values used to locate and

and generate the size zone boundaries are -0.75, -1.17, and -1.59; the zone partitioning generated from this approach is illustrated in Figure 4.3 b.

The simulation proceeds in the following steps:

Step 1: At the start of the simulation, the contents of the vessel are assumed to be uniform. The initial flow field is calculated using viscosity model parameters that are calculated from the initial PSD.

Step 2: The initial flow field is used to compute the axial location of the zoning partitions and the rate of exchange flow between zones.

Step 3: The multizonal coagulation model is initialized.

Step 4: The coagulation model proceeds until a large enough change in any of the viscosity model parameters in any of the zones is detected (thus signifying a strong possibility that the flow field has changed). The viscosity parameters used in the CFD model are re-computed using Equations (3.27) to (3.29) and (4.29) to (4.34).

Step 5: The flow field is updated via CFD simulation utilizing the updated viscosity parameters.

Step 6: Steps 4 and 5 are repeated until the specified simulation end-time is reached.

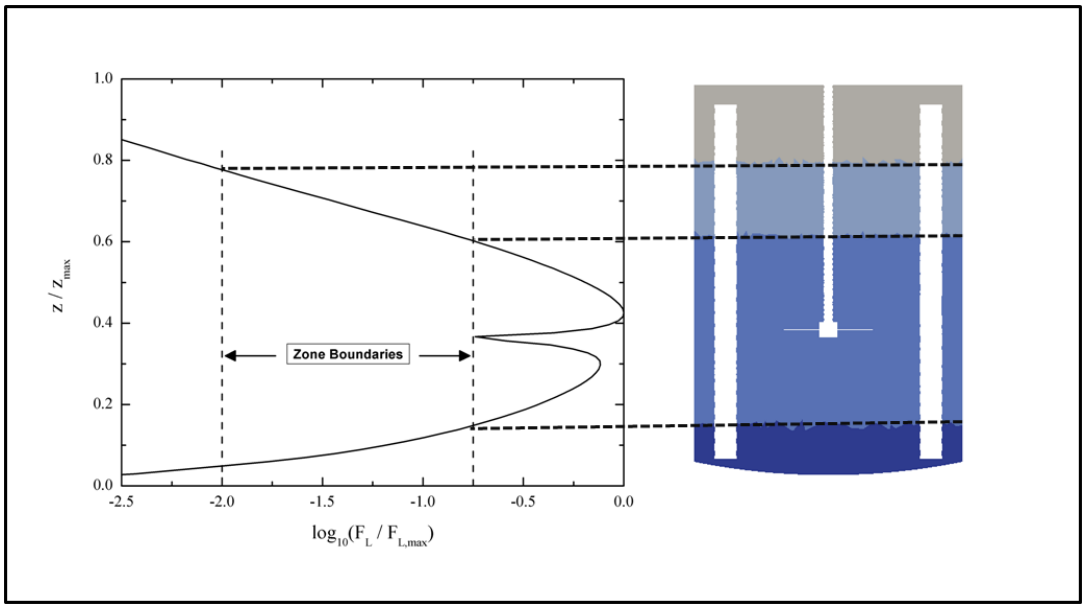

Figure 4.3. (a) Rate of flow exchanged in the vertical direction along the height of a 1 L vessel, as determined from a preliminary CFD flow field. The rate of exchange was rendered dimensionless using the maximum rate of flow exchange which is located in the vicinity of the impeller. (b) The tank was divided into five zones, using four horizontal cut-off boundaries (two above the region of maximum flow exchange and two below). This zoning procedure required two cut-off values of the dimensionless rate of flow exchange ($\log[F_L/F_{L,max}]$ = -0.75, -2.0). Note that the bottom-most zone was very thin compared to the other four zones and hence it is not shown in this diagram.

4.4 Simulation Conditions

To test the framework, a series of simulations were performed in which a concentrated polystyrene latex (d_p = 150 nm, PI = 1.10, ϕ = 0.59) is coagulated via the continuous addition of a salt (sodium chloride) within the well-mixed impeller region for a period of 215 seconds at a temperature of 298 K. The anionic surfactant (sodium persulphate; $a_s = 4.2\times10^{-19}$) concentration was set to 9 mol/m^3, while the final salt concentration at t = 215 s was 140 mol/m^3. The surfactant concentration and salt feed rate were specified such that the amount of coagulation was insignificant in a perfectly-mixed vessel, but very noticeable under inhomogeneous mixing

when local salt concentration would approach and exceed critical coagulation concentration and collision efficiency approaches 100 % (i.e. $\beta = \beta_{fast}$ and the rate of coagulation is governed by Brownian motion).

All CFD simulations were run using POLY3D (*Rheosoft Inc*.), a commercial 3D finite element code using the numerical techniques described earlier in the paper. Post-Processing was carried out using customized FORTRAN routines and Paraview (*Kitware*). Based on the objective of maintaining a constant volumetric power input, the impeller rotational speed must be lowered when the vessel is scaled-up, based on the following relationships:[87]

$$\frac{P}{V} \propto N_I^3 D_I^2 \tag{4.36}$$

$$N_{I,2} = N_{I,1}\left(\frac{D_{I,1}}{D_{I,2}}\right)^{\frac{2}{3}} \tag{4.37}$$

Based on this scale-up approach, when reactor volume is increased by a factor of ten, the impeller rotational rate should be multiplied by a factor of approximately 0.60.

The population balance model was coded in FORTRAN. The solution for the resulting system of ODEs was computed with DLSODE, a general-purpose, open source, multi-step explicit numerical scheme. DLSODE uses a multi-step backward differentiation formula (BDF) when presented with stiff problems.[126] The integral term contained within the coagulation kernel was evaluated using a simple composite midpoint method. Coagulation rate coefficients were re-calculated only when there was a change in any of the parameters that governed the rate of particle coagulation. The number of pivot points was varied between 20 and 200; it was found

that mesh size of 100 pivot points (per zone) provided a grid-independent solution. All of the simulation results presented in this work were run on an Intel Core 2 Quad Q6600 (2.4 GHz) desktop computer. In order to determine the number of subdivisions required to obtain a solution that is independent of the number of zones specified, a series of simulations were run in which the number of zones was varied from five to eleven in odd increments. Examining the end-time PSDs under various conditions, it was determined that dividing the reactor into nine zones was sufficient to ensure the solution was not grid dependent under the current zoning scheme. For a nine-zone system complete simulation times ranged from approximately 45 minutes to 90 minutes depending on the operational regime in the CFD simulations (laminar or transition), and the frequency with which the flow field required updating. The frequency at which the flow field was updated was adjusted by setting the tolerance of relative change in the PSD-dependent viscosity parameters to ensure the final PSDs were independent of the update frequency.

4.5 Results & Discussion

One of the key changes made to the coagulation kernel when it was adapted from the works of Coen *et al.*[99] and Fortuny *et al* [100] was the modification of the expression used to calculate the inverse Debye length to incorporate a particle concentration effect. Equation (4.14) indicates that, for constant surface coverage conditions, an increase in solids content will lead to a reduction in the thickness of the Debye length. Therefore the thickness of the double layer surrounding the particles is reduced as the solids volume fraction is increased, which allows the particles to pack closer together before repulsive forces become too great. The modified expression has two effects; in addition to the obvious reduction in latex stability with increasing solid content, the rheological behavior of the latex is affected as well. The reduction in the thickness of the double

layer reduces the effective diameter of the latex particle (i.e. the diameter of the polymer particle plus a layer of interaction). Although Equation (4.34) should not be mistaken for a rigorous model, the expression quantifies an important observation in electrostatically-stabilized systems: for constant surface coverage conditions, large particles can be packed closer together than smaller particles. Experimentally it has been observed that for a constant volume fraction of polymer, latexes comprised of small particles will be more viscous than latexes comprised of large particles.[65] However Equation (4.34) qualitatively underestimates the size-dependent effective maximum polymer packing fractions, especially for small particles where κ and $d_{p,i}$ are of a similar order of magnitude. This is illustrated in Figure 4.4.

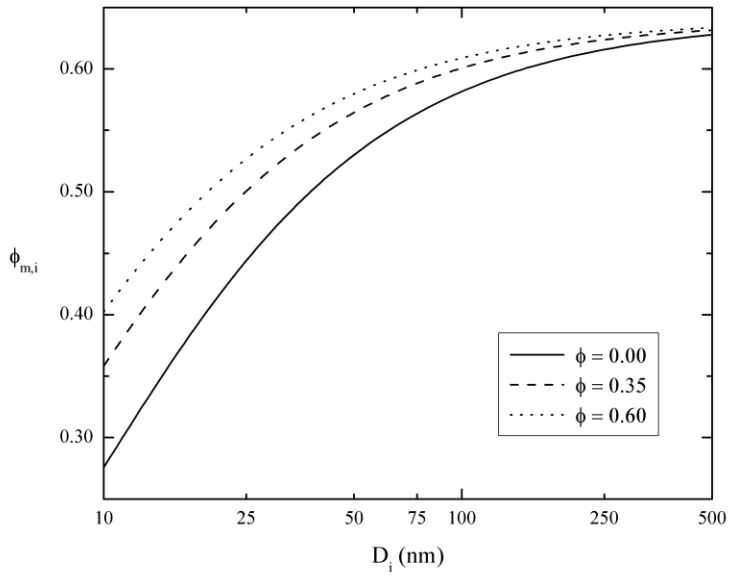

Figure 4.4. Effective maximum packing fraction, as used in Equation (4.30), for monodisperse latexes with varying (overall) polymer particle volume fraction.

Conceptually, if one was to take a monodisperse latex and increase the solids concentration, the increase in inter-particle interactions would continually push the maximum solids concentration upwards until $\phi = \phi_{m,i}$. It can be seen from Equation (3.28) in Chapter 3 that the key rheological parameters are functions of ϕ and $\phi_{m,i}$, so the rheological model behavior will be slightly different as a result (viscosity predictions will be lower).

To estimate the tank Reynolds number for a Carreau-Yasuda fluid, it was assumed that the infinite shear viscosity can be used to ascertain the most probable mixing regime inside the vessel. Preliminary simulation results indicated that the shear rates within the impeller region are sufficiently high that latex viscosity in this region can be approximated by the infinite shear viscosity. At the very least, the mixing Reynolds number calculated using the infinite shear viscosity can serve as an upper bound when designing mixing systems for high solid content latexes, although recent studies suggest that the onset of turbulence in non-Newtonian fluids is somewhat delayed compared to Newtonian fluids.[109] The mixing Reynolds number is defined as

$$\mathrm{Re} = \frac{\rho N_I D_I^2}{\eta_\infty} \tag{4.38}$$

Scaling the reactor volume by a factor of ten will result in a scaling in reactor diameter by factor of approximately 2.15, provided geometric similarity is maintained. As stated prior, impeller rotational speed is reduced by a factor of 0.6, so it can be ascertained from Equation (4.38) that the Reynolds number will scale by a factor of approximately 2.75. As a general guideline, a tank Reynolds number of 100 is considered the approximate cut-off between laminar and transition flow, although the point at which inertial forces become important can vary significantly for different mixing configurations and fluid types.

The behavior of a mixing system operating in the laminar regime with Re ~ 100 may change substantially upon scale-up. Figure 4.5 shows the evolution of the flow field with vessel scale (maintaining a constant P/V ratio) along a vertical slice at the center of the vessel (note: $15 < \mathrm{Re} < 100$). The flow field seen at the 1 L scale corresponds to the flow field seen throughout the laminar regime. This was verified by multiplying the relevant viscosity parameters by a factor of 10^6 and re-running the simulation – the solution flow field is essentially identical. In this region, the solution is independent of viscosity as gravity forces can be neglected. At the 10 L and 100 L scales, it can be seen that fluid convection begins to alter the flow field within the vessel, altering the shape of the flow field and possibly improving the degree of mixing within the reactor, as the rate of decay of dimensionless axial flow away from the impeller region is lessened slightly. This result runs contrary to casual expectations, but it is a result of a change in flow regime during process scale-up.

The most immediate objective was to examine the impact of process scale-up on the predictions generated by the computational framework. Using the simulation conditions described in the previous section, the time-dependent evolution of the overall PSD in a 10 L vessel is shown in Figure 4.6a. The overall PSD was computed from the zone PSDs using a volume-weighted average. The PSDs remained constant for the first 170 s, at which point there is a distinct change in the overall PSD, as indicated by the appearance of a large particle population. This suggests a scenario in most of the particles within the impeller region coagulated together very quickly once the local concentration of coagulant exceeded the CCC. At this point, a significant reduction in the total surface area of the particles within this zone will result in the CCC increasing to a point

where the rate of coagulation is reduced drastically. The peak of the large population at 215 s is shifted towards a slightly larger particle diameter compared to the large population peak at 170 s, suggesting that there is some coagulation between the large particles and small particles. During this time period, the tail of the large particle distribution does not shift as much as the peak, indicating that there is little coagulation between pairs of large particles. This is not surprising as other studies have shown that the coagulation rate coefficient for a pair of large particles is much lower than the rate coefficient for a large particle – small particle pair (which, in turn, is larger than the rate coefficient for a pair of small particles), a consequence of the highly-curved double layers of the small particles.[99] It is worth noting that $t = 170$ s corresponds to the first time period at which the flow field is automatically updated.

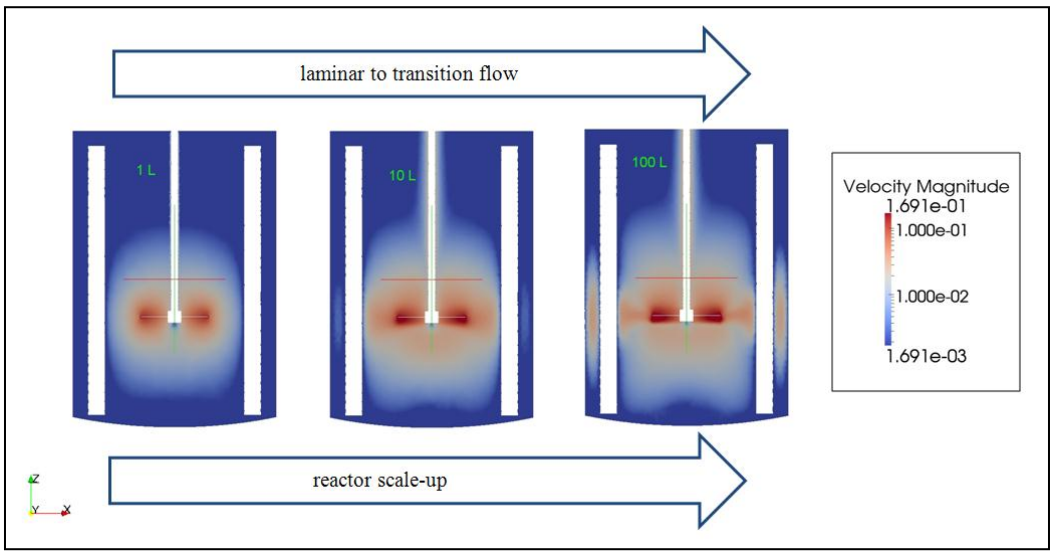

Figure 4.5. Vertical cross-sectional slices showing the change in flow intensity as the tank geometry is scaled from 1 L to 100 L. N_I is set to 100 RPM at the 1-L scale, 59.9 RPM at the 10-L scale and 35.9 RPM at the 100-L scale. Flow data is from CFD simulations based on the initial PSD (dp = 150, PI = 1.10, 59 vol.-% solids) and reactor conditions (T = 298 K, [S] = 9 mol/m^3).

An assessment of the zone-by-zone PSDs after 215 s (see Figure 4.6b) suggests that, regardless of changes in the hydrodynamics due to a significant reduction in viscosity within the impeller region, there is significant segregation outside the impeller region of the vessel. None of the small particles contained within the uppermost region (zone 9) coagulated, while essentially all of the particles in the impeller region (zone 5) coagulated together to form large particles. The presence of a tiny peak of small particles seen in zone 5 is likely a result of ongoing exchange with the zones immediately above and below it (zones 4 & 6). Comparing this tiny peak with the relatively larger peak of large particles seen in zone 7 suggests that small particles entering the well-mixed impeller region are quickly consumed via coagulation with themselves and with larger particles. Such information regarding spatial variations in PSD is often impossible to obtain experimentally, particularly inside commercial vessels where sampling is likely to be done in one region only. Given the system dynamics, the topmost and bottommost zones can be treated as completely segregated if the timescale of the coagulation process is in the order of seconds. However the simulation results suggest that if the feed of coagulant is terminated and the contents of the vessel are allowed to mix for a period of hours, the spatial variation in PSD will eventually disappear.

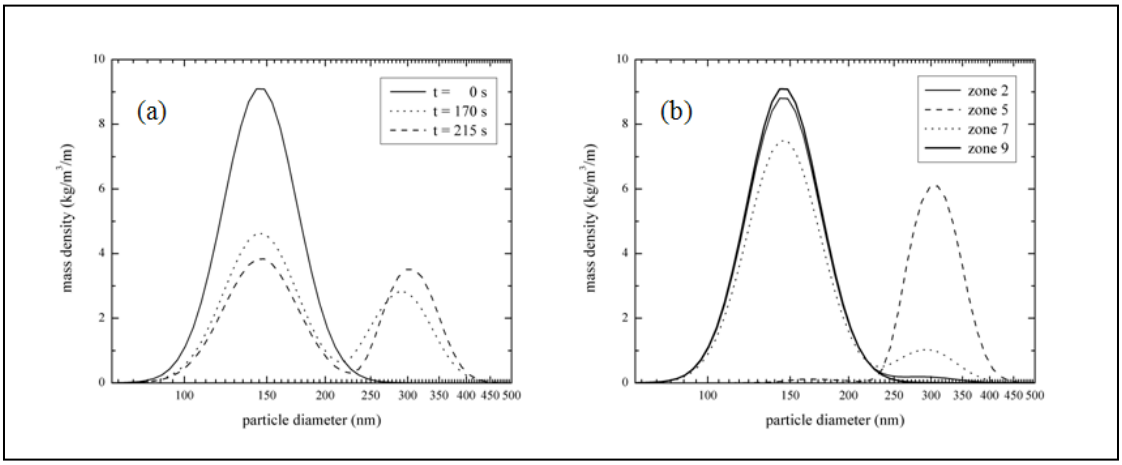

Figure 4.6. Simulation predictions for a 10 L vessel in which coagulant was continuously fed into the vessel in the impeller zone. T = 298 K; N_I = 59.9 RPM; [S] = 9 mol/m^3. At t = 215 s, the concentration of coagulant was 140 mol/m^3. a) Predicted evolution of the particle size distribution in a 10 L vessel over a period of 215 seconds b) Zone-by-zone breakdown of the PSD at t = 215s.

The same set of simulation conditions were used to compare the evolution of PSD inside a perfectly mixed tank and 1 L and 10 L vessels where the time-dependent dynamics of mixing cannot be ignored. The results are shown in Figure 4.7. The distribution obtained for a perfectly mixed system is included to show that poor mixing can have a drastic impact on the final PSD obtained during a coagulation process. The final PSDs obtained for the 1 L and 10 L vessel suggest that the process scales well between 1 L and 10 L reactors. However, close examination of the magnified large peaks suggests that the mixing dynamics in the 10 L vessel are slightly slower compared to the 1 L vessel, despite the appearance of improved mixing when examining the CFD flow fields (Figure 4.5). This was confirmed through a cursory examination of the final zone-by-zone distributions (not shown). This finding is not surprising given that the rate of flow exchanged scales with interface surface area rather than volume, as discussed below. Further improvements to the zoning algorithm, including the ability to allow for a more complex

arrangement of zones within the network is necessary to ensure that the slight discrepancy is not an artifact of a limited zoning algorithm and is indicative of a slight change in the mixing dynamics.

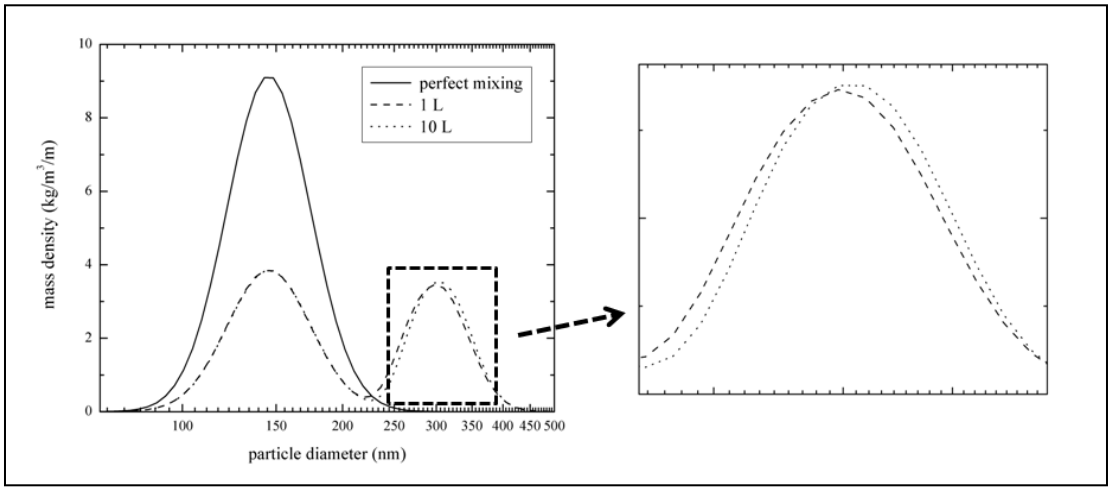

Figure 4.7. Comparing the PSDs obtained at *t* = 215 s in vessel in which coagulant was continuously fed into the vessel in the impeller zone. T = 298K; [S] = 9 mol/m^3. At t = 215 s, the concentration of coagulant was 140 mol/m^3. N_I was set to 100 RPM at the 1-L scale and 59.9 at the 10-L scale. The "perfectly mixed" vessel represents a reactor where conditions can be adjusted to ensure that the timescale of mixing is must faster than the timescale of other dynamic processes (coagulation, polymerization, heat transfer, etc.).

It must be noted that predicting the performance-related impact of scale-up is simplified if flow is confined within the laminar regime across reactor scales, such that the shape of the flow field is independent of Reynolds number. The network of zones/CFD hybrid model becomes redundant as the flow field must only be computed once (at the start of the simulation). The key performance indicator for predicting reactor performance within such systems is the mixing time within in each zone of the vessel, where

$$\theta_{m,z} \equiv \frac{V_z}{\sum_{z,y \neq i} Q_{z,y}} \tag{4.39}$$

Preliminary simulation work indicates that $\theta_{m,i}$ increases with reactor scale, as the rate of flow exchanged is proportional to the surface area of the interfaces between zones; with the current zoning algorithm, the interface surface area corresponds to the cross sectional area of the vessel. We intend to investigate this in more detail in future work.

The original intent was to run a set of simulations at three vessel scales; however convergence of the CFD flow field was poor at the 100 L scale when the flow field required updating. The coagulation of particles leads to a formation of a secondary population of larger particles. Considering a constant solids volume fraction, once the proportion of larger particles reaches a fraction of roughly 20%, the overall viscosity of the latex will begin to drop. When the initial PSD is specified near the loading limit, a broadening of the PSD can push the loading limit high enough to drop the latex viscosity by a factor of 10^2. At the 100 L scale, this pushes operating further into the transition regime (the tank Re approaches 1000 – 10,000) and the CFD software was no longer capable of providing a converged solution. Limiting the study to reactor volumes less than 100 L is not an option as the intention is to develop a framework for scale-up that can predict performance at full commercial scale where tank volumes can reach 100 m^3. Expanding the applicability of the framework to functions in all flow regimes will also expand its applicability to a larger range of latex concentrations. Thus the integration of a turbulent CFD code is a necessity to harness the full capabilities of the framework once the population balance is expanded from a coagulation model to a full emulsion polymerization kinetic model. Thus

efforts are underway to adapt the framework to function with CFD software that successfully predicts fluid flow in the turbulent regime, as was attempted previously by Elgebrandt *et al.*[17]

4.6 Conclusions

The hybrid network of zones population balance/CFD computational framework demonstrated in this work has the potential to capture information that is often difficult to isolate experimentally. The packing model developed by Pishvaei *et al.*[65] has been extended to provide a means of estimating the rheological parameters of broader, more realistic PSDs. The utility of the framework is demonstrated by using the zone-by-zone PSD information to explain some of the trends seen in the time-evolution of the volume-averaged PSDs and the PSD of the final product. Further improvements to the zoning algorithm are needed to ensure that model predictions are not numerical artifacts of a simple zoning algorithm and this work is ongoing. The current framework is limited in scope to investigating particle coagulation in vessels operating in the laminar regime of mixing. Given the presence of turbulence in commercial vessels, expanding the framework via the integration of a turbulent CFD code is a priority; as is the incorporation of a complete emulsion polymerization model. Further development and refinement of the computational framework outlined herein will yield a tool that has the potential to reduce commercialization costs by reducing the amount of pilot plant experimentation required to ensure scalability of product quality.

Chapter 5

Using a Computational Framework to Model the Scale Up of Polymer Latex Reactors

5.1 Introduction

Polymer latex products, which are colloidally-stable dispersions of nanoscale polymer particles dispersed in a continuous medium, are used in a wide range of applications, including paints, adhesives and protective coatings. Due to the rising cost of petroleum-based solvents, the demand for aqueous polymer latex products will continue to grow so long as researchers continue to develop novel products with improved properties. Latex properties are determined by both the formulation (e.g. choice of monomer, stabilizer, initiator, etc…) and the production process. While all polymer latexes are created through the creation, stabilization and growth and coagulation of particles, the precise manner in which these different phases of the process are carried out can drastically affect the properties and value of the final product. By carefully-controlling the nucleation and growth of particles in the reactor, particle size can be manipulated to obtain different particle size distributions (PSDs).

From the perspective of process productivity, there is a strong interest in increasing the solids content of existing polymer latex formulations to increase reactor throughput, reduce shipping costs and improve the quality of end-use products.[30] Most industrial latex formulations are characterized by monodispersed PSDs and contain between 40 and 60 vol.-% solids. However,

by carefully controlling particle nucleation, growth and coagulation, it is possible to produce bimodal PSDs and obtain stable products with solids content as high as 75 vol.-%. Such a high solid content is obtainable because the small particles are engineered to fit in the interstices of the large particle matrix.

The shape of the PSD must be properly chosen in order to obtain concentrated latexes that are both stable and fluid (i.e. low viscosity). Due to the fine control required, the production of bimodal latexes is challenging even at the laboratory scale.[9] As reactor size is increased, production becomes ever more challenging as it becomes increasingly difficult to maintain fine control over the composition of the entire reactor. In many cases, the process is further complicated by the fact that HSC latexes are non-Newtonian fluids, which makes mixing more difficult. While there are a number of heuristic techniques available to guide production scale-up,[10, 127] these heuristics were developed for Newtonian fluids under the assumption that the flow characteristics remain either fully-laminar or fully-turbulent during scale-up. Computational fluid dynamic (CFD) simulation software has been widely-adapted by industry because it provides information on the flow characteristics inside a reactor, information that often difficult to obtain from experiment alone.[13] When the flow information provided by CFD simulation is combined with a descriptive process model, for example an emulsion polymerization process model, it becomes possible to model the scale-up process.

Population balance models (PBMs) are considered the state-of-the-art approach for modeling the production of polymer latexes[128] because they, by their inherent structure, provide detailed information on the PSD. While it is possible to incorporate simple reaction kinetics directly in

the CFD simulation by defining additional conservation equations, directly integrating a detailed emulsion polymerization PBM into the CFD simulation is impractical as modern computers are unable to process the resulting system of equations. An alternative approach to the direct incorporation of the process model within the CFD simulation code is to program the models separately, but employ them sequentially.[78] The flow field computed from CFD can be used to divide the reactor domain into a number of interacting zones,[80] with each zone assumed to be well-mixed (homogenenous). Each of these individual zones is made up of many CFD mesh cells and the resulting network of zones (or zone grid) is much coarser than the CFD mesh. Multiple instances of the PBM (one per zone) are then solved simultaneously on the zone grid. The rate of material and energy transport between these zones is determined from the flow field, which may be updated if the bulk fluid properties change appreciably (for example, due to an increase/decrease in fluid viscosity). The hybrid multizonal CFD model framework retains the information provided by the CFD simulation, but reduces the computational cost significantly. The general methodology for such a framework was formalized in a series of papers published by Bezzo *et al.* [78, 80, 81, 120] and its applicability was demonstrated across a small selection of chemical and biochemical processes.

Over the past ten years, researchers have explored the potential of hybrid multizonal/CFD frameworks to model emulsion polymerization and polymer latex coagulation. A simple, two compartment model framework developed by Alexopoulos *et al.* for liquid-liquid dispersion in suspension polymerization [83] and later emulsion polymerization [15] was one of the earliest attempts. Later, Elgebrandt *et al.* [17] were the first group to adapt the general hybrid multizonal/CFD framework to emulsion polymerization; their model was limited in scope to

lower solid content latexes and a simplified process model. In Chapter 4, we developed a hybrid multizonal/CFD framework to explore the impact of non-homogeneous mixing on the controlled coagulation of high solid content latexes. The initial work focused on the scale-up of a process where a high solid content latex was deliberately coagulated by feeding in an electrolyte. The study was intended to test the performance of the hybrid model framework in modeling a controlled coagulation process, noting that the formation of undesired coagulum and scrap is an important consideration at the industrial scale. The initial work was restricted to studying particle coagulation (no polymerization) and reactor conditions were specified to ensure that flow remained laminar upon vessel scale-up.

This chapter builds on the preliminary computational framework we designed to study coagulation and examines the scale-up of a semi-batch styrene emulsion polymerization process used to produce a latex with a bimodal particle size distribution. The focus is on the critical step in which the small particle population is created *ab initio*. The framework is employed to investigate the impact of changing the characteristic blend time on this critical nucleation stage and the resulting final product PSD. The rate of secondary particle population is very sensitive to the surfactant concentration, while particle stability is very sensitive to the local ion concentration, so this particular portion of the production process is ideal for examining the framework's expanded capabilities.

5.2 Simulation Conditions

5.2.1 Description of Process

The hybrid modeling framework, previously used assess the feasibility of scaling up a controlled coagulation process,[88] was extended to investigate a full emulsion polymerization process. While the emulsion homopolymerization of styrene is not a particularly-intriguing process from an industrial perspective, the kinetics of styrene polymerization are reasonably straightforward, making it an ideal system around which to develop and test a computational framework. Most importantly, a number of research groups have developed and experimentally-validated population balance models for this system.[99, 129] While the simulation predictions presented in this work have not been validated experimentally, the models comprising the framework have been validated separately in the past. The population balance process model utilizes a styrene kinetic model that has been experimentally validated under batch[99] and semi-batch[103] operation. The numerical methods used to solve the PBM were adapted from the code developed by Vale *et al.*[8, 128] which was validated experimentally when it was used to model the homopolymerization of vinyl chloride.[7] The CFD simulation was performed with Fluent, a commercial code that has been tested and experimentally validated to provide good predictive capabilities in a variety of mixing applications.[106, 130]

The viscosity of an aqueous polymer latex is highly-dependent on the size distribution and the concentration of particles comprising the dispersed phase. For a given concentration of particles, the viscosity of a latex characterized by a bimodal PSD will, in general, be lower than a similar latex with a monodispersed particle size distribution. Multimodal PSDs are generally produced

through the use of multiple particle nucleation steps or a single particle nucleation step in the presence of seed particles. The first set of particles created will, *ceteris paribas*, grow larger than particles that are nucleated in subsequent steps and hence the large mode of the PSD will henceforth be referred to as the primary particle mode/population. The primary particles may be produced *in situ* (one-pot) or in a separate reactor to be used as a seed (multi-pot). The creation of secondary and tertiary particle populations is generally carried out *in situ* and this process step is the most challenging and important step in the process. The surfactant and monomer are fed into the reactor to encourage the nucleation of a secondary particle population may interact with the primary particle population, thereby affecting the number of small particles created or even destabilizing the primary particle lattice. For this reason the computational framework is used to investigate the scale-up challenges associated with the nucleation of a secondary particle population in a seeded system and the subsequent growth of both particle populations to obtain a final product with a moderately-high dispersed-phase concentration (~ 50-wt.-% solids).

5.2.2 Description of the Recipes

At the start of the simulation ($t = 0$), the latex is composed as follows, noting that all ingredients are specified on a kg per kg of water (aqueous phase) basis: 0.1 kg polystyrene particles; 0.1 kg monomer (styrene), partially swelling the particles; 3.0×10^{-3} kg initiator (potassium persulphate / KPS); 5.0×10^{-3} kg of anionic surfactant (sodium dodecyl sulphate / SDS). The shape of the initial particle population is monodisperse; it follows a Gaussian distribution, with a mean unswollen diameter of 150 nm and a standard deviation of 5 nm.

In the previous chapter we used the hybrid model framework to model coagulation with a fixed liquid level. In this chapter, the framework is used to investigate and model one of the most challenging steps in the production of bimodal latexes: the *in situ* creation of a second particle population. To ensure the kinetic model was good, we chose to test the framework by modeling styrene emulsion polymerization, a previously-validated system. The creation of the small particle population involves the rapid introduction of surfactant and initiator into the reactor in order to encourage the formation of particles via micellar nucleation. Conversely, the growth of the bimodal population involves a much slower feed of styrene monomer into the vessel. The particle growth process is much slower than the particle creation step. One of the limitations in the current framework is the inability to model the rising liquid level within the reactor. This limitation arises from the fixed nature of the zone grid; modeling a change in liquid level would necessitate that the volume and shape of the irregularly-shaped zones be updated frequently using a custom CFD simulation code with a moving mesh. For reactions where the relative liquid level does not change drastically, it may be pragmatic to model the hydrodynamics using an average liquid level. Strictly speaking, the reactor should be re-zoned frequently to account for a rising

liquid level. However, if the process-critical stage is relatively short, it is not unreasonable to approximate the liquid level as constant during this stage.

Two sets of reaction simulations were run. The main set of simulations assesses the impact of a localized reactant feed on small particle nucleation stage (evaluated by examining the PSD of the final product) across a series of geometrically-similar reactors of varying volumetric scale. An ancillary set of simulations was run in which the mixing limitations in the small particle nucleation step are eliminated in order to assess the impact of scale-up (i.e. changes in the mixing/blend time scale) on the particle growth stage. The main difference between the two simulation scenarios is illustrated in Figure 5.1. Both sets of simulations were run at a polymerization temperature of 70 ℃. For the purposes of simplification, it was assumed that the process was isothermal. The assumption of isothermal operation is realistic at the laboratory scale, but it becomes increasingly-tenuous as the amount of surface area per unit volume of fluid will decrease as the reactor is scaled-up. Note that reactant feeds are specified in terms of total mass added per kg of water present at the start of the reaction (kg / kg H_2O).

In the main set of simulations, the particle nucleation phase involves feeding in 3.0×10^{-3} kg / kg H_2O of KPS and 3.0×10^{-2} SDS over a period of 4 minutes. The reactants are fed in to a localized region near the impeller, as is illustrated in Figure 5.1. A non-instantaneous feed was chosen as it was found that an instantaneous feed resulted in latex destabilization even at the smallest reactor scale. Once the initiator and surfactant have been fed in, 1.1 kg / kg H_2O of styrene monomer is slowly fed into the reactor over a period 102 minutes, in order to maintain a high instantaneous

conversion. The total reaction time simulated is 105 minutes. At the industrial scale, reaction times of three to four hours are common (due to heat transfer limitations), but a reaction time of 1.75 hours is reasonable for the purposes of testing the framework. The small particle nucleation period is longer than the initiator / surfactant feed period of 4 minutes, but, it is still only a small fraction of the overall reaction time.

In the ancillary set of simulations, at $t = 0$, 3.0×10^{-3} kg / kg H_2O KPS and 3.0×10^{-2} kg / kg H_2O SDS are dispersed instantaneously through the entire vessel, along with 0.5 kg / kg H_2O of styrene. After 30 minutes, 0.7 kg / kg H_2O of styrene is slowly fed into the vessel over a period of 75 minutes. The instantaneous dispersal of SDS, KPS and styrene at the start of the simulation ensures that there are no mixing limitations during the small particle nucleation step. Under these conditions, the framework can be used to examine the impact of scale-up on the particle growth stage.

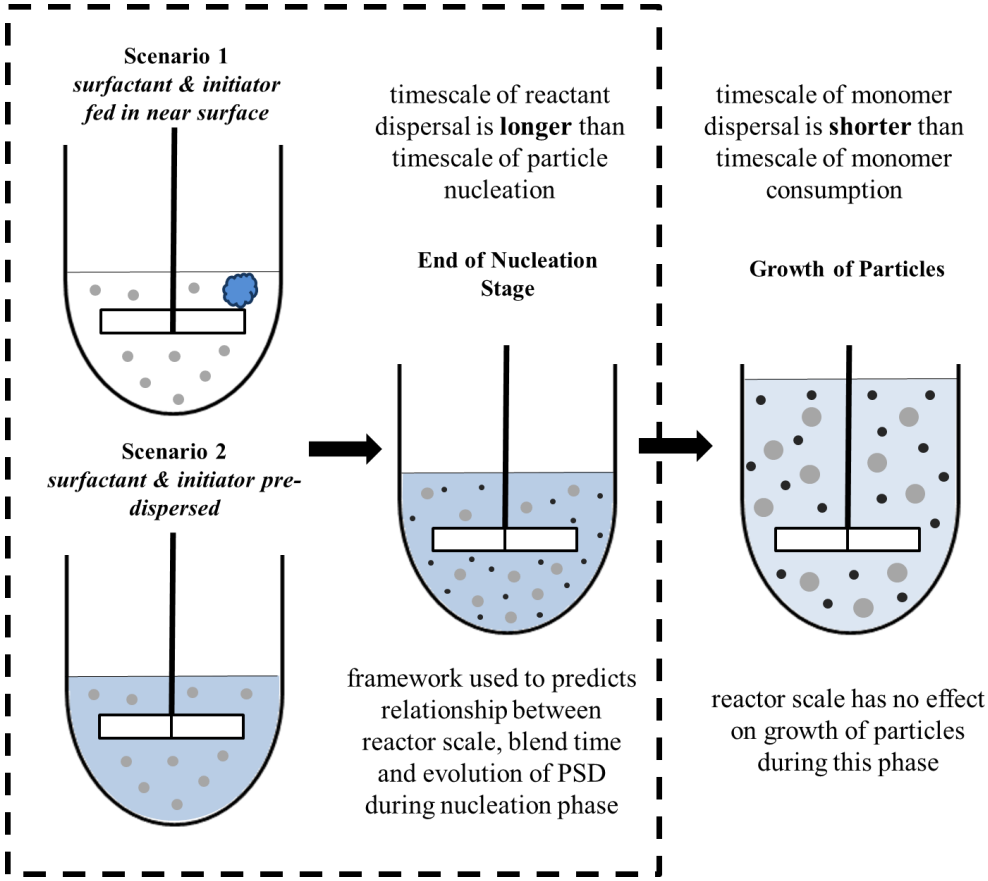

Figure 5.1. Schematic illustrating the emulsion polymerization scenarios that were investigated via the simulation framework. In the first scenario, initiator, surfactant and monomer are fed into the vessel within a small region at the start of the simulation. The dispersal of the reactants is not instantaneous; the size of the reactor will affect blend performance which, in turn, will affect the evolution of the latex PSD during the nucleation phase. In the second scenario, the initiator, the surfactant and a fraction of the total monomer are premixed during the nucleation phase. The framework is used to predict the impact of non-instantaneous monomer dispersal during the particle growth phase.

5.2.3 Description of the Mixing System

In order to investigate the impact of reactor scale-up, CFD simulations were run across three (geometrically similar) reactor scales: 1 L, 100 L and 10 m^3, corresponding to tank diameters (T) of 9.69×10^{-2} m, 4.50×10^{-1} m and 2.09 m, respectively. The mixing system consisted of a four-

bladed 45° pitched-blade turbine and two round baffles. The liquid level was equal to 75% of the tank diameter in the Scenario 1 simulations (e.g. ~ 7.27×10^{-2} m for the 1 L tank) and 85% in the Scenario 2 simulations (e.g. ~ 8.24×10^{-2} m), rather than 140% as it was in Chapters 3 and 4. The CFD simulations are run using a lower liquid level because it is assumed that the critical mixing step occurs at an intermediate point in the process when the liquid level is lower.[37] Besides the change in the liquid level, the remaining tank proportions were the same as those listed in Chapter 3. In the base case, a 1 L laboratory reactor, the impeller rotational speed (N_I) is set to 100 RPM, which is sufficient for blending and emulsification at the laboratory scale.[127] Reactor scale-up is performed by maintaining geometric similarity, such that the relative dimensions of the vessel and impeller system (e.g. the impeller-to-tank diameter ratio) do not change with scale-up. Three different scale-up approaches are investigated via simulation: constant holding power per unit volume (P/V), constant applied torque per unit volume (T_Q/V) and constant reactant blend time (t_{blend}). The required adjustments to the impeller rotational rate (N_I) are computed using classic heuristics,[10] which assume that the fluid is Newtonian and that the reactor is operating under fully-turbulent conditions. This set of assumptions is reasonable given that when the secondary particle population is created, the latex solids content is below 10 vol.-% and the tank Reynolds number at the 1-L scale is ~2.1×10^4. This indicates that the system is likely to be operating in (or near) the fully-turbulent regime at all reactor scales simulated. In turbulent conditions, where viscous forces can be neglected, drag-velocity analysis can be used to show that the volumetric power consumption of the impeller can be represented by:

$$\frac{P}{V_R} \propto N_I^3 D_I^2 \tag{5.1}$$

It follows that the torque of the impeller, on a per-unit-volume basis can be represented by:

$$\frac{T_Q}{V_R} \propto N_I^2 D_I^2 \tag{5.2}$$

Maintaining a constant P/V input involves multiplying N_I by a factor of $10^{-2/9}$ for every increase in reactor volume by a factor of 10 (e.g. an increase in D by a factor of $10^{1/3}$). From Equation (5.2) it follows that multiplying N_I by a factor of $10^{-1/3}$ for every increase in reactor volume by a factor of 10 will maintain a constant T_Q/V. Under fully turbulent conditions the dimensionless mixing time $\left(N_I t_{blend}\right)$ is constant, such that N_I is maintained at 100 RPM when the reactor is scaled-up. The adjustments made to impeller rotational speed as a function of reactor scale and scale-up objective are summarized in Table 5.1. Note that the t_{blend} simulations were not scaled up to 10 m^3, as the motor specifications needed to operate the impeller in a 10 m^3 reactor at 100 RPM would be impossible to meet.

Table 5.1. Change in impeller rotational speed as a function of reactor scale and the scale-up objective. Note that the required adjustment to the impeller rotational speed is computed using heuristic that assume the systems are geometrically similar and that that flow is fully turbulent.

Vessel Scale (m^3)	Scale-Up Objective	Impeller Rotational Speed (RPM)
10^{-3}	-	100.00
10^{-1}	P/V	35.938
	T_Q/V	21.544
	t_{blend}	100.00
10^{1}	P/V	12.915
	T_Q/V	4.6416

Legend:

P/V = constant holding power per unit volume

T_Q/V = constant applied torque per unit volume

t_{blend} = constant blend time

5.3 Framework Components

The computational framework contains three components: (i) a multi-zonal styrene emulsion polymerization population balance model (PBM); (ii) a model of the reactor (CFD simulation); (iii) the automatic zoning algorithm, which uses the hydrodynamic data computed via CFD simulation to automatically generate the zone grid on which the multi-zonal PBM is solved. The manner in which the components work together is depicted in Figure 5.2. In our previous work, the inter-zonal exchange flow rates were periodically updated (via CFD simulation) to account for changes in the flow field that would arise from changes in the latex rheology over the course of the process. In the process simulated in this work, the mixing issues are confined to the particle nucleation stage, which is confined to the first 20 minutes of the reaction. Over this relatively small timeframe, it will be assumed that the liquid level and latex viscosity can be approximated as constant and the flow field does not need to be updated. During the particle growth stage, it is assumed that the timescale of the particle growth dynamics is much larger than the timescale of monomer dispersion (mixing), such that the inter-zonal exchange flow rates do not need to be updated. At higher solids contents where the particle volume fraction approaches the maximum packing limit, latex viscosity will begin to increase rapidly and flow may become segregated. Such a development would lead to a large decrease in the inter-zonal exchange flow rates, invalidating the assumption that the monomer dispersion is instantaneous from the perspective of particle growth; in order to avoid this situation, the final solid content of the process simulated was limited to approximately 55 vol.-%.

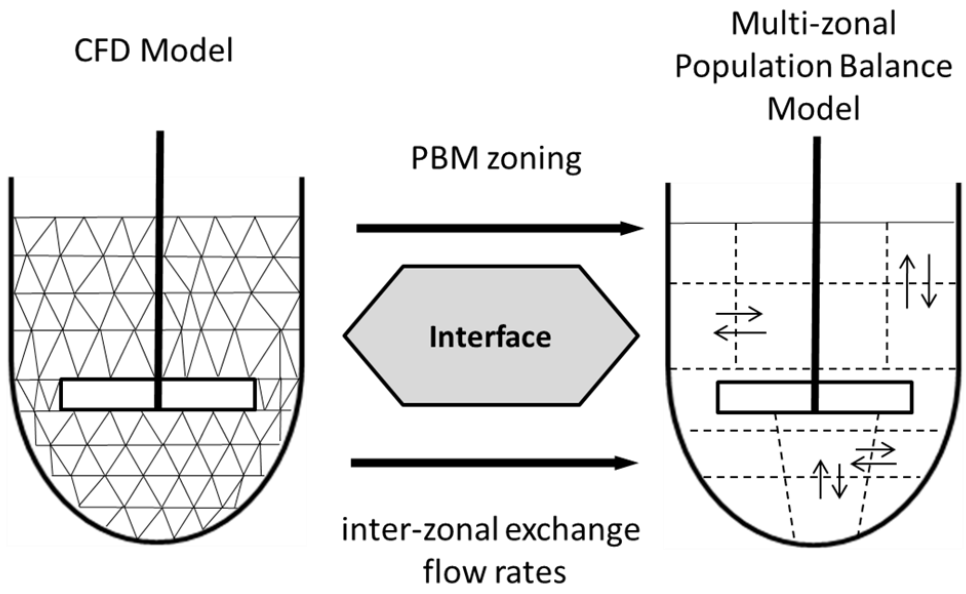

Figure 5.2. Schematic diagram of the framework. Note that the direction of communication is from the CFD model to the PBM model only.

5.3.1 Emulsion Polymerization Model

Early EP process models were based on the assumption that all of the particles in the latex had the same average volume, but the shape of the latex PSD will impact on the dynamics of particle formation and particle growth and the mechanical properties of the final product. As a result, most modern EP models are formulated as population balance models (PBMs) in order to track the details of the PSD (based on the unswollen polymer core). Every particle in a latex can be described using a set of internal coordinates, or states. The most intuitive internal coordinate is the particle size, but there are two more important internal coordinates: radical number and radical chain length. Therefore, the complete particle size distribution can be defined using the number density function $f\left(r,n,R_i\right)$. In practical application, the use of three internal

coordinates yields an intractable set of multidimensional population balance equations (PBEs).[7] There are two kinetic limits commonly employed to reduce the dimensionality of the PBEs to particle size alone: the zero-one (0-1) limit and the pseudo-bulk (PB) limit.

Most commonly, encountered EP systems can be modeled using either the zero one limit or the pseudo bulk limit.[21] Refer to Section 2.2.1 in Chapter 2 for a detailed overview of these two kinetic limits. In a 'zero-one' system, which applies to sufficiently small particles, the entry of a radical into a particle that already contains a growing radical is treated as an 'instantaneous' termination. In a 'pseudo-bulk system', which applies to both large particles and small particles in systems with monomers that propagate very rapidly, the kinetics are treated similarly to a bulk polymerization system. In the emulsion polymerization of styrene, experimental evidence suggests that particles smaller than ~100 nm in diameter should be modeled with zero-one kinetics while particles larger than 120 nm should be modeled with pseudo-bulk kinetics.[85] Given the nature of the EP processes being considered in this work, bimodal PSDs comprised of very large and very small particles, the process model employed in this work is a hybrid zero-one / pseudo bulk PBM.

The overall latex PSD is quantified by defining a radius number density function $f(r,t)$, such that $f(r,t)dr$ is the number of particles per unit volume of aqueous phase with an unswollen radius in the range $[r, r+dr]$. As stated previously, the multi-zonal process model is designed to model the evolution of the PSD within each individual, well-mixed zone. Therefore, the overall

distribution function for the reactor, $f(r,t)$, is computed from the zone number distribution functions $f_z(r,t)$ using the volumetric average

$$f(r,t) = \frac{\sum_z V_z f_z(r,t)}{\sum_z V_z} \tag{5.3}$$

Each zone within the reactor may exchange material (and energy, when applicable) with neighbouring zones. The rate at which flow is exchanged between a zone and its neighbours is computed from the hydrodynamic data provided via CFD simulation. To avoid unnecessary confusion, the zone subscript for most species, kinetic parameters and kinetic coefficients will henceforth be omitted. Unless otherwise noted, all reactant species and species-dependent parameters and coefficients are computed separately for each zone.

To improve clarity, the process model is broken down component-by-component: (i) aqueous phase kinetics; (ii) surfactant adsorption; (iii) monomer partitioning; (iv) particle nucleation; (v) population balance formulation (vi) particle coagulation and (vii) latex rheology.

5.3.1.1 Aqueous Phase Kinetics

Although the locus of polymerization is the polymer particles, what occurs in the aqueous phase plays an important part in the overall kinetic process, essentially controlling the rate of particle formation. The key kinetic events taking place in the aqueous phase in the emulsion polymerization of styrene that has been initiated by a persulphate initiator are schematically

depicted in Figure 5.3, while the reaction scheme (Table 5.2) has been used extensively in other EP modeling publications.[7, 85, 99]

Table 5.2. Aqueous-phase reaction scheme assumed for modeling styrene emulsion polymerization.

Initiator Decomposition	$I-I \xrightarrow{k_d} 2I^{\bullet}$
Propagation	$I^{\bullet} + M \xrightarrow{k_{p1}} IM_1^{\bullet}$
	$IM_i^{\bullet} + M \xrightarrow{k_{pw}} IM_{i+1}^{\bullet}$, $1 \le i \le j_{crit} - 1$
	$E^{\bullet} + M \xrightarrow{k_{p1}} EM_1^{\bullet}$
	$EM_i^{\bullet} + M \xrightarrow{k_{pw}} EM_{i+1}^{\bullet}$, $1 \le i \le j_{Ecrit} - 1$
Termination	$IM_i^{\bullet} + T_j^{\bullet} \xrightarrow{k_{tw}^{i,j}}$ inert products , $1 \le \mathrm{i} \le \mathrm{j}_{crit} - 1$
	$EM_i^{\bullet} + T_j^{\bullet} \xrightarrow{k_{tw}^{i+1,j}}$ inert products , $1 \le \mathrm{i} \le \mathrm{j}_{Ecrit} - 1$
Entry Into Particles	$IM_i^{\bullet} + \text{particle} \xrightarrow{k_{e,particle}(i)} R_i^{\bullet}$, $z \le i \le j_{crit} - 1$
Re-Entry Into Particles	$EM_i^{\bullet} + \text{particle} \xrightarrow{k_{e,particle}(i+1)} R_i^{\bullet}$, $0 \le i \le j_{Ecrit} - 1$
Exit from Particles	$E_{(particle)}^{\bullet} \xrightarrow{k_{dM}} E^{\bullet} +$ particle
Homogeneous Nucleation	$IM_{j_{crit}-1}^{\bullet} + M \xrightarrow{k_{pw}}$ particle
	$EM_{j_{Ecrit}-1}^{\bullet} + M \xrightarrow{k_{pw}}$ particle
Heterogeneous Nucleation	$IM_i^{\bullet} +$ micelle $\xrightarrow{k_{e,mic}(i)}$ particle , $z \le i \le j_{crit-1}$
	$EM_i^{\bullet} +$ micelle $\xrightarrow{k_{e,mic}(i+1)}$ particle , $0 \le i \le j_{Ecrit-1}$

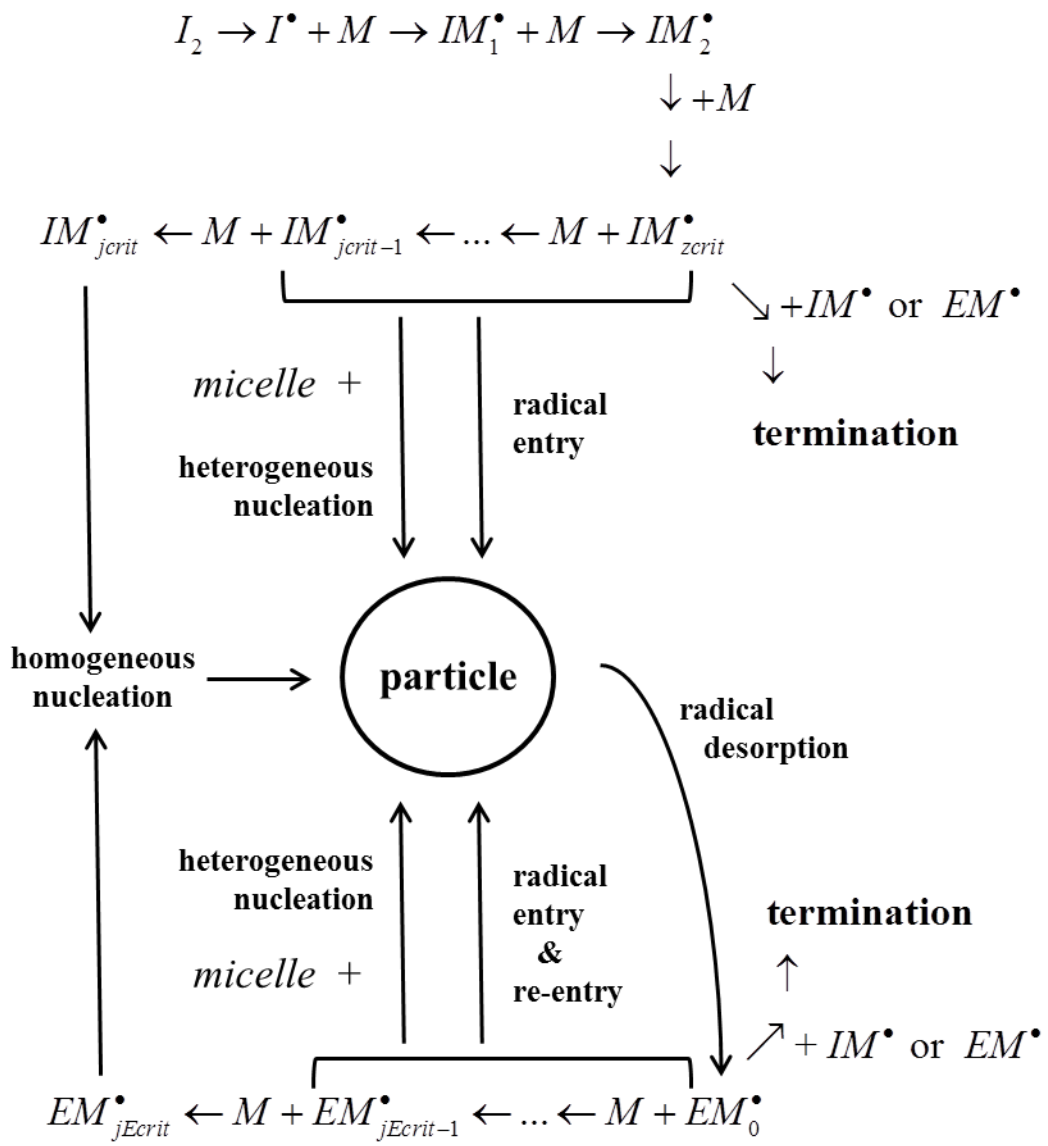

Figure 5.3. Schematic of the aqueous-phase and phase-transfer events that occur in an emulsion polymerization process.[7]

The primary radicals react with the monomer dissolved in the aqueous phase, adding monomer units. Once a sufficient number of monomer units have been added (denoted z_{crit}), the oligomer is surface active and may enter monomer-swollen micelles (if present). This mechanism is known as heterogeneous or micellar nucleation. Surface-active oligomers that are not captured by

micelles or particles will continue to grow in the aqueous phase. However, when an aqueous phase oligomer reaches a critical chain length (denoted j_{crit}), it will become water insoluble and undergo a coil-to-globe transition, excluding water and becoming a precursor particle.[131] This mechanism is known as homogeneous nucleation. The critical chain lengths are dependent on temperature, the water solubility of the monomer and the type of initiator employed (ionic vs. non-ionic). For KPS initiator, the critical chain lengths can be estimated with the following expressions:[99, 132]

$$z_{crit} = 1 - \frac{23{,}000 \text{ J/mol}}{RT \log\left[M\right]_w^{sat}} \qquad j_{crit} = 1 - \frac{55{,}000 \text{ J/mol}}{RT \log\left[M\right]_w^{sat}} \tag{5.4}$$

where $\left[M\right]_w^{sat}$ is the concentration of monomer in the aqueous phase at saturation. The values of z_{crit} and j_{crit} computed with Equation (5.4) are rounded to the nearest integers. In addition to initiator-derived radical species, the aqueous phase will contain radicals that were formed by chain transfer to monomer (or chain-transfer agent, if present) inside particles and then subsequently desorbed from the particles. The concentration of exit-derived radicals is denoted by $\left[EM_i^{\bullet}\right]$, where *i* is the number of monomer units that the radical had added on in the aqueous phase (upon initial exit *i* = 0). These exit-derived radicals are more hydrophobic than their initiator-derived brethren due to the lack of a hydrophilic persulfate chain-end and may re-enter particles or micelles without further propagation in the aqueous phase. For styrene, the exit-derived radical will undergo homogeneous nucleation after adding two monomer units in the aqueous phase ($j_{Ecrit} = 2$). The concentration of the aqueous phase radicals can be computed via the following set of rate equations:

$$\frac{d[I]}{dt} = -2k_d[I] + \delta_{z,z_{feed}} \frac{F_I}{V_w Mw_I} \tag{5.5}$$

$$\frac{d[I^\bullet]}{dt} = 2 f_I k_d [I] - k_{p1}[I^\bullet][M]_w \tag{5.6}$$

$$\begin{aligned}\frac{d[IM_1^\bullet]}{dt} &= k_{p1}[I^\bullet][M]_w - k_{pw}[IM_1^\bullet][M]_w \\ &\quad -[IM_1^\bullet]\left(\sum_{j=1}^{jcrit-1} k_{tw}^{1,j}[IM_j^\bullet] + \sum_{j=0}^{jEcrit-1} k_{tw}^{1,j+1}[EM_j^\bullet]\right)\end{aligned} \tag{5.7}$$

$$\begin{aligned}\frac{d[IM_i^\bullet]}{dt} &= k_{pw}\left([IM_{i-1}^\bullet] - [IM_i^\bullet]\right)[M]_w \\ &\quad -[IM_i^\bullet]\left(\sum_{j=1}^{jcrit-1} k_{tw}^{i,j}[IM_j^\bullet] + \sum_{j=0}^{jEcrit-1} k_{tw}^{i,j+1}[EM_j^\bullet]\right)\end{aligned} \tag{5.8}$$

for $i < z_{crit}$

$$\begin{aligned}\frac{d[IM_i^\bullet]}{dt} &= k_{pw}\left([IM_{i-1}^\bullet] - [IM_i^\bullet]\right)[M]_w \\ &\quad -[IM_i^\bullet]\left(\sum_{j=1}^{jcrit-1} k_{tw}^{i,j}[IM_j^\bullet] + \sum_{j=0}^{jEcrit-1} k_{tw}^{i,j+1}[EM_j^\bullet]\right) \\ &\quad -k_{e,part}^i[IM_i^\bullet]\frac{N_t}{NA} - k_{e,mic}^i[IM_i^\bullet][mic]\end{aligned} \tag{5.9}$$

for $z_{crit} \le i < j_{crit}$

$$\frac{d\left[EM_0^\bullet\right]}{dt} = \Phi_{des} - k_{p1}\left[EM_0^\bullet\right][M]_w - \left[EM_0^\bullet\right]\left(\sum_{j=1}^{jcrit-1} k_{tw}^{1,j}\left[IM_j^\bullet\right] + \sum_{j=0}^{jEcrit} k_{tw}^{1,j+1}\left[EM_j^\bullet\right]\right) - k_{e,part}^{1}\left[EM_0^\bullet\right]\frac{N_t}{N_A} - k_{e,mic}^{1}\left[EM_0^\bullet\right][mic] \quad (5.10)$$

$$\frac{d\left[EM_i^\bullet\right]}{dt} = k_{pw}\left(\left[EM_{i-1}^\bullet\right] - \left[EM_i^\bullet\right]\right)[M]_{aq} - \left[EM_i^\bullet\right]\left(\sum_{j=1}^{jcrit-1} k_{tw}^{i+1,j}\left[IM_j^\bullet\right] + \sum_{j=0}^{jEcrit-1} k_{tw}^{i+1,j}\left[EM_j^\bullet\right]\right) - k_{e,part}^{i+1}\left[EM_i^\bullet\right]\frac{N_t}{N_A} - k_{e,mic}^{i+1}\left[EM_i^\bullet\right][mic] \quad (5.11)$$

for $1 \le i < j_{Ecrit}$

where F_I is the mass feed rate of initiator into the feed zone, if applicable. The rate of desorption of $\left[EM_0^\bullet\right]$ radicals from the particles to the aqueous phase is given by

$$\Phi_{des} = \frac{1}{N_A}\int_0^\infty k_{des}[M]_p \bar{n} f(r,t)\, dr \quad (5.12)$$

where k_{des} is the desorption rate coefficient and $\bar{n}$ is the average number of radicals per particle. Due to the large number of reactions that must be accounted for within the aqueous phase, obtaining independent values for of all the parameters that govern aqueous phase activity is a challenge.[21] In this work, all of the kinetic coefficient and parameter values were adapted from other groups' experimental and modeling work (refer to Table 5.3 and Table 5.4).

Table 5.3. Kinetic rate coefficient equations for styrene emulsion polymerization as implemented in the population balance model

$k_p = 1/\left(1/k_{p0} + 1/k_{diff}\right)$ [m^3 mol^{-1} s^{-1}]	(Russell *et al.*)[133]
$k_{p0} = 238.06\times10^{-3}\exp\left(12.10 - 3.909\times10^3/T\right)$ [m^3 mol^{-1} s^{-1}]	(Meadows *et al.*)[129]
$k_{diff} = 4\pi\sigma_r N_A\left(D_{mon} + D_{rd}\right)$ [m^3 mol^{-1} s^{-1}]	(Russell *et al.*)[133]
$D_{rd} = k_{p0}\left[M\right]_p \alpha^2/6$ [m^2 s^{-1}]	(Russell *et al.*)[133]
$D_{mp} = \begin{cases} 10^{\left(29.51\phi_p + 53.14\phi_p^2 - 36.03\phi_p^3 - 1.583\right)} & \text{for } \phi_p < 0.80 \\ 9.0\times10^{-10}\exp\left(-19.16\phi_p\right) & \text{for } \phi_p > 0.80 \end{cases}$ [m^2 s^{-1}]	(Russell *et al.*)[133]
$k_d = 1.0\times10^{-6}\exp\left(-1.6148\times10^4\left[\frac{1}{T} - \frac{1}{323.15}\right]\right)$ [s^{-1}]	(Meadows *et al.*)[129]
$k_t = k_{t0}\exp\left(-A\left[1/V_f - 1/V_{f,sat}\right]\right)$ [m^3 mol^{-1} s^{-1}]	(Xie *et al.*)
$k_{t0} = 1.34\times10^7\exp\left(-14340/RT\right)$ [m^3 mol^{-1} s^{-1}]	(Taylor *et al.*)[134]
$A = 6.64\times10^6\exp\left(-4986/T\right)$	(Xie *et al.*)
$V_f = V_{fm}\phi_m + V_{fp}\phi_p$	(Marten and Hamielec)[135]
$V_{f,sat} = V_{fm}\left[M\right]_p^{sat} Mw_m/\rho_m$	(Marten and Hamielec)[135]
$V_{fm} = 0.025 + 1.0\times10^{-3}\left(T - T_{gm}\right)$	(Marten and Hamielec)[135]
$V_{fp} = 0.025 + 4.8\times10^{-4}\left(T - T_{gp}\right)$	(Marten and Hamielec)[135]
$\phi_m = \left[M\right]_p Mw_m/\rho_m$	
$\phi_p = 1 - \phi_m$	

Table 5.4. Miscellaneous model parameters for styrene emulsion polymerization, as implemented in the population balance model

$f_I = 1.0$	
$\alpha = 7.4\times10^{-10}$ [m]	(Coen *et al.*)[99]
$k_{p1} = 10k_{p0}$ [m^3 mol^{-1} s^{-1}]	
$k_{pw} = 2k_{p0}$ [m^3 mol^{-1} s^{-1}]	
$\sigma_r = 5.0\times10^{-10}$ [m]	(Coen *et al.*)[99]
$Mw_m = 1.04\times10^{-3}$ [kg mol^{-1}]	
$\rho_m = 104.152\left(\frac{0.7397}{\left[0.2603^{\left(1.0+\left[1-T/636\right]^{0.3009}\right)}\right]}\right)$ [kg m^{-3}]	(Perry's)[136]
$\rho_p = 1000\begin{pmatrix}1.067-5.02\times10^{-4}\left[T-273.15\right]\\-1.35\times10^{-7}\left[T-273.15\right]^2\end{pmatrix}$ [kg m^{-3}]	(Orwol)[137]
$p_{ij} = 0.25$	(Gilbert)[4]
$D_{mw} = 2.699\times10^{-12}T\cdot\left(2.1482\times10^{-2}\left[\frac{\left(T-281.585\right)+}{\sqrt{\left(8078.4+\left[T-281.585\right]^2\right)}}\right]-1.2\right)$ [m^2 s^{-1}]	(Meadows *et al.*)[129]
$T_{gm} = -184.95$ [K]	(Marten and Hamielec)[135]
$T_{gp} = 366.65$ [K]	(Marten and Hamielec)[135]
$b_s = 2.1$ [m^3/mol]	(Coen *et al.*)[99]
$V_s = 3.85\times10^{28}$ [m^3]	[138]
$V_m = Mw_m / \left(\rho_m N_A\right)$ [m^3]	
$K_{mic} = 1.68\times10^4$ [mol^{-1}]	[138]
$r_F = 8.0\times10^{-9}$ [m]	(Coen *et al.*)

The aqueous phase termination rate coefficient is computed with the modified von Smoluchowski[4] equation:

$$k_{tw}^{i,j} = 2\pi p_{ij}\sigma_r N_A D_{mw}\left(i^{-1/2} + j^{-1/2}\right) \tag{5.13}$$

where p_{ij} is the spin ratio (assumed to be ¼ for short chain species) and σ_r is the distance at which the radicals centers react (taken to be the van der Waals radius of the monomer).

The rates of radical entry into particles and micelles are assumed to be diffusion-controlled:[4]

$$k_{E,mic}^{i} = \frac{4\pi r_{mic} N_A D_{mw}}{i^{1/2}} \tag{5.14}$$

$$k_{E,part}^{i} = \frac{4\pi r_s N_A D_{mw}}{i^{1/2}} \tag{5.15}$$

where micelle radius is computed as a function of the aggregation number, n_{agg} and number of carbon atoms per chain that reside in the interior, N_c.

$$r_{mic} = \frac{3\times10^{-10}}{4\pi}\left(\left[27.4 + 26.9N_C\right]n_{agg}\right)^{1/3} \tag{5.16}$$

Similarly, the rate of radical exit from particles is dependent on the diffusivity of monomer in both the particle and aqueous phase:[103]

$$k_{des} = \frac{3D_{mp}D_{mw}}{\left(K_{mpw}D_{mp} + D_{mw}\right)r_s^2} \tag{5.17}$$

where $K_{mpw} = \left[M\right]_p / \left[M\right]_w$ is the partition coefficient for monomer between the particle and aqueous phase.

5.3.1.2 Surfactant Adsorption

The adsorption of the surfactant onto the surface of the latex particles is assumed to follow a Langmuir adsorption isotherm, the same approach employed by both Coen[99] and Meadows:[129]

$$A_s = a_s\left(1+\frac{1}{[S]_w b_s}\right) \tag{5.18}$$

where A_s is the area actually occupied by a single surfactant molecule and a_s is the minimum area a surfactant molecule can occupy. Meadows *et al.*[129] used a linear fit on the data from Pirma and Chen[139] to compute a_s as a function of temperature and ionic strength.

$$a_s = 1\times10^{-20}(a_0 + a_1 T)(1+b_1 I) \tag{5.19}$$

$$\text{where } a_0 = -1.3304\times10^{-1} \qquad a_1 = 2.0316\times10^{-1} \qquad b_1 = -2.418 \tag{5.20}$$

where

$$I = 3[I]+[S] \tag{5.21}$$

when the initiator (KPS) which is a 1:2 electrolyte and the surfactant (SDS) is a 1:1 electrolyte with a homogeneously-distributed counter-ion.[99]

The concentration of surfactant in the aqueous phase can be computed by subtracting the amount of surfactant adsorbed onto the latex particles from the total amount of surfactant added to the reactor per unit volume of aqueous phase.

$$[S]_w = [S] - \frac{A_{tot}}{N_A A_S} \tag{5.22}$$

where A_{tot} is the total surface area of the swollen latex particles. Combining equations (5.18) and (5.22) leads to the following quadratic relationship:

$$[S]_w^2 + \left(\frac{A_{tot}}{a_s N_A} + \frac{1}{b_s} - [S]\right)[S]_w - \frac{[S]}{b_s} = 0 \tag{5.23}$$

Similarly, the positive root of equation (5.23) is used to compute $[S]_w$. The micelle concentration can then be computed with the following relationship:

$$[mic] = \max\left(0, \frac{[S]_w - CMC}{n_{agg}}\right) \tag{5.24}$$

The critical micelle concentration, often expressed as a constant in EP models, will change, in the presence of additives such as salt and as a function of temperature. In particular, the CMC is very sensitive to added electrolyte; the addition of 1×10^{-2} mol/L of NaCl reduces the CMC of SDS by more than a factor of 2.5.[140] The fit performed by Meadows *et al.*[129] on the extensive data compiled by Mukerjee and Mysels[140] for sodium dodecyl sulphate (SDS) is not a first principles model, but it is acceptable for the purposes of this work.

$$CMC = \left(a_0 + a_1 T + a_2 T^2\right)\left(\frac{b_0 + b_1 I}{c_0 + c_1 I}\right) \tag{5.25}$$

where $a_0 = 1.539\times10^{-1}$ $a_1 = -9.7902\times10^{-4}$ $a_2 = 1.6391\times10^{-6}$
$b_0 = 0.9995$ $b_1 = 1.1955$ $c_0 = 1.0$ $c_1 = 29.34$

It has been found that in the case of sodium dodecyl sulphate (SDS) and anionic surfactants in general, the addition of salt and other impurities will cause aggregation number, and thus micelle size to increase. Bales *et al.*[141] developed the following semi-phenomenological model to compute the aggregation number as a function of surfactant and salt concentration:

$$n_{agg} = 49.5\left(\frac{0.27[S] + 0.73[S]_w + [NaCl] + 3[I]}{CMC_0}\right)^{1/4} + \Delta n_{agg} \tag{5.26}$$

where CMC_0 is the critical micelle concentration in the absence of added ionic species. The relationship presented by Bales has been modified to include the contributions of the initiator, potassium persulphate. This falls in line with the data presented in other literature, such as

Giannetti *et al.*[138], where the contributions of all cationic species are taken into account when computing the CMC and n_{agg} . Water insoluble species may be solubilized within the micelles, increasing the aggregation number until the solubilisation limit is reached. For styrene monomer, for example, the number of additional solubilized molecules per micelle, X_A, is given as follows:

$$X_A = K_{mic,eq}\left[M\right]_w \tag{5.27}$$

where $K_{mic,aq}$ is the partition coefficient of styrene between the micelle and aqueous phases.[138] This relationship can be used to compute the increase in n_{agg} by evaluating the change in micelle area per head group before and after monomer addition[138]:

$$\Delta n_{agg} = 2X_A \frac{V_m}{V_S} \tag{5.28}$$

where V_s and V_m are the hydrophobic volumes of the surfactant tail (C_{12} for SDS) and the monomer, respectively. In spite of the highly precise manner in which is possible to compute the micelle surface area for particle capture, it is important to note that industrial surfactants will contain a combination of anionic and non-ionic components and impurities. There will likely be variations in the CMC and aggregation number from one batch of surfactant to another, thus, in industrial application, parameters determined from in-house experimental measurement should provide improved predictive capability over the use of Equations (5.25) to (5.28). If the model is being developed to perform over a wide range of temperatures and in the presence of added electrolytes, the empirical models are preferred to experimental constants, as the CMC and n_{agg} values are likely be sensitive to the conditions inside the reactor.

5.3.1.3 Monomer Balance

The total mass of monomer in the system is given by:

$$\frac{dm_m}{dt} = \delta_{z,z_{feed}} F_m - \left(R_{pw} + R_{pp}\right) Mw_m V_m + Q\left(\mathbf{m}_m\right) \tag{5.29}$$

where F_m is the mass feed rate of monomer into the feed zone, $Q_z\left(\mathbf{m}_m\right)$ is the net rate of monomer flowing into zone *z* due to flow exchanged with neighbouring zones, and Mw_m is the molar mass of monomer. The total rate of monomer consumption in each zone, R_p is a sum of the rate of polymerization in the particles R_{pp} and in the aqueous phase R_{pw}:

$$R_{pp} = \frac{k_p}{N_A} \int_0^\infty \left[M\right]_P (r) \overline{n} f_z(r,t) dr \tag{5.30}$$

$$R_{pw} = 2 f_I k_d \left[I\right] + k_{pw} \left[M\right]_w \left(\sum_{i=1}^{j_{crit}-1} \left[IM_i^\bullet\right] + \sum_{i=0}^{j_{Ecrit}-1} \left[EM_i^\bullet\right] \right) \tag{5.31}$$

The mass of monomer inside the swollen polymer particles is computed with the following expression:

$$m_{m,p} = Mw_m V_w \frac{4\pi}{3} \int_0^\infty \left[M\right]_{p,sat} r_s^3 f\left(r,t\right) dr \tag{5.32}$$

Initially, $\left[M\right]_p$ is set to equal $\left[M\right]_p^{sat}$, which is assumed to be a function of particle radius:[4]

$$\left[M\right]_p^{sat}(r) = \left[M\right]_{p,\infty}^{sat} \tanh\left(r / r_f\right) \tag{5.33}$$

where r_f is a parameter that expresses the radius at which $[M]_p$ approaches the limiting value of $[M]_p^{sat}$. The concentration of monomer in the aqueous phase, $[M]_w$,is also initially set to $[M]_w^{sat}$ to provide an initial estimate of the amount of monomer dissolved in the aqueous phase

$$m_{m,w} = [M]_w \, Mw_m V_w \tag{5.34}$$

The mass of monomer droplets in the system is

$$m_{m,d} = m_m - m_{m,w} - m_{m,p} \tag{5.35}$$

If $m_{m,d} > 0$, monomer droplets are present in the system. If $m_{m,d} < 0$, a new estimate of $m_{m,P}$ is computed from

$$m_{m,p} = m_m - m_{m,w} \tag{5.36}$$

$[M]_p$ is subsequently computed with the following expression:

$$[M]_p = \frac{m_{m,P}}{Mw_m \frac{4\pi}{3} \int_0^\infty r^3 f(r,t)\, dr + \rho_p m_{m,p}} \tag{5.37}$$

where the denominator of Equation (5.37) is an expression for computing the swollen volume of the polymer particles. $[M]_w$ is then updated using the semi-empirical expression developed by Vanzo *et al.*:[142]

$$\frac{[M]_w}{[M]_w^{sat}} = \left(\frac{[M]_p}{[M]_p^{sat}} \right)^{0.6} \tag{5.38}$$

Subsequently, $m_{m,w}$ is updated using Equation (5.34) and a new value of $m_{m,p}$ is computed from Equation (5.36). The new estimate of $m_{m,p}$ is compared to the value at the previous iteration and the iterative procedure ends once the relative change in $m_{m,p}$ is less than a specified tolerance.

5.3.1.4 Particle Nucleation

As schematically shown in Figure 5.3 and discussed above, initiator derived radicals and transfer-derived radicals that reach a surface-active length may enter into micelles, resulting in heterogeneous (micellar) nucleation. The rates of heterogeneous nucleation due to initiator-derived and exit-derived radicals are given as follows:

$$R_{mic,I} = [mic] \sum_{i=z}^{jcrit-1} k_{E,mic}^{i} \left[IM_i^{\bullet} \right] \tag{5.39}$$

$$R_{mic,E} = [mic] \sum_{i=0}^{jEcrit-1} k_{E,mic}^{i+1} \left[EM_i^{\bullet} \right] \tag{5.40}$$

When initiator-derived and exit-derived radicals reach their respective critical lengths, they will precipitate out, forming precursor particles. The rates of homogeneous nucleation are given by:

$$R_{\hom,I} = k_{pw} \left[IM_{jcrit-1}^{\bullet} \right] [M]_W \tag{5.41}$$

$$R_{\hom,E} = k_{pw} \left[EM_{jEcrit-1}^{\bullet} \right] [M]_W \tag{5.42}$$

The total rate of particle nucleation is the summation of Equations (5.39) - (5.42):

$$R_{nuc} = R_{mic,I} + R_{mic,E} + R_{\hom,I} + R_{\hom,E} \tag{5.43}$$

All nucleated particles are assumed to have the same unswollen radius, r_{nuc} as the numerical predictions are insensitive to the value of r_{nuc}, provided it is chosen pragmatically (e.g. 5 nm). [99] Therefore, r_{nuc} was computed with the following expression:

$$r_{nuc} = r_{mic} + \left(\frac{3}{4\pi} \frac{j_{crit} Mw_m}{N_A \rho_P} \right)^{\frac{1}{3}} \tag{5.44}$$

5.3.1.5 Particle Population Balance Model

For a given zone *z*, the EP PBEs can be written in a general form by defining a vector distribution, $\mathbf{f}_z(r,t)$ that groups the individual number density functions. For analytical solutions, the PBEs are often written using particle volume as an internal coordinate, but for numerical solutions, it is preferable to use the un-swollen particle radius as an internal coordinate. The PBM employed is a hybrid of the zero-one and pseudo-bulk model. For each zone in the reactor, the overall hybrid balance expression can be written as follows:

$$\frac{\partial}{\partial t}\mathbf{f}_z(r,t) = \chi(r_s)\frac{\partial}{\partial t}\mathbf{f}_z(r,t)\Big|_{0-1-MP} + \left(1-\chi(r_s)\right)\frac{\partial}{\partial t}\mathbf{f}_z(r,t)\Big|_{PB}\mathbf{m} \tag{5.45}$$

where $\mathbf{m}$ is specified to ensure that the dimensionality of the pseudo-bulk contribution matches that of the zero-one contribution:

$$\mathbf{m} = \left[\frac{f_{z,0}(r,t)}{f_z(r,t)} \quad \frac{f_{z,1p}(r,t)}{f_z(r,t)} \quad \frac{f_{z,1m}(r,t)}{f_z(r,t)} \right]^T \tag{5.46}$$

In the zero-one model, the overall distribution is a sum of the individual distributions, such that

$$f_z(r,t) = f_{z,0}(r,t) + f_{z,1P}(r,t) + f_{z,1M}(r,t) \tag{5.47}$$

where $f_{z,0}(r,t)$ is the distribution of particles containing no free radicals, $f_{z,1P}(r,t)$ is the distribution of particles containing a polymeric free radical and $f_{z,1M}(r,t)$ is the distribution of particles containing a monomer derived free radical.

The transition between zero-one kinetics and pseudo-bulk kinetics is a gradual process. The Gilbert group suggested that a cross-over radius range is 50 nm – 60 nm for styrene.[85, 143] The smoothing function, $\chi(r_s)$, is formulated such that the dynamics of particles with a swollen radius less than 50 nm are modeled exclusively using zero-one kinetics and the dynamics of all particles with swollen radii larger than 60 nm are modeled using pseudo-bulk kinetics. Within the cross-over range, the overall particle dynamics are smoothed using the following function:

$$\chi(r_s) = \begin{cases} 1.0 & \text{for } r_s \le r_l \\ \left(\frac{r_u^3 - r_s^3}{r_u^3 - r_l^3} \right) & \text{for } r_l < r < r_u \\ 0.0 & \text{for } r_s \ge r_u \end{cases} \tag{5.48}$$

where $r_l = 50 \text{ nm}$ and $r_u = 60 \text{ nm}$. Given that the particle-specific termination rate coefficient is a function of particle volume rather than particle radius, a smoothing function that is linear with respect to particle volume was deemed to be acceptable for the demonstrative purposes of this work. A smoothing function based on the error function was tested as well, but the numerical predictions did not change noticeably.

Both the 0-1-MP and PB terms take on the same general form, that of a system of linear hyperbolic balance laws:

$$\left.\frac{\partial}{\partial t}\mathbf{f}_z(r,t)\right|_X = -\frac{\partial}{\partial t}\left[\dot{\mathbf{r}}(r,\mathbf{y}_z)\mathbf{f}_z(r,t)\right]_X + \mathbf{s}(\mathbf{f}_z,r,\mathbf{y}_z)_X \qquad \text{for X = 0-1, PB} \quad (5.49)$$

$$\dot{\mathbf{r}}(r,\mathbf{y}) = \dot{\mathbf{v}}(r,\mathbf{y})/4\pi r^2 \quad (5.50)$$

The subscript *X* is omitted in subsequent expressions, but it should be noted that the following terms will be strongly influenced by the kinetic limit because they are functions of $\bar{n}$: (i) $\dot{\mathbf{v}}(r,\mathbf{y})$, (ii) R_{pp} and (iii) k_{des}.

Within the zero-one framework, the average number of radicals per particle is computed from the particle number density distributions directly:

$$\bar{n}_{0-1}(r,t) = \frac{f_1(r,t)}{f(r,t)} \quad (5.51)$$

where $f_1(r,t) = f_{1P}(r,t) + f_{1M}(r,t)$.

There are two widely-used expressions available for computing $\bar{n}$ under pseudo-bulk kinetic conditions.[21] The method employed in this work is the steady-state approximation that was originally published by O'Toole almost fifty years ago.[144] Under the assumption that CLD termination may be neglected and that the rates of radical entry, desorption and termination are much faster than nucleation, coagulation, growth and inflow/outflow, $\bar{n}(v,t)$ [144] can be computed as:

$$\bar{n}_{PB}(r,t) = aI_m(a)/4I_{m-1}(a) \quad (5.52)$$

where $a = \sqrt{8\rho N_A v/k_t}$ and $m = k_{des}N_A v/k_t$ are the argument and order of the modified Bessel function of the first kind $I_m(a)$ [7], respectively.

For the 0-1-MP model:[7]

$$\mathbf{f} = \begin{bmatrix} f_0 & f_{1p} & f_{1m} \end{bmatrix}^T \tag{5.53}$$

Conversely, the PB model only requires one number distribution per zone due to the absence of radical compartmentalization.

$$\mathbf{f} = f \tag{5.54}$$

The discretization is performed over a domain range of $[r_{nuc}, r_{max}]$, where r_{nuc}, computed via Equation (5.44), is the size of a nucleated particle and r_{max}, the truncated maximum particle size, which is chosen to be sufficiently large to minimize numerical error. The domain is discretized using the finite volume (FV) method. The FV method is suitable because it conserves the number of particles, allows for simple incorporation of the point source term (i.e. particle nucleation) and is compatible with fixed pivot method,[8, 128] which is was chosen as the method of discretization of the source term in Chapter 4. The domain is divided into M contiguous cells, $C_i = \left[r_{i-1/2}, r_{i+1/2} \right]$, $1 \le i \le M$, with the following properties: size $\Delta r_i = \left(r_{i+1/2} - r_{i-1/2} \right)$ cell centers $r_i = \frac{1}{2}\left[r_{i+1/2} + r_{i-1/2} \right]$. The average number density of particles in cell C_i at time t is:

$$\bar{\mathbf{f}}_{z,i}(t) = \frac{1}{\Delta r_i} \int_{r_{i-1/2}}^{r_{i+1/2}} \mathbf{f}_z(r,t)\,dr \tag{5.55}$$

Applying the FV method (i.e. integrating equation (5.49) over C_i and dividing by Δr_i) yields the following set of semidiscrete equations:

$$\frac{d}{dt}\bar{\mathbf{f}}_{z,i}(t) = -\frac{1}{\Delta r_i}\left[\dot{\mathbf{r}}(r_{i+1/2}, \mathbf{y}_z)\mathbf{f}_{z,i+1/2}(t) - \dot{\mathbf{r}}(r_{i-1/2}, \mathbf{y}_z)\mathbf{f}_{z,i-1/2}(t) \right] + \bar{\mathbf{s}}_i(\mathbf{f}_z, \mathbf{y}_z) \tag{5.56}$$

Equation (5.56) is an exact relation; however, the numerical solution requires that suitable numerical approximations be made for both the flux and the source terms.

The numerical flux is computed at the cell boundaries $\left[r_{i-1/2}, r_{i+1/2}\right]$ using a Godunov scheme. The number density of particles at the cell boundaries must be reconstructed from the known cell average number densities. The model described in this work employs a fifth order weighted essentially non-oscillatory (WENO) reconstruction scheme, a robust high resolution scheme in which the approximation is reconstructed from multiple stencils based on the local solution structure. For further details on the WENO family of schemes the reader is referred to Liang *et al.*[145] and Rong *et al.*[146] The reconstruction procedure provides left and right hand approximations to the values of $\mathbf{f}_z(r,t)$ at the cell boundaries $\left[r_{i-1/2}, r_{i+1/2}\right]$. The rate coefficient of volumetric growth is computed as follows:

$$K(r_i, \mathbf{y}) = \frac{k_p M w_m \left[M\right]_P}{N_A \rho_P} \tag{5.57}$$

where k_p is the propagation rate coefficient. The full list of kinetic parameters used to model styrene is listed in Table 5.3.

Following Equation (5.50), the growth rate is computed the model-appropriate expressions for $\dot{\mathbf{v}}$, which are listed in Table 5.5. Since $\dot{\mathbf{r}} \geq 0$, the numerical flux is computed using the left hand approximations values at the boundary such that

$$\mathbf{f}_{z,i-1/2}(t) = \mathbf{f}^{-}_{z,i-1/2}(t) \tag{5.58}$$

The source function includes contributions from particle nucleation, particle aggregation and flow exchanged between zones. Integrating $\mathbf{s}(\mathbf{f}_z, r, \mathbf{y}_z)$ over C_i and dividing by Δr_i yields

$$\bar{\mathbf{s}}_{z,i}(\mathbf{f},\mathbf{y}) = \left[\mathbf{R}(r,\mathbf{y}_z)\mathbf{f}_z(r,t)\right]_i + \bar{\mathbf{a}}_i(\mathbf{f}_z,\mathbf{y}_z) + \mathbf{Q}_z(\mathbf{f}_{z,i}(t)) + \mathbf{n}\frac{\delta(v-v_i)}{\Delta r_i}R_{nuc}(\mathbf{y}_z) \qquad (5.59)$$

where the various terms account for the kinetic coupling between particles of different types, particle aggregation, particle inflow and outflow and particle nucleation. The definitions of $\dot{\mathbf{v}}$, $\mathbf{R}$, $\mathbf{a}$ and $\mathbf{n}$ will differ between the 0-1-MP and the PB model. These definitions are summarized in Table 5.5.

The aggregation vector $\mathbf{a}$ is composed of birth terms and death terms. The generic birth and death terms between particles of type *g* and particles of type *h* can be written as follows:

$$B^v = \left(1 - \frac{1}{2}\delta_{gh}\int_{v_{nuc}}^{v}\beta(v-v',v')\,f_{z,g}(v-v')\,f_{z,h}(v')dv'\right) \qquad (5.60)$$

$$D^v = -f_{z,g}(v)\int_{v_{nuc}}^{\infty}\beta(v,v')\,f_z(v')dv' \qquad (5.61)$$

The fixed pivot method of Kumar and Ramkrishna[121] is used to obtain approximations for these terms using volume as the internal coordinate. These terms, $\bar{B}^v_{z,i}$ and $\bar{D}^v_{z,i}$ are then be converted to their radial equivalents using the following relationship: $\bar{B}^v_{z,i}\Delta v_i = \bar{B}^r_{z,i}\Delta r_i$ and $\bar{D}^v_{z,i}\Delta v_i = \bar{D}^r_{z,i}\Delta r_i$

Table 5.5. Definition of the terms appearing in Equation (5.59) for the 0-1-MP and the PB model[128]

0-1-MP Model	$\dot{\mathbf{v}} = K\begin{bmatrix}0 & 1 & 0\end{bmatrix}$ $\mathbf{R} = \begin{bmatrix} -\rho_T & \rho_T & \rho_T + k_{des} \\ \rho_I & -\rho_T - k_{tr}[M]_P & k_p^1[M]_P \\ \rho_E & k_{tr}[M]_P & -\rho_T - k_{des} - k_p^1[M]_P \end{bmatrix}$ $\mathbf{a} = \begin{bmatrix} \frac{1}{2}\int_{v_{nuc}}^{v-v_{nuc}} \beta(v-v',v')\left[f_0(v-v') f_0(v') + f_1(v-v') f_1(v)\right] dv' \\ - f_0(v)\int_{v_{nuc}}^{\infty} \beta(v,v') f(v') dv' \\ \\ \int_{v_{nuc}}^{v-v_{nuc}} \beta(v-v',v') f_0(v-v') f_{1P}(v) dv' \\ - f_{1P}(v)\int_{v_{nuc}}^{\infty} \beta(v,v') f(v') dv' \\ \\ \int_{v_{nuc}}^{v-v_{nuc}} \beta(v-v',v') f_0(v-v') f_{1M}(v) dv' \\ - f_{1M}(v)\int_{v_{nuc}}^{\infty} \beta(v,v') f(v') dv' \\ \\ \end{bmatrix}$ $\mathbf{n} = \begin{bmatrix}0 & 1 & 0\end{bmatrix}$
PB Model	$\dot{\mathbf{v}} = K\overline{n}_{PB}$ $\mathbf{R} = 0$ $\mathbf{a} = \frac{1}{2}\int_{v_{nuc}}^{v-v_{nuc}} \beta(v-v',v') f(v-v') f(v) dv'$ $- f(v)\int_{v_{nuc}}^{\infty} \beta(v,v') f(v') dv'$ $\mathbf{n} = 1$

The kinetic coupling term is approximated using the simplest solution, a second order approximation:

$$\left[\mathbf{R}(r,\mathbf{y}_z)\mathbf{f}_z(r,t)\right]_i = \mathbf{R}(r_i,\mathbf{y}_z)\bar{\mathbf{f}}_{z,i}(t) + O(\Delta r_i^2) \tag{5.62}$$

As noted by Vale[7], this formulation is convenient for integration over time. The cell pivots are the cell centers, v_i, where $v_i = 4/3\pi r_i^3$; the particles in C_i are concentrated at the representative pivot points such that, for particles of type *g:*

$$f_{z,g}(v,t) = \sum_{i=1}^{M} N_{z,i}^{g}\delta(v - v_i) \tag{5.63}$$

$$f_z(v,t) = \sum_{i=1}^{M} N_{z,i}\delta(v - v_i) \tag{5.64}$$

$$\bar{f}_i^{\,v}(t) = \frac{N_i(t)}{\Delta v_i} \tag{5.65}$$

$$N_{z,i}(t) = \sum\nolimits_g N_{z,i}^{g}(t) \tag{5.66}$$

When particles of size v_j and v_k aggregate together, their combined volume, $\hat{v} = v_j + v_k$, may fall between two pivot points. C_i will receive a contribution from every particle born between the range $\left[v_{i-1}, v_{i+1}\right]$. For particles born between v_{i-1} and v_i such that $\left(v_{i-1} \le \hat{v} \le v_i\right)$, the fraction contributed to C_i is

$$a(\hat{v}, v_i) = \frac{\hat{v} - v_{i-1}}{v_i - v_{i-1}} \tag{5.67}$$

For particles born between v_{i-1} and v_i, the fraction contributed to C_i follows a similar expression:

$$b(\hat{v}, v_i) = \frac{v_{i+1} - \hat{v}}{v_{i+1} - v_i} \tag{5.68}$$

These lever-rule expressions ensure that the particle number and mass are preserved. For fixed grids, such as the ones employed in this work, the particle combinations that result in a particle from cells *i* and *j* being born in $\left[v_{i-1}, v_{i+1}\right]$ and the associated $a(\hat{v}, v_i)$ and $b(\hat{v}, v_i)$ values are computed only once: at the start of the simulation.

The discretized birth and death terms are obtained by integrating Equations (5.60) and (5.61) over C_i, dividing by Δr_i and substituting in Equations (5.63) and (5.64):

$$\bar{B}^r_{z,i} = \frac{1}{\Delta r_i}\left(\sum_{\substack{j,k \\ v_{i-1} \le \hat{v} \le v_i}}^{i-1-j} a(\hat{v})\beta(r_j, r_k, \mathbf{y}_z) N^g_{z,j} N^h_{z,k} + \sum_{\substack{j,k \\ v_i \le \hat{v} \le v_{i+1}}}^{i-1-j} b(\hat{v})\beta(r_j, r_k, \mathbf{y}_z) N^g_{z,j} N^h_{z,k} \right), \quad \text{g} \neq \text{h} \tag{5.69}$$

$$\bar{B}^r_{z,i} = \frac{1}{\Delta r_i}\left(\sum_{\substack{j,k \\ v_{i-1} \le \hat{v} \le v_i}}^{i-1-j} (1 - \frac{1}{2}\delta_{j,k}) a(\hat{v})\beta(r_j, r_k, \mathbf{y}_z) N^g_{z,j} N^g_{z,k} + \sum_{\substack{j,k \\ v_i \le \hat{v} \le v_{i+1}}}^{i-1-j} (1 - \frac{1}{2}\delta_{j,k}) b(\hat{v})\beta(r_j, r_k, \mathbf{y}_z) N^g_{z,j} N^g_{z,k} \right) \tag{5.70}$$

$$\bar{D}^r_{z,i} = -\frac{1}{\Delta r_i} N^g_{z,i}(t) \sum_{j=1}^{M} \beta(r_i, r_j, \mathbf{y}_z) N_{z,j}(t) \tag{5.71}$$

The aggregation vector is computed from the discretized birth and death terms, Equations (5.69) - (5.71), with the specific expressions being dependent on whether the terms are being calculated

for the 0-1-MP component or the PB component of the PBM. Note that Equation (5.69) stands in for the terms where different two particles of different classes of particles are aggregating (e.g. N^0 with N^{1P}), while Equation (5.70) stands in for the terms where particles of the same class are aggregating with each other (e.g. N^{1P} with N^{1P}).

The flow exchange term Q is computed using the connectivity and flow exchange information computed with the automatic zoning algorithm.

$$Q(\mathbf{f}_{z,i}(t)) = \sum_{\substack{y \\ y \neq z}}^{\mathbf{z}} \frac{q_{y,z}\overline{\mathbf{f}}_{y,i}(t)}{V_y} - \frac{\overline{\mathbf{f}}_{z,i}}{V_z}(t)\sum_{\substack{y \\ y \neq z}}^{\mathbf{z}} q_{z,y} \qquad y, z \in \mathbf{Z} \tag{5.72}$$

where $q_{y,z}$ is the rate of flow in the direction from zone *y* into zone *z*. Note that material between connected zones is exchanged in both directions, with the net rate of flow exchanged being equal to $\left(q_{y,z} - q_{z,y}\right)$. If zones are unconnected, $q_{y,z} = q_{z,y} = 0$.

Equations (5.56) and the continuous phase mass balance equations $(\mathbf{y}_z)$ are integrated with time using an implicit-explicit (IMEX) solution scheme. The kinetic coupling terms $(\mathbf{Rf})$ are very stiff and are handled implicitly, whereas the coagulation, advection and interzonal flow terms are highly non-linear and are therefore treated explicitly. A variable step-size, first order forward-backward Euler scheme was adopted to compute $\overline{\mathbf{f}}^{n+1}$

$$\overline{\mathbf{f}}^{\mathbf{n+1}} = \overline{\mathbf{f}}^{\mathbf{n}} + \Delta t\left(\mathbf{L}_{\mathbf{E}}^{\mathbf{n}} + \mathbf{L}_{\mathbf{I}}^{\mathbf{n+1}}\right) \tag{5.73}$$

Both the pseudo-bulk and zero-one kinetic models contain explicit components that are gathered into a vector:

$$\mathbf{e}_i = \chi(r_i)\mathbf{e}_i^{0-1} + \left(1-\chi\left(r_i\right)\right)\mathbf{m}\mathbf{e}_i^{PB} \tag{5.74}$$

The inclusion of $\mathbf{m}$ changes the dimensionality of $\mathbf{e}_i^{PB}$ to match that of $\mathbf{e}_i^{0-1}$, such that the only term that differs between $\mathbf{e}_i^{PB}$ to $\mathbf{e}_i^{0-1}$ is the advective term, such that the explicit vector can be computed as follows:

$$\mathbf{e}_i = \mathbf{n}\frac{\delta_{i,1}}{\Delta r}R_{nuc} + \bar{\mathbf{a}}_i + Q(\mathbf{f}_{z,i}(t)) - \frac{\chi\left(r_i\right)}{\Delta r_i}\left(\mathbf{h}_{i+1/2} - \mathbf{h}_{i-1/2}\right)^{0-1} + \frac{1-\chi\left(r_i\right)}{\Delta r_i}\left(\mathbf{h}_{i+1/2} - \mathbf{h}_{i-1/2}\right)^{PB} \tag{5.75}$$

The time discretization then reads as:

$$\bar{\mathbf{f}}_{i,z}{}^{n+1} = \bar{\mathbf{f}}_{i,z}{}^{n} + \Delta t\left(\mathbf{e}_{i,z}^{n} + \mathbf{R}(r_i, \mathbf{y}_z^{n+1})\bar{\mathbf{f}}_{i,z}{}^{n+1}\right) \tag{5.76}$$

The implicit component is linear in $\mathbf{f}$, so Equation (5.76) may be re-arranged to yield a relationship explicit in $\bar{\mathbf{f}}_{i,z}{}^{n+1}$:

$$\bar{\mathbf{f}}_{i,z}{}^{n+1} = \left[\mathbf{I} - \Delta t\mathbf{R}(r_i, \mathbf{y}_z^{n+1})\right]^{-1}\left(\bar{\mathbf{f}}_{i,z}{}^{n} + \Delta t\mathbf{e}_{i,z}^{n}\right) \tag{5.77}$$

The inverse matrices appearing in (5.77) are computed analytically. Since **R** is initially known at t^n and not at t^{n+1}, an iterative procedure is used, whereby $\mathbf{R}^n$**,** calculated at t^n with $\mathbf{y}^n$ is used to calculate an approximation of $\bar{\mathbf{f}}^{n+1}$. This approximation is used to compute an approximation of $\mathbf{y}^{n+1}$ which is then used to compute another approximation of $\mathbf{R}^{n+1}$. The cycle is repeated until a specified convergence is achieved. Typically, the number of iterations required is small and the computational resources required are insignificant with respect to that of evaluating $\mathbf{e}_{i,z}^{n}$.

5.3.1.6 Coagulation Kernel

Modeling the rate of particle coagulation in emulsion polymerization systems is a challenge due to the complexity of the phenomena involved and the lack of suitable physical models. The widely-used DLVO framework does not always provide good quantitative predictions when it is used to model the aggregation rate of colloids. Regardless, it has been shown that many experimental results cannot be predicted in a physically-coherent manner without the inclusion of a coagulation kernel.[7] In many cases it is possible to fit certain model parameters (such as the Hamaker constant) to obtain coagulation rate coefficients that correctly predict experimental results, even in conditions where DLVO theory may not be applicable. For further information on the use of DLVO-theory based coagulation kernels, refer to Vale & McKenna.[8]

The coagulation kernel used in this study is the same coagulation kernel that was outlined in detail in the previous chapter in Section 4.2.3. The coagulation rate coefficient between two particles of size *i* and *j*, β_{ij} is computed from the Fuchs-modified Muller-Smoluchowski[94] equation:

$$\beta_{ij} = \frac{2k_B T}{3\eta_s W_{ij}}\left(2 + \frac{r_i}{r_j} + \frac{r_j}{r_i}\right) \tag{5.78}$$

where η_s is the viscosity of the dispersion medium and k_B is the Boltzmann constant. The Fuchs' stability ratio (W_{ij}) , which is the inverse of the collision efficiency, accounts for the presence of colloidal interactions between the particles. The normalized stability ratio is computed with the expression:[123]

$$W_{ij} = \frac{\int_0^{\infty} \frac{\exp\left(\frac{V_{\text{int}}(s)}{k_B T}\right)}{s^2} ds}{\int_0^{\infty} \frac{\exp\left(\frac{V_A(s)}{k_B T}\right)}{s^2} ds} \tag{5.79}$$

As defined in Equation (5.79), W_{ij} is equal to unity in the complete absence of repulsive potential, which is helpful when model predictions are compared against experimental data. To simplify matters, the hydrodynamic interaction effects not included in this coagulation model, although they could be incorporated in the stability model (see Section 3.2 in Chapter 3 for details). The expressions used to compute the ionic charge distribution surrounding the latex particles include additional terms to account for concentration effects at higher solid contents. The modified expression for the inverse Debye length is:

$$\kappa = \sqrt{\left(\frac{4\pi e^2}{\varepsilon k_B T}\right)\left(\frac{2N_A I + \frac{A_{tot}\sigma}{e}}{1-\phi}\right)} \tag{5.80}$$

Based on the experimental data obtained by Kemmere *et al.* for high solid content styrene emulsion polymerization systems,[41] the contributions of shear-induced (orthokinetic) coagulation were neglected in favour of a strictly Brownian (perikinetic) aggregation kernel. Orthokinetic coagulation is thought to be prevalent in systems where very larger particles (greater than ~ 1 μm in diameter) are exposed to regions of high shear rates ($\gamma > 100$ s^{-1}). Melis *et al.*[44] numerically solved the generalized Fuchs-Smoluchowski diffusion-convection equation for a pair of spherical particles located in an extensional flow field and found that an adjusted particle Peclet number could be used to determine whether orthokinetic coagulation is likely to be prevalent under a

given set of conditions. In a subsequent modeling effort (the EP of vinyl acetate), Melis *et al.* note that the average particle Peclet number computed for a reaction at the laboratory scale is much lower than the threshold beyond which orthokinetic coagulation must be taken into account.[42] As was concluded in Chapter 3, it would be incorrect to assume that the orthokinetic mechanism can be neglected under most conditions. There are a number of semi-empirical combined coagulation kernels available in the literature [43, 45, 46] and Lattuada and Morbidelli recently developed a kernel that can be applied in both shear-dominated and Brownian-dominated conditions.[47] Unfortunately the Lattuada and Morbidelli is much more computationally-intensive due to iterative procedure required to compute the parameters that account for hydrodynamic interactions between particles.

5.3.1.7 Latex Rheology

The non-Newtonian rheology was modeled with the Carreau-Yasuda model, which has been shown to correctly capture the shearing behavior of concentrated latexes;[5]

$$\eta(\dot{\gamma}) = \eta_{\infty} + \frac{\eta_0(t) - \eta_{\infty}(t)}{\left[1 + (\dot{\gamma}\tau)^a\right]^{(1-m)/a}} \qquad \left(\text{for } \dot{\gamma} < \dot{\gamma}_{th}\right) \tag{5.81}$$

where η_0 is the zero-shear viscosity, η_{∞} is the infinite-shear viscosity, τ is the characteristic time for the onset of shear-thinning and γ_{th} is the shear rate beyond which the latex will begin to shear thicken. The adjustable parameters a and m were set to 1.0 and 0.65, respectively, which has been shown to provide the best fit to their experimental data.[5] The four model parameters $\left(\eta_0, \eta_{\infty}, \tau, 1/\gamma_{th}\right)$ are dependent on the latex solid content (ϕ) and the (PSD-dependent)

effective maximum packing fraction ($\phi_{m,}$) according to general form of the Krieger-Dougherty equation.

$$\xi(t) = \xi_s \left(1 - \frac{\phi(t)}{\phi_{m,\xi}(t)} \right)^{-[\eta]_\xi \phi_{m,\xi}} \qquad \xi = \eta_0, \eta_\infty, \tau, \left(1/\dot{\gamma}_{th}\right) \tag{5.82}$$

The intrinsic viscosity ($[\eta]$) and hard sphere maximum packing fraction parameters ($\phi_{,}$) needed to utilize Equation (5.82) can be found in Table 3.1 in Chapter 3.

The maximum packing fraction of a polymer latex made up of *m* discrete particle sizes was calculated using the approach proposed by Pishvaei *et al.*[65] The formulae are not listed here as they are the exact same as those appearing in Chapter 4; refer to Equations (4.29) to (4.34) in Section 4.2.5. For a more detailed background on modeling the packing characteristics of latexes with bimodal and multimodal PSDs, refer to Section 2.2.4 in Chapter 2.

5.3.2 CFD Model

The mixing time in reactors can be measured both experimentally and numerically using transient concentration (homogenization) curves. The homogenization curves are computed via CFD simulation in two steps. First, the fully-developed flow field is computed assuming that the latex can be simulated as a single-phase fluid. After the fully-developed flow field has been computed, the transient dispersion of a buoyantly-neutral tracer species is superimposed on the flow field to determine the homogenization curves.

The computational mesh was designed and generated in Gambit 2.4 (Ansys) using hexahedral cells, as the use of hexahedral cells in place of tetrahedral cells will reduce the number of cells required to obtain a grid-independent flow field and therefore reduce the resulting computation time.[13] The entire three-dimensional structure of the tank was simulated in order to allow for the asymmetric placement of tracer when computing homogenization times. The majority of the simulation data was obtained on a 3D grid of a half-full tank, corresponding to a liquid level-to-tank diameter ratio of 0.75, while a small number of simulations were run on a grid representing the liquid level at the end of the process (a height-to-diameter ratio of 1.5). The number of hexahedral cells required to achieve grid-independence (for the overall flow patterns) varied between 3.10×10^5 and 4.41×10^5 as the tank aspect ratio varied between 0.75 and 1.4, respectively. A two-dimensional slice of the computational grid is shown in Figure 5.4. In turbulent conditions, the flow field is expected to be unsteady due to baffle interactions. Given the large size of the grid and the desire to develop a framework that could be run with modest computing resources, a steady-state simulation approach was employed to compute the flow fields. Montante *et al.* compared simulated 95% mixing times obtained using a steady-state flow field with values obtained experimentally and the results were within 5% under most conditions.[106] The boundary conditions are identical to those reported in Chapter 4: (i) constant angular velocity along the impeller surface; (ii) no slip condition at the baffles and along the vessel wall; (iii) no normal velocity at the fluid surface, which is assumed to be flat. The CFD simulation was implemented in Fluent 6.3 using the steady-state Multiple Reference Frame (MRF)[105] method to address the rotation of the impeller. Under these conditions, the governing equations for fluid flow for the steadily rotating frame as expressed as:

$$\frac{\partial \mathbf{v}}{\partial t} + \nabla \cdot \mathbf{v}_r \mathbf{v} + (\boldsymbol{\Omega} \times \mathbf{v}) = -\frac{1}{\rho} \nabla p + \nabla \bar{\bar{\tau}} + \frac{1}{\rho} \left[\frac{\partial \left(-\rho \overline{u'^2} \right)}{\partial x} + \frac{\partial \left(-\rho \overline{u'v'} \right)}{\partial y} + \frac{\partial \left(-\rho \overline{u'w'} \right)}{\partial z} \right] \quad (5.83)$$

$$\nabla \cdot \mathbf{v}_r = 0 \quad (5.84)$$

where $\boldsymbol{\Omega}$, the angular velocity, is the product of the impeller rotational speed and a unit vector in the direction of the axis of rotation ($\boldsymbol{\Omega} = N_I \hat{a}$). The MRF momentum balance includes one additional term $(\boldsymbol{\Omega} \times \mathbf{v})$, which accounts for the Coriolis and centripetal accelerations. For further details on the MRF formulation, refer to the Fluent User's Manual.[105] The rightmost terms $\left(-\rho \overline{u_i' u_j'} \right)$ are the Reynolds stresses that must be modeled in order to close Equation (5.84), which is handled using the standard *k*-ε model. Fluid viscosity was modeled using the Equation (5.81), although, strictly speaking, the *k*-ε turbulence model was not developed for use with non-Newtonian fluids. During the mixing-critical stage, the solids content of the latex is less than 40 vol.-%, so the latex will behave as a Newtonian fluid regardless.

Mixing performance was measured by running transient species-tracking simulations, during which the flow field is fixed. The concentration-time data from the transient species-tracking simulations is then used to compute 95% mixing (blend) times for varying reactor scales and scale-up objectives. A sphere of tracer, equal to 1% of the total liquid volume, was added close to the liquid surface and the dynamic distribution of the tracer inside the reactor was then calculated by solving a Reynolds-averaged time-dependent scalar (Φ) transport equation, assuming a constant fluid density:

$$\frac{\partial \Phi}{\partial t} + \nabla \cdot \mathbf{v}\Phi = \frac{1}{\rho} \nabla \cdot \left(D_m \nabla \Phi - \frac{\mu_t}{\sigma_t} \nabla \Phi \right) \tag{5.85}$$

where μ_t is the turbulent viscosity and σ_t is the turbulence Schmidt number, which was set to 0.1, which was the value recommended by Montante *et al.*[106] The diffusivity of the tracer was set to 6×10^{-10} m^2/s, which is the diffusivity of SDS in water at 70 °C, as estimated with using the Wilke-Chang equation.[4] Setting the tracer diffusivity to zero did not alter blend times considerably, confirming the expectation that the contribution of molecular diffusivity to tracer dispersion is negligible. The boundary condition for the species balance considers zero species flux along the tank walls, the impeller surface and the liquid surface. The initial condition was a species mass fraction equal to 1.0 in the feed zone and 0.0 elsewhere. A visual representation of the initial conditions used in all of the transient tracer species balance simulations is shown in Figure 5.4. The time step adopted for the transient tracer dispersion simulations was 0.125 s, as suggested by the simulation data compiled by Montante *et al.*[106]

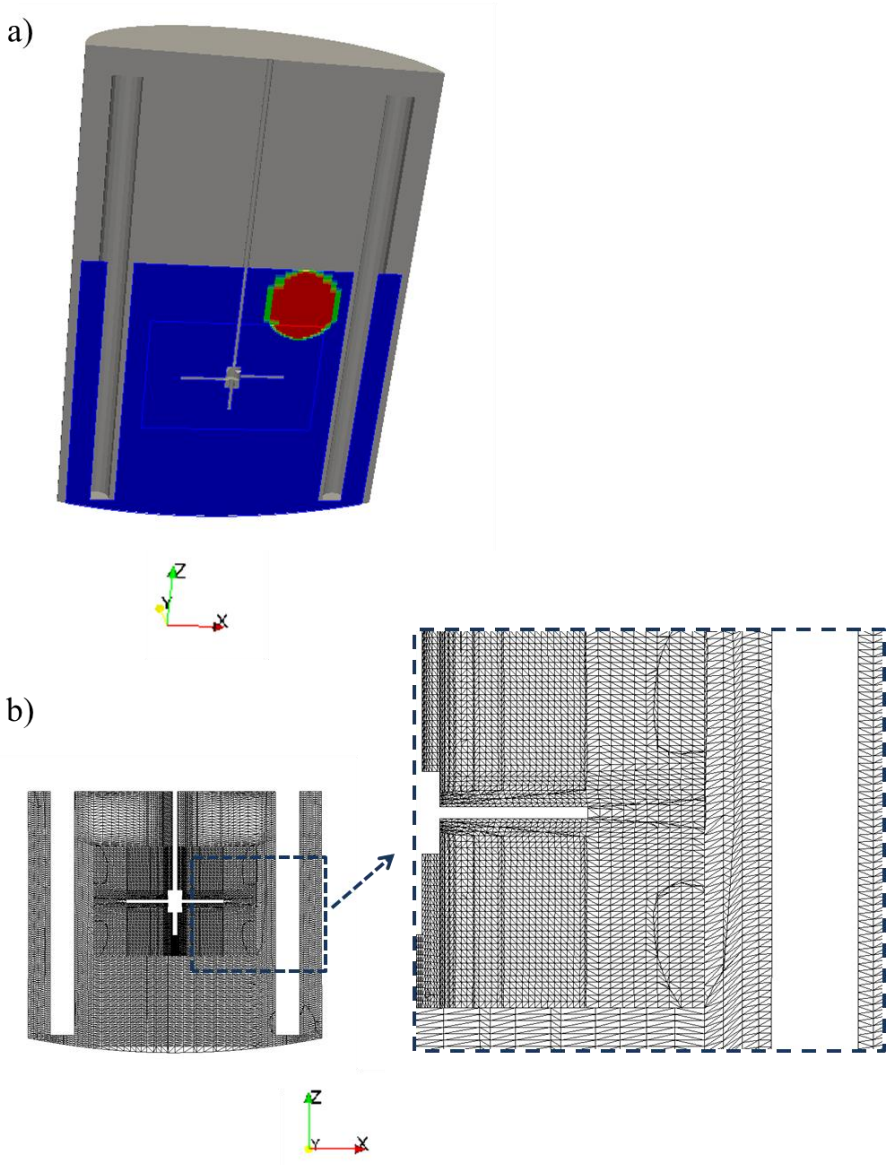

Figure 5.4. Computational grid: (a) Three-dimensional structure of the vessel showing the main features and the liquid level; this corresponds to the liquid level during the secondary particle nucleation phase of the emulsion polymerization process (under the simulation conditions specified). The reactant feed zone, which is also the tracer injection location in the transient species tracking simulations, is highlighted in red. (b) Two-dimensional slice of the computational mesh showing the hexahedral elements and the grid refinement near in the impeller where velocity gradients are expected to be highest.

5.3.3 Automatic Zoning Algorithm

The automatic zoning algorithm employed in our previous work was capable of dividing the vessel into a series of vertical slices based on the axial flow profile. The algorithm was applied under the premise that poor flow in the vertical direction was responsible for inhomogeneous mixing within the vessel.[88] The built-in User Defined Functions (UDFs) capability provided with Fluent facilitated the incorporation of a more advanced automatic zoning algorithm, allowing one to create the coarse grid zoning based on the spatial distribution of a metric related to mixing performance rather than the flow profile directly. The automatic zoning algorithm employed in this work is simply an adaptation of the layer-by-layer automatic zoning algorithm developed by Seppälä.[86] The layer-by-layer algorithm itself is an extension of the delta algorithm originally proposed by Bezzo *et al.*[80] For a generalized presentation of the layer-by-layer zoning algorithm, the reader is best-served by referring to the original work of Seppälä.[86] Details regarding the specific implementation of the layer-by-layer algorithm within our work are presented below. The tracer-time front $t_{front}(c)$ was the cell property used to generate the PBM grid. Unlike the tracer mass fraction, $t_{front}(c)$ is time-independent; the tracer injection simulation must be near-completion (homogenization) in order to generate the $t_{front}(c)$ distribution. While there are other flow properties that may be associated with the mixing performance of a given vessel (e.g. the velocity field), the $t_{front}(c)$ distribution retains information regarding the tracer (reactant) feed location. As illustrated in Figure 5.5, the automatic zoning algorithm consists of four steps: (1) initialization, (2) preliminary zone generation, (3) merging of tiny zones, and (4) aggregation of data for output.

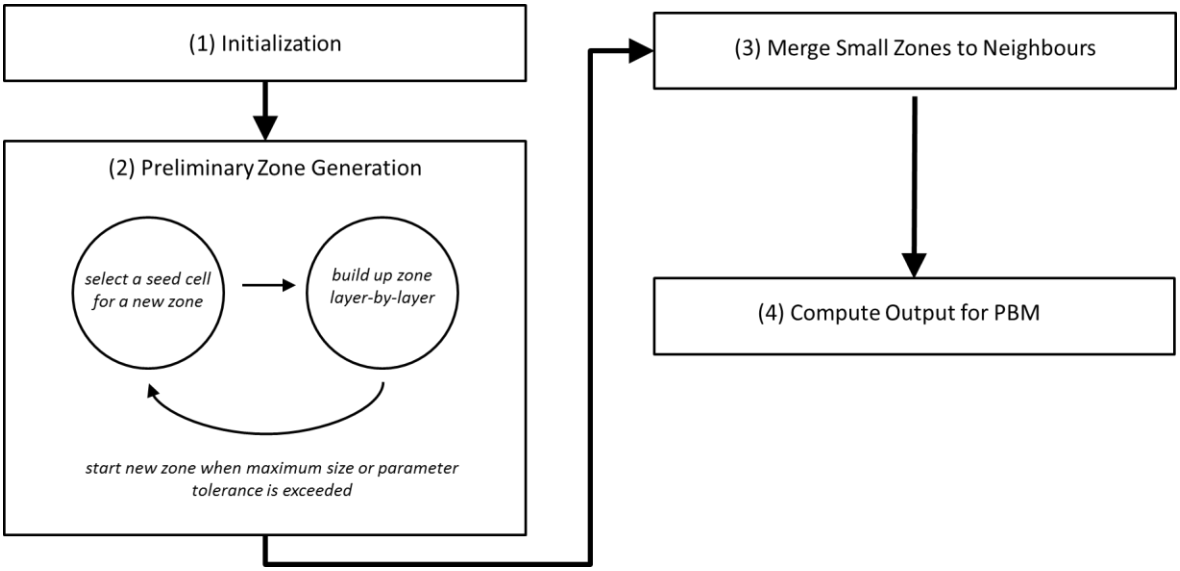

Figure 5.5. Schematic representation of the automatic zoning algorithm used to generate the zone grid.

The initialization step consists of marking all of the CFD cells as unassigned and computing the minimum $C_{\min}$ and maximum number of cells $C_{\max}$ allowed within a single zone. In order to ensure the number of zones created remains independent of the number of cells that will be zoned, C_{mesh}, the size range is computed from a user-specified zone range, where $N_{z,\min}$ and $N_{z,\max}$ are the minimum and maximum number of zones that may be created.

$$C_{\min} = \frac{C_{mesh}}{N_{z,\max}} \qquad C_{\max} = \frac{C_{mesh}}{N_{z,\min}}$$

Following initialization, the first seed cell is chosen. The algorithm is designed to ensure that the first zone is the feed region. Given that

$$t_{front}(c) = 0.0 \quad \forall c \in \text{ feed region}$$

the seed cell chosen for the first zone can be guaranteed to be a part of the region where the tracer was injected (i.e. the feed region) if the criteria for choosing a seed cell is simply the cell that has

minimal value of $t_{front}(c)$. Once a seed cell is chosen, the tolerance $\Delta\varsigma(c_{seed})$ for the zone is computed. The following function will provide reasonable $\Delta\varsigma(c_{seed})$ values under most circumstances:

$$\Delta\varsigma(c_{seed}) = \max\left\{\Delta\varsigma_{\min}, a_{\varsigma}\left(t_{front}(c_{seed}) - \varsigma_0\right)\right\} \tag{5.86}$$

Setting $\varsigma_0 = \overline{t}_{front}$ will ensure that $\Delta\varsigma(c_{seed})$ will approach zero as $t_{front}(c_{seed})$ approaches $\overline{t}_{front}$. A minimum tolerance $\Delta\varsigma_{\min}$ is specified to ensure that $\Delta\varsigma$ does not cross a minimum threshold. If the frequency distribution of $t_{front}(c)$ is not a normal about $\overline{t}_{front}$, ς_0 may be set to another value, such as the median or mode of the frequency distribution. The second adjustable parameter a_{ς} can be used to adjust the order-of-magnitude of the computed tolerance.

Once the seed cell has been selected and the zone tolerance parameter has been computed, the zone is grown through the addition of eligible neighbouring cells. An eligible neighbouring cell is defined as a cell that shares at least one face with a cell that belongs to the zone that is being created. In the layer-by-layer algorithm Θ_{LBL}, all unattached neighbouring cells are added to the zone as a layer as shown schematically in Figure 5.6. After the addition of each layer, the range of t_{front}, $\delta\varsigma$, is computed:

$$\delta\varsigma = t_{front,\max}\Big|_{c\in z_i} - t_{front,\min}\Big|_{c\in z_i} \tag{5.87}$$

If $\delta\varsigma \le \Delta\varsigma$, the zone is said to homogeneous in t_{front} within the computed tolerance and another layer is added. If the tolerance is exceeded, the construction of the zone is completed and a new zone is started. There are a number of additional rules specified to control zone construction. A

new zone is automatically started if all of the neighbouring cells have already been assigned to other zones or if the addition of another layer would cause the size of z_i (i.e. the specified in number of cells) to exceed $C_{\max}$. In order to ensure that all zones will attain a minimum size (provided eligible neighbour cells are still available for addition), a lower size tolerance value is specified. The lower size tolerance value is set to $C_{\min}/4$ and it overrides $\Delta\varsigma(c_{seed})$.

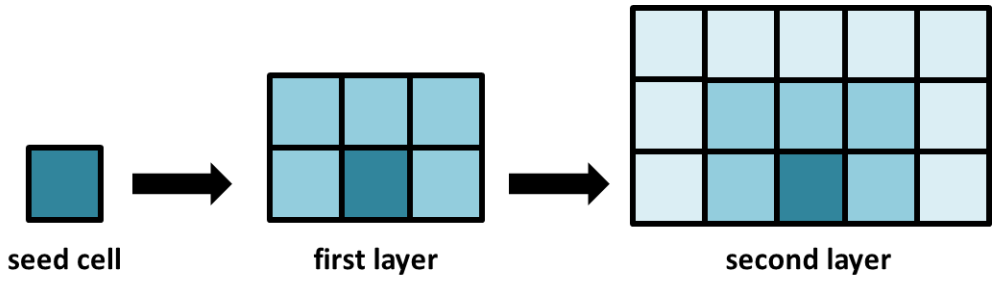

Figure 5.6. Illustration of the layer-by-layer algorithm for automatic zone construction.

The use of a relative tolerance will reduce the number of zones comprising only a few cells, but tiny zones will still be generated when small areas of unassigned cells are caught between existing zones and near vessel boundaries.[80] The presence of many tiny zones will increase the computational resources required to solve the PBM without significant improvement the predictive capabilities of the framework. The objective of the merge step is to merge any zones that are smaller than $C_{\min}$ with neighbouring zones. The merge operation will cycle through all of the neighbouring zones and attach the undersized zone to the neighbouring zone that minimizes a modified property variability δ_{merge}:

$$\delta_{merge} = \frac{\delta\varsigma}{\Delta\varsigma} + \frac{C_{z,merge}}{C_{\max}} \tag{5.88}$$

To account for the fact that best potential merger (i.e. the merge operation that minimizes the aggregate variability $\delta\varsigma$) may result in a zone that is larger than $C_{\max}$, the merge is penalized rather than restricted outright. Some merge operations will result in the creation zones that are still undersized; these zones will be continually merged with neighbouring zones until all zones are larger than the computed minimum size, $C_{\min}$.

Once the merge operation is complete, the output files responsible for passing data on to the PBM are created. The volume and connectivity of each zone is recorded, along with the interzonal flow rates and mean shear rate in each zone. The volumetric rate of flow exchanged between interconnected zones is computed by looping through all cell faces in the domain. Faces that do not fall on an interface between cells do not contribute to the interzonal flow rate array. If a cell does fall on an interface between two zones, the direction of the flow will determine which array entry the flow will contribute to. For example, the interface $I_{i,j}$ is comprised of a number of cell faces. The flow across some faces will be from zone i to zone j, while the flow across other faces will be from zone j to zone i. Thus the flow rate across the interface is split into two components: $q_{i,j}$ and $q_{j,i}$, where $q_{i,j}$ is the sum of flow from all the faces on the interface $I_{i,j}$ for which the flow direction is from zone i to zone j; if the flow direction is instead from zone j to zone i, the flow is added to $q_{j,i}$. Note that for zone i, the total rate of flow exiting the zone is $\sum_{j,j\neq i} q_{i,j}$, while the total rate of flow entering the zone is $\sum_{j,j\neq i} q_{j,i}$. Given that the flow field is computed at steady-state,

$$\sum_{j,j\neq i} q_{i,j} - \sum_{j,j\neq i} q_{j,i} \approx 0$$

If the net rate of flow is not zero (within a small tolerance), the PBM may suffer from convergence issues, so the algorithm will check the net discrepancy between total flow entering all zones and total flow exiting all zones.

The shear rate magnitude used to compute fluid viscosity in the PBM is a scalar quantity. The average shear rate for each zone $\left(\dot{\gamma}_c\right)$ is computed as a volume average as follows:

$$\dot{\gamma}_z = \frac{\sum_{c \in z} \dot{\gamma}_c v_c}{V_z} \tag{5.89}$$

where v_c is the volume of an individual CFD mesh cell.

5.4 Results & Discussion

All simulations were performed on a desktop computer equipped with an Intel Core 2 Quad 6600 @ 2.40 GHz and 6.0 GB of RAM. Approximate computation times for each framework component were as follows:

- CFD flow field simulation ~ 1.5 hours
- CFD tracer dispersion simulation ~ 0.25 to 2.5 hours (dependent on vessel scale)
- automatic zoning algorithm ~ 3 minutes
- multi-zonal PBM ~ 2.5 to 10 hours for 100 zones (dependent on vessel scale)

Total simulation time per case ranged between 4.5 hours and 15 hours, with the larger reactor scales requiring more computation time per case. The simulation time required for tracer dispersal simulations was proportional to the number of time steps required to completely disperse the tracer. PBM simulation time was dependent on the occurrence of particle nucleation and particle

coagulation, as the time step size was reduced while these events are occurring at high rates during the reaction.

5.4.1 Blending Simulations & Zone Generation

In generating the PBM mesh, the objective was to divide the PBM into a series of interconnected zones. While the contents of each individual zone are assumed to be homogeneous, the arrangement of zones is designed to capture the effect of vessel inhomogeneity on the evolution of PSD within the PBM. The feed zone is the only zone on the PBM grid that is both fixed in size and shape; this step was taken in order to ensure that the concentration of species entering the first zone is independent of vessel scale. This approximates an assumption that the diameter of the feed dip pipe would increase in proportion to the tank diameter, but it would be possible to examine other scenarios.

The PBM grid is generated using a transient inert tracer species balance simulation. As the tracer is dispersed through the vessel, its local mass fraction will continue to evolve until it reaches a state of uniform concentration throughout the entire vessel. The mixing time can be expressed quantitatively using a number of metrics. In this work, the blend time is defined as the time taken to reduce the maximum variation in tracer concentration by 95% from its initial value. The variation in tracer concentration can be expressed in a dimensionless, bounded form as follows:

$$U(t) = \frac{\Delta_{\max}(t=0) - \Delta_{\max}(t)}{\Delta_{\max}(t=0)} \tag{5.90}$$

where $\Delta_{\max}(t)$ is computed from the distribution of tracer mass fraction (C_{tr}) throughout the vessel.

$$\Delta_{\max}(t) = \max\left(C_{tr,\max} - \bar{C}_{tr}, \bar{C}_{tr} - C_{tr,\min}\right) \tag{5.91}$$

By definition, $U\left(t=0\right)=0.0$ and $U(t)=1.0$ when the system is fully-homogeneous. The blend time $\left(t_{blend}\right)$ is defined as the time required for $U(t)$ to reach 0.95. The mixing curves for the set of simulations where the reactor was scaled-up maintaining constant P/V are plotted in Figure 5.7. The simulation blend times can be read off of Figure 5.7 by observing where the mixing curves intersect the upper horizontal axis (the ordinate). The blend time data for all simulations is summarized graphically in Figure 5.8. The blending time data presented in Figure 5.7 suggests that if the vessel is scaled-up maintaining a constant P/V ratio, blend time increases from approximately 6.5 seconds at the 1-L scale, to 11 seconds at the 100-L scale and, finally, to 29.5 seconds at the 10-m^3 scale. It is noted that blend time is expected to increase by roughly a factor of 2.7 for an increase in vessel volume by a factor of 100.[87] The increase in blend time from the 100 L scale to the 10-m^3 scale closely matches expectation, while the increase in blend time between the 1-L and 100-L vessel scales is less than expected. This discrepancy may be partially explained by the fact that the 1 L vessel is operating at a Reynolds number close to the threshold of 10^4 that is typically used to characterize the turbulent regime $(N_{\mathrm{Re}} \approx 2.1\times10^4)$ and thus is not operating in the fully-developed region. Examination of Figure 5.8 reveals that when the 1 L vessel is scaled up to 100 L with the objective of maintaining a constant blend time, the computed blend time actually drops from 6.5 seconds to 4.2 seconds. The scale-up heuristics were developed under the assumption that flow at both scales is fully-turbulent, so the drop in blend time indicates that the 1 L vessel is operating in the transitional-regime. However the discrepancy between blend times when the vessel is scaled up based on constant T_Q/V is also

lower than expected (3.7:1 vs. 4.6:1 expected in accordance with Equation (5.2)), which serves as a reminder that, when possible, it is important to validate the heuristic guidelines and CFD simulation data experimentally during the scale-up process.

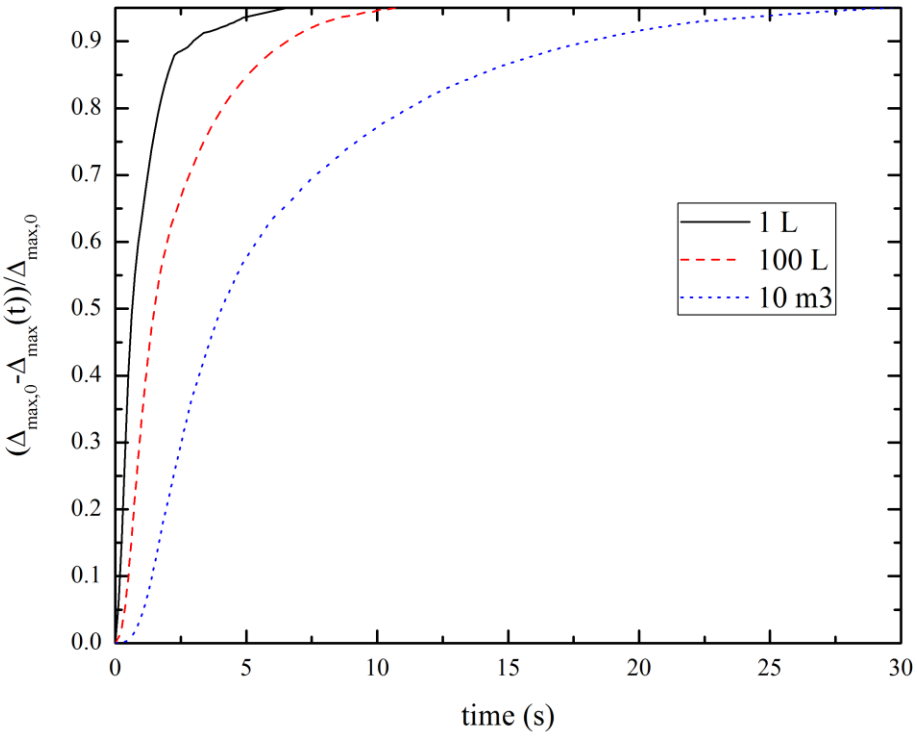

Figure 5.7. Simulation results showing the effect vessel scale-up on the time evolution of the normalized tracer concentration variability, as defined by Equation (5.91). Reactor volume is scaled from 1 L to 10 m^3, adjusting the impeller rotational speed to maintain a constant volumetric power input (P/V ratio). Feed was injected near the liquid surface level.

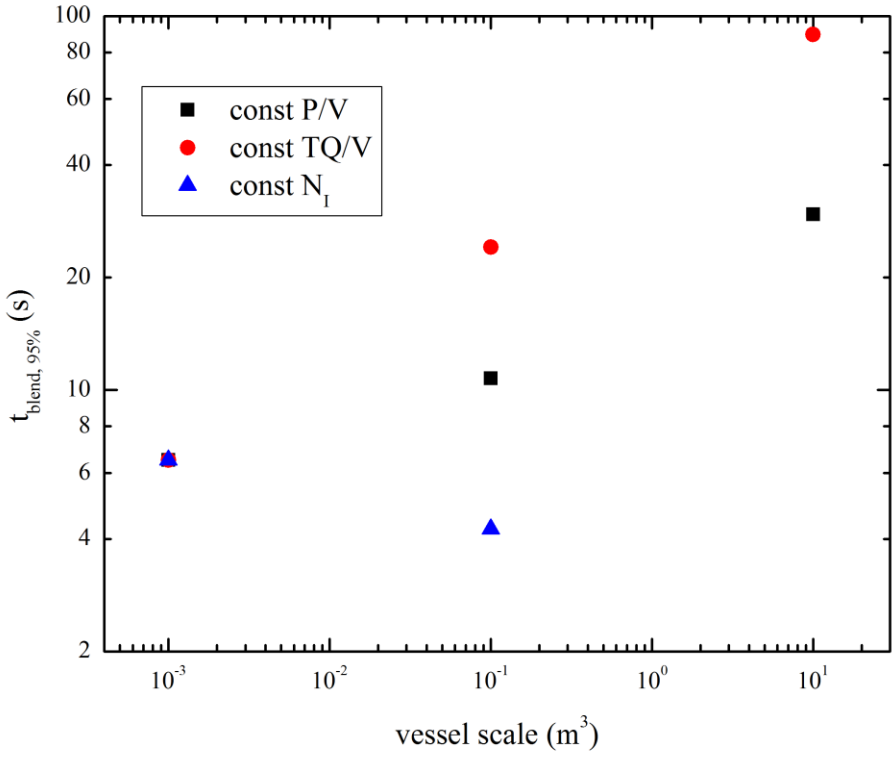

Figure 5.8. Variation in the computed 95% blend time with (i) vessel scale and (ii) scale-up approach. $\eta \approx 5.9 \times 10^4$ kg/m/s. Note that geometric similarity is always maintained. Maintaining a constant t_{blend} at 10 m^3 would be physically unrealizable due to motor requirements, so this simulation was not run.

Although the blend time data provides useful information with regards to changes in mixing performance with reactor scale-up, the tracer mass fraction distribution cannot be used to divide the vessel into a series of zones because the tracer distribution data is time-dependent and the final steady-state is uniform. Fortunately the transient information provided by the tracer distribution simulations can be captured by setting up an automatic routine to record the time at which every cell within the CFD mesh is visited by the tracer. This time, henceforth referred to as the tracer front time (t_{front}), will be lower for cells that are visited by the tracer early in the

simulation and highest for the cells that are visited last. The cell is assigned a t_{front} value corresponding to the earliest time at which the tracer mass fraction inside the cell equals or exceeds a minimum threshold. The minimum threshold is chosen such that every cell will have been assigned a t_{front} value by the time the simulation reaches a steady state. The largest value at which this is possible equals $\bar{C}_{tr}$, the volume-averaged tracer mass fraction. For this reason, the maximum value of t_{front} in the domain is the time required to completely distribute the tracer throughout the vessel or the 100% blend time.

At the conditions specified, all of the CFD mesh cells received tracer, although there were a few (< 10) cells where t_{front} was around five times the 95% blend time. The distribution of tracer to a few segregated cells within the vessel domain often requires a large number of additional time steps, so the tracer mass fraction threshold can be reduced to reduce computation time. In this work, the threshold was set equal to $\bar{C}_{tr}/10$. The reduction in the tracer mass fraction threshold is reasonable as it is the relative shape of the t_{front} distribution (i.e. the histogram), not the absolute values within the t_{front} distribution that determine the corresponding zone network. Note that if fluid viscosity is very high and mixing is poor, a large proportion of the domain may be completely-segregated. These segregated cells should be aggregated into their own separate zones in order to capture the impact of the segregation within the framework.

Figure 5.9 shows the evolution of both the flow field and the tracer front distribution with scale (maintaining a constant P/V ratio) along a vertical slice at the center of the vessel. The general

shape of the flow pattern observed across all three scales is very similar, although the volume-averaged velocity magnitude increases as the reactor is scaled-up. The similarity of the flow patterns is expected as the smallest vessel is characterized by a Reynolds numbers of 1×10^4 and flow is said to be fully-turbulent for $Re > 1 \times 10^4$. The increase in blend time with reactor scale is apparent when looking at the tracer front distributions; the 10 m^3 tank features a sizeable area near the bottom of the tank where mixing is slow compared to small scale vessels. The asymmetry in the tracer front-time distribution in the upper region of the tank arises from the off-center feed location.

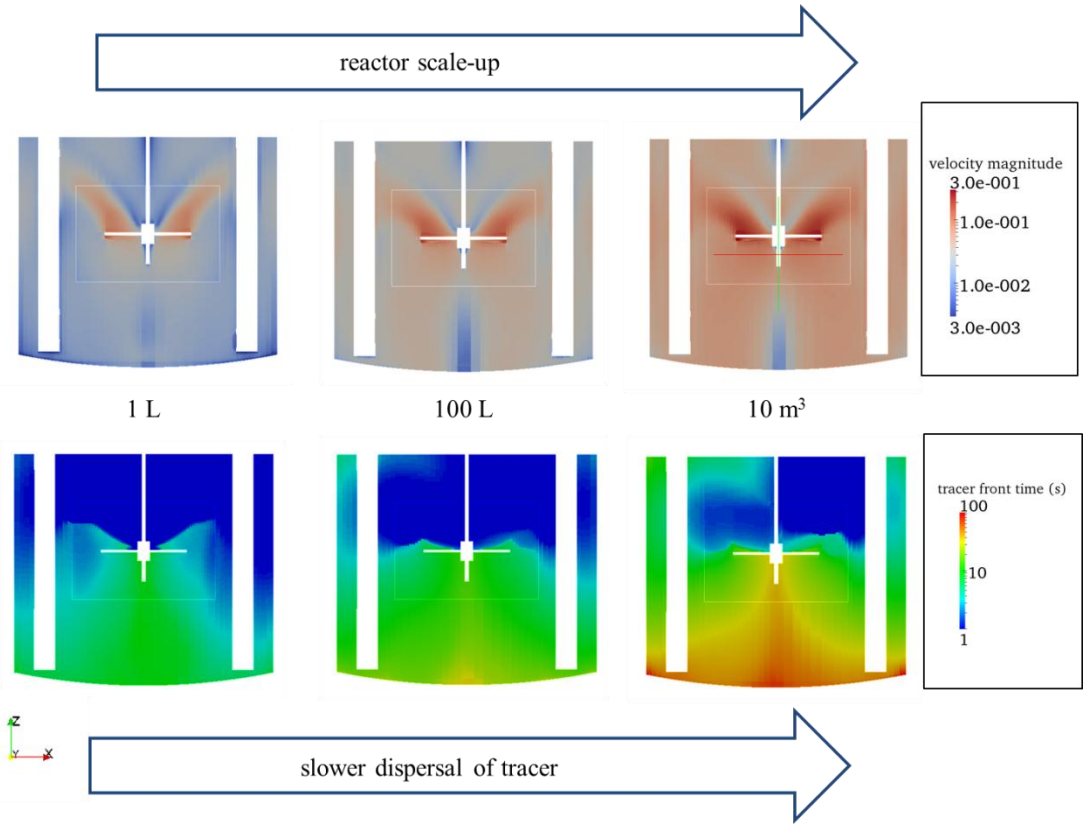

Figure 5.9. Vertical cross-sectional slices showing the change in flow intensity (top) and tracer dispersion performance (bottom) as the tank geometry is scaled from 1 L to 10 m^3. The impeller rotational speed is adjusted with the objective of maintaining a constant volumetric holding power input (P/V ratio). N_1 is set to 100 RPM at the 1-L scale, 35.9 RPM at the 100-L scale and 12.9 RPM at the 10-m^3 scale. Flow data is from CFD simulations based on the conditions at the start of the reaction ($\eta \approx 5.9 \times 10^4$ kg/m/s).

As the blend time data presented in Figure 5.8 suggests, the choice of scale-up approach will have a large impact on mixing performance, as can be seen more clearly through closer examination of Figure 5.10, a compilation showing the cross sectional contours of the tracer front distribution at the 100 L scale. The contour plots provide additional details regarding the segregation within the vessel that are not apparent from the 95% blend time values alone. Independent of scale-up approach, the most segregated regions of the vessel are at the bottom of the tank, both directly underneath the impeller and behind the baffles. When the reactor is scaled-up with the objective

of maintaining a constant mixing time (t_{blend}), which is not at all realistic, the tracer reaches the most segregated portions of the vessel within ten seconds. However, when the vessel is scaled-up maintaining a constant delivered torque per unit volume (T_Q/V), there are regions where the tracer will take nearly 100 seconds to visit. The network of zones grid used for the PBM should be of sufficient resolution (i.e. a sufficient number of zones) in order to capture the contribution of segregated regions to the overall evolution of the process kinetics.

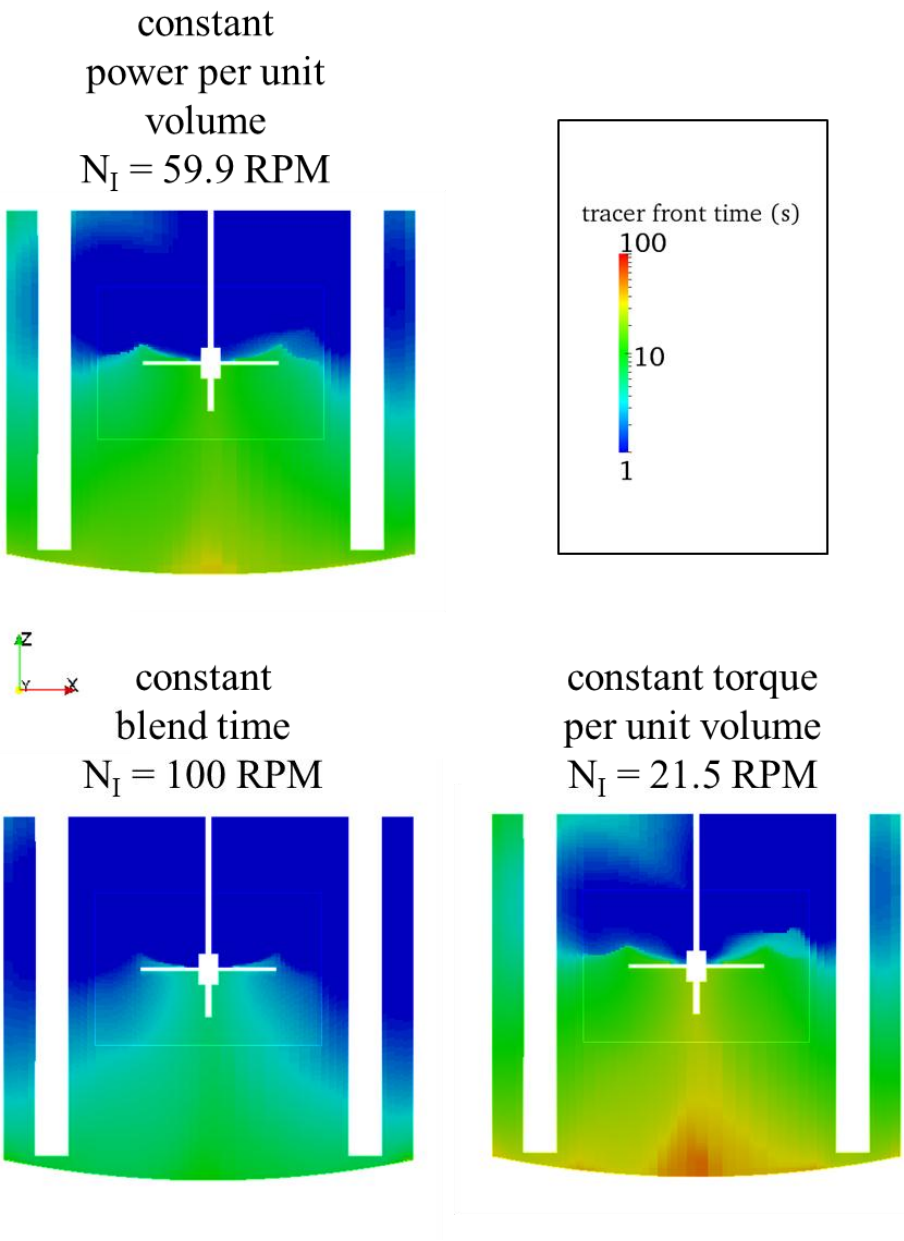

Figure 5.10. Vertical cross sectional slices of a vessel at the 100-L scale showing the variation in the tracer front time distribution with scale-up objective. Flow data is from CFD simulations based on the conditions at the start of the reaction ($\eta \approx 5.9 \times 10^4$ kg/m/s).

Once the t_{front} distribution is obtained, the zone grid is generated using the layer-by-layer zoning algorithm. The algorithm was designed with the potential of employing more than one property to build the zone structure, but the tracer front time (t_{front}) was the sole property used in this work. The tolerances used to zone the reactor based on the distribution of t_{front} values were as follows:

$$\Delta\varsigma_{\min} = 0.35 \qquad a_{\varsigma} = 0.080 \qquad \varsigma_0 = \overline{t}_{front}$$

A typical zone distribution is shown in Figure 5.11. The computation time required to zone one CFD domain is around 60 seconds; the relatively short computation time is one of the strengths of the layer-by-layer algorithm.[86] The number of zones generated is not controlled directly; rather the range is specified by adjusting $N_{z,\min}$ and $N_{z,\max}$, the minimum and maximum number of cells per zone, respectively. A grid independence test, based on the PSD obtained in at 10-m^3 scale (the most computationally-intensive scenario due to extensive concentration gradients) after 1.75 h was performed to determine the number of zones required within the population balance model to render the simulation output grid independent. The results indicated that approximately 100 zones were required to achieve zone grid independence and this was achieved by setting $N_{z,\min}$ and $N_{z,\max}$ to 80 and 150, respectively. In the simulations presented in this work, the number of zones generated varied between 99 and 102.

Closer examination of Figure 5.11 reveals that the zones generated with the layer-by-layer algorithm are visually blocky and do not match the contours of tracer front time exactly. The blocky shape of the zones is characteristic of the layer-by-layer zoning algorithm. The final shape of the zones can be designed to closely follow the contours of the property data sets used to generate the zones by reducing the tolerance terms used to determine whether to reject an

additional layer of cells during the growth of a zone. The drawback to reducing the tolerance terms by orders of magnitude is the creation of a glut of small zones, characterized by cell sizes less than 1% of $N_{z,\min}$. While these tiny zones are eliminated during the merge/clean-up operation, the computational time required during both the generation stage and the merge stage increase may increase from around one minute to over an hour and one of the main advantages of the layer-by-layer algorithm is lost. However, this approach may still potentially be computationally faster than an algorithm in which zones are generated on a cell-by-cell basis, while maintaining the cell-by-cell algorithms strength of generating zone contours that closely match the property contours. Employing a zone structure that more closely matches the shape of the tracer-front contours may reduce the number of zones required to achieve zone-grid independence in the PBM. Thus the increase in computational resources required for zoning may be offset by a reduction in the computational resources required to resolve the PBM. The impact of the zone shape on the performance of the PBM may be investigated in future work.

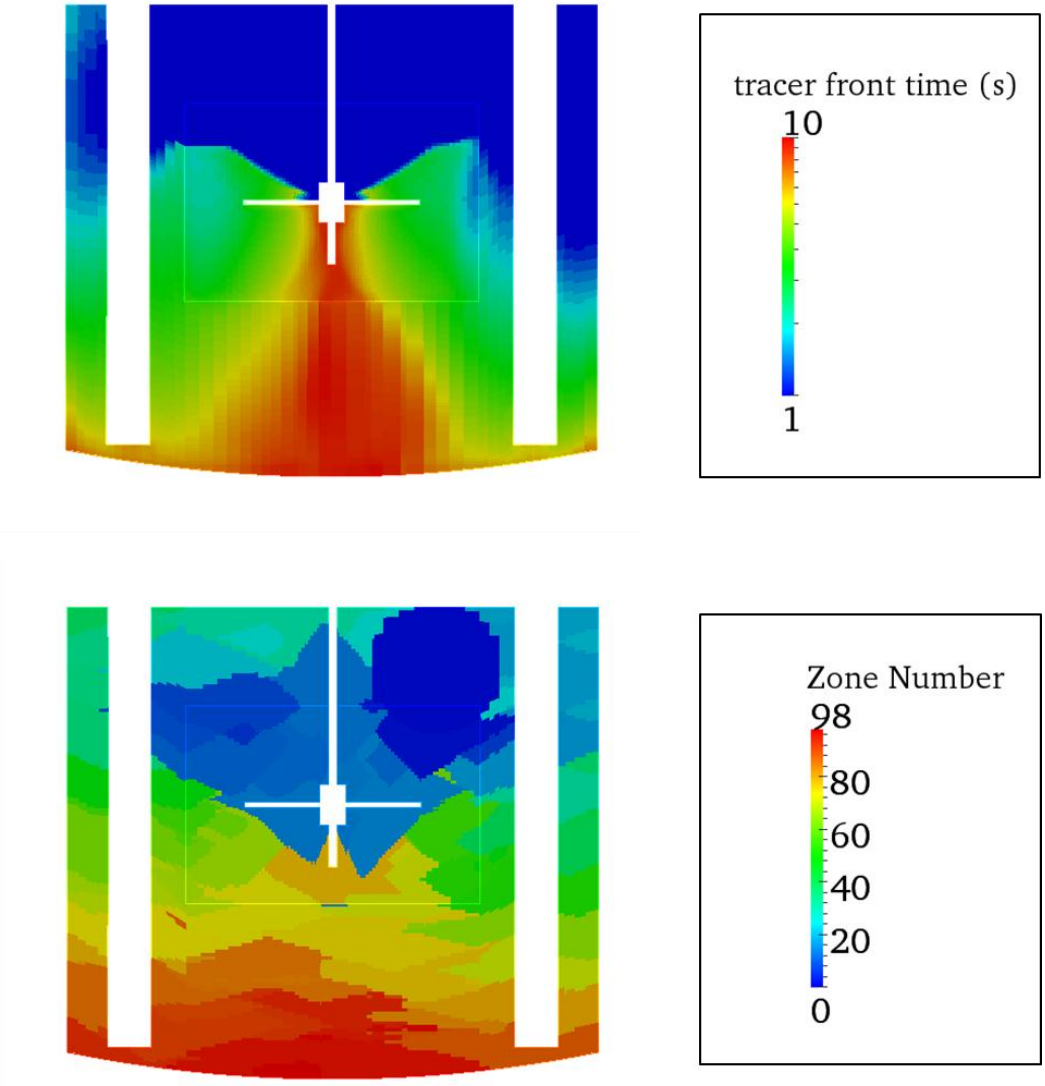

Figure 5.11. Schematic demonstrating the adaptation of the tracer front distribution to generate the network-of-zones grid for the 1 L vessel. $\eta \approx 5.9 \times 10^4$ kg/m/s; N_I = 100 RPM. The large circular zone is the feed zone.

5.4.2 Framework Predictions

A primary objective of this work was to demonstrate the use of a computational framework for predicting how changes to the macro-mixing length, inherent to process scale-up, may affect the properties of the final polystyrene latex. The key property of focus in this work is the PSD. As mentioned in the introduction, changes in the PSD will affect the ease with which the product can be processed, the productivity (via the achievable solids concentration), and the performance in end-use applications such as film formation time and the permeability of the film. The inherent complexity of the emulsion polymerization process dictates that further advances in the framework will be beneficial, potentially providing meaningful guidance towards a larger scope of potential issues, such as heat transfer considerations, production yield and product molecular weight(s).

The main objective of scale-up is to design a large scale mixing system that achieves the same mixing quality as a laboratory tank.[87] In very large reactors, achieving a similar mixing quality may be impossible, in which case the objective is to understand how changes in the length and time scale influence product quality, so that conditions at the large scale may be altered in order to overcome these differences. In the production of polymer latexes, particularly high solid content latexes, achieving the correct proportion of large particles and small particles is necessary in order to meet productivity and quality objectives.[30] One of the most important objectives in the production of concentrated polymer latexes is the timely dispersion of reactants throughout the vessel. The associated scale-up method towards achieving this objective is to maintain a consistent blend time across reactor scales. If the flow regime is fixed (i.e. both the laboratory and

commercial vessels rely on turbulent mixing), the process blend time is inversely proportional to the impeller rotational speed.[87] Maintaining a constant blend time (t_{blend}) is generally not feasible due to the increased energy and torque requirements associated with maintaining a constant impeller rotational speed during scale-up. For a process utilizing a pitched-blade turbine agitation system within the turbulent regime, the scale-up from a 1 L laboratory vessel to a 10 m^3 commercial vessel requires approximately 450 times the amount of holding power per unit volume and the gearbox would be have to deliver roughly 3000 times the amount of torque per unit volume of latex being produced. Conversely, the most pragmatic scale-up approach, assuming that motor size will be restricted at the largest scales, is to maintain a constant delivered torque per unit volume (T_Q/V). In between these two extremes lies the recommended "first-guess" approach:[10] delivery of a constant holding power per unit volume (P/V) across a wide range of vessel scales.

CFD simulation, when used in isolation, can provide helpful information to process engineers. It has already been shown that predicted blend time will increase from 6.5s to around 90s (an increase by a factor of 14) when scaling up from 1 L to 10 m^3 when the impeller rotational rate was adjusted to maintain constant T_Q/V. This is less than the change predicted by classical heuristics alone, whereby blend time is expected to increase by a factor of 21.5, and it can be attributed to a transition from mostly-turbulent to fully-turbulent mixing. The advantage of incorporating CFD simulation into a framework containing a population balance model lies in being able to directly predict the impact of different scale-up approaches on final product properties, a more direct indicator of productivity than process blend time.

As stated above, one of the current restrictions of the framework presented in this work is the fixed arrangement of the network-of-zones. Many latex products are produced in semi-batch process, whereby the liquid height will change over the course of reaction. The mixing performance of a reactor may change as the liquid level rises. In a reactor agitated with a single impeller, mixing performance is known to be very poor if the aspect ratio (the ratio of liquid level to vessel diameter) increases beyond 1.5.[87] The network of zones generated at a low liquid level will differ from the network of zones generated at a high liquid level, as can be seen in Figure 5.12. The general shape of the zones in the lower region of the tank remains the same if the feed location does not change with liquid level (e.g. using a feed pipe to ensure the feed is introduced near the impeller), as the flow profile in the bottom of the tank maintains a similar shape. However, the size of the automatically-generated zones will increase with liquid height unless the zoning parameters, $N_{z,\min}$ and $N_{z,\max}$ are adjusted in proportion with the relative change in the liquid level.

The most pragmatic solution for dealing with a variable liquid level (with a fixed feed location) may be to generate the zones using the maximum liquid level. The upper region zones could be initially specified as empty and the flow-exchange information could be updated periodically to account for the changing location of the liquid surface. The case where the feed region changes with liquid level (e.g. a surface feed) is more challenging, as the time required for reactants to spread to the lower regions of the tank will increase as the liquid level rises. The network-of-zones grid would need to be reshaped periodically, requiring the aggregation and redistribution of data as the location and shapes of the individual zones would change. There is no guarantee that the PBM predictions will remain accurate as multiple aggregation and redistribution operations

are carried-out over the course of a full simulation, unless the resolution of the zone grid is increased substantially.

Fortunately the framework can produce meaningful predictions for semi-batch processes if the kinetic events that are affected by mixing performance are restricted to short time periods, over which liquid level can be assumed to be constant. In the production of a bimodal polystyrene latex, it would not be unreasonable to propose that the *in situ* generation of the secondary particle population is the production step which is most strongly affected by the mixing performance of the reactor. A change in the number density of small particles produced will subsequently affect the growth of both the small and large particles, leading to changes in the diameter ratio between and volume proportion of small particles to large particles. Concurrently it is important to demonstrate that the last step in the process, the growth of both populations, is not restricted by the mixing capabilities of the vessel at the largest scale.

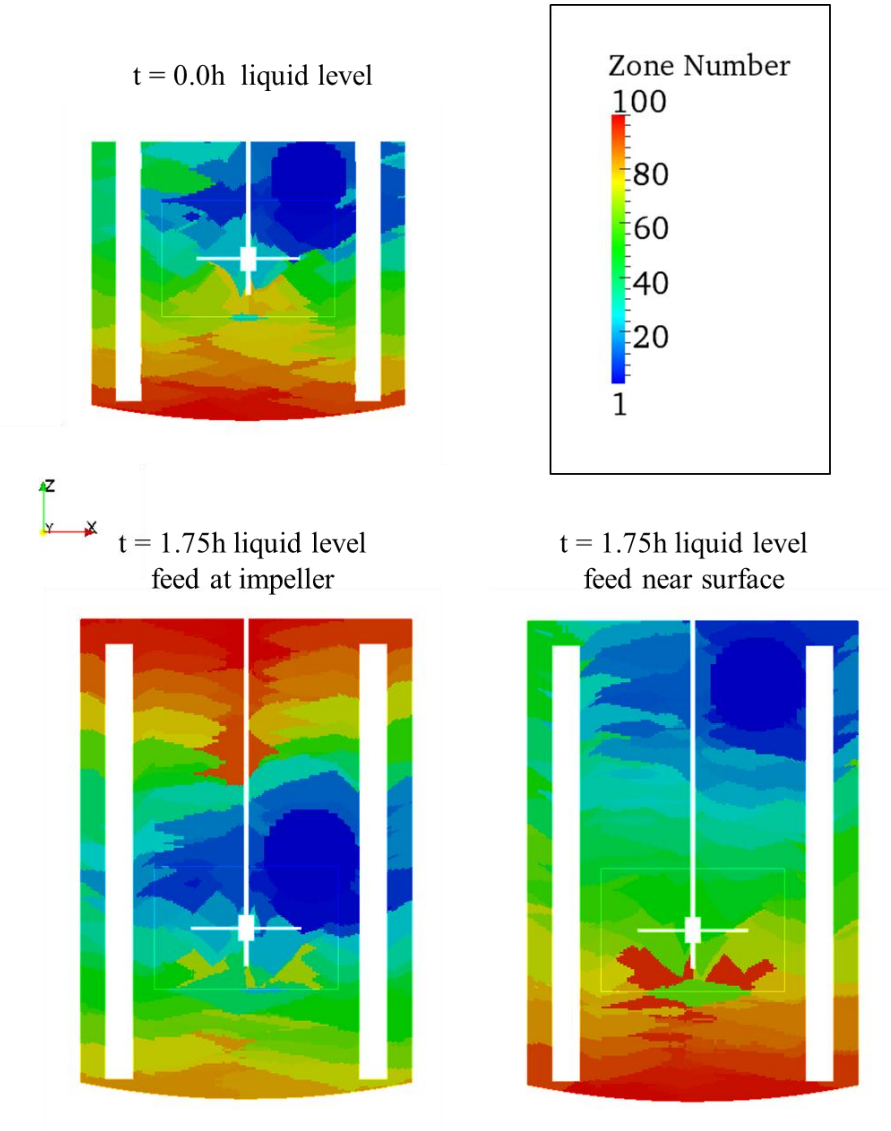

Figure 5.12. Illustrating the effect of changing the vessel height and the tracer injection location on the layout of the PBM grid generated for a 10 m^3 vessel with the LBL automatic zoning algorithm. $\eta \approx 5.9 \times 10^4$ kg/m/s; N_I = 12.9 RPM.

As outlined in Section 5.2.2, two approaches to initiator and surfactant addition were examined: (i) feeding the initiator and surfactant into the reactor at the liquid surface over a short time frame and (ii) instantaneously dispersing the initiator and surfactant to eliminate the effects of slow mixing. In the first scenario, the secondary particle population is created by feeding in a shot of

surfactant and initiator over a period of approximately five minutes. The inability of the reactor to instantaneously disperse the reactants results in a concentration gradient, with the concentration of surfactant and initiator being highest in the feed zone. This has two effects. The first effect is a high local micelle concentration, leading to an increased rate of micellar nucleation. The second effect is an increase in the local ionic strength which affects particle stability and thus the rate of particle coagulation. The localized concentration gradients during this short nucleation phase will have a large impact on the PSD of the final product, as can be seen via examination of Figure 5.13. There are two trends to note as the vessel is scaled-up using the constant P/V criterion. The first trend is the widening of the large mode, a trend that asserts itself even when departing from perfect mixing to the 1-L scale. The probable cause of this widening is rapid particle coagulation within the reactor zones where local ion concentration exceeds a critical coagulation concentration (CCC). At the 1-L scale and 100-L scale, the peak of the large mode remains around 340 nm in diameter. This suggests that the small particles, as they're formed via micellar nucleation, are rapidly coagulating with the large particles and with other small particles. Large particles, due to their lower number concentration are much less likely to collide and coagulate with other large particles.[99]

The second scale-up effect seen in Figure 5.13 is the change in the peak diameters of both modes, which is only seen at the 10-m^3 scale. The large particle mode drops from 340 nm to around 310 nm in diameter, while the small particle mode increases from roughly 15 nm to 25 nm in diameter. The mass fraction of small particles is also much higher at the 10-m^3 scale compared to all others. The rate of particle nucleation appears to be higher at the 10-m^3 scale; the fact that the effect is not seen at the 100-L scale suggests that the time scale of rapid particle coagulation may

be faster than the time scale of micellar nucleation (i.e. if the reactor was scaled-up gradually, one would observe issues with regards to rapid particle coagulation before observing changes with regards to particle nucleation). However, examining the final N_p values (refer to Figure 5.14), the number of particles actually decreases from approximately 2.2×10^{22} m^{-3} at the 1-L and 100-L scales to 1.4×10^{22} m^{-3} at the 10-m^3 scale. The enhanced rate of particle nucleation has a secondary effect on the final PSD arising from the competitive growth between the two sets of particles. The cross-over diameter between zero-one and pseudo-bulk for styrene is around 110 nm, such that the free radicals are compartmentalized within the small particles, but not within the large particles. The growth rate of the large particles is proportional to the aggregate volume of the large particle population while the growth of the small particles is proportional to their number concentration. The small particles will continue to grow at a constant rate, notwithstanding ongoing particle coagulation, while the growth of large particles tends to accelerate as they grow in volume. The enhanced nucleation rate of small particles leads to a larger proportion of the polymerization occurring within the smaller particles and slower growth in the mean volume of the large particle population. This reduces the transient divergence in the competitive growth rate between the two populations, which results in a narrower diameter ratio between the large mode and small mode in the final product. At the 10-m^3 scale, the large particle PSD is wider and has a large tail skewed towards a higher diameter, suggesting an increased rate of large particles coagulating with other large particles.

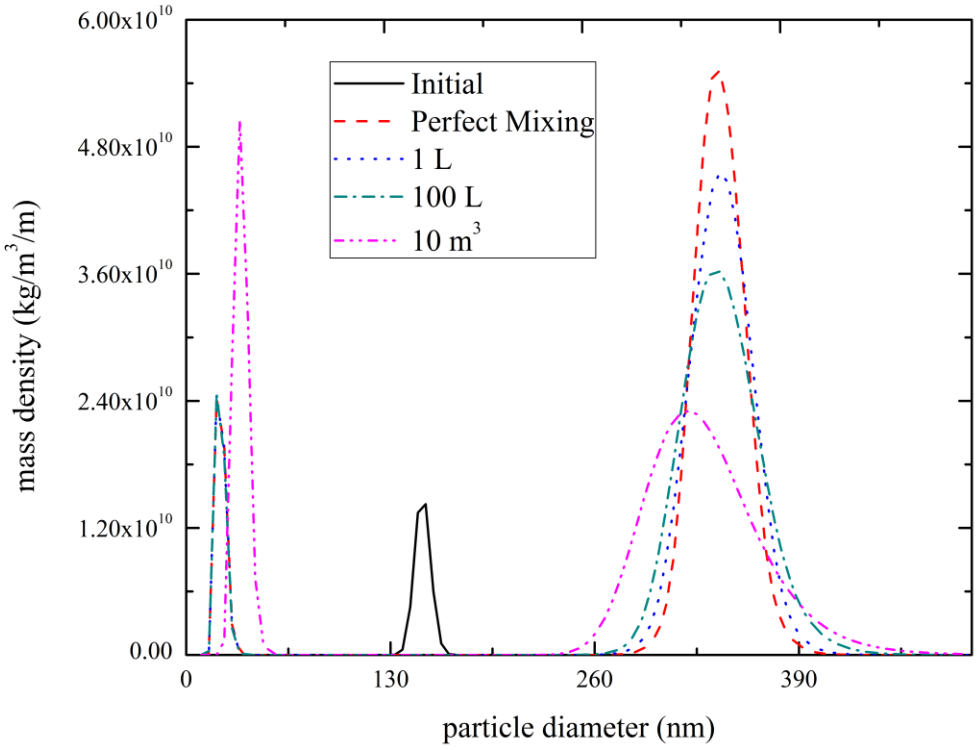

Figure 5.13. Simulation results predicting the PSD of the latex product obtained at the end of a semi-batch process (t = 1.75 hours. The initial polystyrene latex is a low solids content monomodal latex comprised of particles with a mean diameter of 150 nm. A second mode of particles is nucleated via an injection of surfactant and initiator and the two modes are then grown together over a period of 1.75 hours. Scale-up is performed maintaining constant P/V. Note that the PSD of the initial latex is included for reference.

If one considers the feed zone itself, it is apparent why the increase in vessel length scale leads to an increase in local reactant concentration. The volume of the feed zone will scale proportionally with reactor volume, while the surface area of the feed zone, which exchanges flow with its neighbours, increases with reactor volume to a power of 2/3. If the flow field remained constant across vessel scales, the residence time of reactants within the feed zone would increase proportionally to the vessel's length scale (i.e. volume divided by surface area). Examining

Figure 5.9, it can be seen that the average velocity magnitude increases as the reactor is scaled-up with the P/V approach, but the increase in velocity is not proportional to the reactor length scale and there is an increase in residence time (within the zone), except when the vessel is scaled up with a constant t_{blend}. This zonal residence time, referred to as the zonal mixing time in Chapter 4 is expressed as:

$$\theta_{m,z_{feed}} = \frac{v_{z_{feed}}}{\sum_{y \neq z_{feed}} Q_{z_{feed},y}} \tag{5.92}$$

Under fixed kinetic conditions (a constant rate of consumption and a constant feed rate), an increase in $\theta_{m,z_{feed}}$ would result in the surfactant and initiator reaching a higher concentration in the feed zone. Under simulated process conditions, an equilibrium concentration is not achieved, but the rate of particle production and particle coagulation in the feed zone increase with reactor scale-up, except under the constant t_{blend} approach.

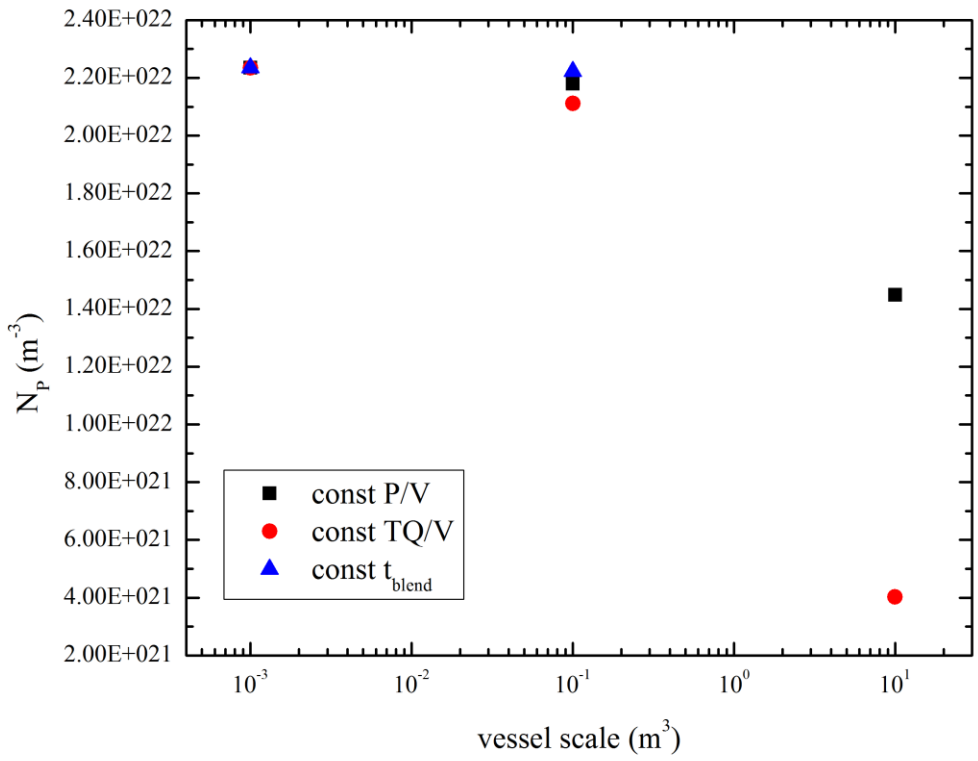

Figure 5.14. Predicted impact of reactor scale-up on Np using the polymerization conditions described in Figure 5.13. The initial polystyrene latex is a low solids content monomodal latex comprised of particles with a mean diameter of 150 nm. A second mode of particles is nucleated via an injection of surfactant and initiator and the two modes are then grown together over a period of 1.75 hours.

The second scenario simulated was a styrene EP process in which the surfactant and initiator, along with some additional monomer, are distributed uniformly in the reactor at t = 0. The remaining monomer is fed into the vessel from t = 20 minutes onwards. This ensures that the reactant concentration is uniform during the nucleation stage, but the exchange of material across zones is allowed during the growth stage in order to predict if the mixing capabilities of the reactor are fast enough to eliminate effects due to a concentration gradient in the monomer as it is dispersed from the feed zone. Essentially, the objective of the second scenario was to isolate any

changes in PSD with scale-up due to the particle growth phase, the phase in which the liquid height in the vessel changes appreciably. Due to the fixed configuration of the zone network model, it is assumed that all of the PBM zones grow proportionally to the change in liquid volume. In a thorough model, the inter-zonal flow rates would need to be adjusted to account for a change in zone surface area, which would offset some of the increase in θ_{m,z_i} due to an increase in zone volume. However it can be seen in Figure 5.15 that there is little change in the final product PSDs with reactor scale-up, when the impeller speed is adjusted to maintain a constant P/V. If the inter-zonal flow rates were increased in proportion to zone surface area, the predicted mixing performance would improve rather than deteriorate, so this modification would not affect the conclusion arrived at through simulation results. These simulation results also suggest that the timescale for particle growth is much longer than the timescale of mixing, such that the monomer dispersion could be approximated as instantaneous. Therefore, in the scenario in which initiator, monomer and surfactant are fed in semi-batch, the discrepancy in particle size distributions seen during scale-up arise during the stage in which the small particle population is created. If the surfactant and initiator are introduced rapidly to keep the small particle nucleation stage short, the approximations of constant liquid level and constant fluid properties are acceptable. It must be noted that the nucleation phase lasts for around 20 minutes, so one must bear in mind that the approximation of a constant liquid level is acceptable only when the framework is used as a preliminary assessment tool to guide pilot plant experimentation. Further advancements in both the models that comprise the computational framework and our mechanistic understanding of the phenomena governing the kinetics of emulsion polymerization are required before the capital-intensive process of experimental scale-up can be eliminated in favour of an entirely-computational approach.

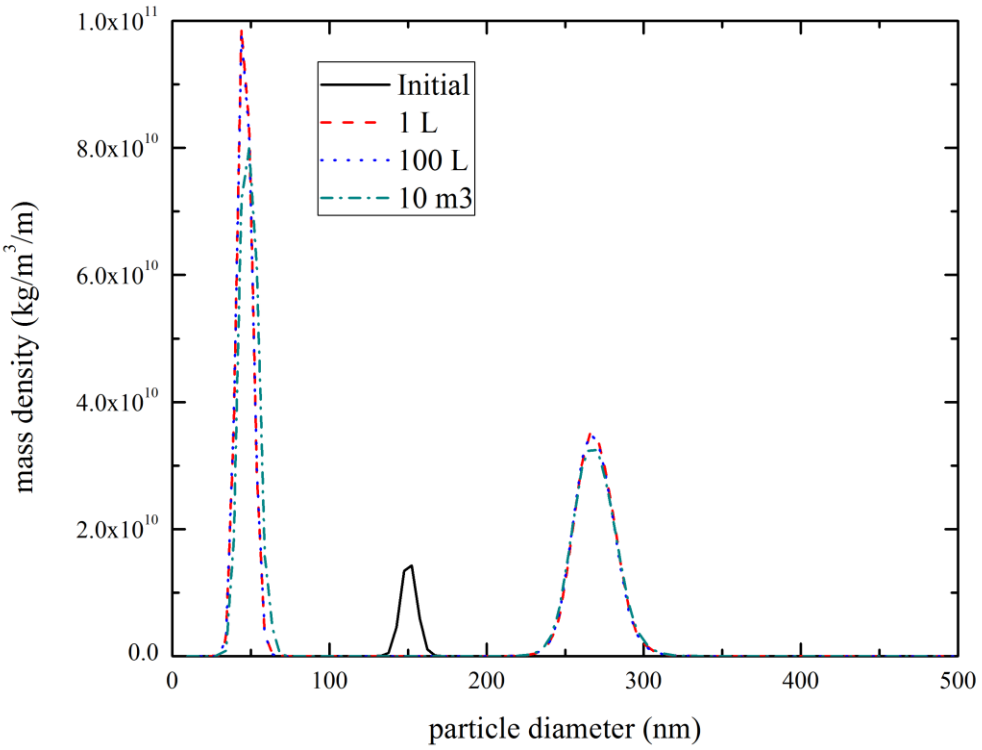

Figure 5.15. Simulation results predicting the PSD of the latex product obtained at the end of a semi-batch process (t = 1.75 hours). The initial polystyrene latex is identical to the initial latex described in Figure 5.13. The surfactant, initiator and an extra 50 wt.-% monomer are pre-dispersed in the vessel at the start of the simulation to eliminate the effect of reactor inhomogeneity on the particle nucleation step. Styrene is fed into the reactor over a period of 1.75 hours to growth the two particle modes together. Note that the PSD of the initial latex is included for reference.

The framework may also be used to examine the difference in predicted product PSD for different scale-up approaches. The t_{front} contours (Figure 5.10) showed that the degree of inhomogeneity is relatively poor when the vessel is scaled-up while prioritizing equipment limitations

(maintaining a constant volumetric torque). The accompanying snapshot of the final PSDs (Figure 5.16) yields two further points of information. First, the quality of the final product at the 1-L scale is duplicated at the 100-L scale when the impeller rotational speed is maintained at 100 RPM, as expected due to the slight reduction in blend time. Second, the increased rate of micellar nucleation (due to local accumulation of surfactant), which is seen at the 10-m^3 scale in Figure 5.13, is also observed at the 100-L scale when the reactor is scaled-up based on maintaining a constant T_Q/V. While the product quality may be acceptable at the 100-L scale, the PSD of the product obtained at the 10-m^3 scale is vastly different from the product obtained at the 1-L scale, as can be seen Figure 5.17. The non-zero particle mass density at 500 nm indicates that the maximum cell size employed within the PBM was not large enough to accurately capture the performance of the 10-m^3 vessel where mixing is very slow. At particle diameters of 500 nm, the high shear rates generated in the impeller region and near the baffle walls will increase the rate of particle coagulation. Scrap formation could become a serious issue in a reactor where mixing is poor. If the framework presented results similar to Figure 5.17 for an actual industrial process, it would be advisable to reduce the surfactant and initiator feed rates before running the experiments at the pilot- or mini-plant scale.

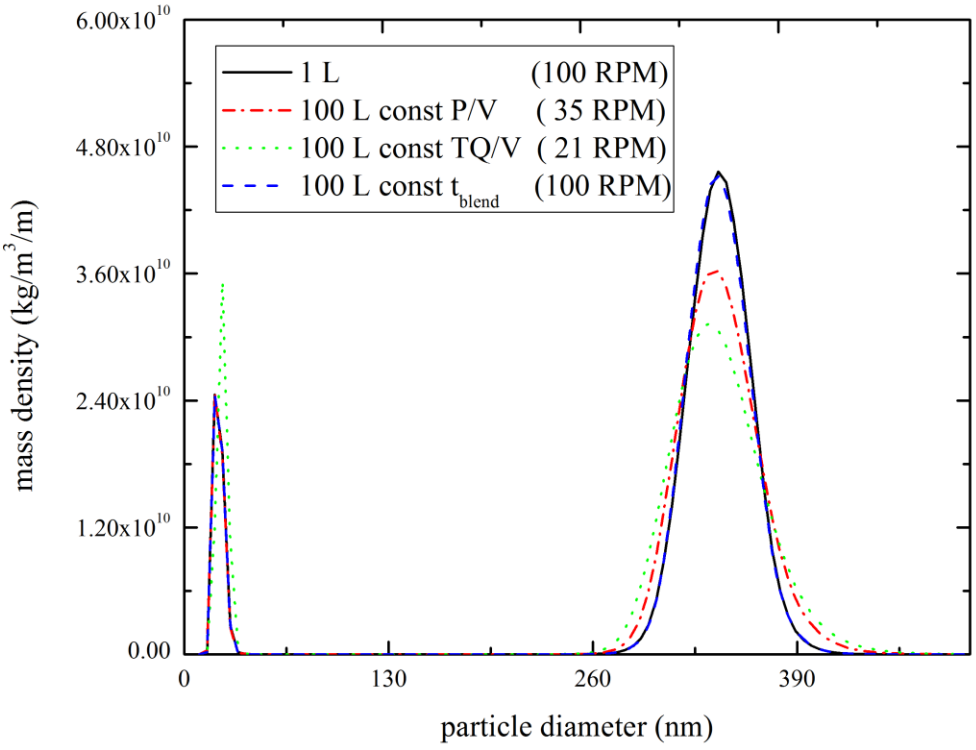

Figure 5.16. Simulation results demonstrating the impact of vessel scale-up criteria on the PSD of the final latex, varying the scale-up objective. The three simulations run at the 100-L scale were scaled-up from the 1-L base case scenario by adjusting the impeller rotational speed to meet three different scale-up objectives. The polymerization conditions are identical those described in Figure 5.13. The initial polystyrene latex is a low solids content monomodal latex comprised of particles with a mean diameter of 150 nm. A second mode of particles is nucleated via an injection of surfactant and initiator and the two modes are then grown together over a period of 1.75 hours.

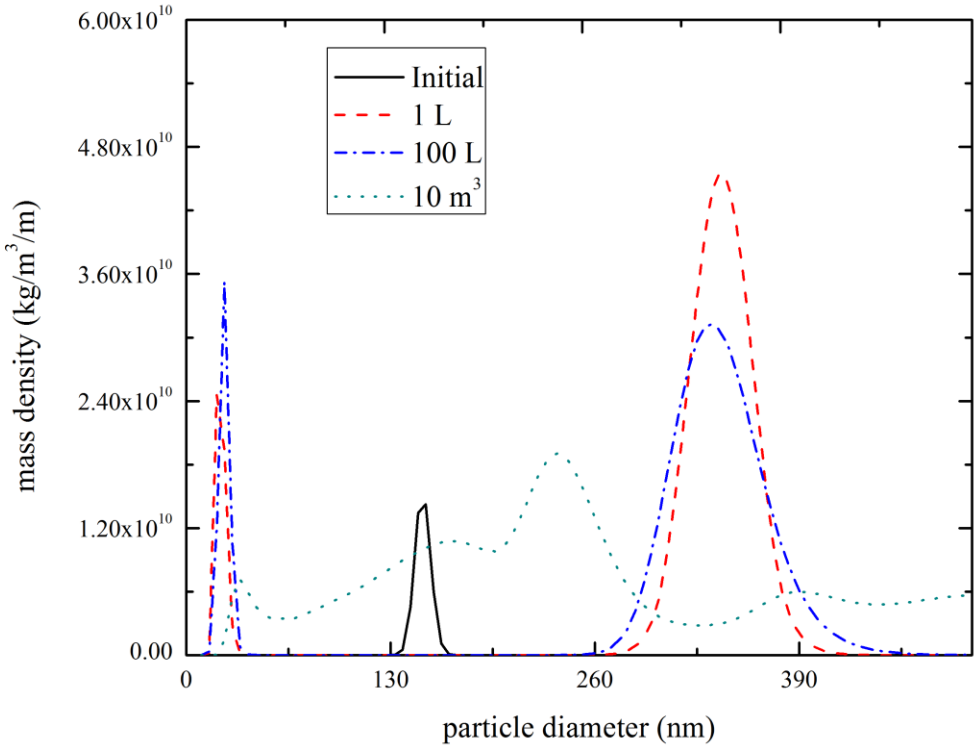

Figure 5.17. Simulation results demonstrating the impact of vessel scale-up criteria on the PSD of the final latex. The reactor is scale-up from 1 L to 10 m^3 using the constant torque-per-unit-volume (T_Q/V) approach. The polymerization conditions are identical those described in Figure 5.13. The initial polystyrene latex is a low solids content monomodal latex comprised of particles with a mean diameter of 150 nm. A second mode of particles is nucleated via an injection of surfactant and initiator and the two modes are then grown together over a period of 1.75 hours.

The packing model developed by Pishvaei *et al.*[5] may be used to compute estimates of the packing parameters and, therefore, predict *a priori* latex rheological properties using the PSD data. In Figure 5.18a, the relationship between reactor scale and the theoretical zero-shear maximum packing fraction of the product latex is shown. The zero-shear maximum packing fractions can be entered into the Kreiger-Dougherty equation to produce estimates of the latex viscosities at zero shear, which is shown in Figure 5.18b. The estimates of maximum packing

fraction appear to be very high, although this can be partially-explained by the very wide PSDs. At the 10-m^3 scale, the final particle size distribution is especially wide if the process is scaled-up with a constant T_Q/V, leading to a product with a lower zero-shear viscosity compared to the product obtained from the same process when it is scaled-up with a constant P/V. Finally it is noted that the viscosity is lowest (which is desirable) at the 1 L scale; this is due to the fact that the PSD at the 1 L scale has diameter and mass ratios that are closer the optimum from a perspective of maximizing particle packing.

The above simulation work establishes the combined CFD/PBM framework is a very useful tool for modeling the scale-up of emulsion polymerization processes. Such results would otherwise be unavailable for consideration during the scale-up process. The objective of this work was to establish the approach, build the required interface and run a set of preliminary calculations. Future work will extend the functionality of the framework. For example, the assumption of isothermal operation should be relaxed. At large reactor scales, the model predicts an accumulation of reactants in the vicinity of the feed zone. The enhanced rate of particle nucleation and coagulation observed in this zone may lead to the formation of a local hotspot due to two mechanisms: (i) an increase in the concentration of small particles increases the local rate of polymerization and (ii) excessive particle coagulation could lead to an increase in local fluid viscosity, potentially reducing rate of flow and, hence, energy exchanged between the zone and its surroundings. Any changes in reactor temperature would be accompanied by changes in fluid viscosity, so the model framework is especially well-suited for modeling non-isothermal operation.

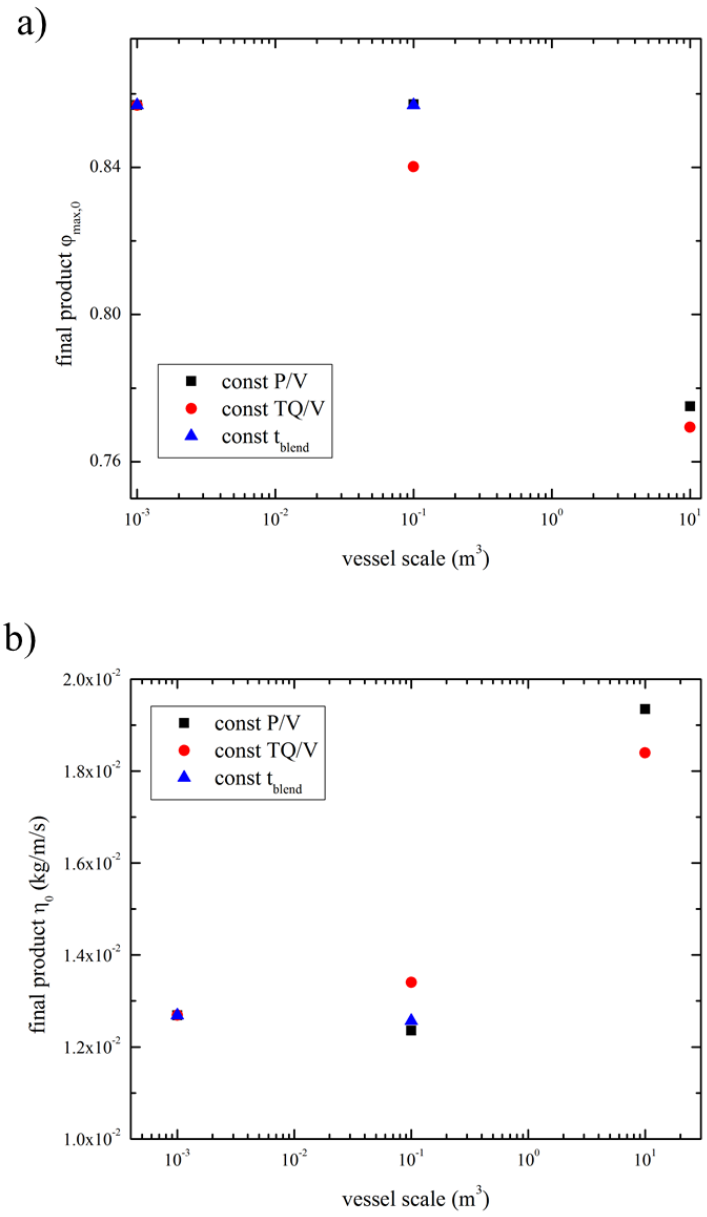

Figure 5.18. Variation in a) the theoretical maximum packing fraction and b) the zero-shear viscosity of the final product latex with (i) vessel scale and (ii) scale-up approach. Note that geometric similarity is maintained. The polymerization conditions are the same as those described briefly in Figure 5.13. The initial polystyrene latex is a low solids content monomodal latex comprised of particles with a mean diameter of 150 nm. A second mode of particles is nucleated via an injection of surfactant and initiator and the two modes are then grown together over a period of 1.75 hours.

5.5 Conclusion

The hybrid network-of-zones population balance / CFD computational framework is capable of providing unique insight into the scale-up of emulsion polymerization processes, while still being economical enough to apply in an industrial environment. Tracer dispersion simulations indicate that, under realistic conditions, the amount of time required to blend reactants that are introduced under semi-batch feed will increase with reactor scale. The blending data can be used to divide the reactor into a network-of-zones to directly model and predict the impact of a longer reactant blend time on the time-evolution of latex PSD during a semi-batch styrene EP. The framework predicts that limitations in reactant blending will affect the PSD and rheological properties of the final product. When blending is particularly poor, latex destabilization and scrap formation may become an issue. From an industrial point of view, the framework holds promise as a tool for developing scale-up rules and strategies that minimize differences in PSD upon scale-up. Application of the framework is currently limited to processes where the mixing restrictions are critical over a short time frame only, such that the liquid level can be assumed to be constant. Future development will focus on improving the framework to accommodate large changes in the liquid level and relaxing the assumption of isothermal operation, so that the framework will be applicable to a wider range of emulsion polymerization processes.

Chapter 6

Concluding Remarks

6.1 Summary of Results

The emergence of robust and affordable computational fluid dynamics (CFD) software has revolutionized process scale-up, as process engineers no longer have to rely solely on heuristics (and experience) to ensure that primary mixing objectives are met at each successive process scale. The production of polymer latexes via emulsion polymerization is, however, a highly complex process with multiple mixing-objectives. For such a process, the development of a process model that accounts for non-homogeneity in the flow field will reduce the time and money required for scale up, production and, finally, commercialization. Due to the computational resources required, it is currently it is unfeasible to program a population balance equation-based process model directly into the CFD simulation code, but hybrid modeling, where the process model is solved on a much coarser mesh, has emerged as a viable approach. It had been demonstrated that a combined CFD-population balance modeling (PBM) approach could be used to study the effect of reactor configuration on the mechanically-induced coagulation of polymer lattices, but the process model was heavily-simplified. A survey of the literature suggested that the development of a combined CFD-PBM modeling framework that was designed to investigate process scale-up was the next logical step.

As explained in Chapter 3, recent advances in our understanding of colloidal interactions between polymer latex particles has resulted in the emergence of a DLVO-based coagulation kernels that is capable of reproducing theoretical results, hitherto only available through a time-consuming

solution to the Smoluchowksi convection-diffusion aggregation equation in two dimensions over a full range of shearing conditions. Researchers are in disagreement as to whether shear-induced coagulation is relevant in emulsion polymerization at the laboratory scale, but its effect is known to be an issue at the industrial scale and is thought to be caused by turbulence. Our preliminary CFD simulations suggest that while the amount of turbulence in the flow increases with reactor scale, the maximum rate of shear due to turbulence inside the reactor may not. However, further simulation work with more refined computational meshes will be necessary in order to confirm that the characteristics of the trailing vortices, where the highest shear rates are encountered, are being captured properly. At both the laboratory and commercial scales, the maximum shear rate is large enough to influence the overall rate of particle aggregation, but not under all conditions. Larger particles and particles with more diffuse stabilization layers will be more sensitive to mechanical coagulation and may be affected within a larger region of the vessel. A comparison of a state-of-the-art coagulation model with a less computationally-intensive coagulation model suggests that the latter model will over-predict the influence of mechanical shear on the rate of particle coagulation. The discrepancy can be reduced (but not eliminated) by replacing the standard particle Peclet number with a Peclet number modified to account for interparticle interactions. If the dispersed media has a high ionic strength, as would be encountered when a latex is purposefully-coagulated via the addition of an electrolyte, the effects of mechanical agitation will be largely diminished.

In Chapter 4, using a previously-published emulsion polymerization process model, a hybrid CFD-PBM framework was constructed to examine the effects of process scale-up on the coagulation of high solids content latexes. The study was restricted to reactors operating under

the laminar and early transition regimes. Using specialized CFD simulation code that had been developed and experimentally-validated for non-Newtonian fluids, it was shown that the framework could be used to investigate the impact of reactor scale-up on the development of the latex particle size distribution over the course of a reaction.

As described in Chapter 4, the first version of the framework was restrictive. The CFD simulation code, POLY3D, was not adapted to study turbulent flow and the automatic zoning algorithm was simplistic in nature. To assuage some of the framework's limitations, a recently published automatic layer-by-layer zoning algorithm was implemented within with Fluent®, a commercial CFD package designed to model both laminar and turbulent flow. By manipulating the transient species-tracking simulation data, it is possible to compute the amount of time it takes the reactants, which are fed in near the impeller tip, to reach every region of the reactor. The approach of using transient species-tracking data to compartmentalize the reactor has not been previously-published. The network of zones generated using this technique allows us to directly include the influence of inhomogeneous mixing inside the process model.

Combined with an up-to-date styrene emulsion polymerization population balance model, it was demonstrated in Chapter 5 that the framework is well-suited to investigating the scale-up of styrene emulsion polymerization, where the target PSD was bimodal. Simulation results indicated that the slow dispersal of surfactant and initiator, a problem that emerges at the pilot- and commercial- scales, results in much higher rates of particle nucleation and particle coagulation in and near the feed zone, resulting in the final product having a different particle size distribution. Three approaches to scale-up were examined (geometric similarity was assumed) and it was found that the final PSD was reproduced only when the reactor was scaled up based on the

objective of maintaining a constant blend time. As the reactor's blend time increases, the reproduction of the laboratory-scale PSD worsened, regardless of the scale. This shows that very relevant results can be determined using this framework that, otherwise, are unavailable in reactor design.

6.2 Recommendations

During this feasibility study, focus was concentrated on the approach, building the interface and preliminary calculations. In order to examine a wider range of emulsion polymerization processes, the framework, as demonstrated in Chapter 5, should be extended account for a variable liquid level. Without a variable liquid-level functionality programmed into the process model, the framework is restricted to modeling emulsion polymerization reactions where the mixing-critical step of the reaction occurs over a short time period.

It is recommended that the framework be extended by incorporating a set of energy balance equations into the process model, along with means of estimating the heat transfer coefficient at the reactor wall using CFD simulation. The assumption of isothermal operation may be invalid, particularly in reactors where mixing is poor and larger reactor scales where the volume-normalized surface available for heat transfer is reduced. By incorporating a set of energy balance equations into the process model, the framework may be a useful tool for studying the emergence of hotspots in the reactor.

In order to model a wider range of semi-batch processes, the multizonal process model must be designed to capture the effect of mixing restrictions which play out over a larger timescale where liquid level will increase. Tracer dispersal simulations indicate that the pattern of tracer dispersion varies near the surface of the latex (i.e. momentum near the free surface is affected by the surface boundary conditions), but does not vary much below the surface. Using experimental flow-visualization and quantification techniques (e.g. particle imaging velocimetry), it may be possible to develop a correction factor such that CFD simulation results based on a full tank can be used to generate the process model grid and the interzonal flow rates could be updated each time the liquid level changes by a threshold value.

While the latest coagulation models are able to account for both shear-related and DLVO-related interaction forces, the complex procedure required to compute the fitting parameters at every time step is a problem. There are two solution approaches that may be investigated: (i) the generation of a large, multi-dimensional data set that tabulates the parameter values for a given set of particle radii, particle surface potentials and ionic strength; (ii) the creation of a simplified procedure for computing the parameters and prefactors that does not require root-finding for a function containing an integral term. The former approach (data tables) is used in industrial processes, but the latter approach may be more practical for our purposes. Due to the transient nature of turbulence, the use of a more accurate transient turbulence model (i.e. a Large Eddy-type turbulence model) may offer improved insight regarding the influence of reactor scale on the spatial distribution of the particle Peclet number. The coagulation model could be further augmented by including (separately) the contributions of surface coagulation, which is brought about by foaming at the liquid-air interface at the surface. Further developments in state-of-the-art

coagulation modeling combined with a more-advanced CFD simulation framework may justify the use of the hybrid model framework to study the impact of vessel scale-up on the mechanically-induced coagulation of polymer latexes.

Finally, it is noted that while the models used to construct the framework were chosen because they had been modeled experimentally, there is still a need to validate the predictive capabilities of the hybrid CFD/PBM modeling approach with experimentally obtained data. The best opportunity to validate the framework at large reactor scales lies with industry, due to the large amount of confidential process plant data already available. Within the academic research community, pilot-scale experimentation may be possible, and the use of scale-down models as an alternative validation technique also warrants investigation.

References

1. de la Cal, J. C.; Leiza, J. R.; Asua, J. M.; Butte, A. Emulsion Polymerization. In *Handbook of Polymer Reaction Engineering;* Meyer, T., Keurentjes, J., Eds.; Wiley-VCH Verlag GmbH & Co.: Weinheim, Germany, 2005; pp 249-322.

2. Blackley, D. C. *Polymer latices : science and technology;* Chapman & Hall: London; New York, 1997; .

3. Smith, W. E.; Ewart, R. H. *J. Chem. Phys.* **1948**, *6*, 592-599.

4. Gilbert, R. G. *Emulsion Polymerization: A Mechanistic Approach;* Academic Press Limited: San Diego, USA, 1995; .

5. Pishvaei, M.; Graillat, C.; McKenna, T. F.; Cassagnau, P. *J. Rheol.* **2007**, *1*, 51-69.

6. Ouzineb, K.; Graillat, C.; McKenna, T. F. *J. Appl. Polym. Sci.* **2005**, *3*, 745-752.

7. Vale, H. Population Balance Modeling of Emulsion Polymerization Reactors: Applications to Vinyl Chloride Polymerization, University Claude Bernard Lyon 1, Lyon, France, 2007.

8. Vale, H. M.; McKenna, T. F. *Prog. Polym. Sci.* **2005**, *10*, 1019-1048.

9. Boutti, S.; Graillat, C.; McKenna, T. F. *Polymer* **2005**, *4*, 1223-1234.

10. Oldshue, J. Y. *Fluid Mixing Technology;* McGraw-Hill: New York, NY, 1983; , pp 574.

11. Versteeg, H. K.; Malalasekera, W. *An introduction to computational fluid dynamics: The finite volume method;* Pearson - Prentice Hall: Harlow, England, 2007; , pp 503.

12. Wang, H.; Chen, H.; Periaux, J. *Int. J. Numer. Methods Fluids* **2010**, *1*, 98-118.

13. Marshall, E. M.; Bakker, A. Computational fluid mixing. In *Handbook of Industrial Mixing;* Paul, E. L., Atiemo-Obeng, V. A. and Kresta, S. M., Eds.; Wiley-Interscience: Hoboken, NJ, 2004; pp 257-343.

14. Foucault, S.; Ascanio, G.; Tanguy, P. A. *Ind. Eng. Chem. Res.* **2006**, *1*, 352-359.

15. Alexopoulos, A. H.; Kiparissides, C. Prediction of particle size distribution in non-homogeneous particulate systems: Two compartment model of an emulsion polymerization reactor. In *International symposium on polymers in dispersed media.* McKenna, T. F., Bourgeat-Lami, E. and Elaissari, A., Eds.; Lyon, 2004; pp 34-36.

16. Elgebrandt, R. C.; Romagnoli, J. A.; Fletcher, D. F.; Gomes, V. G.; Gilbert, R. G. *Chem. Eng. Sci.* **2005**, *7*, 2005-2015.

17. Elgebrandt, R. C.; Fletcher, D. F.; Gomes, V. G.; Romagnoli, J. A. A framework for modeling particle size effects in emulsion polymerization systems using computational fluid mechanics linked to a detailed population balance model. In *16th European Symposium on Computer Aided Process Engineering and 9th International Symposium on Process Systems Engineering;* Marquardt, W., Pantelides, C. C., Eds.; Elsevier B.V.: 2006; pp 551-556.

18. Harkins, W. D. *J. Am. Chem. Soc.* **1947**, *6*, 1428-1444.

19. Chern, C. S. *Prog. Polym. Sci.* **2006**, 443-486.

20. Kohut-Svelko, N.; Pirri, R.; Asua, J. M.; Leiza, J. R. *Journal of Polymer Science Part A: Polymer Chemistry* **2009**, *11*, 2917-2927.

21. Thickett, S. C.; Gilbert, R. G. *Polymer* **2007**, *24*, 6965-6991.

22. Chern, C.; Lin, C. *Polymer* **1999**, *1*, 139-147.

23. Zubitur, M.; Mendoza, J.; Cal, J. C. d. l.; Asua, J. M. *Macromol. Symp.* **2000**, *1*, 13-22.

24. Achilias, D. S.; Kiparissides, C. *Macromolecules* **1992**, *14*, 3739-3750.

25. Zubitur, M.; Asua, J. M. *Polymer*, **2001**, *14*, 5979-5985.

26. Boutti, S.; Graillat, C.; McKenna, T. F. *Macromol. Symp.* **2004**, *1*, 383-398.

27. Ai, Z.; Zhou, Q.; Xie, C.; Zhang, H. *J. Appl. Polym. Sci.* **2007**, *3*, 1815-1825.

28. Greenwood, R.; Luckham, P. F.; Gregory, T. *J. Col. Int. Sci.* **1997**, *1*, 11-21.

29. Smith, W. E.; Zukoski, C. F. *J. Rheol.* **2004**, *6*, 1375-1388.

30. Guyot, A.; Chu, F.; Schneider, M.; Graillat, C.; McKenna, T. F. *Prog. Polym. Sci.* **2002**, *8*, 1573-1615.

31. Schneider, M.; Claverie, J.; Graillat, C.; McKenna, T. F. *J. Appl. Polym. Sci.* **2002**, *10*, 1878-1896.

32. Greenwood, R.; Luckham, P. F.; Gregory, T. *Colloid Surf. A* **1998**, *1-3*, 139-147.

33. Schneider, M.; Graillat, C.; Guyot, A.; Betrémieux, I.; McKenna, T. F. *J. Appl. Polym. Sci.* **2002**, *10*, 1935-1948.

34. Schneider, M.; Graillat, C.; Guyot, A.; McKenna, T. F. *J. Appl. Polym. Sci.* **2002**, *10*, 1916-1934.

35. Schneider, M.; Graillat, C.; Guyot, A.; McKenna, T. F. *J. Appl. Polym. Sci.* **2002**, *10*, 1897-1915.

36. Boutti, S.; Graillat, C.; McKenna, T. F. *Polymer* **2005**, *4*, 1189-1210.

37. Boutti, S.; Graillat, C.; McKenna, T. F. *Polymer* **2005**, *4*, 1211-1222.

38. Mayo, F. R.; Lewis, F. M. *J. Am. Chem. Soc.* **1944**, *9*, 1594-1601.

39. Heuts, J. P. A.; Russell, G. T.; Smith, G. B.; van Herk, A. M. *Macromol. Symp.* **2007**, *1*, 12-22.

40. Buback, M.; Egorov, M.; Gilbert, R. G.; Kaminsky, V.; Olaj, O. F.; Russell, G. T.; Vana, P.; Zifferer, G. *Macromol. Chem. Phys.* **2002**, *18*, 2570-2582.

41. Kemmere, M. F.; Meuldijk, J.; Drinkenburg, A. A. H.; German, A. L. *J. Appl. Polym. Sci.* **1998**, *12*, 2409-2421.

42. Melis, S.; Kemmere, M.; Meuldijk, J.; Storti, G.; Morbidelli, M. *Chem. Eng. Sci.* **2000**, *16*, 3101-3111.

43. Forcolin, S.; Marconi, A. M.; Ghielmi, A.; Butte, A.; Storti, G.; Morbidelli, M. *Plast. Rubber Compos.* **1999**, *3*, 109-115.

44. Melis, S.; Verduyn, M.; Storti, G.; Morbidelli, M.; Baldyga, J. *AICHE J.* **1999**, *7*, 1383-1393.

45. Lowry, V.; El-Aasser, M. S.; Vanderhoff, J. W.; Klein, A. *J. Appl. Polym. Sci.* **1984**, *12*, 3925-3935.

46. Lowry, V.; El-Aasser, M. S.; Vanderhoff, J. W.; Klein, A.; Silebi, C. A. *J. Col. Int. Sci.* **1986**, *2*, 521-529.

47. Lattuada, M.; Morbidelli, M. *J. Colloid Interface Sci.* **2011**, *1*, 42.

48. Heller, W.; Peters, J. *J. Colloid Interface Sci.* **1970**, *4*, 592-605.

49. Peters, J.; Heller, W. *J. Colloid Interface Sci.* **1970**, *4*, 578-585.

50. Heller, W.; De Lauder, W. B. *J. Colloid Interface Sci.* **1971**, *1*, 60-65.

51. Heller, W.; Peters, J. *J. Colloid Interface Sci.* **1971**, *2*, 300-307.

52. Delauder, W. B.; Heller, W. *J. Colloid Interface Sci.* **1971**, *2*, 308-313.

53. Ottewill, R. H. Stability of polymer colloids. In *Polymeric Dispersions: Principles and Applications;* Asua, J. M., Ed.; Kluwer Academic Publishers: Boston, 1997; pp 31-48.

54. Hoffman, R. L. *J. Rheol.* **1998**, *1*, 111-123.

55. Einstein, A. *Annalen der Physik* **1906**, *2*, 289-306.

56. Einstein, A. *Annalen der Physik* **1911**, *3*, 590-590.

57. Sudduth, R. D. *J. Appl. Polym. Sci.* **1993**, *1*, 25-36.

58. Krieger, I. M.; Dougherty, T. J. *J. Rheol.* **1959**, *1*, 137-152.

59. Mooney, M. *J. Col. Sci.* **1951**, *2*, 162-170.

60. Sudduth, R. D. *J. Appl. Polym. Sci.* **1993**, *1*, 123-147.

61. Ouchiyama, N.; Tanaka, T. *Ind. Eng. Chem. Fundam.* **1980**, 338-340.

62. Ouchiyama, N.; Tanaka, T. *Ind. Eng. Chem. Fundam.* **1981**, 66-71.

63. Ouchiyama, N.; Tanaka, T. *Ind. Eng. Chem. Fundam.* **1984**, 490-493.

64. Ouchiyama, N.; Tanaka, T. *Ind. Eng. Chem. Fundam.* **1986**, *1*, 125-129.

65. Pishvaei, M.; Cassagnau, P.; McKenna, T. F. *Macromol. Symp.* **2006**, *1*, 63-71.

66. Sukumar, N. *Int J Numer Methods Eng* **2003**, *1*, 1-34.

67. Bharat K., S. *Applied Numerical Mathematics* **2000**, *4*, 361-369.

68. Bathe, K. J. *Finite Element Procedures;* 1996; .

69. Danckwerts, P. *Applied Scientific Research* **1952**, *4*, 279-296.

70. Kresta, S. M.; Brodkey, R. S. **2004**, 19-87.

71. Mohr, W. D.; Saxton, R. L.; Jepson, C. H. *Industrial & Engineering Chemistry* **1957**, *11*, 1855-1856.

72. Aref, H. *J. Fluid Mech.* **1984**, 1-21.

73. Szalai, E. S.; Alvarez, M. M.; Muzzio, F. J. **2004**, 89-143.

74. Aubin, J.; Fletcher, D. F.; Xuereb, C. *Exp. Therm. Fluid Sci.* **2004**, *5,* 431-445.

75. Brown, D. A. R.; Jones, P. N.; Middleton, J. C.; Papadopoulos, G.; Arik, E. B. **2004**, 145-256.

76. Kukukova, A.; Aubin, J.; Kresta, S. M. *Chem. Eng. Res. Design* **2009**, *4,* 633-647.

77. Joshi, J. B.; Nere, N. K.; Rane, C. V.; Murthy, B. N.; Mathpati, C. S.; Patwardhan, A. W.; Ranade, V. V. *The Canadian Journal of Chemical Engineering* **2011**, *4,* 754-816.

78. Bezzo, F.; Macchietto, S.; Pantelides, C. C. *Comp. Chem. Eng.* **2004**, *4,* 501-511.

79. Bezzo, F.; Macchietto, S.; Pantelides, C. C. *AICHE J.* **2003**, *8,* 2133-2148.

80. Bezzo, F.; Macchietto, S. *Comp. Chem. Eng.* **2004**, *4,* 513-525.

81. Bezzo, F.; Macchietto, S.; Pantelides, C. C. *AIChE J.* **2005**, *4,* 1169-1177.

82. Gresch, M.; BruÌˆgger, R.; Meyer, A.; Gujer, W. *Environ. Sci. Technol.* **2009**, *7,* 2381-2387.

83. Alexopoulos, A. H.; Maggioris, D.; Kiparissides, C. *Chem. Eng. Sci.* **2002**, *10,* 1735-1752.

84. Schäfer, M.; Yianneskis, M.; Wächter, P.; Durst, F. *AICHE J.* **1998**, *6,* 1233-1246.

85. Jung, S. M.; Gomes, V. G. *Chemical Engineering Science* **2011**, *18,* 4251.

86. Seppälä, M. Automatic zoning for combined CFD and multiblock modelling, Helsinki University of Technology, 2008.

87. Hemrajani, R. R.; Tatterson, G. B. Mechanically stirred vessels. In *Handbook of Industrial Mixing;* Paul, E. L., Atiemo-Obeng, V. A. and Kresta, S. M., Eds.; Wiley-Interscience: Hoboken, NJ, 2004; pp 345-390.

88. Pohn, J.; Heniche, M.; Fradette, L.; Cunningham, M.; McKenna, T. *Chem. Eng. Technol.* **2010**, *11*, 1917-1930.

89. Ramkrishna, D. *Population Balances: Theory and Applications to Particulate Systems in Engineering;* Academic Press: London, UK, 2000; , pp 355.

90. Fuchs, N. *Zeitschrift für Physik A Hadrons and Nuclei* **1934**, *11*, 736-743.

91. Smoluchowski, M. v. *Z. Phys. Chem.* **2010**, 129.

92. Verwey, E. J. W. *The Journal of Physical and Colloid Chemistry* **1947**, *3*, 631-636.

93. Hong, J. Effects of Agitation in Emulsion Polymerization - Kinetic and Mechanistic Study of Coagulum, 2008.

94. M.V., S. *Zeitschrift fur Physik* **1916**, 557-585.

95. Batchelor, G. K.; Green, J. T. *J. Fluid Mech.* **1972**, *02*, 375.

96. Behrens, S. H.; Christl, D. I.; Emmerzael, R.; Schurtenberger, P.; Borkovec, M. *Langmuir* **2000**, *6*, 2566-2575.

97. Honig, E. P.; Roebersen, G. J.; Wiersema, P. H. *J. Colloid Interface Sci.* **1971**, *1*, 97.

98. Jia, Z.; Gauer, C.; Wu, H.; Morbidelli, M.; Chittofrati, A.; Apostolo, M. *J. Colloid Interface Sci.* **2006**, *1*, 187-202.

99. Coen, E. M.; Gilbert, R. G.; Morrison, B. R.; Leube, H.; Peach, S. *Polymer*, **1998**, *26*, 7099-7112.

100. Fortuny, M.; Graillat, C.; McKenna, T. F. *Ind Eng Chem Res* **2004**, *23*, 7210-7219.

101. Hogg, R.; Healy, T. W.; Fuerstenau, D. W. *Trans. Faraday Soc.* **1966**.

102. Liu, B.; Hsu, J. *J. Chem. Phys.* **2009**, *4*, 044106.

103. Zeaiter, J.; A. Romagnoli, J.; W. Barton, G.; G. Gomes, V.; S. Hawkett, B.; G. Gilbert, R. *Chem. Eng. Sci.* **2002**, *15*, 2955-2969.

104. Immanuel, C. D.; Cordeiro, C. F.; Sundaram, S. S.; Meadows, E. S.; Crowley, T. J.; III, F. J. D. *Comput. Chem. Eng.* **2002**, *7-8*, 1133.

105. Fluent **2006**.

106. Montante, G.; Mostek, M.; Jahoda, M.; Magelli, F. *Chem. Eng. Sci.* **2005**, *8-9*, 2427-2437.

107. Deglon, D. A.; Meyer, C. J. *Minerals Eng* **2006**, *10*, 1059-1068.

108. Gori, F.; Boghi, A. *Int. Commun. Heat Mass Transfer* **2011**, *6*, 696.

109. Rudman, M.; Blackburn, H. M. *Appl. Math. Modelling* **2006**, *11*, 1229-1248.

110. Doraiswamy, D.; Grenville, R. K.; Etchells, A. W. *Ind Eng Chem Res* **1994**, *10*, 2253-2258.

111. Wu, B.; Chen, S. *Biotechnol. Bioeng.* **2008**, *3*, 700-711.

112. Nouri, J. M.; Hockey, R. M. *J. Chem. Eng. Jap.* **1998**, *5*, 848-852.

113. Pishvaei, M.; Graillat, C.; McKenna, T. F.; Cassagnau, P. *Polymer* **2005**, *4*, 1235-1244.

114. Kostansek, E. *Journal of Coatings Technology and Research* **2004**, *1*, 41-44.

115. Tatterson, G. B. *Fluid mixing and gas dispersion in agitated tanks;* McGraw-Hill: New York, NY, 1991; , pp 548.

116. Kresta, S. M.; Krebs, R.; Martin, T. *Chem. Eng. Technol.* **2004**, *3*, 208-214.

117. Mavros, P. *Chem. Eng. Res. Des.* **2001**, *2*, 113-127.

118. Patel, H.; Ein-Mozaffari, F.; Dhib, R. *Comput. Chem. Eng.* **2010**, *4*, 421-429.

119. Maggioris, D.; Goulas, A.; Alexopoulos, A. H.; Chatzi, E. G.; Kiparissides, C. *Chem. Eng. Sci.* **1998**, S315-S322.

120. Bezzo, F.; Macchietto, S.; Pantelides, C. C. *Comp. Chem. Eng.* **2000**, *2-7*, 653-658.

121. Kumar, S.; Ramkrishna, D. *Chemical Engineering Science* **1996**, *8*, 1311-1332.

122. Butté, A.; Storti, G.; Morbidelli, M. *Macromolecular Theory and Simulations* **2002**, *1*, 37-52.

123. McGown, D. N. L.; Parfitt, G. D. *J. Phys. Chem.* **1967**, *2*, 449-450.

124. Eastman, J. Colloid Stability. In *Colloid Science;* Cosgrove, T., Ed.; 2009; pp 36-49.

125. Coesnon, B.; Heniche, M.; Devals, C.; Bertrand, F.; Tanguy, P. A. *Int. J. Numer. Methods Fluids* **2008**, *4*, 427-449.

126. Radhakrishnan, K.; Hindmarsh, A. C. **1993**.

127. Kemmere, M. F. Batch emulsion polymerization: A chemical engineering approach, Eindhoven University of Technology, Eindhoven, 1999.

128. Vale, H. M.; McKenna, T. F. *Ind Eng Chem Res* **2007**, *2*, 643-654.

129. Meadows, E. S.; Crowley, T. J.; Immanuel, C. D.; Doyle, F. J. *Ind Eng Chem Res* **2003**, *3*, 555-567.

130. Guha, D.; Dudukovic, M. P.; Ramachandran, P. A.; Mehta, S.; Alvare, J. *AICHE J.* **2006**, *5*, 1836-1846.

131. Hansen, F. K.; Ugelstad, J. *J. Polym. Sci. Polym. Chem. Ed.* **1978**, *8*, 1953-1979.

132. Maxwell, I. A.; Morrison, B. R.; Napper, D. H.; Gilbert, R. G. *Macromolecules* **1991**, *7*, 1629-1640.

133. Russell, G. T.; Napper, D. H.; Gilbert, R. G. *Macromolecules* **1988**, *7*, 2141-2148.

134. Taylor, D. R.; van Berkel, K. Y.; Alghamdi, M. M.; Russell, G. T. *Macromolecular Chemistry and Physics* **2010**, *5*, 563-579.

135. Marten, F. L.; Hamielec, A. E. *J Appl Polym Sci* **1982**, *2*, 489-505.

136. Green, D. W.; Perry, R. H. **2008**.

137. Orwoll, R. **2007**, 93-101.

138. Giannetti, E. *AICHE J.* **1993**, *7*, 1210-1227.

139. Piirma, I.; Chen, S. *J. Colloid Interface Sci.* **1980**, *1*, 90-102.

140. Mukerjee, P.; Mysels, K. J. *NSRDS-NBS* **1971**, 1-222.

141. Bales, B. L.; Messina, L.; Vidal, A.; Peric, M.; Nascimento, O. R. *The Journal of Physical Chemistry B* **1998**, *50*, 10347-10358.

142. Vanzo, E.; Marchessault, R. H.; Stannett, V. *J. Colloid Sci.* **1965**, *1*, 62.

143. Coen, E. M.; Peach, S.; Morrison, B. R.; Gilbert, R. G. *Polymer* **2004**, 3595-3608.

144. O'Toole, J. T. *J. Appl. Polym. Sci.* **1963**, *4*, 1291-1297.

145. Jiang, G.; Shu, C. *Journal of Computational Physics* **1996**, *1*, 202.

146. Wang, R.; Feng, H.; Spiteri, R. J. *Applied Mathematics and Computation* **2008**, *1*, 433.